

**SUPERHYDROPHOBIC SURFACES FOR ELECTRONIC
PACKAGING AND ENERGY APPLICATIONS**

A Ph. D Thesis
Presented to
The Academic Faculty

by

Yan Liu

In Partial Fulfillment
of the Requirements for the Degree
on Polymer Textile & Fiber Engineering in the
School of Materials Science & Engineering

Georgia Institute of Technology
August 2013

Copyright © 2013 by Yan Liu

**SUPERHYDROPHOBIC SURFACES FOR ELECTRONIC
PACKAGING AND ENERGY APPLICATIONS**

Approved by:

Dr. Wong, C. P., Advisor
School of Materials Science & Engineering
Georgia Institute of Technology

Dr. Wang, Z. L.
School of Materials Science & Engineering
Georgia Institute of Technology

Dr. Hess, Dennis W.
School of Chemical & Biomolecular
Engineering
Georgia Institute of Technology

Dr. Jacob, Karl
School of Materials Science &
Engineering
Georgia Institute of Technology

Dr. Yao, Donggang
School of Materials Science &
Engineering
Georgia Institute of Technology

Date Approved: May 2013

To my husband Ziyin Lin, my daughter Elaine Y. Lin, my parents, and my parents in law
for their endless love, support, and encouragement

ACKNOWLEDGEMENTS

I would like to express my sincere gratitude to my advisor Prof. C. P. Wong for his guidance, support, and encouragement during my Ph.D study. His dedications to research and knowledge in electronic packaging area greatly inspire me. I would like to extend my gratitude to my thesis committee members, Prof. Zhonglin Wang, Prof. Dennis W. Hess, Prof. Karl Jacob, and Prof. Donggang Yao, for their invaluable discussion and advice.

I am grateful to the following faculty, administrator and staff in the School of Materials Science and Engineering, School of Polymer, Textile, and Fiber Engineering, and School of Electrical Engineering, for their guidance and support during my study. They are Dr. Meilin Liu, Dr. Anselm Griffin, Dr. Rao Tummula, Dr. Youjiang Wang, Dr. Yolande Berta, Dr. Yong Ding, Dr. Ajeet Rohatgi, Ms. Angie Beggs, Mr. Rusty Edwards, Ms. Susan Bowman, Ms. Hope Payne, Ms. Shirley Manchester, Ms. Jasmin Frett-Hodge, and Ms. Sheri Calhoun.

I would like to thank my collaborators and program managers. They are Dr. Arnab Das, Dr. Sheng Xu, Dr. Chen Xu, Dr. Ya Yang, Dr. Ian B. Cooper, Dr. Sehoon Yoo, Dr. J. Choi, Mr. Chinmay Honrao, and Dr. Markondeya Raj Pulugurtha.

I would like to acknowledge the help and discussion from my co-workers: Dr. Kyoung-Sik Moon, Dr. Yaogang Yao, Dr. Yonghao Xiu, Dr. Wei Lin, Dr. Rongwei Zhang, Dr. Owen Hildreth, Mr. Ziyin Lin, Ms. Zhuo Li, Mr. Liyi Li, Mr. Zhenkun Wu, Mr. Wentian Gu, Miss Chia-Chi Tuan, Dr. Chen Yang, Dr. Jintang Shang, Dr. Mingxiang Chen, and Dr. Lixi Wang, Dr. Zhongzheng Yang, Dr. Yanqing Ma, Dr. Pengli Zhu. Mr. Guoyun Zhou, Mr. Yuncun Zhou. I also want to thank the undergraduate students who worked hard with me, Mr. Shu Zhang, and Miss Xueying Zhao.

Last but not the least, I would like to thank my husband, Mr. Ziyin Lin, for his love and support in my study and life. My special thanks also give to my parents (Mr. Xiaochun Liu and Ms. Zhenmei Leng), my parents in law (Mr. Yongzheng Lin and Ms. Zhiyun Xu), and my daughter Elaine Y. Lin, for their encouragement and care during my study.

TABLE OF CONTENTS

	Page
ACKNOWLEDGEMENTS	iv
LIST OF TABLES	vi
LIST OF FIGURES	vi
SUMMARY	vi

CHAPTER

1	INTRODUCTION	1
1.1	Introduction of superhydrophobic surfaces	1
1.2	Fabrication of superhydrophobic surfaces	8
1.2.1	Top-down approach	8
1.2.1.1	Templating	8
1.2.1.2	Lithography	10
1.2.1.3	Metal Assisted Chemical Etching	13
1.2.1.4	Plasma Etching	15
1.2.2	Bottom up approach	17
1.2.2.1	Lay-by-layer deposition	17
1.2.2.2	Chemical vapor deposition	18
1.2.2.3	Sol-gel method	20
1.3	Applications of superhydrophobic surfaces	22
1.3.1	Anti-icing/fogging	22
1.3.2	Anti-reflection for solar cells	24

1.3.3	Friction reduction	29
1.3.4	Water/oil separation	30
1.4	Challenge and Research Objectives	31
1.4.1	Challenges	31
1.4.1.1	Oil repellent	31
1.4.1.2	Electronic packaging	32
1.4.1.3	Tunable wettability	32
1.4.1.4	The robustness of superhydrophobic surfaces	32
1.4.2	Research objectives	33
1.4.2.1	Understanding the structure effect on superoleophobicity and transition between Wenzel and Cassie states	33
1.4.2.2	Developing robust superhydrophobic SiC surfaces	33
1.4.2.3	Investigating superhydrophobic-superhydrophilic reversible wettability coating	33
1.4.2.4	Exploring the applications of superhydrophobic surfaces in electronic packaging	34
1.4.2.5	Exploring the applications of superhydrophobic surfaces in solar cells	34
2.	SILICON SURFACE STRUCTURE-CONTROLLED OLEOPHOBICTY	35
2.1	Introduction	35
2.2	Experimental Details	37
2.3	Results and Discussion	38
2.3.1	Effect of etchant solution concentration and etching time on hydrophobicity and oleophobicity	41
2.3.2	Transition from Cassie state to Wenzel state	50
2.4	Conclusions	56

3. A COMBINED ETCHING PROCESS TOWARD ROBUST SUPERHYDROPHOBIC SiC SURFACES	58
3.1 Introduction	58
3.2 Experimental details	61
3.3 Results and Discussion	62
3.3.1 Surface morphology and roughness	62
3.3.2 Hydrophobic treatment	66
3.3.3 The robustness of superhydrophobic SiC	72
3.3.4 Luminescence Property	74
3.4 Conclusions	75
4. REVERSIBLE SUPERHYDROPHOBIC-SUPERHYDROPHILIC TRANSITION OF ZNO NANOROD/EPOXY COMPOSITE FILMS	76
4.1 Introduction	76
4.2 Experimental	78
4.2.1 ZnO nanorod growth and surfactant treatment	78
4.2.2 ZnO nanorods/epoxy resin composites	79
4.2.3 Plasma etching and hydrophobic treatment	79
4.2.4 Abrasion resistance test	79
4.2.5 UV irradiation and surface characterization	80
4.3 Results and Discussion	80
4.3.1 Superhydrophobic ZnO nanocomposites	80
4.3.2 UV-induced wettability change	85
4.3.3 Mechanical robustness of the nanocomposites	89
4.4 Conclusions	91
5. SUPERHYDROPHOBIC NANOCOMPOSITES COATING FOR RELIABILITY IMPROVEMENT OF MICROELECTRONICS	93
5.1 Introduction	93

5.2	Experimental Details	96
5.2.1	Formulation of silica/epoxy nanocomposites	96
5.2.2	Fabrication of superhydrophobic surfaces	96
5.2.3	Characterizations	96
5.3	Results and Discussion	99
5.3.1	Superhydrophobic SiO ₂ /epoxy nanocomposites	100
5.3.2	THB test of the superhydrophobic coated TTR	103
5.3.3	Epoxy resin type effect on reliability improvement	106
5.4	Conclusions	109
6. HYBRIDIZING ZNO NANOWIRES WITH MICROPYRAMID SILICON WAFER AS SELF-CLEANING HIGH EFFICIENCY SOLAR CELLS		110
6.1	Introduction	110
6.2	Experimental	112
6.2.1	Si etching:	112
6.2.2	ZnO nanowire growth:	112
6.2.3	Solar cell fabrication:	112
6.3	Results and Discussion	113
6.3.1	Reflectance of hierarchical structures	113
6.3.2	Light tracing simulation of hierarchical structures	118
6.3.3	Hybridizing ZnO NWs and micropylramids for solar cells	124
6.3.4	Self-cleaning solar cells	127
6.4	Conclusions	128
7. HIERARCHICAL ROBUST TEXTURED STRUCTURES FOR LARGE SCALE SELF-CLEANING BLACK SILICON SOLAR CELLS		129
7.1	Introduction	129
7.2	Experimental	131
7.2.1	Hierarchical Si etching:	131

7.2.2	Superhydrophobic coating:	131
7.2.3	Solar cell fabrication:	132
7.2.4	Characterization:	132
7.3	Results and Discussion	133
7.3.1	Fabricated hierarchical structure by MACE	133
7.3.2	Effect of nanostructure size on light reflectance	136
7.3.3	Effect of nanostructure size on light reflectance	139
7.3.4	Superhydrophobic black Si	141
7.3.5	Fabricated self-cleaning hierarchical black Si solar cells	144
7.4	Conclusions	146
8. HIGH REFRACTIVE INDEX AND TRANSPARENT NANOCOMPOSITES AS ENCAPSULANT FOR HIGH BRIGHTNESS LED PACKAGING		147
8.1	Introduction	147
8.2	Experimental	149
8.3	Results and Discussion	150
8.3.1	Crystal phase effect	152
8.3.2	Silane treatment effect	157
8.3.3	Filler loading effect	160
8.3.4	Particle size effect	162
8.3.5	Reliability test	163
8.4	Conclusions	165
9	Future Work	167
9.1	Patterned superhydrophobic/superhydrophilic surfaces for different applications	167
9.1.1	Test vehicles design	168
9.1.2	Hydrophilic Surface Formation on SiN	170
9.1.3	Hydrophobic Surface Formation on Cu	170

9.1.4	Selective wettability and self-patterning demonstration on TVs	171
9.1.5	Conclusions and future work	173
9.2	High refractive index core-shell nanophosphors for high brightness LEDs	174
9.2.1	Proposed work	177
9.3	Mechanically robust superhydrophobic surfaces	181
APPENDIX A: AUTHOR'S PUBLICATIONS		183
REFERENCES		188

LIST OF TABLES

	Page
Table 2.1 Feature Size of textured Si (111) surfaces using Au assisted etching for different time, measured from SEM cross-section images. Si (111) surfaces were etched in HF/H ₂ O ₂ /H ₂ O (v/v/v 2:5:10) solution.....	46
Table 2.2 Young's contact angle θ_Y and apparent contact angles θ_A of Si (111) surfaces using Au assisted etching. Si (111) samples were etched in HF/H ₂ O ₂ /H ₂ O solution (v/v/v 2:5:10) for 40 min.	53
Table 2.3 Young's contact angle θ_Y and apparent contact angles θ_A of Si (100) pyramid structures after KOH etching.	55
Table 3.1 Roughness of textured SiC using different etching methods measured by AFM	65
Table 3.2 Surface roughness of Pt-assisted etching of SiC for different time	65
Table 3.3 Contact angle and hysteresis of hydrophobic treated rough SiC surfaces	69
Table 4.1 Contact angle and contact angle hysteresis of superhydrophobic nanocomposites with different ZnO NRs filler loadings.	84
Table 4.2 Abrasion test of superhydrophobic surfaces.	89
Table 5.1 Potential IC encapsulants	95
Table 5.2 List of epoxy resin, curing agent and catalyst used in this study.....	98
Table 5.3 Contact angle and contact angle hysteresis of epoxy silica nanocomposites with different reactive ion etching time.	102
Table 6.1 Sunrays simulation parameters for determining optical loss in air	120
Table 6.2 Effect of ZnO seed layer thickness variation on average weight reflectance (AWR) values	122
Table 6.3 Effect of ZnO nanowire length variation on AWR values	123

Table 7.1 Weighted reflectance on different textured surfaces	139
Table 7.2 Weighted reflectance on different textured surfaces	141
Table 8.1 Properties of silicone OE 6630	152
Table 8.2 Refractive index and relative transmittance of TiO ₂ nanocomposites with different filler loadings	161
Table 8.3 Refractive index of 1 wt.% TiO ₂ nanocomposites synthesized via hydrothermal method for different times	163
Table 8.4 Transmittance of nanocomposites before and after reliability test	165
Table 9.1 Contact angle and hysteresis of superhydrophobic Cu surface	171

LIST OF FIGURES

	Page
Figure 1.1 Contact angle of a liquid droplet wetted to a rigid solid surface.....	1
Figure 1.2 Illustration of Wenzel (top) and Cassie (bottom) States	3
Figure 1.3 Cosine of the apparent contact angle θ^* on a textured surface, as a function of the cosine of the Young angle θ measured on the same surface, yet flat.....	4
Figure 1.4 Images of advancing angle and receding angle.....	5
Figure 1.5 The self-cleaning mechanisms for Lotus-Effect surfaces	6
Figure 1.6 Surface structure of a lotus leave.....	6
Figure 1.7 SEM images of micro or nano structure naturally occurring superhydrophobic surfaces (a and b) butterfly wings, (c and d) strider's legs (e and f) cicada's wings.	7
Figure 1.8 Illumination of lotus leaf replication process (a) SEM image of lotus leaf (b) SEM image of positive replica.....	9
Figure 1.9 Illumination of using anodic aluminum oxide (AAO) template for the extrusion of high-density polyethylene (HDPE) nanofiber (a) FE-SEM images of HDPE nanofiber surfaces observed from the top and (b) cross-section.....	10
Figure 1.10 (left) SEM image of a 440-nm-diameter double-layer polystyrene surface after 120 s of oxygen plasma treatment. (right) SEM images (60°) of the size-reduced polystyrene beads and the water contact angle measurement on the corresponding modified surfaces (insets). The diameters of polystyrene beads and water contact angles on these surfaces were measured to be (a) 400 nm, 135° , (b) 360 nm, 144° , (c) 330 nm, 152° , and (d) 190 nm, 168° . Bar: 1 μm	11
Figure 1.11 (a) Schematic diagram of the hierarchical surfaces produced by a single EBL-exposure and double EBL-exposure process. (b) A macroscopic superhydrophobic surface with 2 mm linear dimension (c and d) Double EBL-exposure sample with	

secondary ridges. Both images were taken at a 45 ° tilt. The primary blocks are of the dimension of about 10 μ m × 10 μ m × 8 μ m. The secondary ridges show a 70 nm width and 200 nm periods. 12

Figure 1.12 SEM images of the superhydrophobic photopatternable PTFE/SU-8 nanocomposite coating (Scale bars in (a)–(c): 100 μ m; in (d): 50 μ m). (c) Contact-angle measurements for different thicknesses of the PTFE nanoparticle layers. (e-h) Illustrations of synthesis and microfabrication processes to achieve photo-patternable superhydrophobic nanocomposite coatings. 13

Figure 1.13 (a and b) SEM cross sectional and top view images of fabricated Si NW arrays by metal assisted chemical etching (c) Water contact angle images of fabricated and RTA treated Si NWs (d) A schematic of the hydrophilic (silanol) and hydrophobic (siloxane) groups formed on Si NWs covered with SiO₂..... 15

Figure 1.14 Schema of the deposition process, (a) photoresist over-etching by an inductive SF₆ plasma, (b) deposition of C₄F₈ layer using a capacitive C₄F₈ plasma, (c) final structure. (d and e) SEM micrographs of the Si surface after deep reactive ion etching and SF₆ plasma etching. 16

Figure 1.15 Top-view and cross section SEM images of a (PDDA-silicate/PAA) *12 / (PAH/SiO₂)*4 film (b) deposited on a quartz substrate after calcination. UV-Vis transmission spectra of coatings deposited on quartz substrates. (a) Calcined (PDDA-silicate/PAA)*12 film; (b) calcined (PDDA-silicate/PAA)*12/(PAH/SiO₂)*4 film; (c) the film in (b) after CVD of a POTS layer; (d) bare quartz substrate..... 18

Figure 1.16 Typical SEM images of CNT arrays on silicon substrates: (a) cylindrical CNT arrays with 6 μ m radius, 30 μ m pitch, and 25 μ m height; (b) cylinder CNT arrays with 10 μ m radius, 60 μ m pitch, and 11 μ m height; (c) cylindrical CNTs arrays with 10 μ m radius, 60 μ m pitch, and 90 μ m height; (d) as-grown CNT array surfaces..... 19

Figure 1.17 SEM images (a) Si islands fabricated by etching a SiO ₂ -masked Si(100) substrate in KOH. (b) Si nanowires grown on the Si islands with Au clusters on the tips of the nanowires. The scale bars are 5 μm.....	20
Figure 1.18 SEM images of top layers obtained by spin coating of 5 wt % TMS-silica nanoparticles-containing solutions. Scale bar, 200 nm. Image of a glass plate coated with a superhydrophobic antireflective bilayer coating.....	21
Figure 1.19 (a) Schematic illustration of the preparation route to form the PS-Sis. SEM images of the surfaces of PS-SIs film (SiO ₂) 0.7 wt%) (b) dip-etched by THF solution, and (c) treated by dodecanethiol solution with SET. Inset images indicate the CA of a 5 μL water drop on the corresponding surface.	22
Figure 1.20 Test of anti-icing properties in naturally occurring “freezing rain”. (a) Untreated side of an aluminum plate after the natural occurrence of “freezing rain”. (b) Treated side of the aluminum plate coated with a superhydrophobic composite after the “freezing rain”. (c) Satellite dish antenna after the freezing rain. (d) Close-up view of the area labeled by a red square in (c)	23
Figure 1.21 (a) Schematic drawing of the synthesis and hydrogen-bond driven stabilization of titanate nanobelts. (b) SEM image of (b) SEM images and water droplet image on the as-prepared superhydrophobic TNB/FAS film (c) Photograph of an ITO substrate deposited with superhydrophilic coatings (bottom) and a control ITO substrate without any coating deposition (upper) taken from a refrigerator to the humid laboratory air.	24
Figure 1.22 Roadmap projections of solar electricity generation (in billion kWh/yr) from 2000 to 2050 for the Baseline and Roadmap cases	25
Figure 1.23 General structure of a PV module	26
Figure 1.24 Nanodome a-Si:H solar cell structure. SEM images taken at 45° on (a) nanocone quartz substrate and (b) a-Si:H nanodome solar cells after deposition of multilayers of materials on nanocones. Scale bar 500 nm. (c) Schematic showing the	

cross-sectional structure of nanodome solar cells. (d) Schematic showing the self-cleaning mechanism. (e) Change of FF, J_{sc} , V_{oc} and power efficiency during a cycle of the self-cleaning process.	28
Figure 1.25 (A-D) Outline of the templating procedures for fabricating antireflective silicon pillar arrays by using nonclose-packed colloidal monolayer as template. (E) Experimental (solid) and RCWA-simulated (dotted) specular reflection at normal incidence from a flat silicon wafer and a 60 min etched silicon pillar array.	29
Figure 1.26 Scanning electron microscopy (SEM) image of a silicon nanograting structure.....	30
Figure 1.27 Cleaning process of a water surface polluted by oil (colored by a blue dye), using a weak magnet to move the foam.....	30
Figure 1.28 Simple instrument fabricated by ourselves was used to separate the mixture of diesel oil and water	31
Figure 2.1 Mechanism of Metal assisted chemical etching	39
Figure 2.2 Geometrical structures that can lead to superoleophobicity.....	40
Figure 2.3 Oil contact at surface structures with inclined walls.	41
Figure 2.4 SEM images of the surface morphologies from Au assisted etching of Si (111) surfaces; Si (111) etched in HF/H ₂ O ₂ /H ₂ O (v/v/v 1:5:10) for a) 10 min, b) 30 min, c) 60 min, and d) 180 min.	42
Figure 2.5 (a) Contact angles of water, ethylene glycol, and hexadecane on Si (111) surfaces generated by Au assisted etching in HF/H ₂ O ₂ /H ₂ O (v/v/v 1:5:10) for different times at room temperature.(b) Contact angle hysteresis of water and hexadecane on the etched Si (111) surfaces described in (a).	43
Figure 2.6 (a) Contact angles of the surfaces etched by Au-assisted etching of Si (111) surfaces in HF/H ₂ O ₂ /H ₂ O (v/v/v 2:5:10) solution for various times. (b) Contact angle hysteresis of water and ethylene glycol on the etched surfaces.	45

Figure 2.7 SEM images of the surface morphologies from Au assisted HF/H ₂ O ₂ /H ₂ O etching on Si (111) surfaces; Si(111) etched in HF/H ₂ O ₂ /H ₂ O (v/v/v 2:5:10) for a) 20 min, b) 40 min, c) 60 min and d) 120 min	47
Figure 2.8 SEM images of cross section from Au assisted HF/H ₂ O ₂ /H ₂ O etching on Si (111) surfaces; Si(111) etched in HF/H ₂ O ₂ /H ₂ O (v/v/v 2:5:10) for 40 min. The contact angle images of hexadecane are shown in the inset.....	48
Figure 2.9 (a) Contact angles of surfaces etched by Au-assisted etching of Si (111) in HF/H ₂ O ₂ /H ₂ O (v/v/v 3:5:10) solution for water, ethylene glycol and hexadecane. (b) Contact angle hysteresis of the etched surfaces with water and ethylene glycol.....	49
Figure 2.10 SEM images of the surface morphologies from Au assisted HF/H ₂ O ₂ /H ₂ O etching of Si (111) surfaces; Si (111) etched in HF/H ₂ O ₂ /H ₂ O (v/v/v 3:5:10) for a) 20 min, b) 40 min, c) 60 min and d) 90 min	50
Figure 2.11 Chemical Structures of five silanes used for surface hydrophobic treatment on Si wafers.....	52
Figure 2.12 Cosine of apparent contact angle θ_A on a textured Si (111) surface as a function of the Young's angle θ_Y	54
Figure 2.13 Cross section of Si (100) pyramid structures after KOH etching.....	55
Figure 2.14 Cosine of apparent contact angle θ_A on a textured Si (100) surface as a function of the Young's angle θ_Y	56
Figure 3.1 The tetrahedral crystal structure of SiC	59
Figure 3.2 SEM images of SiC using different etching methods (a) MAE (b) RIE (c) combined MAE and RIE.....	63
Figure 3.3 Three dimensional and one dimensional AFM images of SiC using different etching methods (a) MAE, (b) RIE and (c) combined MAE and RIE.....	64
Figure 3.4 Illustration of PFOS treatment on SiC.....	67
Figure 3.5 XPS survey of porous SiC before and after silane treatment	67

Figure 3.6 High resolution C1s spectra of (a) porous SiC before silane treatment, (b) porous SiC after silane treatment.....	68
Figure 3.7 (a) Water contact at surface structures with inclined walls (b) Laplace pressure (p) changes with height (h) and half width of two adjacent inclined walls (R_0).....	71
Figure 3.8 (a) The relationship between pH and the CA on a porous SiC surface by MAE and RIE combined etching (b) Typical water contact angle image on superhydrophobic SiC surfaces	73
Figure 3.9 PL intensity of bulk SiC and etched porous SiC (etched by combined MAE and RIE).....	75
Figure 4.1 (a) Schematic of the fabrication process for superhydrophobic ZnO nanorod composite film and its transition to superhydrophilic film under UV irradiation (b) PFOS and OTS silane treatment on ZnO nanorod composites	81
Figure 4.2 (a) X-ray diffraction of ZnO nanorods. (b-d) SEM images of ZnO nanorods composites with different filler loadings after 15 min RIE etching (b) 17% filler loading (c) 33% filler loading (d) 50% filler loading. The scale bar is 2 μ m.....	83
Figure 4.3 (a) Contact angle and contact angle hysteresis of ZnO nanorods composites with different filler loadings (b) Water droplet images of different filler loading ZnO nanocomposites in contact angle measurements.....	84
Figure 4.4 Water contact angle of ZnO nanocomposite modified by PFOS and OTS as a function of UV irradiation time	86
Figure 4.5 XPS spectra of Zn 2p _{3/2} of ZnO nanocomposites modified by (a) PFOS (b) OTS before and after UV irradiation	88
Figure 4.6 Schematic of the abrasion test employed to evaluate robustness on a superhydrophobic surface.	90
Figure 4.7 Schematic of the nanocomposite surface before and after abrasion test	90
Figure 4.8 Reversible transition between superhydrophobicity induced by silane treatment and superhydrophilicity induced by UV irradiation	91

Figure 5.1 (a) Optical image of triple track resistors (b) TEM image of silica nanoparticles	97
Figure 5.2 Illustration of (a) O ₂ plasma etching of epoxy/SiO ₂ nanoparticle composite films for surface rough structures. (b) Hydrophobic treatment with PFOS on nanocomposite surface.....	99
Figure 5.3 Surface morphology from SEM images: surface before etching (a), O ₂ plasma etched for 5 min (b), and 15 min (c)	101
Figure 5.4 Contact angle and hysteresis for silica nanocomposite surfaces etched for different time.....	102
Figure 5. 5 Configuration of THB testing hardware.....	104
Figure 5.6 Resistance (a) and leakage current (b) change of uncoated, cycloaliphatic epoxy coated and superhydrophobic silica/cycloaliphatic epoxy composite coated samples change with time in the reliability test in 85 °C/85 %RH chamber under 13.4 Volts-DC bias.....	107
Figure 5.7 Resistance (a) and leakage currents (b) change of uncoated, bis-A epoxy coated and superhydrophobic silica bis-A epoxy composite coated samples change with time in the reliability test in 85 °C/85 %RH chamber under 13.4 Volts-DC bias	108
Figure 6.1 A schematic of the hierarchical ZnO NW-Si solar cell.	114
Figure 6.2 Surface morphology of hierarchical ZnO NWs on a pyramidal Si surfaces under low (a) and high (b) magnifications, as well as cross section views under low (c) and high (d) magnifications.	116
Figure 6.3 (a) Front light reflectance of ZnO NWs on pyramidal Si comparing with planar Si, pyramidal Si, and pyramidal Si with ZnO seed layer (b) Simulated light reflectance of the ZnO NW solar cell. red: Sunrays simulation data on planar surface; blue: Sunrays simulation data on textured surface; black: experimental data for ZnO NWs on pyramidal Si.....	117

Figure 6.4 The reflection of incident light on (a) pyramidal Si (b) planar Si. The effective refractive index profile of the interface between air and (c) ZnO NWs on pyramidal Si (d) ZnO NWs on planar Si.....	118
Figure 6.5 Refractive index (n) and extinction coefficient (k) curve of crystal ZnO and ZnO nanowires.....	119
Figure 6.6 Light reflectance of ZnO NW solar cell with different ZnO NW lengths.....	121
Figure 6.7 Light reflectance of ZnO NW solar cell with different ZnO seed layer thicknesses (a) and different ZnO NW lengths (b)	124
Figure 6.8 Hierarchical ZnO NWs after screen printing process showing that only the NWs on some of the pyramid tips were destroyed by the process.	126
Figure 6.9 I-V curve of ZnO NW/pyramidal Si screen printed solar cell.....	126
Figure 6.10 Self-cleaning superhydrophobic ZnO nanowire solar cell (a) water droplet on self-cleaning surface with a contact angle of 171° (b) schematic view of the self-cleaning property.	128
Figure 7.1 The (a) schematic and (b) mechanism of metal assisted chemical etching	133
Figure 7.2 (a) Front light reflectance of micropyramidal Si with nanotexturing, compared with planar Si and pyramidal Si. (b) The reflection of incident light on a bare smooth Si, Si micro pyramids and hierarchically textured Si wafer. The images showing the difference in light reflection on three wafers.....	135
Figure 7.3 SEM images of hierarchical textured Si wafers with different micro pyramid sizes (a) pyramid size 5 μm (b) 20 μm (c) 25 μm. The nano texturing was generated by Au-assisted chemical etching for 4 min.....	137
Figure 7.4 Front light reflectance comparison of micropyramidal Si and hierarchical structure Si etched by Au-assisted chemical etching (a) Effect of different micro size pyramids (b) Effect of different nano size texturing.....	138
Figure 7.5 (a-c) Silicon pyramid surface with Au layers of thickness of, 2 nm, 5 nm and 10 nm respectively (d-f) SEM images of hierarchical textured Si wafers with different	

nano texturing sizes (d) 2nm Au (e) 5 nm Au (f) 10 nm Au. The nano texturing was generated by Au-assisted chemical etching for 4 min.	140
Figure 7.6 Silicon two scale rough surfaces of different magnifications resulting from pyramid size 20 μm + nanostructure from Au-assisted HF/H ₂ O ₂ etching for different time (a) 30s, (b) 1 min, (c) 2 min, (d) 4 min, (e) 10 min	143
Figure 7.7 (top) Contact angle and (bottom) contact angle hysteresis on Si (100) surface with 20 μm pyramid size, etched by Au assisted etching in HF/H ₂ O ₂ /H ₂ O (v/v/v 1:5:10) for different time at room temperature (bottom).....	144
Figure 7.8 Schematic of screen printed hierarchical black Si solar cells. The inset is the cross section of hierarchical Si with surface passivation layers	145
Figure 8.1 Relation of RI and light extraction efficiency	151
Figure 8.2 TEM images of TiO ₂ nanoparticles obtained via the hydrothermal method after 6 hrs reaction (the scale bar is 25 nm)	152
Figure 8.3 XRD patterns of TiO ₂ nanoparticles prepared via hydrothermal process for 6hrs (a) 0.25 M (b) 6M HCl.....	154
Figure 8.4 Crystal structure of TiO ₂ (a) anatase (b) rutile	155
Figure 8.5 (a) Refractive index (b) Transmittance of 1% TiO ₂ nanocomposites film composed of different crystal phase TiO ₂ nanoparticles	156
Figure 8.6 Chemical structure of (a) Vinyltrimethoxysilane	157
Figure 8.7 The dispersion of TiO ₂ in silicone diluted by toluene (a) as synthesized TiO ₂ (b) Vinyltrimethoxysilane modified TiO ₂ (c) trimethoxy(7-octen-1-yl)silane modified TiO ₂ with different magnifications	158
Figure 8.8 Light transmittance of 1 wt% TiO ₂ nanocomposites thin film (20 μm) modified by different chain length vinyl silanes	159
Figure 8.9 (a) Refractive index (b) Transmittance of different filler loading TiO ₂ nanocomposites film after silane treatment	160

Figure 8.10 Transparency demonstration of glass slides coated with different filler loading TiO ₂ nanocomposites (20μm thickness)	161
Figure 8.11 Transmittance of 1% TiO ₂ nanocomposites composed of TiO ₂ nanoparticles synthesized with different times.	163
Figure 8.12 Reliability test conditions	164
Figure 8.13 RI of 5 wt.% TiO ₂ nanocomposites before and after reliability test	165
Figure 9.1 10x reduction in 3D IC interconnection pitch and stand-off height as compared to flip-chip.	167
Figure 9.2 (a) Coplanar no-flow underfill, and (b)-(d) Schematic of SAM molecule coating for self-patterning underfill (selectively located on hydrophilic areas and subsequent bonding with a mating IC/TSV).....	168
Figure 9.3 Test vehicle design (a) and fabrication process (b) with patterned Cu and SiN	169
Figure 9.4 Morphology of etched copper at different etching time (a) 12 hrs (b) 24 hrs (c) 48 hrs (d) Illumination of PFOS coating on etched Cu.	171
Figure 9.5 Superhydrophobic/superhydrophilic patterned wettability process.	172
Figure 9.6 Demonstration of water droplet (a) and epoxy resin (828:4221=1:1) (b) on TVs. The inset is the side view of water droplet on TVs. The droplet stayed in hydrophilic SiN part.....	173
Figure 9.7 Commercial underfill UF 8806G on TVs after spin coating.	173
Figure 9.8 (a) Comparison of different phosphor mixing methods for white LEDs based on a blue LED chip, including yellow phosphors, yellow/red phosphors, and green/ red phosphors. (b) Relationship between light extraction efficiency and RI of the encapsulant; schematic of light extraction from a GaN LED chip.	175
Figure 9.9 (a) Proposed structure of novel nanophosphor with a QD core and a phosphor shell. (b) Schematic of polymer composite with well dispersed nanophosphor; the	

diameter of nanophosphor should be smaller than one tenth of wavelength of the incident light source to avoid the light scattering.	177
Figure 9.10 Reverse microemulsion method for silica coated CdSe QDs synthesis	180
Figure 9.11 Effective RI of nanophosphor-composite vs CdSe QDs mass and volume fraction.	181

SUMMARY

Superhydrophobic surfaces, which display water contact angles of larger than 150° , have attracted more and more attention due to their importance in both fundamental research and practical applications. This dissertation is mainly focused on the fundamental understanding and applications of superhydrophobic surfaces.

First, superoleophobic Si surface was fabricated by metal-assisted chemical etching. The geometry shape of the etched Si was controlled by the etching time and etchant concentration. Compared to Young's contact angle, the apparent contact angles of low surface energy liquids showed a transition from a Cassie to a Wenzel state when different silane treatments were applied to the silicon surface. The relationship between the re-entrant angles of etched surface structures and the contact angle transition between Cassie and Wenzel behavior on etched Si (111) surfaces was demonstrated.

In addition, robust porous superhydrophobic SiC was fabricated by a combination of Pt-assisted etching and reactive ion etching. It was found that the surface roughness of combined etchings increased dramatically comparing with metal-assisted etching or reactive ion etching only. The superhydrophobicity of the SiC surface showed a good long-term stability in temperature-humidity chamber, and the pH values showed little effect on the superhydrophobicity of SiC surface. In addition, enhancement of porosity-induced photoluminescence intensity was found in the superhydrophobic SiC samples. Such surfaces may have a great potential for microfluid device, thermal ground plane and biosensor applications.

This study also explores the reversible transition between superhydrophobicity and superhydrophilicity on a ZnO nanorod/epoxy composite film. The epoxy resin serves as an adhesion and stress relief layer, and leads to improved mechanical robustness. The

ZnO nanorods were exposed after oxygen reactive ion etching of the epoxy matrix. A subsequent chemical treatment with fluoroalkyl and alkyl silanes resulted in a superhydrophobic surface with a water contact angle up to 157.8° and a hysteresis as low as 1.3° . Under UV irradiation, the water contact angle decreased gradually, and the surface eventually became superhydrophilic because of the UV induced decomposition of alkyl silanes and hydroxyl absorption on ZnO surfaces. A reversible transition of surface wettability was realized by alternations of UV illumination and surface treatment.

Based on the study of superhydrophobic surfaces, we explored the application of superhydrophobic surfaces in electronic packaging. Superhydrophobic silica/epoxy nanocomposite coating serves as an encapsulant to improve the electronic device reliability. Such superhydrophobic coating showed good stability under humidity at elevated temperatures and was applied on the triple track resistors test coupons. It was found that the self-cleaning encapsulant can successfully improve the test device reliability, and the coated TTR showed less degradation of resistance and leakage current in the temperature humidity bias test. In addition, the effect of epoxy resin on reliability improvement was studied.

We further explored the applications of superhydrophobic surfaces in solar cells. Two multi-functional solar cells with self-cleaning, low reflection and high efficiency properties were built up by coating or etching methods. First, a novel hierarchical structure integrating ZnO nanowire arrays on Si micropylamids was employed as an effective anti-reflection layer for improving the energy conversion efficiency. This structure displays a broadband reflection suppression in the 300-1200 nm range, with an average weighted reflectance of 3.2%. A cost effective screen printed solar cell was fabricated based on this hierarchical structure. A conversion efficiency of 16.0 % was obtained, which is the highest for any solar cell fabricated using ZnO nanostructures as the antireflection coating layer. In addition, a surface modification enabled a self-cleaning property for solar cells. Second, hierarchical textured silicon was explored for

large scale, low reflection, and self-cleaning solar cells, which was constructed from micropyramids with nanostructures added by Au-assisted electroless chemical etching. A front average weighted reflectance of 1.4%, which is one of the lowest values of reported black Si solar cells. The effect of micro and nano scale roughness on light reflection suppression was studied. A conversion efficiency of 8.1% of solar cells was obtained, and it was further improved to 16.5% after surface passivation of Al_2O_3 and SiN.

CHAPTER 1

INTRODUCTION

This chapter gives a brief introduction of superhydrophobic surfaces, methods to make superhydrophobic surfaces and potential applications of superhydrophobic surfaces.

1.1 Introduction of superhydrophobic surfaces

The surface wettability is a very important property for solid materials, which is determined by the balance between the adhesive and cohesive forces.[1-2] The Young's equation describes the surface wetting behavior of a liquid on a perfectly flat and rigid surface.[3]

$$\gamma_{SL} + \gamma_{LG} \cos \theta_Y = \gamma_{SG}$$

in which γ_{SL} , γ_{LG} and γ_{SG} are the surface energies between solid and liquid, liquid and gas, and solid and gas. γ_{SL} can be estimated by

$$\gamma_{SL} = \gamma_{SG} + \gamma_{LG} - \sqrt{\gamma_{SG} * \gamma_{LG}}$$

The contact angle (CA, θ_c), as shown in Figure 1.1, is the angle between the liquid–vapor interface and the solid–liquid interface.

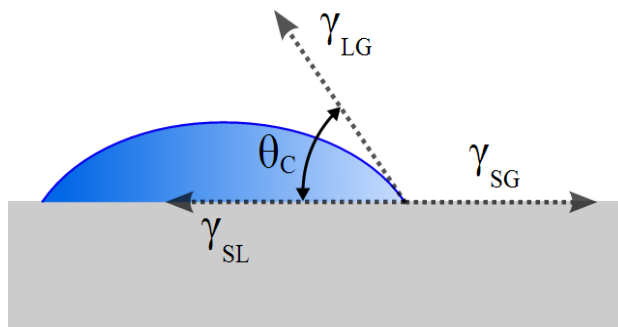


Figure 1.1 Contact angle of a liquid droplet wetted to a rigid solid surface. [4]

When the CA is larger than 90° , the surface is considered hydrophobic; when the CA is smaller than 90° , the surface is considered hydrophilic. The static CA is close to Young's contact angle θ_Y for a flat surface.

For rough surfaces, Wenzel model and Cassie–Baxter model are used to describe homogeneous wetting and heterogeneous wetting regime respectively (Figure 1.2).[5] The Wenzel model can be described by the following equation:[6]

$$\cos \theta^* = r \cos \theta_Y$$

Where θ^* is the apparent contact angle which corresponds to the stable equilibrium state (i.e. minimum free energy state for the system). The roughness ratio r is defined as the ratio of the actual area of the solid surface to the apparent area. The Wenzel model predicts how the surface roughness affects the wettability. If r is larger than 1, a hydrophilic surface will become more hydrophilic, and a hydrophobic surface will become more hydrophobic.

For hydrophobic surfaces, when surface roughness increases or surface hydrophobicity increases, the water is unlikely to wet the solid surface following the topography. Instead air will be trapped between the water and solid surface. Such phenomenon is described by Cassie model.[7] The Cassie-Baxter equation is

$$\cos \theta^* = f (\cos \theta_Y + 1) - 1$$

where f is the fraction of solid surface wetted by the liquid. The decrease of f will result in an increase of θ^* , and lead to a superhydrophobic surface.

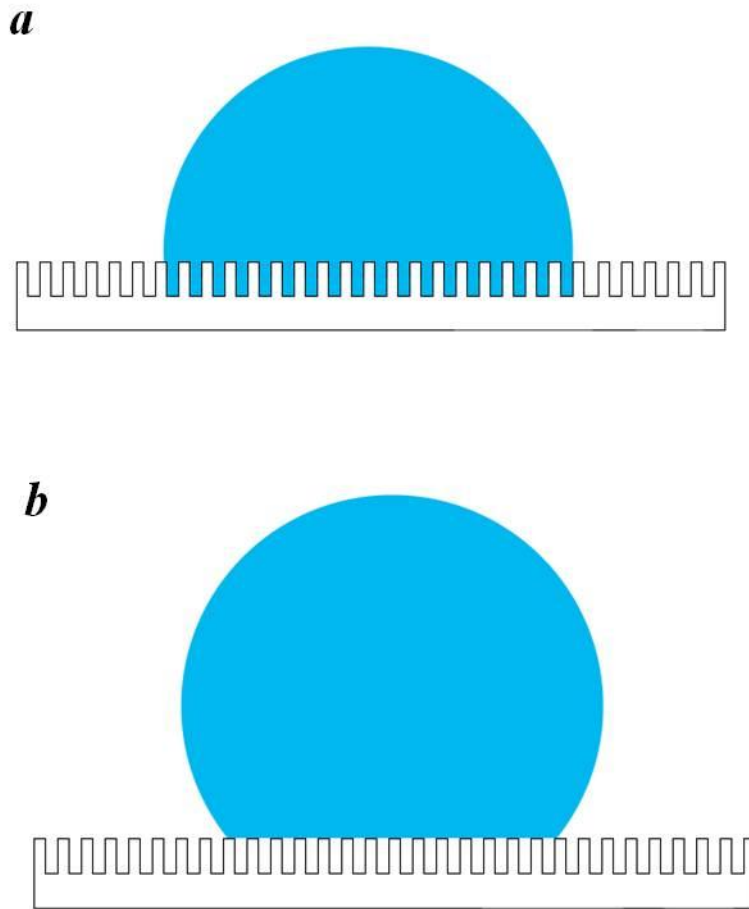


Figure 1.2 Illustrations of Wenzel (top) and Cassie (bottom) States [8]

Tsujii's group compared contact angles θ_f on rough surfaces with contact angles on a flat surface, which is close to the θ_Y (Figure 1.3).[9] The comparison was performed using different liquids to vary θ on the solid surface. $\cos \theta_f$ is plotted as a function of $\cos \theta$, showing the effect of surface roughness. The curve corresponds to the Wenzel state and Cassie state, which intersect at one critical angle θ_c . [8, 10-11]

$$\cos \theta_c = \frac{f - 1}{r - f}$$

When $\theta_Y < \theta_c$, the Wenzel state is thermodynamically more favorable. When $\theta_Y > \theta_c$, the Cassie state is thermodynamically more favorable.

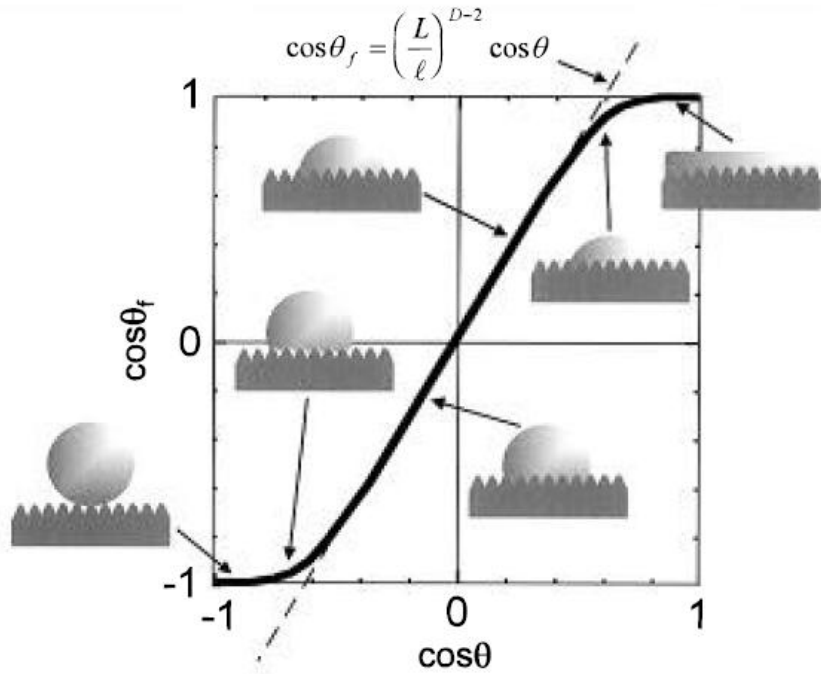


Figure 1.3 Cosine θ^* (apparent contact angle) on a textured surface, as a function of the cosine θ (Young contact angle) measured on the same surface, yet flat.[3]

Superhydrophobic surfaces usually have water CAs greater than 150° , and CA hysteresis smaller than 10° . [12-17] The advancing contact angle is the maximum stable angle, whereas the receding contact angle is the minimum stable angle (Figure 1.4). The difference between advancing CA and receding CA is called contact angle hysteresis. CA hysteresis is essentially the displacement of a contact line by either expansion or retraction of the droplet.

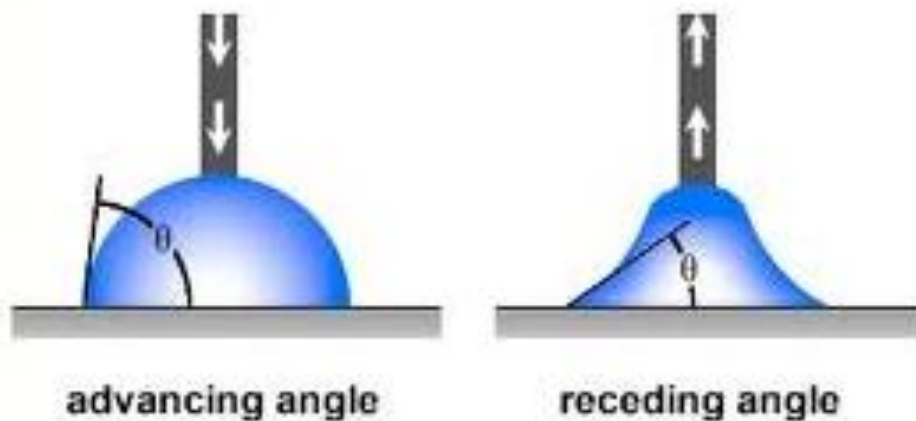


Figure 1.4 Images of advancing angle and receding angle.[18]

Within the last decade, the amazing water repellent properties of many biological surfaces, especially lotus leaves, have attracted great research interest. It is referred to as the lotus effect. The lotus effect is first exploited for technical applications by Professor Wilhelm Barthlott from the University of Bonn.[19] The lotus effect implies two characteristic properties: superhydrophobicity and self-cleaning. The lotus leaves have water CA of 161° , and CA hysteresis of 2° . The self-cleaning of the lotus effect means that particles of dirt can be rolled off and removed by water droplet from the surface with a low tilting angle ($<10^\circ$) as shown in Figure 1.5b. As a comparison, for a common surface shown in Figure 1.5a, the dust particles on the surface cannot be so effectively cleaned.

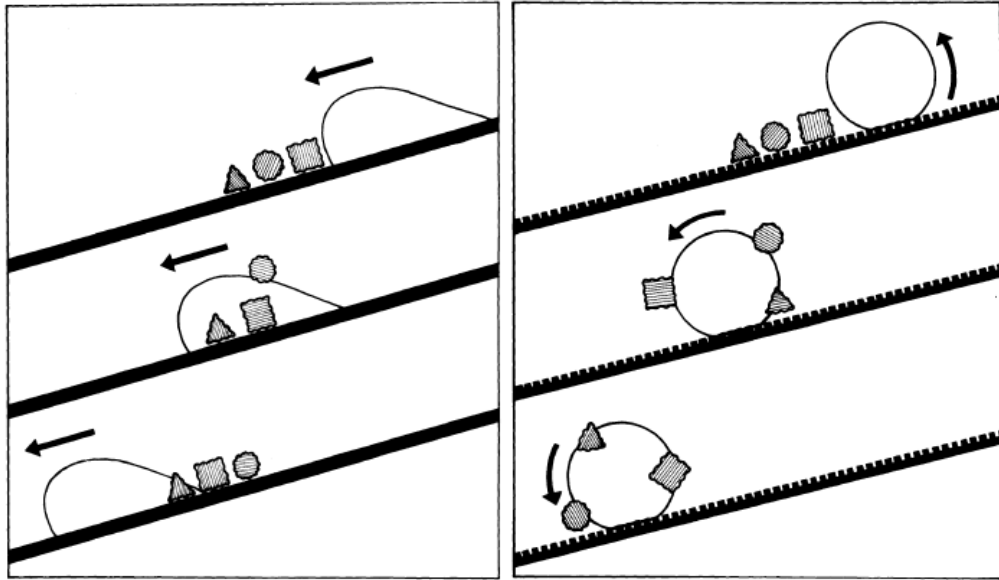


Figure 1.5 The self-cleaning mechanisms for lotus-effect surfaces[20]

Lotuses leaves have very fine surface structures and are coated with hydrophobic wax crystals of several nanometers in diameter. Surfaces that are rough on the nanoscale tend to be more hydrophobic than smooth surfaces because of the reduced contact area between water and solid. For the lotus plant leaves, the actual contact area is only 2-3% of the droplet-covered surface. Figure 1.6 shows the surface structure of a superhydrophobic lotus leaf.

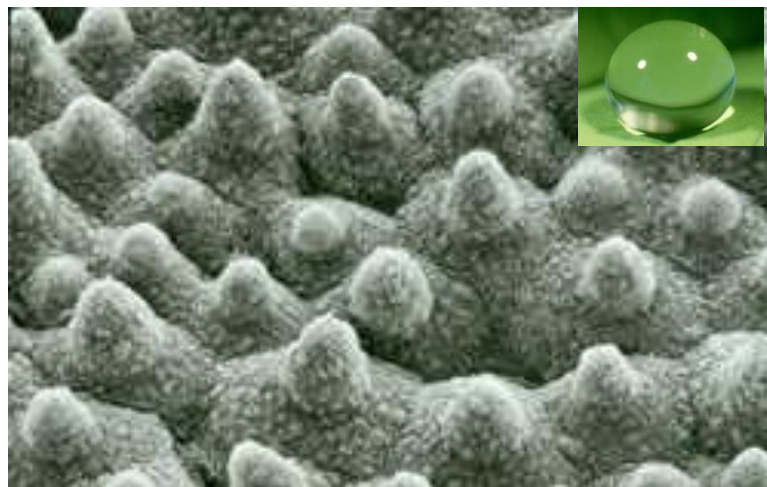


Figure 1.6 Surface structure of a lotus leaf.[21]

Naturally occurring superhydrophobic surfaces can also be found in some insects and plants, such as butterfly wings, strider's legs and cicada's wings (Figure 1.7).[22] From all these examples, it can be found that in order to achieve superhydrophobicity, surfaces usually have hierarchical structures in micro and nano scales, and at the same time with low surface energy.[23] The reported lowest surface energy material has a close-packed, uniformly organized array of trifluoromethyl groups ($-\text{CF}_3$), which has a surface energy of $\sim 6 \text{ mN/m}$ (Surfaces of Fluorinated Polymer Systems).[24] Such surface displays θ_Y of $\sim 120^\circ$, which is the highest water CA that can be obtained on flat surfaces. These two characteristics may be combined together to achieve self-cleaning surfaces.

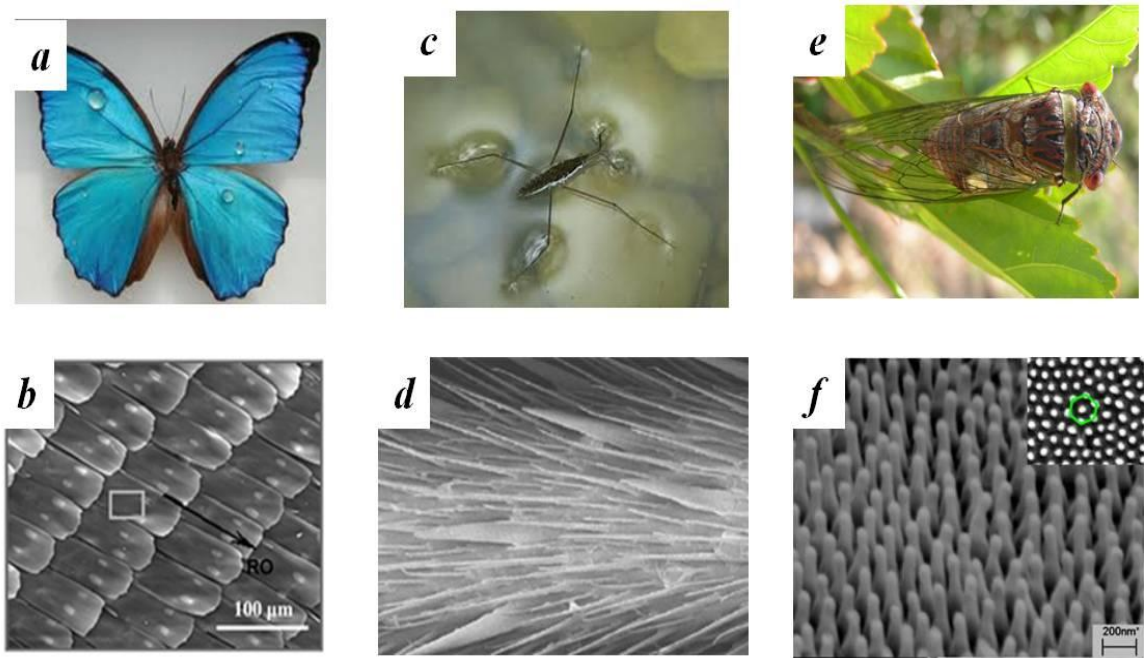


Figure 1.7 SEM images of micro or nano structure naturally occurring superhydrophobic surfaces (a and b) butterfly wings,[25] (c and d) strider's legs [26] (e and f) cicada's wings.[27]

1.2 Fabrication of superhydrophobic surfaces

In order to generate superhydrophobic surfaces, surface roughness and low surface energy are two essential conditions. The approaches to prepare superhydrophobic surfaces are mainly top-down and bottom-up methods. Top-down approaches include lithography, etching, micromachining, and templating, etc. Bottom-up approaches include layer-by-layer assembly, chemical vapor deposition, sol-gel method, etc. More detailed information of each method will be addressed in the following section.

1.2.1 Top-down approach

In this part, we will introduce some commonly used top-down methods for fabricating superhydrophobic surface, such as templating method, photolithography method, plasma etching method, metal-assisted etching method, etc.

1.2.1.1 Templating

Templating method uses a patterned material as a replication template to replicate the features, followed by lifting off or dissolution the templates. Many studies have been reported using templating method to generate superhydrophobic surfaces.[28-31]

Sun M. H. et al. fabricated artificial lotus leaf by nanocasting technology (Figure 1.8).[31] They used poly(dimethylsiloxane) (PDMS) as surface geometry negative template to replicate the lotus leaf structure, then using negative template for a second time replication. Anti-stick monolayer trimethylchlorosilane was applied as a releasing agent for PDMS. The surface structure of lotus leaf was replicated with high fidelity, including both micro and nano texturing on it. The contact angle on the positive replica was 160° , and contact angle hysteresis was 2° . But the contact angle on the negative replica was only 110° . By the templating approach, very complicated topographic pattern was replicated and superhydrophobicity was achieved.

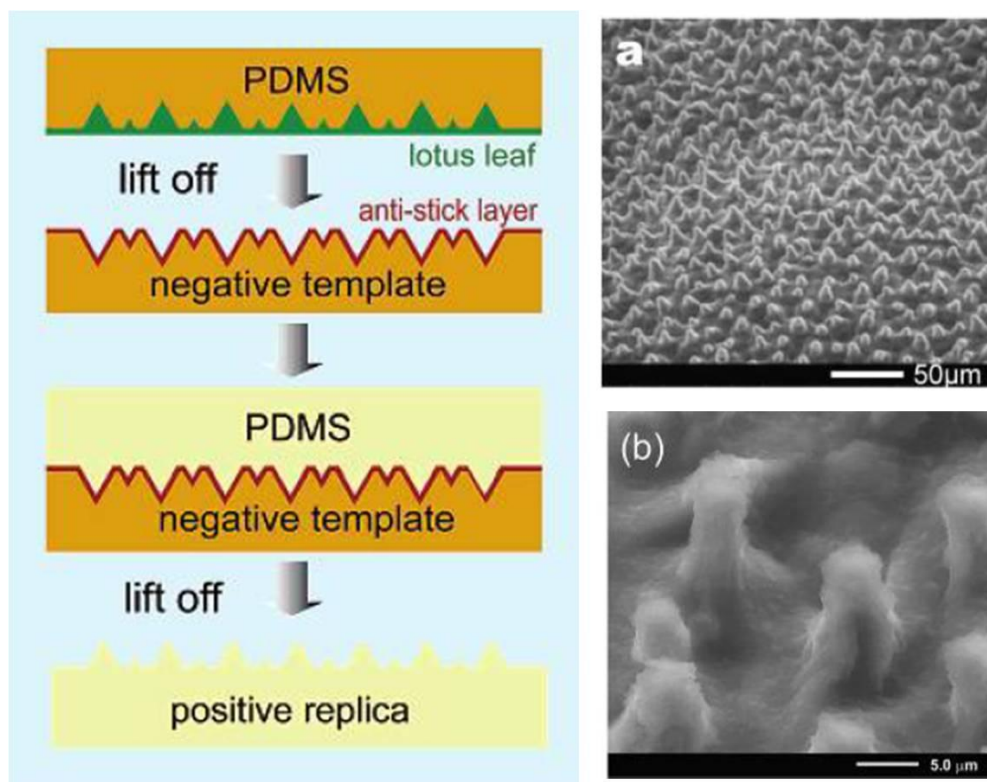


Figure 1.8 Illustration of lotus leaf replication process (a) SEM image of lotus leaf (b) SEM image of positive replica.[31]

In Sheng X. L.'s study,[30] through-hole nanotemplates were used to prepare polymeric nanopatterns with different sizes and heights during anodic aluminum oxide (AAO) template extrusion (Figure 1.9). The high density polyethylene (HDPE) with various sizes was produced under heat and pressure. Different roughness was generated by tuning the diameters of template nanochannels. As a result, superhydrophobic HDPE nanofiber arrays were achieved with CA of $\sim 160^\circ$. Such functional materials can be applied in the fields of agriculture, electronics, and optics.

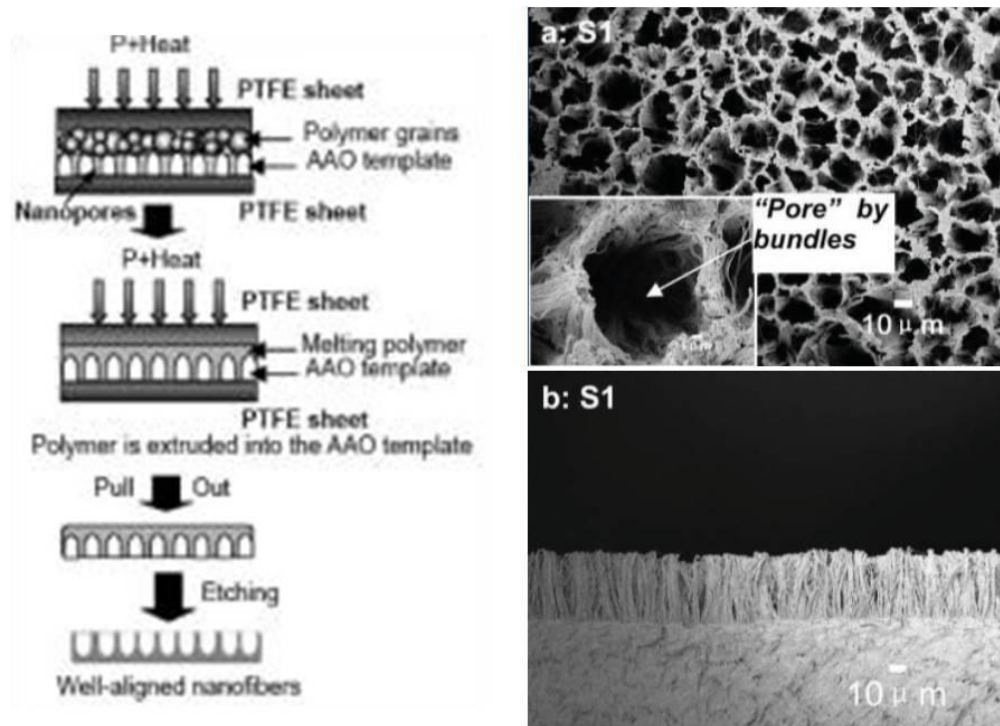


Figure 1.9 Illustration of using AAO template for high-density polyethylene (HDPE) nanofiber extrusion (a) FE-SEM images of HDPE nanofiber surfaces top view and (b) cross-section.[30]

1.2.1.2 Lithography

Lithography methods such as nanosphere lithography, electron-beam lithography, X-ray lithography, have been used to generate desirable features to the substrate.[32-34] The size, spacing, and shape of the texturing can be controlled by the lithography process. The textured surfaces are further coated by low surface energy materials to generate superhydrophobicity.

Nanosphere lithography can pattern large scale nanosphere arrays, and form periodic nanostructure after plasma etching. Shiu J. Y. et al. used spin coating method to form close packed polystyrene (PS) arrays, which was then coated with a gold film and modified with octadecanethiol (Figure 1.10).[33] The water contact angle of the PS

arrays increased from 132° to 168° for 440 nm to 190 nm diameter PS arrays. The water contact angle measured on the gold/ODT-modified double layer PS arrays is $\sim 170^\circ$.

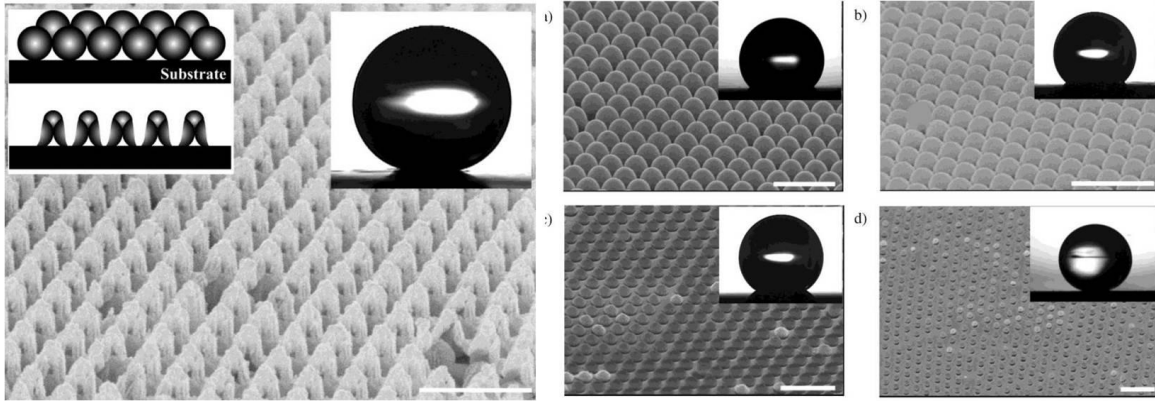


Figure 1.10 (left) SEM image of double-layer polystyrene surface after oxygen plasma treatment. (right) SEM images of polystyrene beads. The insets are the water contact angle measurement on the surfaces. The diameters of polystyrene beads and water contact angles are (a) 400 nm, 135° , (b) 360 nm, 144° , (c) 330 nm, 152° , and (d) 190 nm, 168° . The scale bars are $1\ \mu\text{m}$. [33]

Electron-beam lithography is another method for creating very small structures in the resist that can subsequently be transferred to the substrate material. The advantage is that it can generate desirable geometric features with better control of size, spacing, and shape, and make features even in the nanometer regime. By electron-beam lithography technology, macroscopic hierarchical superhydrophobic surfaces were fabricated (Figure 1.11). [34] The primary and the secondary structures are well controlled, and the structure-property relations of superhydrophobicity can be quantitatively studied. The effect of hierarchical surface structures on wetting and adhesion has been studied systematically. It was found that the advancing CA is insensitive to the spacing, shape, or distribution of the secondary-features. The receding CA of low-adhesion surfaces does not exhibit clear dependency on the secondary-feature spacing, and the receding CA of high-adhesion surfaces increases by approximately 3° per 100 nm increase in secondary-feature spacing. [34]

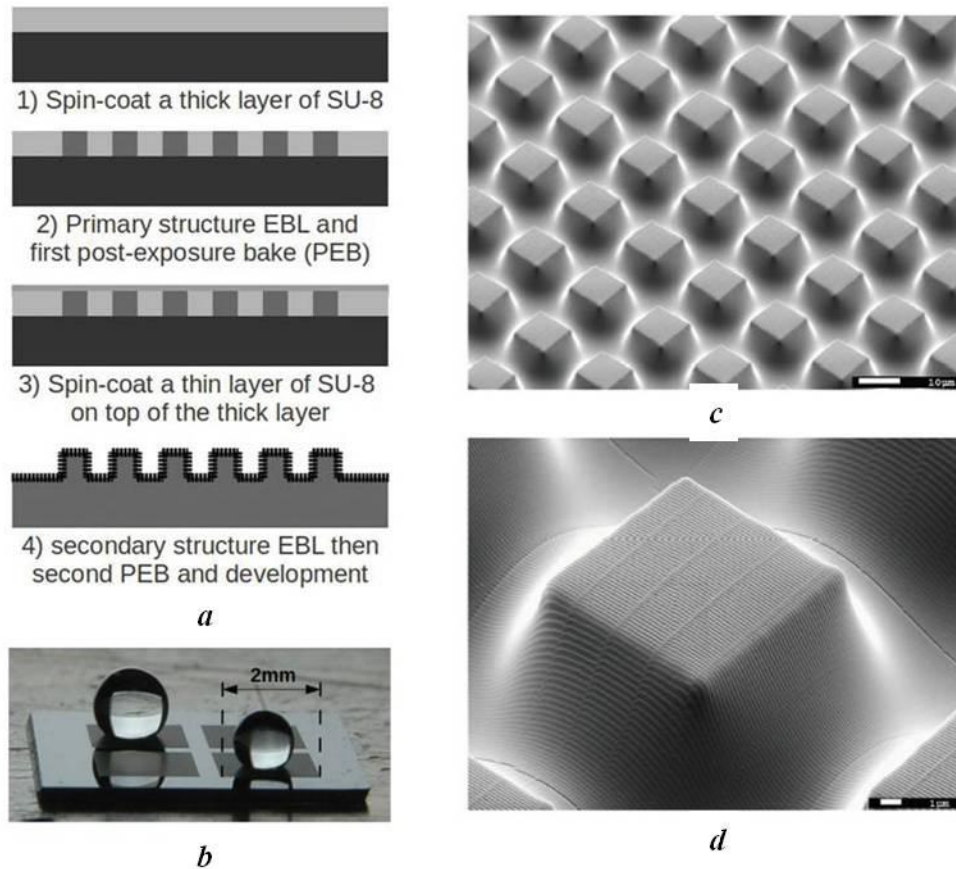


Figure 1.11 (a) Images of the hierarchical surfaces produced by a single electron beam lithography -exposure and double EBL-exposure process. (b) Demonstration of superhydrophobic surface with 2 mm linear dimension (c and d) Double EBL-exposure sample with secondary ridges. The primary blocks are with the dimension of about $10 \mu\text{m} \times 10 \mu\text{m} \times 8 \mu\text{m}$. The secondary ridges have a 70 nm width and 200 nm periods.[34]

Hong L. F. et al. fabricated photopatternable superhydrophobic films by spray coating and thermal immobilization of polytetrafluoroethylene (PTFE) nanoparticles on SU-8 polymer matrix (Figure 1.12).[35] A minimal feature resolution of $10 \mu\text{m}$ has been achieved using the standard photolithography approach. The film displays high water contact angle of 165° , low contact angle hysteresis, and high optical transparency of 80%.

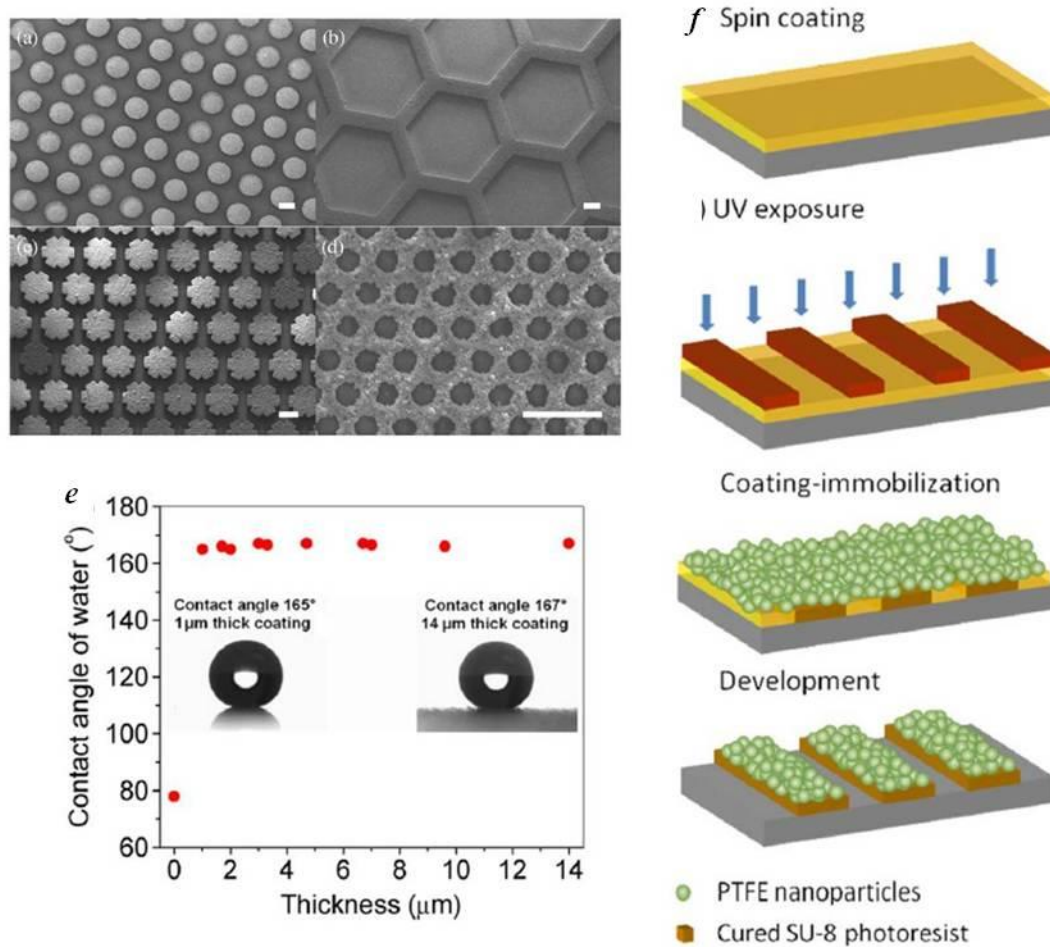
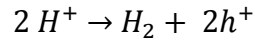
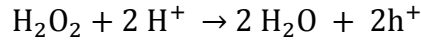


Figure 1.12 SEM images of the superhydrophobic photopatternable PTFE/SU-8 nanocomposite coating (Scale bars in (a)–(c): 100 μm ; in (d): 50 μm). (e) Contact-angle measurements for different thicknesses PTFE nanoparticle layers. (f) Illustrations of fabrication processes to achieve photo-patternable superhydrophobic nanocomposite coatings.[35]

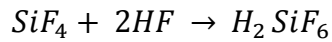
1.2.1.3 Metal-Assisted Chemical Etching

Metal-assisted chemical etching is a low cost method for fabricating various Si nanostructures (nanowires, pores, etc.) and has attracted more and more attention.[36-42] In a typical metal-assisted chemical etching process, a thin layer of noble metal is deposited on Si, and the Si substrate is etched in a solution containing HF and an

oxidative agent. In the etching process, H_2O_2 is reduced at the metal and cathode reaction happens.



At the anode, the Si substrate is oxidized by the injected holes and dissolved, generating hydrofluorosilicic acid.



Metal-assisted chemical etching has been widely used to fabricate straight and well-defined Si pores or wires with diameters as small as 5 nm or as large as 1 μ m. Surface roughness is formed by controlling of the metal particle density, etchant concentration and other etching conditions. For example, superhydrophobic Si nanowires were fabricated by metal-assisted chemical etching and rapid thermal annealing.[43] After metal-assisted chemical etching, the thermal annealing process in oxygen ambient forms siloxane groups on the Si NW surfaces, and lead to significant increase of contact angle to 154.3°. When exposed to air, the contact angle reduces to 0°, due to the re-formation of silanol groups. The wettability conversion of Si NWs between superhydrophobicity to superhydrophilicity was repeated (Figure 1.13).

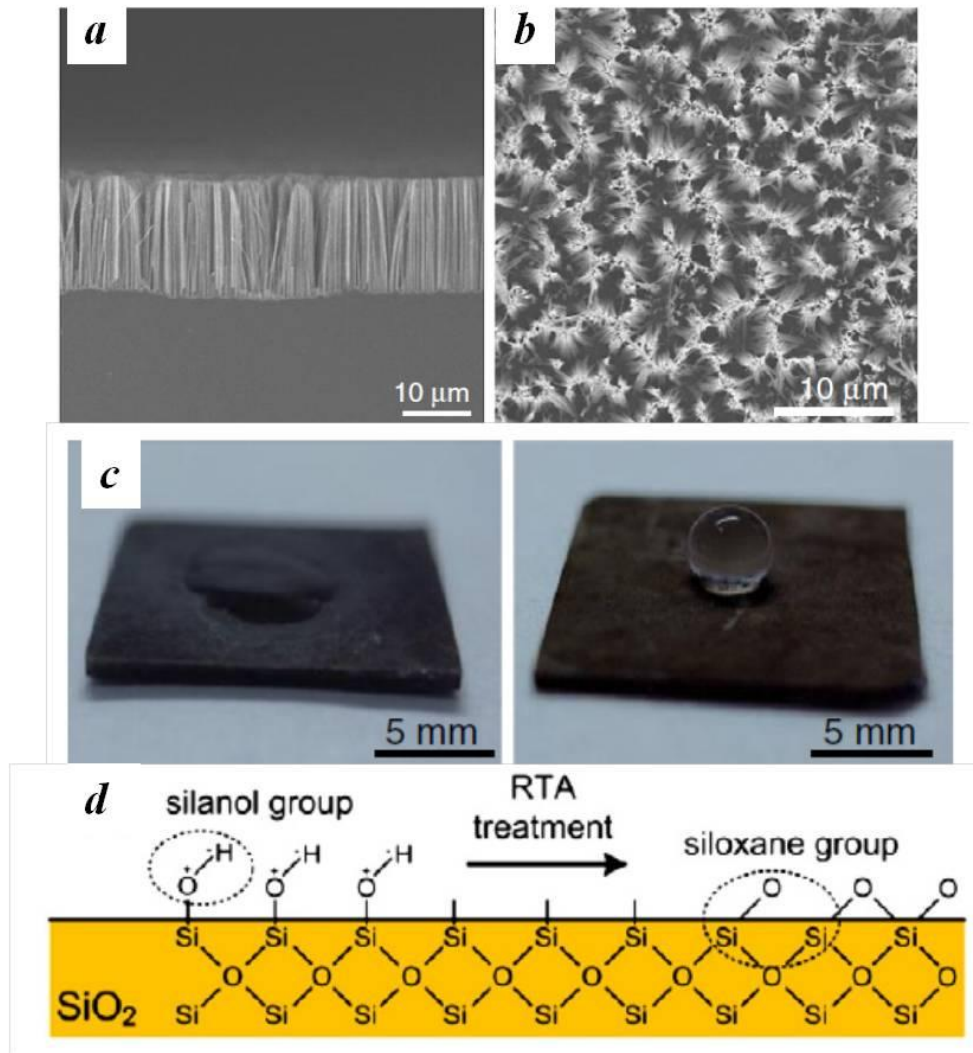


Figure 1.13 (a and b) SEM cross sectional and top view images of Si nanowire arrays by metal-assisted chemical etching (c) Water contact angle images of fabricated and rapid thermal annealing treated Si NWs (d) A schematic of the hydrophilic (silanol) and hydrophobic (siloxane) groups formed on Si nanowires.[43]

1.2.1.4 Plasma Etching

Plasma etching is a dry etching process that reactive atoms or ions are generated by a gas discharge. Oxygen plasma etching has been widely used for polymer etching, which does not require high temperature, and can be used for large scale production (depending on the size of the plasma chamber) with short processing time.[44-46] For example,

superhydrophobic and optical transparent poly(ethylene naphthalate) and polystyrene were fabricated by plasma etching and organosilanes or fluorocarbon coating.[47]

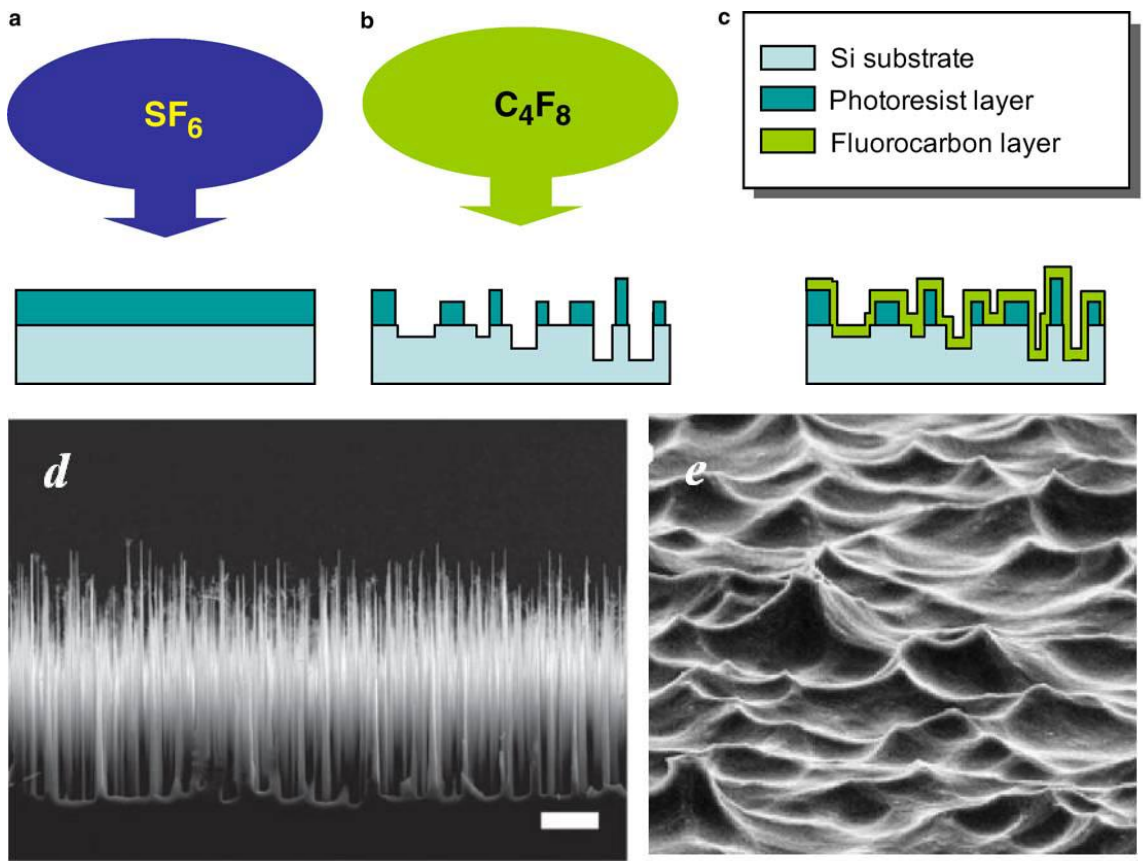


Figure 1.14 (a-c) Fabrication process of superhydrophobic Si. (d and e) SEM micrographs of the Si surface after deep reactive ion etching and SF_6 plasma etching.[47]

Fluorine containing plasmas, such as CF_4 , SF_6 , NF_3 , ClF_3 , have been used to etch Si.[48] The anisotropic etching process can generate deep grooves or walls. For example, high aspect ratio (5-50) Si nanogras can be fabricated by fluorine based deep reaction ion etching process, followed by fluorocarbon coating for superhydrophobic nanostructured silicon surface (Figure 1.14d). Moreover, the roughness on Si wafer can be generated by plasma etching combined with lithography. As shown in Figure 1.14 (a-c, and e), surface roughness on Si was generated by over etching of photoresist by SF_6 plasma treatment. Fluorocarbon layer was coated to further lower the surface energy. As

a result, superhydrophobic Si surface was produced with water contact angle of up to 170°.[49-50]

1.2.2 Bottom-up approach

Comparing with top-down method, bottom-up method involves more complex integration of different components. In this part, we will briefly introduce the typical bottom up methods such as layer-by-layer deposition, chemical vapor deposition and sol-gel method.

1.2.2.1 Lay-by-layer deposition

Layer-by-layer self-assembly processes are widely used for surface modification by alternately depositing positively and negatively charged polymers. The advantage is the easy process and precise control of the layer thickness. This technique is suitable for large area superhydrophobic film deposition.

Li Y. *et al.* reported the fabrication of highly transparent superhydrophobic films by layer-by-layer deposition (Figure 1.15).[51] The layer-by-layer deposition of poly(allylamine hydrochloride) (PAH)/SiO₂ nanoparticle films on top of the poly(diallyldimethylammonium chloride) (PDDA)-silicate/ poly(acrylic acid) (PAA) film, followed by calcination and chemical vapor deposition of a layer of fluoroalkylsilane. The nanosilica serves as antireflection layer to improve the transparency.

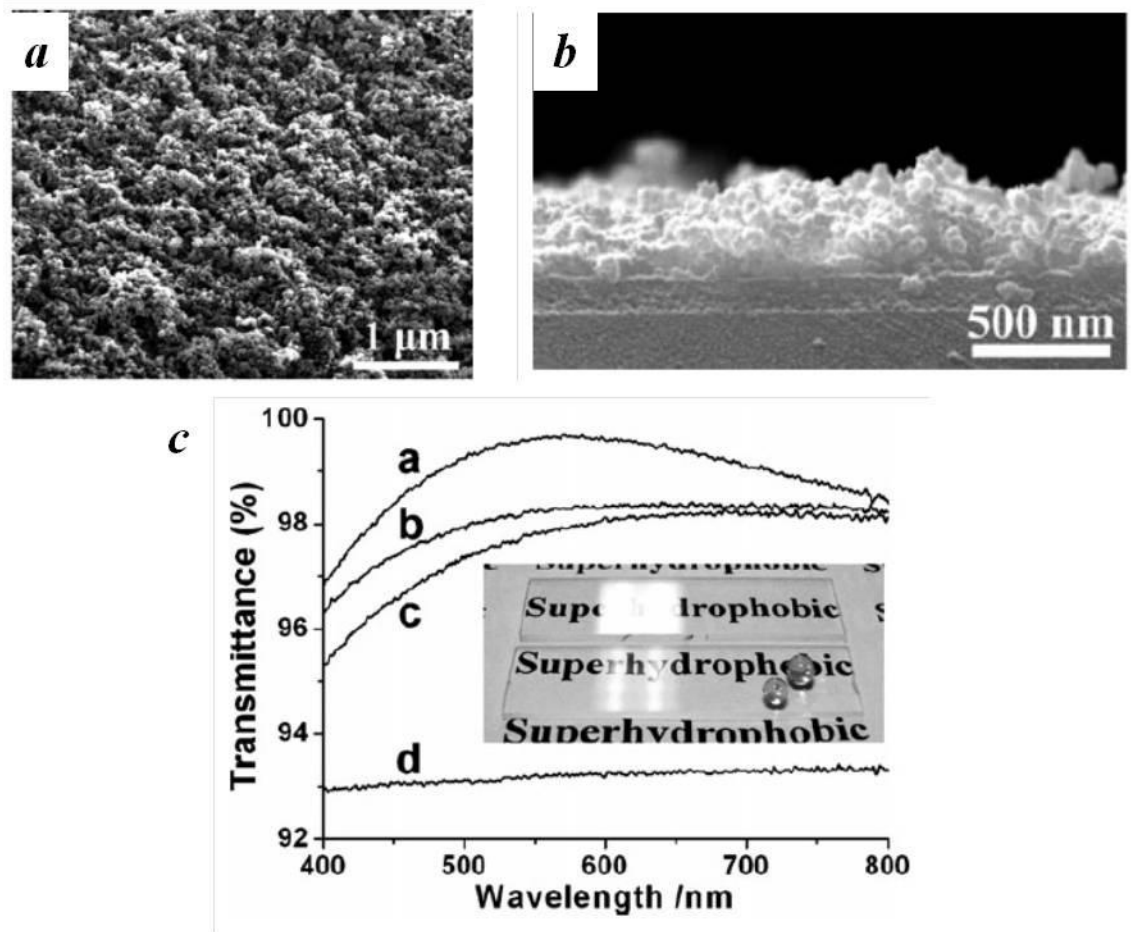


Figure 1.15 (a-b) Top-view and cross section SEM images of a (PDDA-silicate/PAA) $\times 12$ / (PAH/SiO₂) $\times 4$ film deposited on a quartz substrate after calcination. (c) UV-Vis transmission spectra of films on quartz substrates. a. Calcined (PDDA-silicate/PAA) $\times 12$ film; b. calcined (PDDA-silicate/PAA) $\times 12$ / (PAH/SiO₂) $\times 4$ film; c. the film after CVD of a 1H,1H,2H,2H-perfluorooctyltriethoxysilane layer; d. bare quartz.[51]

1.2.2.2 Chemical vapor deposition

Chemical vapor deposition can be combined with photolithography to generate multi-scale roughness for superhydrophobic surfaces, such as carbon nanotube bundles, and Si nanowires. Zhu L. B. *et al.* fabricated two systems with double scale roughness: growing carbon nanotube arrays on patterned silicon wafers (Figure 1.16).[52] The surfaces are coated with 20 nm fluorocarbon films to lower the surface energy. Photolithography was used to pattern a silicon surface with microscale surface roughness,

and the nanoscale roughness on top decreases the contact angle hysteresis to less than 1° . Such surfaces can be potentially applied in microfluidic devices.

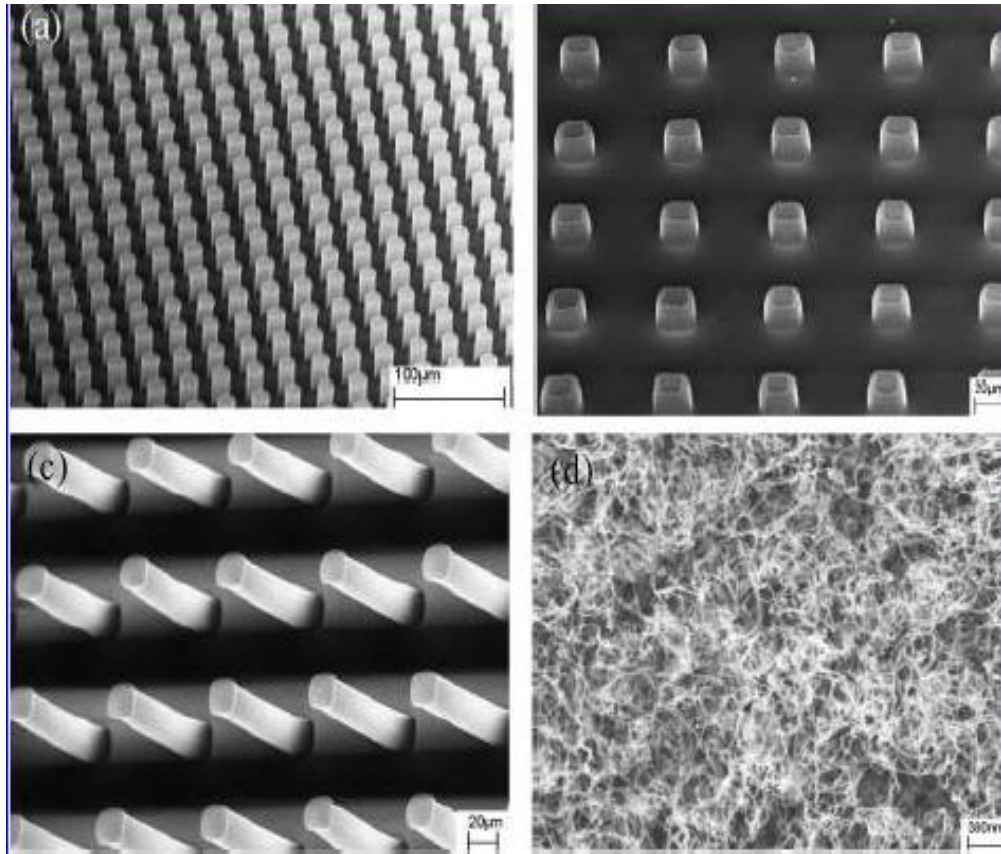


Figure 1.16 Typical SEM images of CNT arrays on silicon substrates: (a-c) cylindrical CNT arrays with different dimensions; (d) as-grown CNT array surfaces.[52]

Cao, L. L. *et al.* grew Si nanowires vertical to the etched Si(111) sidewall surfaces by chemical vapor deposition method (Figure 1.17).[53] Au nanoclusters were deposited onto the etched Si, and Si nanowires were grown with SiCl_4 as the precursor and hydrogen gas (10% in argon by volume) as the carrier gas. The nanowires were grown at 850°C via a vapor-liquid-solid mechanism. The static water contact angle of the hierarchical structure is around 160° .

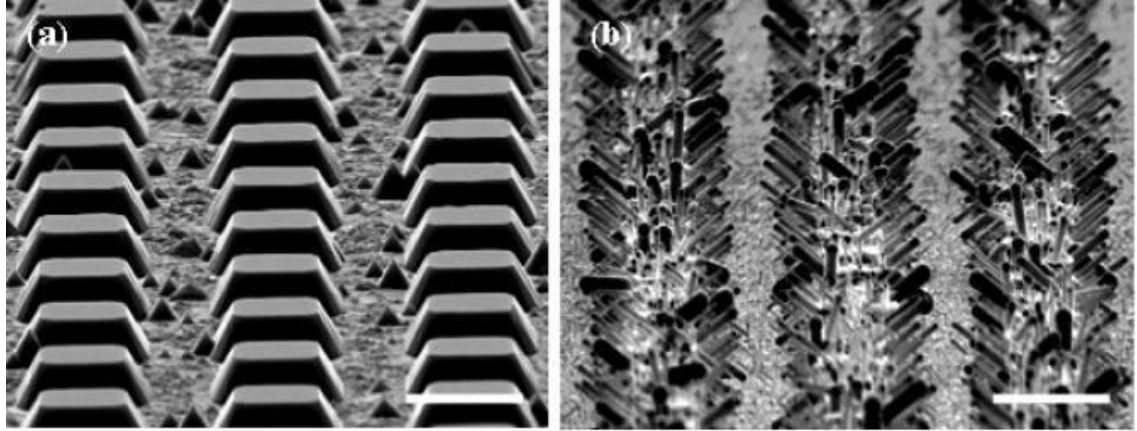


Figure 1.17 SEM images (a) Si islands fabricated by etching a SiO₂-masked Si(100). (b) Si nanowires grown on the Si islands. The scale bars are 5 μm . [53]

1.2.2.3 Sol-gel method

Sol-gel method is a simple and cost-effective process in which a colloidal solution (sol) that acts as the precursor for an integrated network (gel) of either discrete particles or network polymers. Sol-gel method can produce different oxide materials, such as SiO₂, TiO₂, Al₂O₃, etc. [54-55]

Manca M. *et al.* fabricated anti-reflective surfaces by a double-layer coating with trimethylsiloxane (TMS) functionalized silica nanoparticles partially embedding in an organosilica binder matrix, which was produced by a sol-gel method. [56] These two layers turned into a monolithic film after thermal annealing, and the hydrophobic nanoparticles were permanently fixed to the glass substrate. Such surface showed high water contact angle of 168°, and stable self-cleaning effect after 2000 hours of outdoor exposure. It also showed good transparency of 93.6% at 500 nm (Figure 1.18).

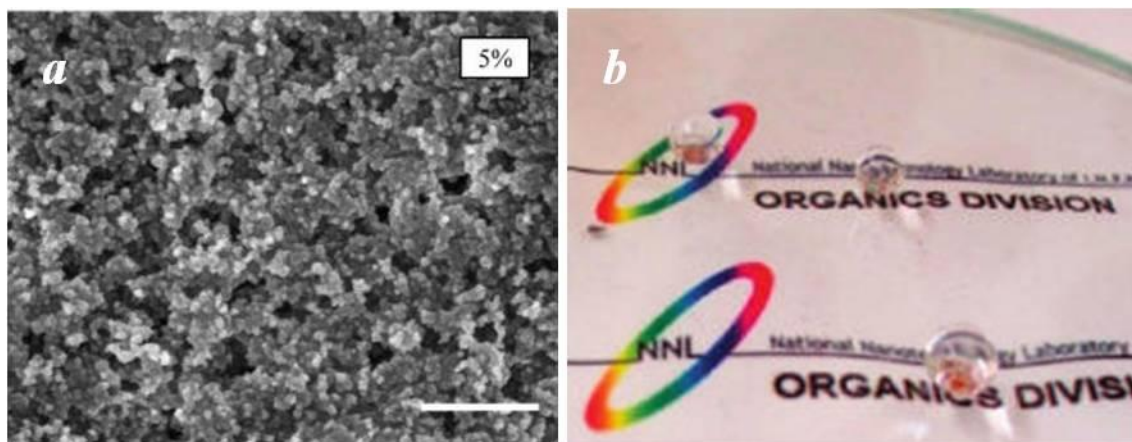


Figure 1.18 (a) SEM images 5 wt% TMS-silica nanoparticles-containing solutions by spin coating. Scale bar, 200 nm. (b) Image of a superhydrophobic antireflective bilayer coating on a glass plate.[56]

Yang S. Y. *et al.* prepared superhydrophobic polystyrene/SiO₂ sol nanocomposite hybrids (PS-SIs). The process for the formation of PS-SIs is shown in Figure 1.19.[57] The methacryloxypropyltrimethoxysilane (MPS)-grafted colloidal SiO₂ sols is produced first. Then PS-SIs is formed via free-radical polymerization using MPS-grafted colloidal silicate, styrene monomer, azoisobutyronitrile (AIBN) initiator, and dimethylformamide (DMF). Finally, surface etching technologies (SET) was employed to generate the rough surface by tetrahydrofuran (THF) and dodecanethiol solution. The surface is consisting of macro-cavities and nanotextures like the lotus surface.

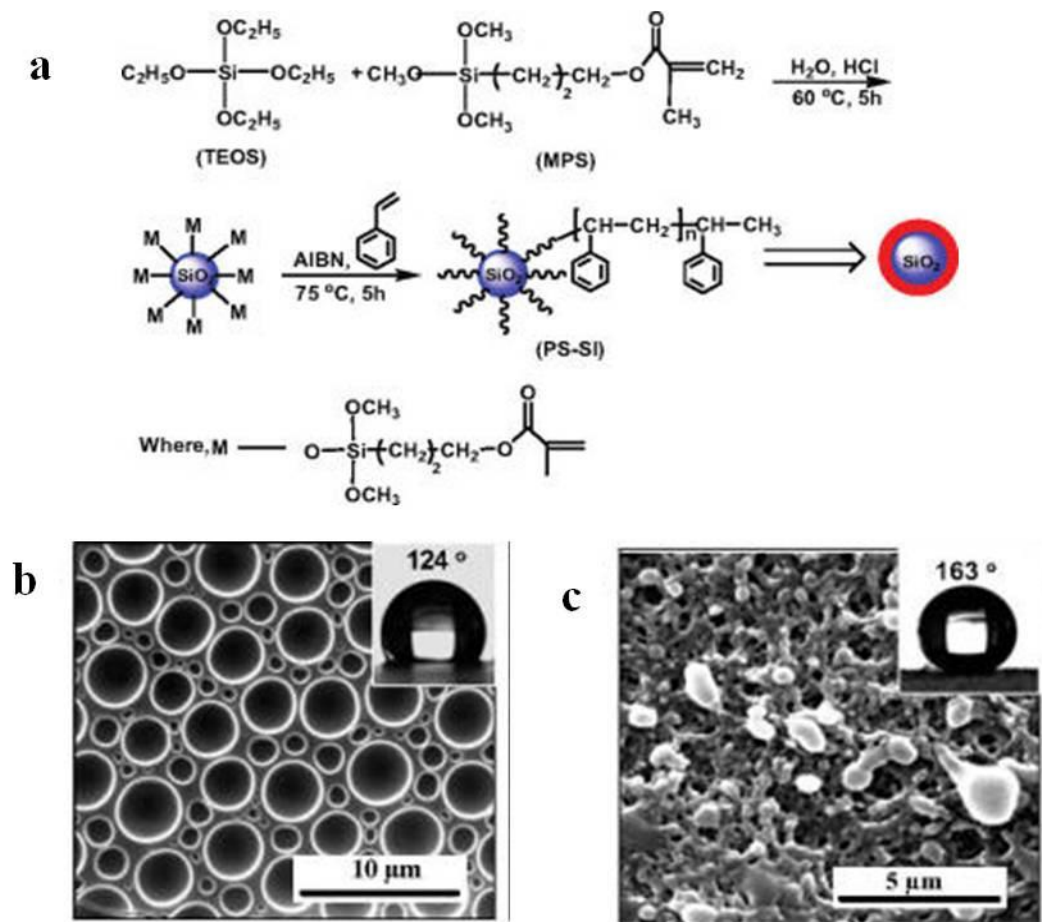


Figure 1.19 (a) Illustration of the formation of the PS-SIs. SEM images of PS-SIs film (b) dip-etched by THF solution, and (c) treated by dodecanethiol solution with SET. Inset images are contact angle measurements.[57]

1.3 Applications of superhydrophobic surfaces

1.3.1 Anti-icing/fogging

Ice or wet snow accumulation on solid substrate, such as airplane wings and electrical transmission lines, will lead to severe damages and can be costly to repair. Cao L. L. et al. demonstrated the anti-icing coating both in the lab condition and outside environments.[58] They found that the size of the particles in these composites is critical for preventing ice formation upon impact of supercooled water (“freezing rain”, “atmospheric icing”, or “impact ice”). Composites with particle size up to 10 μm are all

superhydrophobic, but ice only forms on surfaces with particle size larger than 50 nm. Since with particle size increases, the free energy barrier for heterogeneous nucleation decreases and icing probability increases. In the outside environment testing, they coated the Al plate with the superhydrophobic composites with 50 nm silica particles, and it showed little ice accumulation after one week freezing rain (Figure 1.20). The plate without coating was completely covered by ice. Similar phenomenon was also observed on testing of satellite dish antenna.

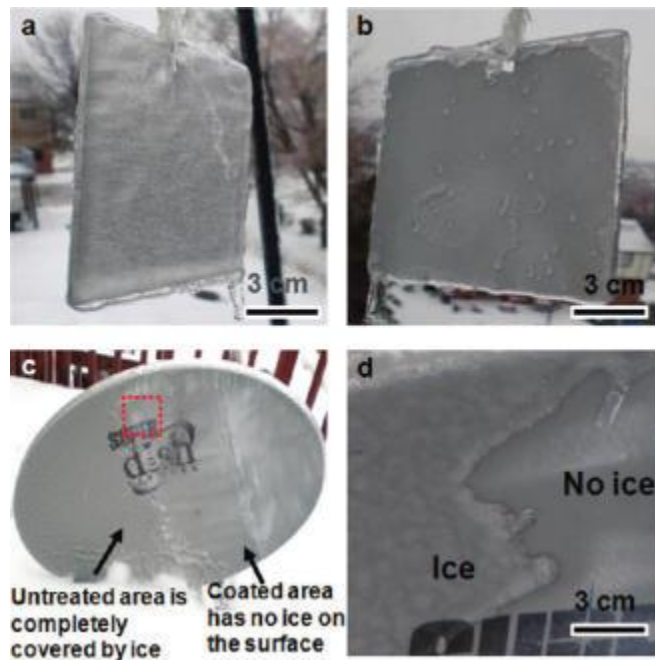


Figure 1.20 Test of anti-icing properties in naturally occurring “freezing rain”. (a) Untreated aluminum plate. (b) aluminum plate coated with a superhydrophobic composite. (c-d) Satellite dish antenna [58]

Superhydrophobic surface can also be applied as anti-fogging coating on transparent glass or plastics. Lai Y. K. *et al.* fabricated transparent and superhydrophobic films using titanate nanobelts by electrophoretic deposition (Figure 1,21).[59] The film showed superhydrophobic property and good anti-fogging performance. After taking out

from a refrigerator (-4 °C) to the humid laboratory air (ca. 50% RH), the quartz slide was fogged immediately, while the coated quartz showed almost no frog accumulation.

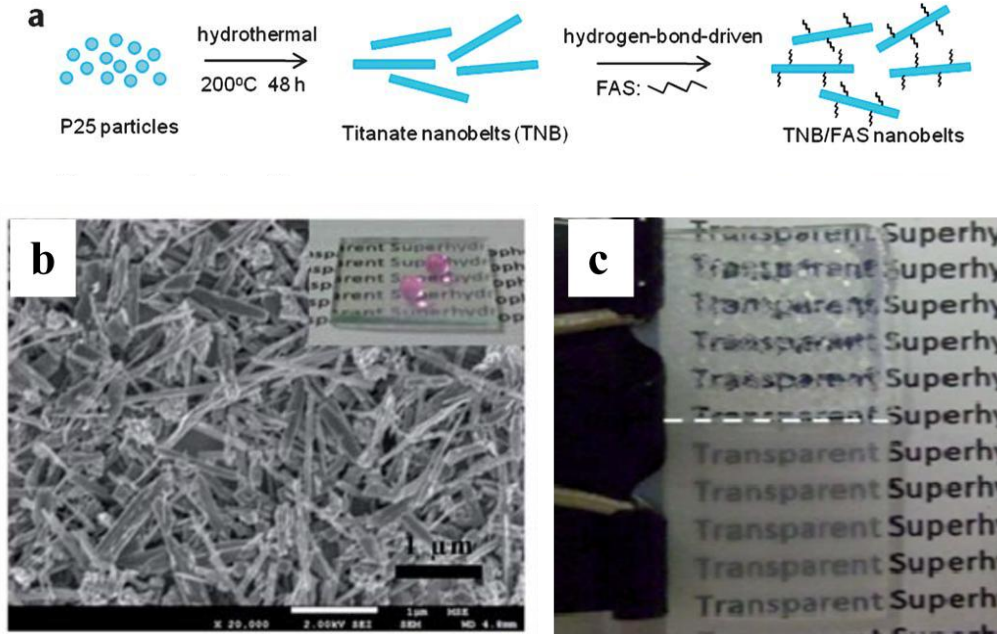


Figure 1.21 (a) Schematic process for synthesizing titanate nanobelts. (b) SEM image of superhydrophobic TNB/fluoroalkylsilane (FAS) film. The inset are water droplet image on the film surface. (c) Photograph of superhydrophilic coatings on ITO (bottom) and a control ITO substrate (upper) taken from a refrigerator to the humid laboratory air.[59]

1.3.2 Anti-reflection for solar cells

According to the International Energy Outlook 2008 Report (IEO Report),[60] world energy consumption is projected to grow by 50% by 2030, driven by the economic growth and expanding populations. We need more energy in the world to ensure adequate global energy supply. Compared to traditional energy sources (fossil fuels, nuclear, coals, etc.), solar energy is among the most long-lasting and environmentally friendly energy sources. Photovoltaic (PV) power, in particular, is one of the most benign forms of electrical power available. It is indispensable in energy production in spacecrafts and

satellites, and is becoming more widely used in consumer products, mainly because it produces no emissions and consumes no fuel, with no hazardous materials involved in PV systems. For the Roadmap case study in Figure 1.22, the annual solar electricity generation projected for 2030 is 360 billion kWh—the amount of electricity consumed by 34 million households., which demonstrates the potential growth of PV system.

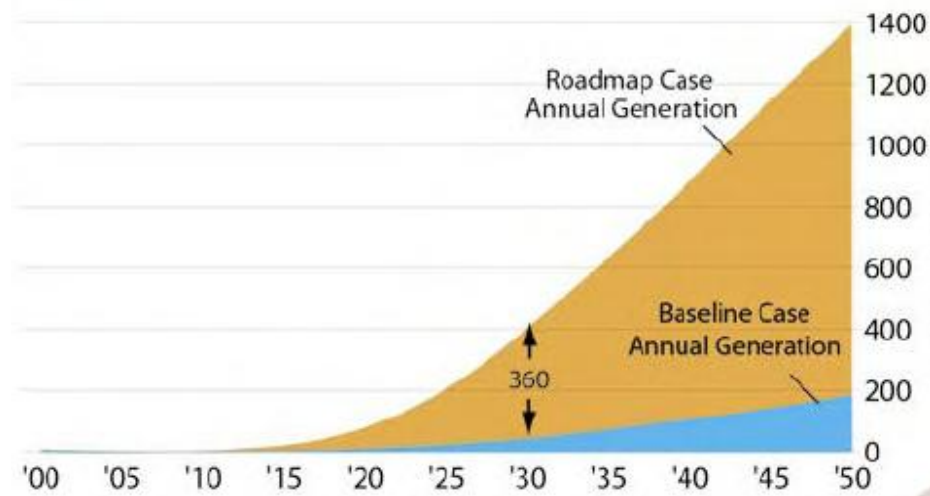


Figure 1.22 Roadmap projections of solar electricity generation (in billion kWh/yr) from 2000 to 2050 for the Baseline and Roadmap cases.[61]

Currently, solar electric-generating devices available on market are mainly composed of crystalline silicon (95%, mainly single-crystalline and multi-crystalline Si) because of its relatively low cost and high efficiency compared to other PV materials.[62] A general PV module structure is shown in Figure 1.23. The cover glass provides the necessary mechanical protection (structural front configuration) while maintaining the transparency necessary for light to go through. The anti-reflection coating reduces the light reflection due to the high reflectance (~38%) on silicon surfaces. The contacts on front and back sides are for free carrier collection. In order to achieve higher efficiency, a series of techniques are employed such as structured front surfaces, antireflection layers (thin oxide), surface passivation etc., as shown in Figure 1.23.

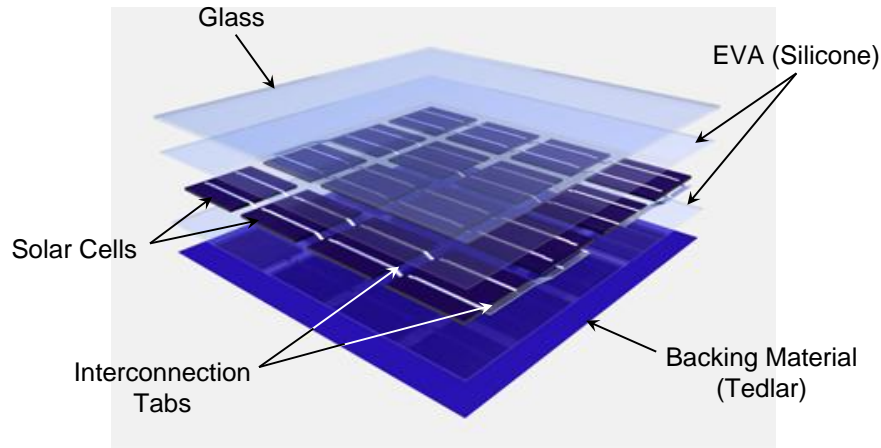


Figure 1.23 General structure of a PV module. [63]

There are two solar cell efficiency loss mechanisms: optical loss and electrical loss.[64-66] Light blocking is a very important practical factor for optical loss. For example, after deployment, particularly in high solar insolation area, there is always dust accumulation on the surface that may reduce the efficiency due to the light blocked by the dust particles. For applications of solar cells, maintenance is necessary to keep the junction boxes and wiring free from moisture and corrosion and to keep the surface of the panel clean enough to allow light through to the Si layers. When the scale of the solar cell increases, maintenance contributes as a main cost. Furthermore, dust build-up on the solar cell arrays is a significantly critical issue and the need for self-cleaning is imperative not only on earth, but also in outer space applications. For outer space applications, spacecrafts such as the Opportunity and the Spirit rovers to Mars had their power supplies reduced to below half of their original values due to accumulated dust blocking sunlight on the array windows.

Many studies have been focused on applying self-cleaning functions to solar cells. For example, Zhu J. *et al.* fabricated novel p-i-n a-Si:H nanodome solar cells with self-cleaning properties.[67] The nanocones were fabricated by Langmuir-Blodgett assembly of close packed monodisperse SiO₂ nanoparticles followed by reactive ion etching. The nanodome solar cell was composed of Ag as a back reflector, transparent conducting

oxide (TCO) as both bottom and top electrode, as well as a thin a-Si:H active layer. The device has a power efficiency of 5.9%, and water contact angle of 141°. The self-cleaning effect of the solar cell was demonstrated by water droplet rolling off the dust from the surface. From figure 1.24, it was found that with dust accumulation on surface, the power efficiency drops by 20% due to the light blocking of dust particles. After the self-cleaning process, the power efficiency was recovered. V_{oc} value remains the same during the whole process.

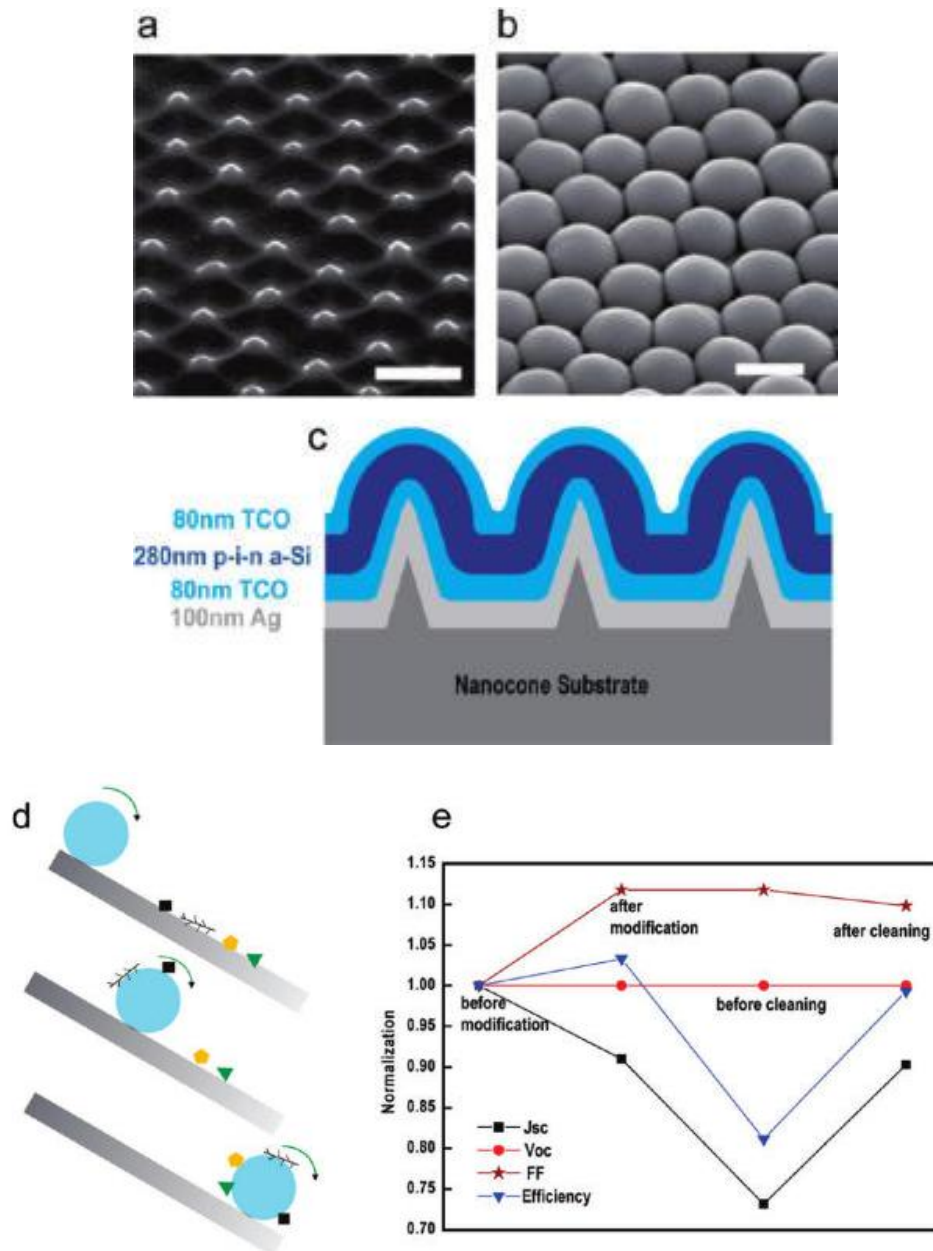
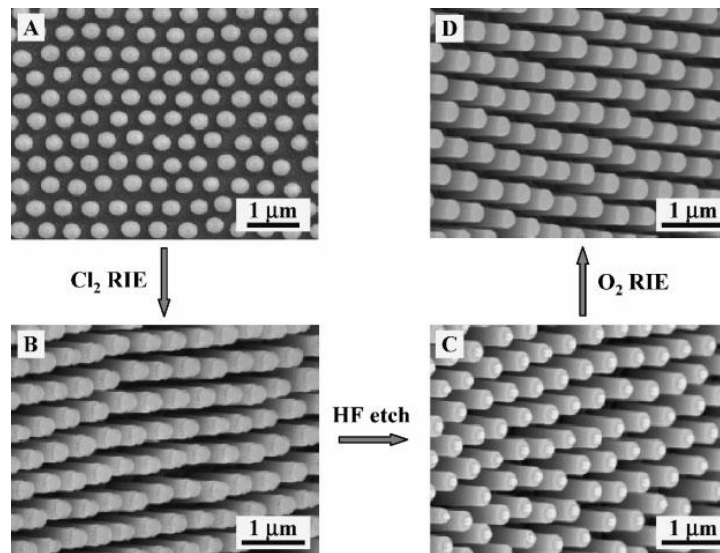


Figure 1.24 Nanodome a-Si:H solar cell structure. SEM images on (a) nanocone quartz substrate and (b) a-Si:H nanodome solar cells. The scale bar is 500 nm. (c) cross-sectional structure of nanodome solar cells. (d) Schematic of the self-cleaning mechanism. (e) Change of FF, J_{sc} , V_{oc} and power efficiency during a cycle of the self-cleaning.[68]

Min W. L. et al. used colloidal templating approaches to fabricate moth-eye anti-reflection coating layer on Si and glass.[69] After an SF_6 reactive ion etching and surface modification, high aspect ratio (up to 10) wafer-scale silicon pillars were produced with superhydrophobicity (Figure 1.25). The water contact angle can achieve 170° with self-cleaning property. For bare Si wafer, it reflects $> 30\%$ of incident light. With moth-eye anti-reflection layer, a much lower light reflection is observed ($< 2.5\%$) over the whole spectrum. Such technology is very promising for developing self-cleaning anti-reflection layer of solar cells.



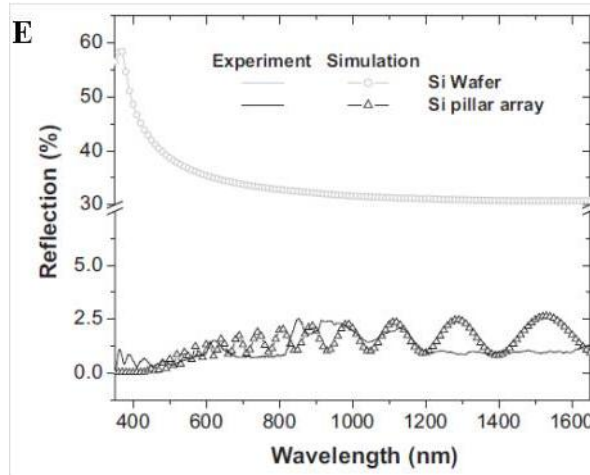


Figure 1.25 (A-D) The procedures for fabricating antireflective Si pillar arrays by using colloidal monolayer silica as etching template. (E) Experimental (solid) and simulated (dotted) specular reflection of a flat silicon wafer and etched silicon pillar array.[69]

1.3.3 Friction reduction

The frictional drag in pipe or tube can affect the transport of oil or liquid. Superhydrophobic surfaces can be potentially used for anti-friction or drag reduction in microfluid channels and microelectromechanical systems (MEMS). The superhydrophobic coating in channels can result in resistance reduction, energy saving and efficiency improvement of the system. For example, Choi C. H. et al. found that the superhydrophobic surfaces with nanograting structures not only reduce the friction in liquid flows under pressure but also enable directional control of the slip (Figure 1.26).[70]

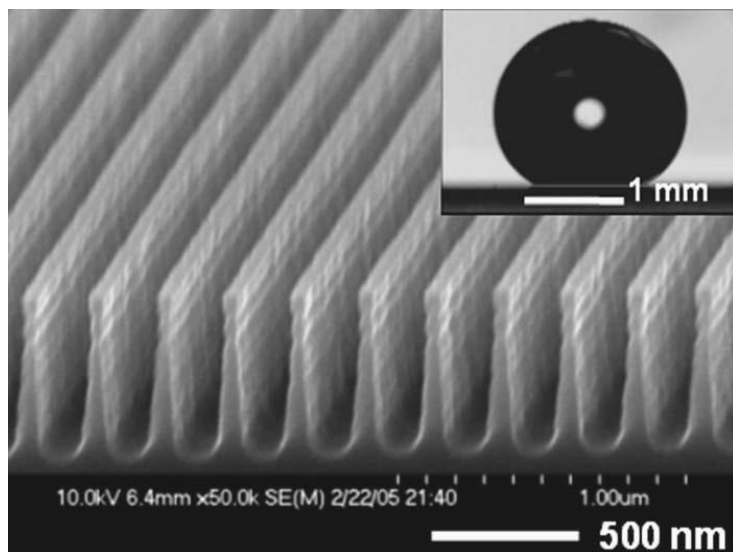


Figure 1.26 SEM image of a Si nanograting structure.[70]

1.3.4 Water/oil separation

The fuel spills such as in the 2010 Deepwater Horizon accident in the Gulf of Mexico lead to severe environmental issues, which raised the efforts for developing low cost system to remove oil contaminates in water. Many studies have been conducted regarding the design of superhydrophobic and superoleophilic films for water and oil mixture separation. For example, Calcagnile P. et al. uses polyurethane foams modified with iron oxide nanoparticles and polytetrafluoroethylene sub-microparticles. The foam was found to effectively absorb the oil by using magnet.[71]

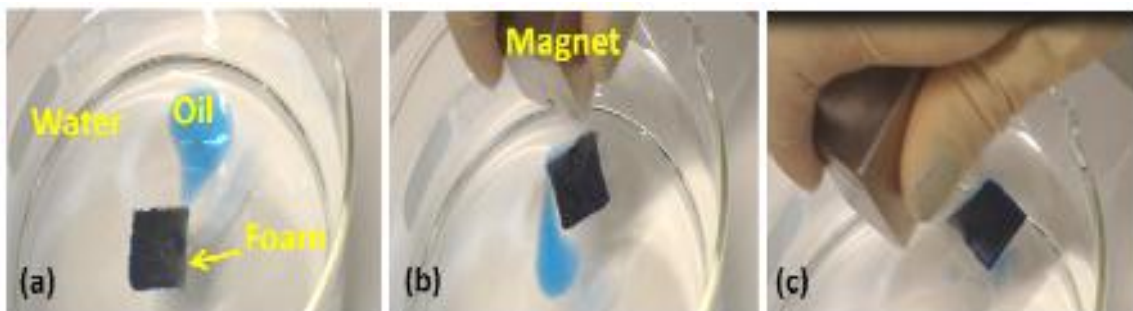


Figure 1.27 Cleaning process of oil (colored by a blue dye) by polyurethane foams in water, using a weak magnet to move the foam.[71]

Wang C. X. et al. utilized hierarchical structure of copper mesh by nitric acid etching and 1-hexadecanethiol modification. The mesh can be used to achieve diesel oil and water separation as shown in Figure 1.28. The water was rolled off and the oil was penetrated through the mesh.[72]

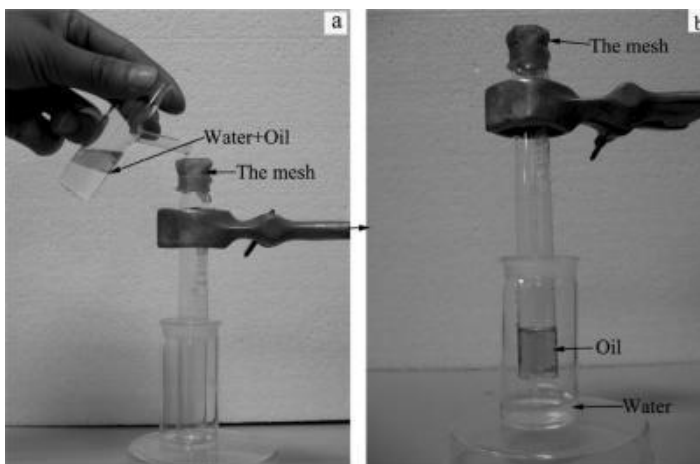


Figure 1.28 Illustration of separation process of the mixture of diesel oil and water.[72]

1.4 Challenge and Research Objectives

1.4.1 Challenges

As mentioned before, there are many approaches for fabricating superhydrophobic surfaces by controlling the surface structure and surface energy. But many challenges still exist, such as fabricating superoleophobic surfaces, surface coating with tunable or patterned wettability, robust superhydrophobic surfaces that can resist moisture, temperature, and abrasions, which may require more research efforts.

1.4.1.1 Oil repellent

One of the challenges for the self-cleaning surface is the oil contamination. Although self-cleaning surface can roll off or repel the water droplet, when oils (such as

hexadecane, octanol etc.) was dipped on the surface, it will spread over the surface and have a contact angle of $\sim 0^\circ$. Therefore, it's quite difficult to fabricate oleophobic or superoleophobic surfaces that can repel low surface energy oils.

1.4.1.2 Electronic packaging applications

Besides the previous mentioned potential applications for superhydrophobic surfaces, there are few studies reported about exploring applications of superhydrophobic surfaces in electronic packaging. In electronic packaging industry, moisture is an important factor that may affect the performance and reliability of microelectronics. When moisture diffuses into the devices, electrocorrosion may occur with the presence of mobile ions.

1.4.1.3 Tunable wettability

Modifying the surface wettability is very important for practical applications, such as inkjet printing, microfluid channels, etc. For those applications, both superhydrophobic (water contact angle larger than 150°) and superhydrophilic surfaces (water contact angle is almost 0°) are very useful. But it's quite challenging to achieve tunable superhydrophobicity and superhydrophilicity on one substrate.

1.4.1.4 The robustness of superhydrophobic surfaces

The robustness of superhydrophobic surfaces includes stability in certain temperature, humidity environment, or even corrosive acid or base environment. Change of surface chemistry will lead to loss of superhydrophobicity and self-cleaning properties. So chemical species coated on surface should have strong chemical bonds under hostile environment in addition to low surface energy. Mechanical robustness is another important property for superhydrophobic surfaces in practical applications. The surface structure change under abrasion may affect the superhydrophobicity. For example, some of superhydrophobic surfaces made of inorganic materials, and the surface structures are

prone to mechanical damage under abrasion forces due to their brittle nature. Further investigation for improving mechanical robustness is quite necessary.

1.4.2 Research objectives

1.4.2.1 Understanding the structure effect on superoleophobicity and transition between

Wenzel and Cassie states

Designing superoleophobic surfaces requires an understanding of the effect of geometrical shape of Si surfaces on the contact angle and hysteresis. Etching conditions such as etching time and etchant concentration were varied to generate different surface geometry and establish oleophobicity/superoleophobicity. The relationship between the re-entrant angle and the CA transition between Cassie and Wenzel behavior on etched Si (111) surfaces needs to be investigated.

1.4.2.2 Developing robust superhydrophobic SiC surfaces

Surface roughness control is very important for achieving superhydrophobicity. However, roughness control of SiC is very difficult due to the high chemical stability of Si-C bonds. We used combined etchings with metal assisted etching and reactive ion etching to modify surface roughness. The stability of superhydrophobic SiC surface in temperature humidity chamber, and also in acidic or basic solutions was studied.

1.4.2.3 Investigating superhydrophobic-superhydrophilic reversible wettability coating

Tuning the surface wettability is of great interest for both scientific research and practical applications, such as inkjet printing, and microfluid channels. By pattern superhydrophobic/superhydrophilic areas, water or ink will keep staying in the hydrophilic part. We explore the reversible transition between superhydrophobicity and superhydrophilicity on a nanocomposite film. A reversible transition of surface wettability can be realized by alternation of UV illumination and surface treatment.

1.4.2.4 Exploring the applications of superhydrophobic surfaces in electronic packaging

Moisture is one of the most detrimental factors to the reliability of microelectronics. Water repelling property such as superhydrophobicity is very demanding for low cost and high reliability microelectronic packaging solution. To improve the device reliability, a conformal coating of organic encapsulant is usually applied on the devices package. We explored low cost and robust superhydrophobic nanocomposites as encapsulant for microelectronics.

1.4.2.5 Exploring the applications of superhydrophobic surfaces in solar cells

In the practical application of solar cells, shading is an important practical issue for light absorption, because the dust accumulation on the solar panel surface may block the incident light and reduces the power output. Therefore, self-cleaning function was proposed to apply to the solar cell by surface functionlization, in order to reduce dust accumulation on the solar cell surface. At the same time, the hierarchical structure made by etching or coating technique leads to gradient change of refractive index, and effectively reduces the light reflection on the surface. These properties make the multi-functional solar cells with low reflection, high efficiency and self-cleaning properties.

CHAPTER 2

SILICON SURFACE STRUCTURE-CONTROLLED OLEOPHOBICITY

Superoleophobic surfaces display contact angles $> 150^\circ$ with liquids that have lower surface energies than does water. The design of superoleophobic surfaces requires an understanding of the effect of geometrical shape of etched silicon surfaces on the contact angle and hysteresis observed when different liquids are brought into contact with these surfaces. This study used metal-assisted etching and various silane treatments to create superoleophobic surfaces on a Si (111) surface. Etching conditions such as etch time and etch solution concentration, played critical roles in establishing oleophobicity of Si (111). When compared to Young's contact angle, the apparent contact angle showed a transition from a Cassie to a Wenzel state for low surface energy liquids as different silane treatments were applied to the silicon surface. These results demonstrated the relationship between the re-entrant angle of etched surface structures and the contact angle transition between Cassie and Wenzel behavior on etched Si (111) surfaces.

2.1 Introduction

Superhydrophobic surfaces are defined by their ability to display a contact angle with water (surface tension $\gamma_{lv} = 72.1$ mN/m) greater than 150° and hysteresis smaller than 10° [73]. Many natural surfaces show superhydrophobic properties, such as cicada wings [2], water strider legs [74], and gecko feet [5]. Lotus leaves are one of the most well known examples among naturally occurring superhydrophobic surfaces [75]. The structure of a lotus leaf consists of a combination of micro and nano roughness along with a low surface energy coating that yields a self-cleaning surface [76-77] commonly

referred to as “lotus effect”. This property has been widely mimicked by artificial structures that are used to reduce stiction in microelectromechanical systems (MEMS) [78], corrosion inhibition [79], and friction reduction [80].

On a rough surface, two superhydrophobic states are usually observed: Wenzel’s state (complete wetting) and Cassie’s state (partial wetting) [81]. The Wenzel equation [6], Eqn (1), describes the effect of surface roughness on the water droplet contact angle:

$$\cos \theta_A = r \cos \theta_Y \quad (1)$$

where θ_A is the apparent contact angle on the rough surface, r is the ratio of the actual solid/liquid contact area to its vertical projected area, and θ_Y is the contact angle on a flat surface defined by Young’s equation. As the roughness (r) increases, the contact angle also increases reflecting an increase in relative hydrophobicity.

The Cassie equation [7] for a porous or composite surface, Eqn. (2), indicates that when the solid surface fraction f is decreased, the apparent contact angle increases.

$$\cos \theta_A = -1 + f(\cos \theta_Y + 1) \quad (2)$$

Although water droplets could roll off lotus leaf surfaces, liquids with low surface tension such as hexadecane ($\gamma_{lv} = 27.5$ mN/m), wet the lotus leaf surface rapidly with a contact angle of $\sim 0^\circ$ [82]. In order to design a superhydrophobic/superoleophobic surface that resists wetting by low surface tension liquids, both surface energy and structure/roughness must be controlled [23, 83]. Fluoropolymer/fluorocarbon materials have one of the lowest surface energies available, which makes such coatings attractive for self-cleaning surfaces [9]. Geometrical shape at the interface with the wetting liquid is also critical in establishing superoleophobicity. Several studies have reported formation of superoleophobic surfaces by designing overhang or re-entrant structures. Extrand C. W. first theoretically analyzed the re-entrant structures which can be employed in oleophobic applications [84]. Tuteja *et al.* created re-entrant structures on electrospun polyhedral oligomeric silsesquioxane (POSS) fiber surfaces to achieve superoleophobicity [82]. Ahuja *et al.* reported that a nanonail topography showed

superoleophobic behavior and inhibited the transition between Cassie-Baxter and Wenzel states without external stimuli [85]. Similar structures could also be fabricated on porous Si films [86]. After coating with fluorinated organic molecules, the porous Si films became super oil-repellent to ethylene glycol and hexadecane with a contact angle greater than 150°.

Although these studies indicated the importance of re-entrant structures in achieving superoleophobicity, they did not provide the evaluation of surface geometry and oleophobicity by the transition from a Cassie to a Wenzel state of different liquids in the wetting diagram, e.g., for ethylene glycol or hexadecane with low surface energies. In this study, we invoke metal-assisted etching and silane treatments to achieve superoleophobicity on Si (111); inclined surface geometrical structures were controlled by variation of etch conditions. Pyramid structures have been formed by KOH etching of Si (100) surfaces to allow further control/variation of the geometrical structures obtained. In addition, five different silanes have been employed to generate different surface coatings with varying surface energies. Results establish how surface geometry influences the hydrophobicity or oleophobicity of Si (111).

2.2 Experimental Details

In order to create oleophobic surfaces, Si (111) wafers were etched in HF/H₂O₂ by a metal-assisted etching technique. The Si (111) surface was first coated with Au nanoparticles by immersing it in an Au coating solution. The Au coating solution was prepared by dissolving 0.03 M KAuCl₄ (99.995%) in a 10 wt % HF aqueous solution (EMD). Etching was then performed in the HF/H₂O₂ solution at room temperature for various times. Different concentrations of etching solution were employed; 1:5:10, 2:5:10 and 3:5:10 volume ratios of 49% HF, 30% H₂O₂, and H₂O. After etching, the Au

nanoparticles were removed by immersing the samples in KI/I₂ solution (100 g KI and 25 g I₂ per 1L H₂O) for 15 s.

Si (100) pyramid structures were generated using n-type silicon (100) wafers with a resistivity of 3-10 Ω-cm. KOH etching was performed in a solution of KOH (3 wt%), water and isopropyl alcohol (20 vol%) at 85°C for 20-30 min.

After forming the surface structures, surface fluorination was performed by treatment of etched Si (111), Si (100) pyramid, flat Si (111) and Si (100) wafers in five different silane solutions, which are 3 mM hexane solutions of aminopropyltriethoxysilane (APS), 3, 3, 3-trifluoropropyl-trichlorosilane (TFPS), dodecyltrichlorosilane (DTS), octadecyltrichlorosilane (ODTS), and perfluorooctyl trichlorosilane (PFOS). The structured Si wafer was immersed in APS for 60 min and in other silane solutions for 30 min, followed by a heat treatment at 150 °C in air for 1 h, to complete the hydrophobic surface modification.

Contact angle measurements of water, ethylene glycol and hexadecane were performed with a Rame-Hart goniometer with a charge-coupled device camera equipped for image capture. Scanning electron microscopy (SEM) LEO 1530 was used to investigate the surface morphology.

2.3 Results and Discussion

Etching mechanism investigations (Figure 2.1) have indicated that the concentrations of HF and H₂O₂ control the etching rate in the vicinity of the Au/Si contact (HF reacts with SiO₂), and the concentration of H₂O₂ also determines hole injection, which is the controlling factor for surface hole concentration at the Au/Si contact [87-88]. Therefore, the H₂O₂ concentration controls the diameter of etched pits (provided that the Au nanoparticles are far away from each other) or the nanostructure size (when the Au nanoparticles are close to each other). In this way, surface structures

can be fabricated to establish the superhydrophobicity and superoleophobicity of Si surfaces.

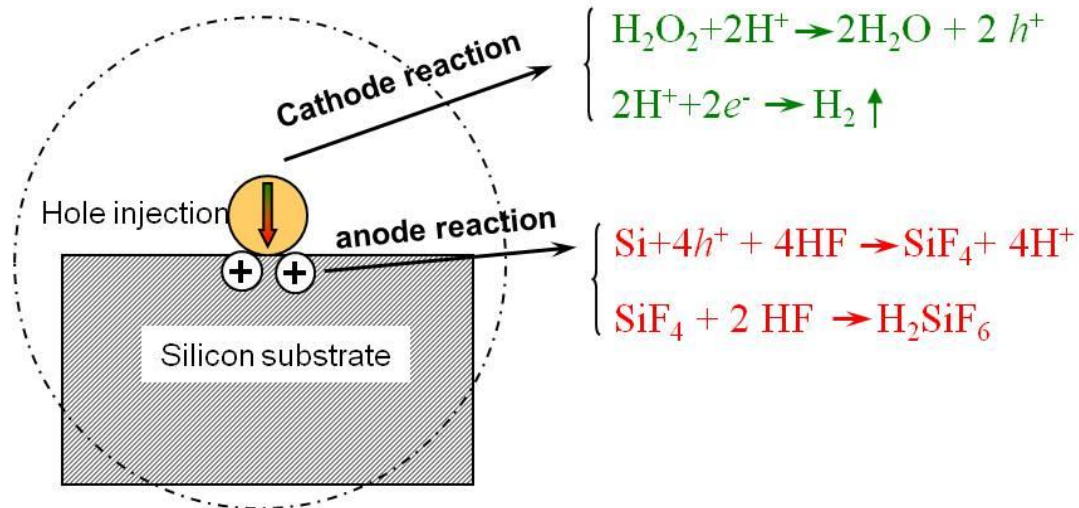


Figure 2.1 Mechanism of metal-assisted chemical etching

For low surface energy liquids such as oils, it is difficult to achieve a high contact angle even on surfaces with low surface energy. In order to achieve superoleophobicity, specific structures, such as the re-entrant geometries shown in Figure 2.2, are essential. The higher the re-entrant angle (Figure 1b, reentrant angle is 90°), the higher the Laplace pressure force, which can effectively prevent the liquids from penetrating into the texture [84]. For oleophobic surface, the second scale roughness does not enhance the oleophobicity. Instead, it may increase the wettability of the surface due to the low surface energy of the liquids, resulting in a Wenzel state. In this situation, the re-entrant angle is critical in achieving the oleophobic/superoleophobic property.

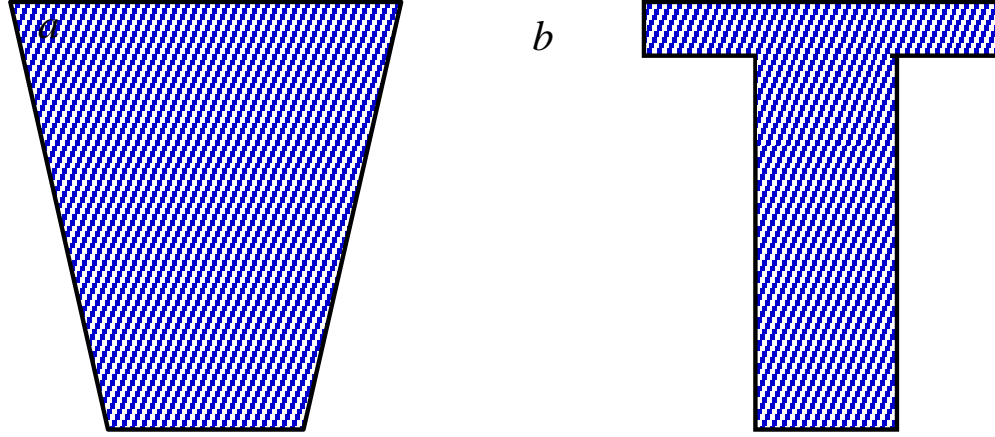


Figure 2.2 Geometrical structures that can lead to superoleophobicity.

Oleophobicity has typically been achieved through the formation of a composite interface (solid/oil and air/oil interfaces) on surfaces with re-reentrant structures. Figure 2.3 illustrates the geometry of oil in contact with inclined walls. The Laplace pressure is important in maintaining a composite interface; the relationship between the Laplace pressure and the inclination angle α can be described by Eqn.(3) [84, 89]

$$\Delta p = p - p_0 = -\frac{\gamma \cos(\theta_Y + \alpha)}{R_0 - h \tan \alpha} \quad (3)$$

where γ is the surface tension of the liquid, θ_Y is Young's contact angle of the liquid on a flat surface, α is the inclination angle/re-entrant angle as shown in Figure 2.3, R_0 is the half width between base edges of two adjacent inclined walls, and p is the pressure on the liquid side of the meniscus. The Laplace pressure is dependent on the surface tension of liquid γ , height h , width R_0 , Young's contact angle θ_Y , and inclination angle α . The higher the inclination angle α , the greater the reduction in Laplace pressure. In a metastable Cassie state, the Laplace pressure affects the hysteresis and can lead to a transition from a Cassie state to a Wenzel state. The transition pressure is related to the Laplace pressure that confines the droplet to the composite surface. For structured surfaces that are inclined relative to the vertical axis, equation (3) indicates that the transition will occur at a lower pressure relative to surfaces without an inclination.

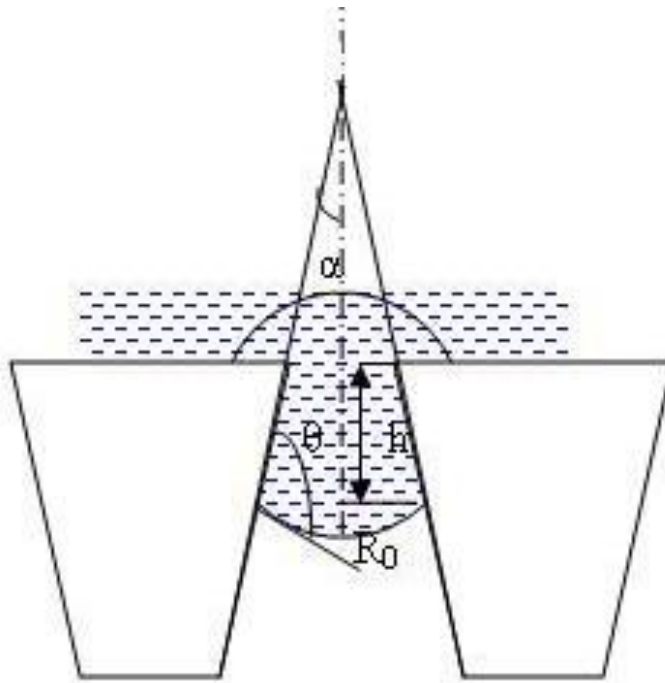


Figure 2.3 Oil contact at surface structures with inclined walls.

2.3.1 Effect of etchant solution concentration and etching time on hydrophobicity and oleophobicity

In this study, Si (111) wafers were etched in a HF/H₂O₂/H₂O solution for different times at room temperature, and then treated by fluoroalkylsilane (PFOS), and the effect of etch time and HF/H₂O₂/H₂O solution concentration on surface hydrophobicity and oleophobicity were investigated. The surface morphology of etched Si with different etching time was shown in Figure 2.4. With an etch solution composition of 1:5:10 HF/H₂O₂/H₂O, the resulting surface structure showed superhydrophobicity and moderate oleophobicity to hexadecane, as shown in Figure 2.5.

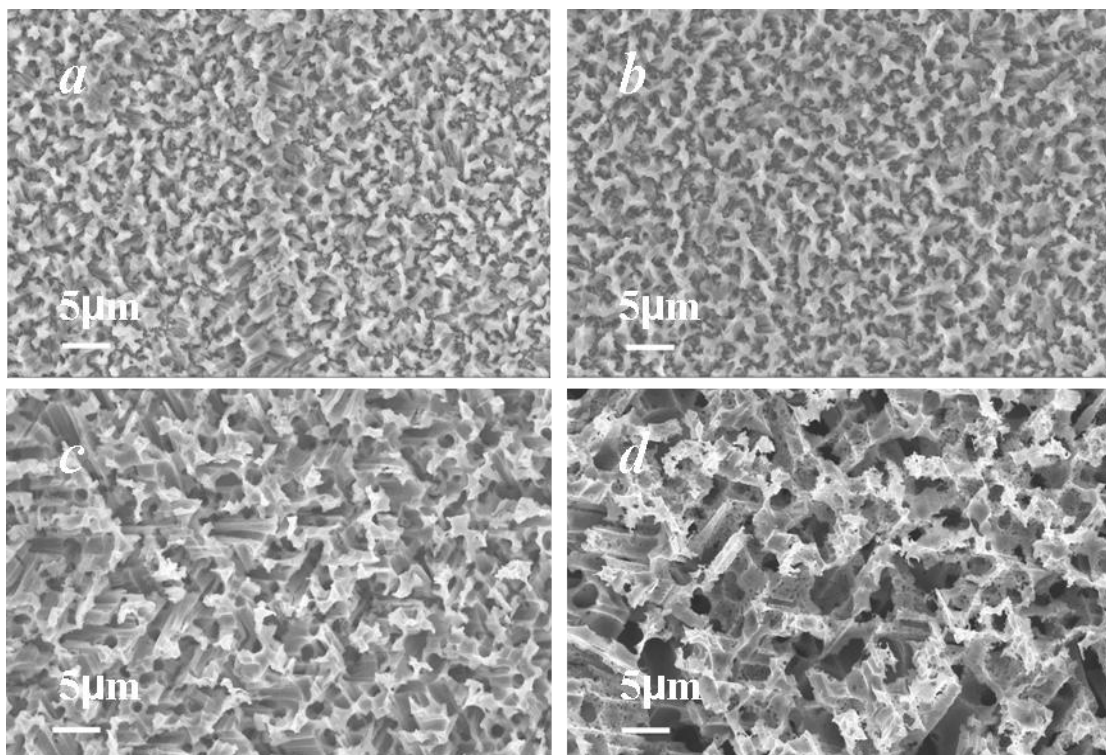


Figure 2.4 SEM images of the surface morphologies from Au assisted etching of Si (111) surfaces; Si (111) etched in HF/H₂O₂/H₂O (v/v/v 1:5:10) for a) 10 min, b) 30 min, c) 60 min, and d) 180 min.

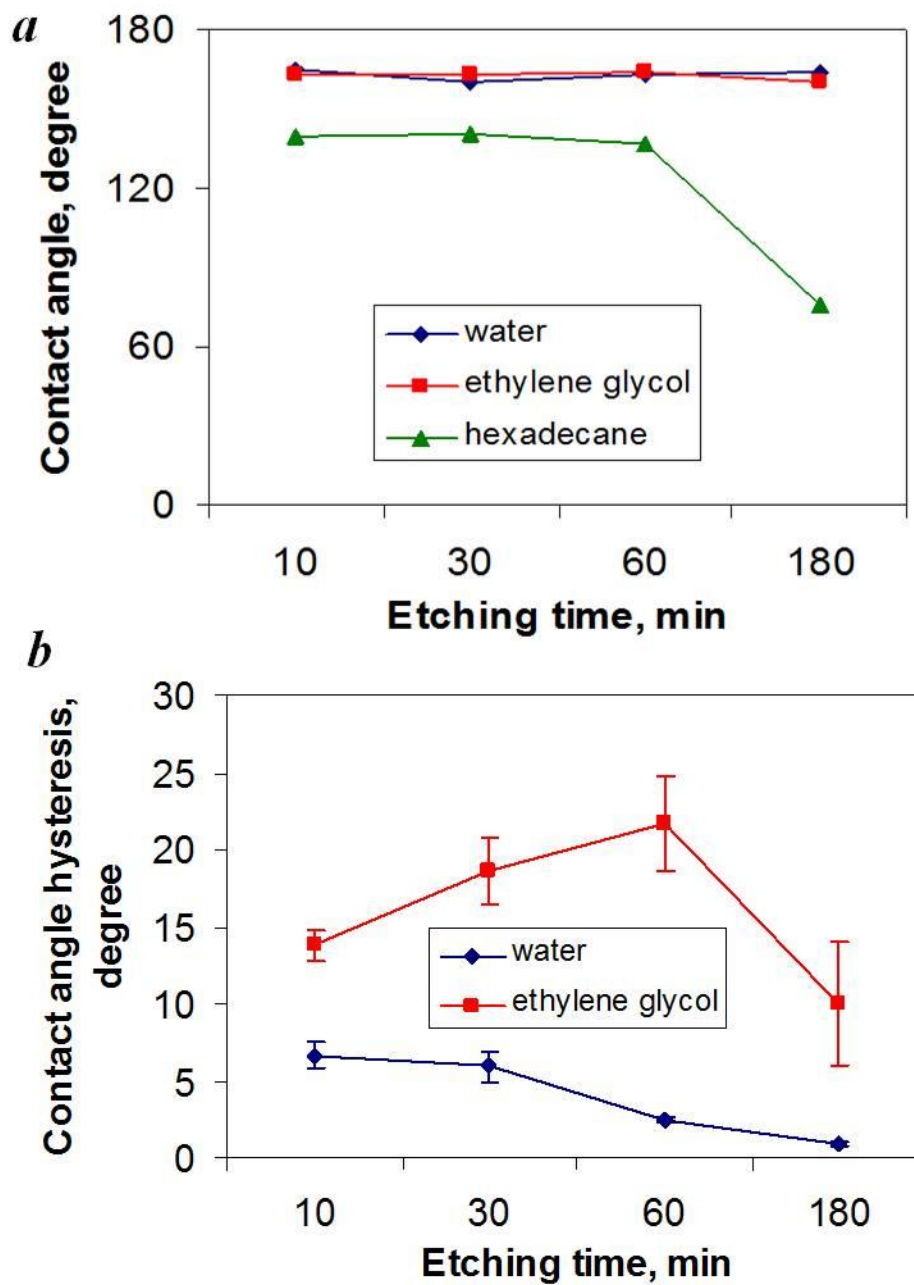


Figure 2.5 (a) Contact angles of water, ethylene glycol, and hexadecane on Si (111) surfaces generated by Au assisted etching in HF/H₂O₂/H₂O (v/v/v 1:5:10) for different times at room temperature.(b) Contact angle hysteresis of water and ethylene glycol on the etched Si (111) surfaces described in (a).

Since Si surfaces etched in 1:5:10 etchant solution did not display superoleophobicity with hexadecane, a higher HF etchant concentration 2:5:10 was employed. The contact angle and contact angle hysteresis data are shown in Figure 2.6. For water and ethylene glycol, both a high contact angle ($>160^\circ$) and a low hysteresis ($<3^\circ$) were achieved with appropriate etching time (~ 40 min etching). For hexadecane, a high contact angle of $\sim 160^\circ$ was also achieved when etching for 40 min. Under these etching conditions, the hexadecane droplet beads up and rolls-off the surface, which indicates that roll-off superoleophobicity and possibly self-cleaning of surfaces using hexadecane or other lyophobic liquids can be achieved using Au assisted Si etching with the 2:5:10 etchant solution. SEM cross-section examination of the Si(111) etched in 2:5:10 solution shows that the key parameter in achieving oleophobic phenomenon is the surface re-entrant angle. As shown in Table 2.1, the 40 min etch gives a re-entrant angle of $\sim 54^\circ$, which shows the best oleophobicity. Although 20 min etch shows similar re-entrant angle of surface structures, the feature spacing and height are much smaller, which resulted in a limited oleophobicity. For the surfaces prepared from 120 min etch, both the feature spacing and height are large. However, the lack of consistent re-entrant structures on the surface resulted in oleophilicity for hexadecane, although superhydrophobicity was achieved.

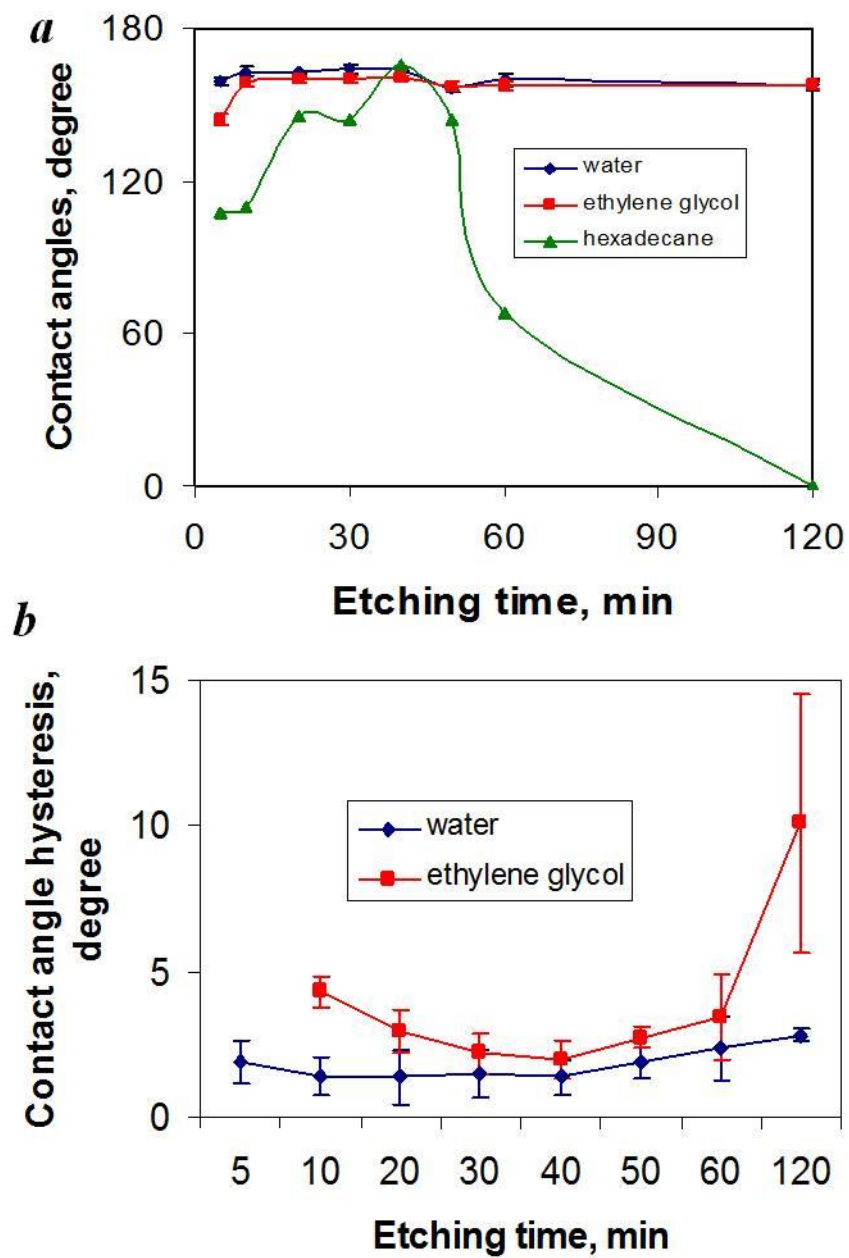


Figure 2.6 (a) Contact angles of the surfaces etched by Au-assisted etching of Si (111) surfaces in HF/H₂O₂/H₂O (v/v/v 2:5:10) solution for various times. (b) Contact angle hysteresis of water and ethylene glycol on the etched surfaces.

Table 2.1 Feature Size of textured Si (111) surfaces using Au assisted etching for different time, measured from SEM cross-section images. Si (111) surfaces were etched in HF/H₂O₂/H₂O (v/v/v 2:5:10) solution.

Etching time	Spacing (μm)	Height (μm)	Re-entrant angle
20min	3.5	12.7	$\sim 54^\circ$
40min	5.4	21.6	$\sim 54^\circ$
60min	6.9	28.1	0-30°
120min	9.0	38.8	random

Surface morphologies of the etched Si (111) surfaces after different etching times are shown in Figure 2.7. When the etching time was larger than 20 minutes, re-entrant geometrical structures were observed. Table 2.1 indicates that the etch depth and distance between re-entrant units changed with the etching time. When the etching time was 40 min, high density re-entrant structures and large etch depth were achieved; these geometrical structures resulted in superoleophobicity of the Si surface with hexadecane. However, when the etch time was greater than 60 min, the hexadecane contact angle decreased dramatically although the etch depth was larger than that observed for 40 min of etching. Similarly, contact angle results are likely due to the lack of re-entrant structures and the large distance between each structural unit; thus, oil can easily enter the gaps which yield a low contact angle with hexadecane.

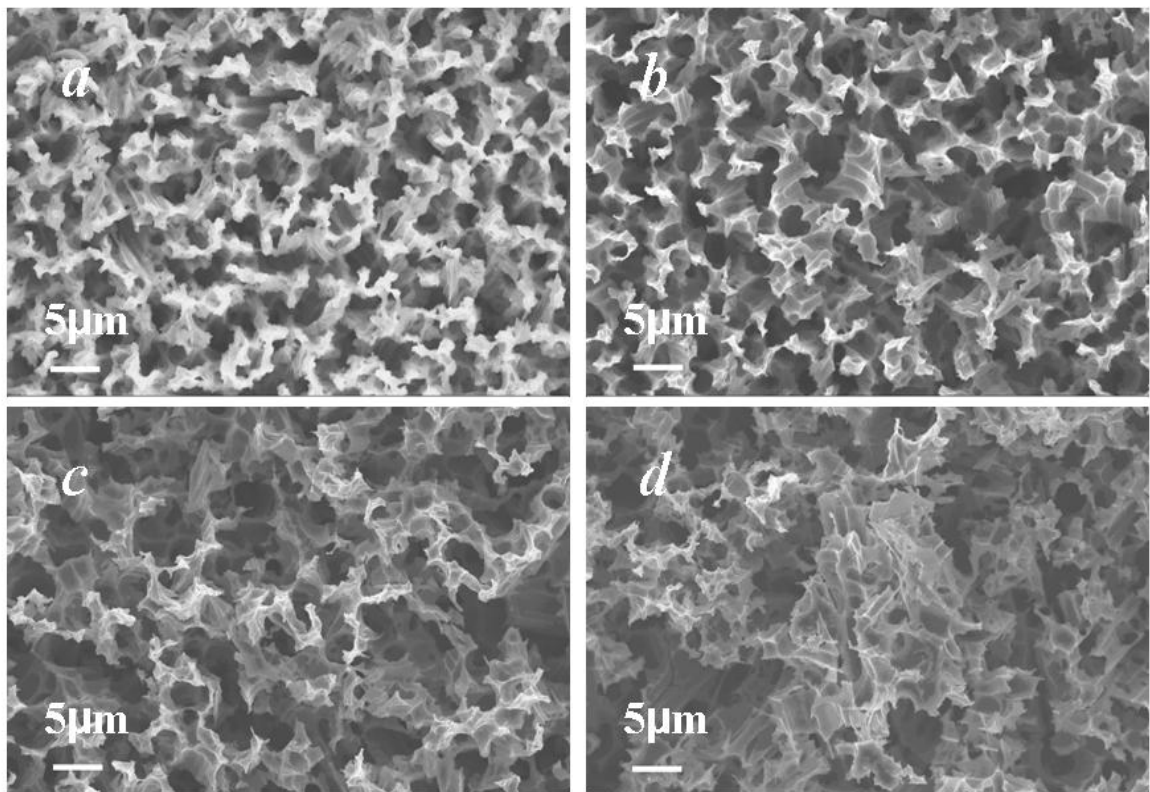


Figure 2.7 SEM images of the surface morphologies from Au assisted HF/H₂O₂/H₂O etching on Si (111) surfaces; Si(111) etched in HF/H₂O₂/H₂O (v/v/v 2:5:10) for a) 20 min, b) 40 min, c) 60 min and d) 120 min

An effective way to increase oleophobicity is to generate re-entrant angle structures, as shown in Figure 2.8, to increase the Laplace pressure. With an increase of inclination angle α , the Laplace pressure increases when the meniscus approaches the top of the structure (i.e., decreasing h). Oleophobicity therefore increases because additional air is trapped between the structures and the contact area is reduced, leading to an increase in apparent contact angle and reduced contact angle hysteresis.

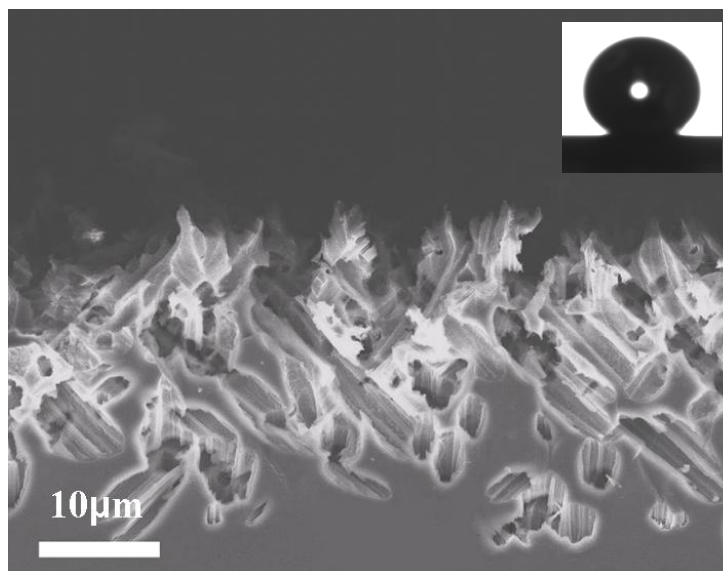


Figure 2.8 SEM images of cross section from Au assisted HF/H₂O₂/H₂O etching on Si (111) surfaces; Si(111) etched in HF/H₂O₂/H₂O (v/v/v 2:5:10) for 40 min. The contact angle images of hexadecane are shown in the inset.

When Si surfaces were etched using 3:5:10 HF/H₂O₂/H₂O etchant, the structure generated showed superhydrophobicity and low hysteresis ($< 10^\circ$) for water droplets. As shown in Figure 2.9, the etched Si (111) displayed a Cassie state for ethylene glycol droplets when the etch time was more than 10 min. In addition, low contact angle hysteresis ($< 10^\circ$) was observed when the etch time was between 20 min and 40 min. For hexadecane, the surface displayed only a Wenzel state. The highest contact angle (133°) was achieved when the etching was performed for 20 min, and the contact angle decreased significantly after 40 min, consistent with SEM results (Figure 2.10). With increased etching times, the re-entrant structures were not well formed on the Si surface. Especially on the top surfaces, the structures are mostly vertical rather than inclined, which is not effective for the generation of oleophobic surfaces, particularly for low surface energy liquids such as hexadecane.

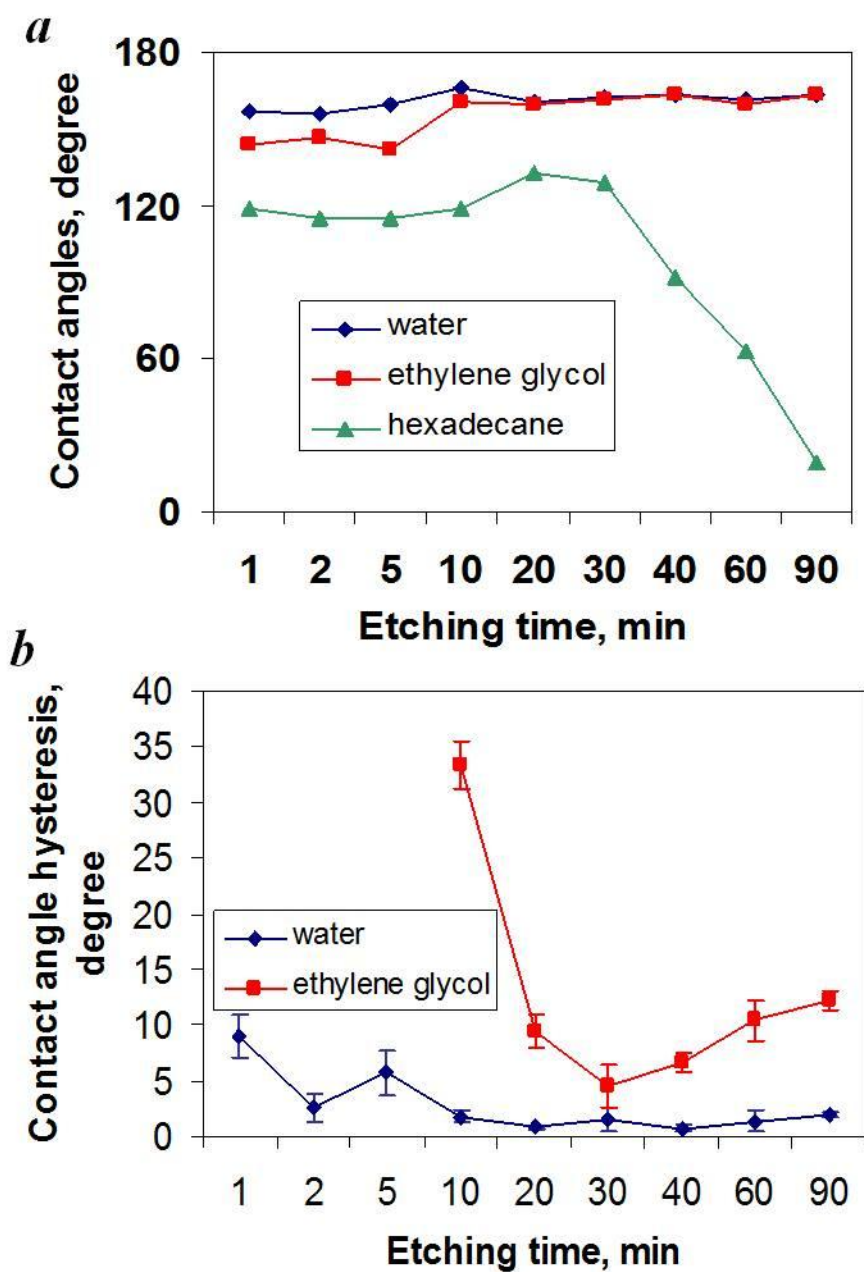


Figure 2.9 (a) Contact angles of surfaces etched by Au-assisted etching of Si (111) in HF/H₂O₂/H₂O (v/v/v 3:5:10) solution for water, ethylene glycol and hexadecane. (b) Contact angle hysteresis of the etched surfaces with water and ethylene glycol.

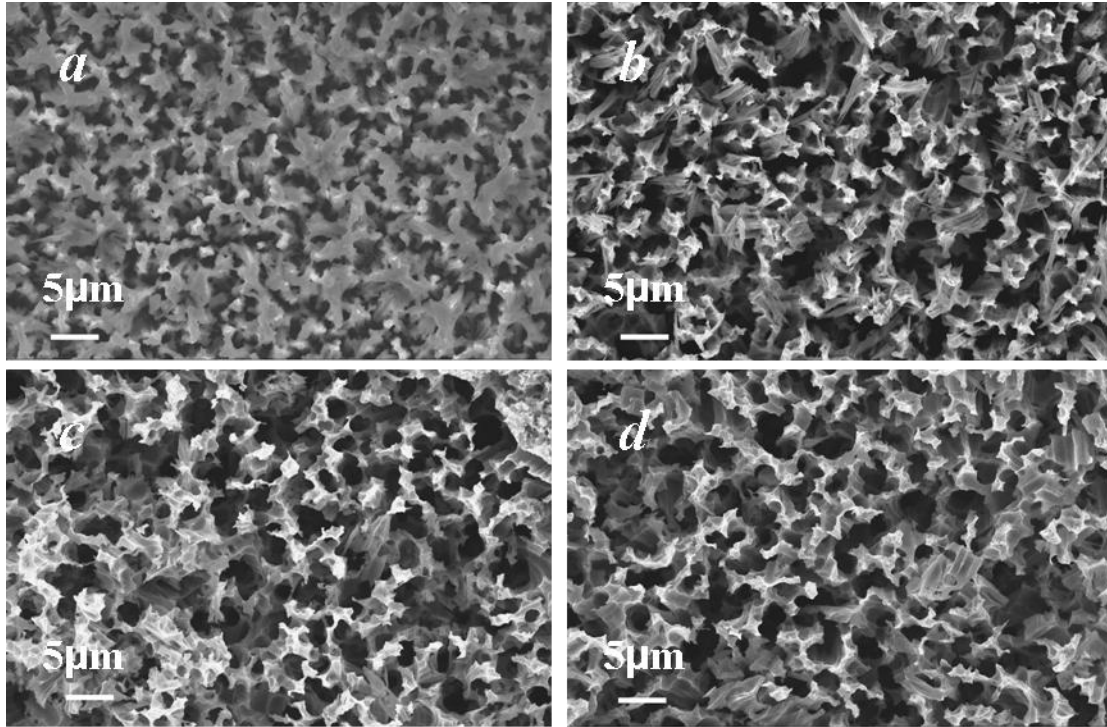
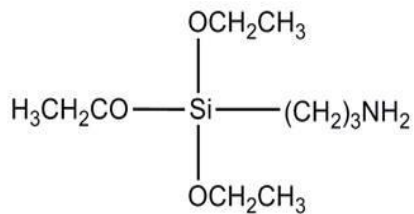


Figure 2.10 SEM images of the surface morphologies from Au assisted HF/H₂O₂/H₂O etching of Si (111) surfaces; Si (111) etched in HF/H₂O₂/H₂O (v/v/v 3:5:10) for a) 20 min, b) 40 min, c) 60 min and d) 90 min

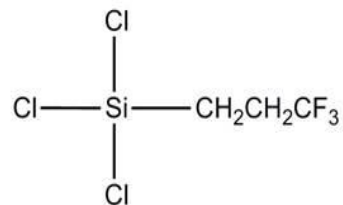
2.3.2 Transition from Cassie state to Wenzel state

Tsujii's group compared contact angles θ^* on rough surfaces with contact angles observed on a flat surface, which is close to the Young's contact angle θ_Y [24, 90]. The comparison was performed using different liquids to vary θ on the solid surface. In our experiments, Si (111) surfaces were etched in 2:5:10 HF/H₂O₂/H₂O etchant solution for 40 min, and then treated with five different silane solutions to vary the surface energies (Figure 2.11). Contact angles of water, ethylene glycol, and hexadecane were then measured on both flat and rough surfaces (Table 2.2). Results indicated that the apparent contact angles θ_A for all three liquids depended monotonically on the Young's contact angle θ_Y . When θ_Y was greater than 90°, the Si (111) surface showed hydrophobic/oleophobic behavior, and when θ_Y was significantly smaller than 90°, it

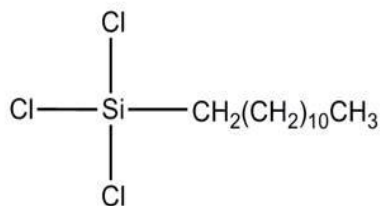
showed hydrophilicity and oleophilicity; however, superhydrophobicity/superoleophobicity can still be observed if the surface is weakly hydrophilic (θ_Y between 60° and 90°). The apparent contact angles of water were all greater than 160° ($\cos \theta_A$ was close to -1) and showed superhydrophobicity for the five different silanes, which indicates that the surface corresponds to a metastable Cassie state. Figure 2.12 shows a wetting diagram ($\cos \theta_A$ vs. $\cos \theta_Y$) for water, ethylene glycol (EG) and hexadecane which displays the transition from a Cassie to a Wenzel state. For all three solvents, the data points collapse onto one curve which crosses the x-axis ($\cos(\theta_A) = 0$ or $\theta = 90^\circ$) at a Young's contact angle of 58 - 62° . According to Eqn. (3), this angle represents the surface structure inclination angle (or re-entrant angle); that is, the curve describes the surface structure (reentrant angle). If the Young's contact angle of a liquid on a surface is smaller than the structure inclination angle, the surface is in a Wenzel state, while surfaces with a Young's contact angle greater than the inclination angle form a Cassie state and a liquid-repellent surface can be obtained. This phenomenon is characterized by a shift of the transition curve from crossing the x-axis at $\cos(\theta_Y) \sim 0$ to ~ 0.5 as a result of the re-entrant angle structure effect. Enhanced hydrophobicity/oleophobicity can be achieved with the combination of re-entrant structure and low surface energy layers. For comparison, on surfaces with pyramidal microstructures (Figure 2.13), the curve of $\cos(\theta_A)$ vs. $\cos(\theta_Y)$ crosses the x-axis near the plot origin (0, 0), as shown in Figure 2.14 and Table 2.3. Furthermore, the slope of this plot is gradual in contrast to measurements on re-entrant surface structures, where the change of apparent contact angle with Young's contact angle is abrupt (Figure 2.14). The comparison of Figure 2.12 and 2.14 shows that the geometry is critical in achieving superoleophobicity since the same silane treatments were used for both textured Si (111) and textured Si (100) surfaces. Surfaces with re-entrant structure can effectively achieve superoleophobicity due to the amplified Laplace pressure demonstrated in eqn. (3).



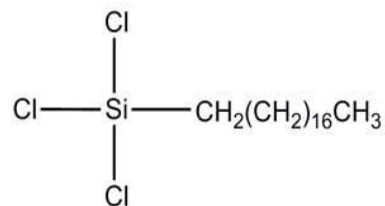
Aminopropyltriethoxysilane (APS)



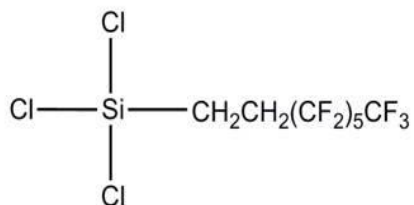
3, 3, 3-trifluoropropyl-trichlorosilane (TFPS)



Dodecyltrichlorosilane (DTS)



Octadecyltrichlorosilane (ODTS)



Perfluorooctyl trichlorosilane (PFOS)

Figure 2.11 Chemical Structures of five silanes used for surface hydrophobic treatment on Si wafers

Table 2.2 Young's contact angle θ_Y and apparent contact angles θ_A of Si (111) surfaces using Au-assisted etching. Si (111) samples were etched in HF/H₂O₂/H₂O solution (v/v/v 2:5:10) for 40 min.

	PFOS		ODTS		DTS	
	X(θ_Y)	Y(θ_A)	X(θ_Y)	Y(θ_A)	X(θ_Y)	Y(θ_A)
H ₂ O	112.4	163.3±1.3	105.4	162.9±2.3	92.3	163.2±1.9
Ethylene glycol	102.5	160.4±1.2	86.3	155.1±2.1	63.5	139.3±1.6
Hexadecane	76.8	161.2±0.8	58.5	5.4±1.4	7.8	4.7±1.6

	TFPS		APS		Untreated	
	X(θ_Y)	Y(θ_A)	X(θ_Y)	Y(θ_A)	X(θ_Y)	Y(θ_A)
H ₂ O	82.1	161.9±0.6	48.1	8.5±2.0	80.7	161.5±1.2
Ethylene glycol	61.7	17.2±2.3	31.3	8.1±2.0	53.5	5.1±1.4
Hexadecane	29	4.8±1.1	4.3	3.8±0.9	5.5	0±0.2

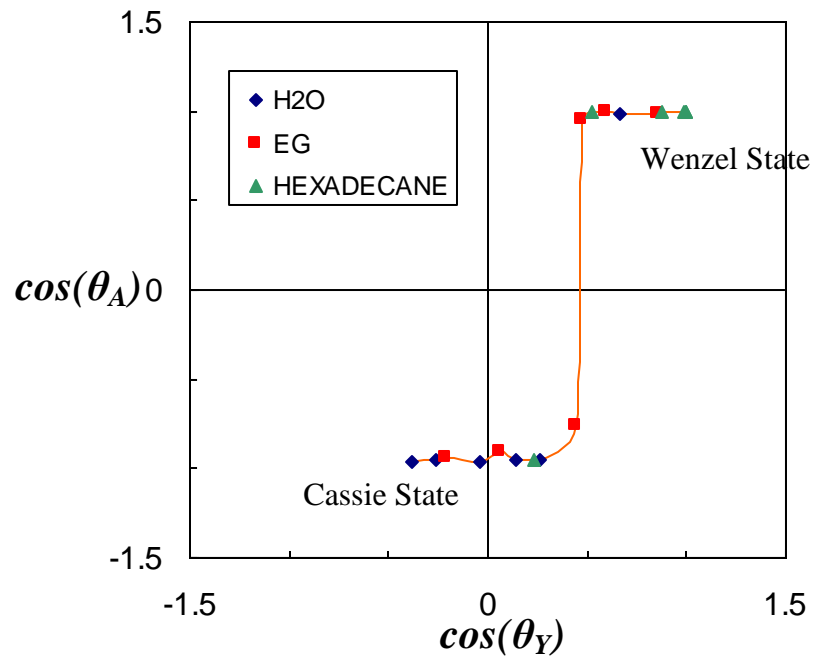


Figure 2.12 Cosine of apparent contact angle θ_A on a textured Si (111) surface as a function of the Young's angle θ_Y .

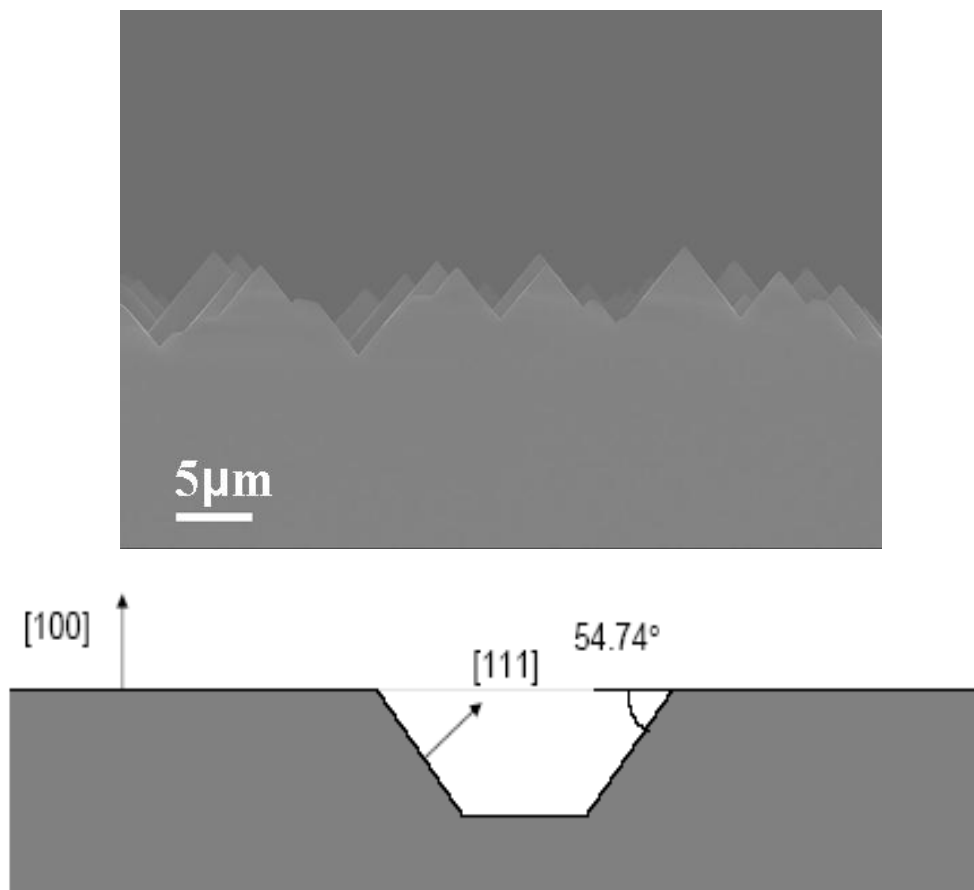


Figure 2.13 Cross section of Si (100) pyramidal structures after KOH etching.

Table 2.3 Young's contact angle θ_Y and apparent contact angles θ_A of Si (100) pyramid structures after KOH etching.

	PFOS		ODTS		DTS	
	X(θ_Y)	Y(θ_A)	X(θ_Y)	Y(θ_A)	X(θ_Y)	Y(θ_A)
H ₂ O	115.6	137.4±0.9	105.7	124.6±0.1	99.5	118.9±0.6
Ethylene glycol	108.1	130.7±1.4	84.9	101.1±2.6	79.0	87.5±1.7
Hexadecane	87.5	100.3±1.5	35.4	6.0±2.5	10.6	5.8±0.9

	TFPS		APS		Untreated	
	X(θ_Y)	Y(θ_A)	X(θ_Y)	Y(θ_A)	X(θ_Y)	Y(θ_A)
H ₂ O	88.5	106.1±0.2	54.7	64.5±2.0	75.0	80.2±1.2
Ethylene glycol	63.1	73.3±0.2	33.3	37.7±2.2	49.6	37.0±2.4
Hexadecane	39.2	11.4±0.4	17.4	5.0±1.3	5.9	3.2±0.5

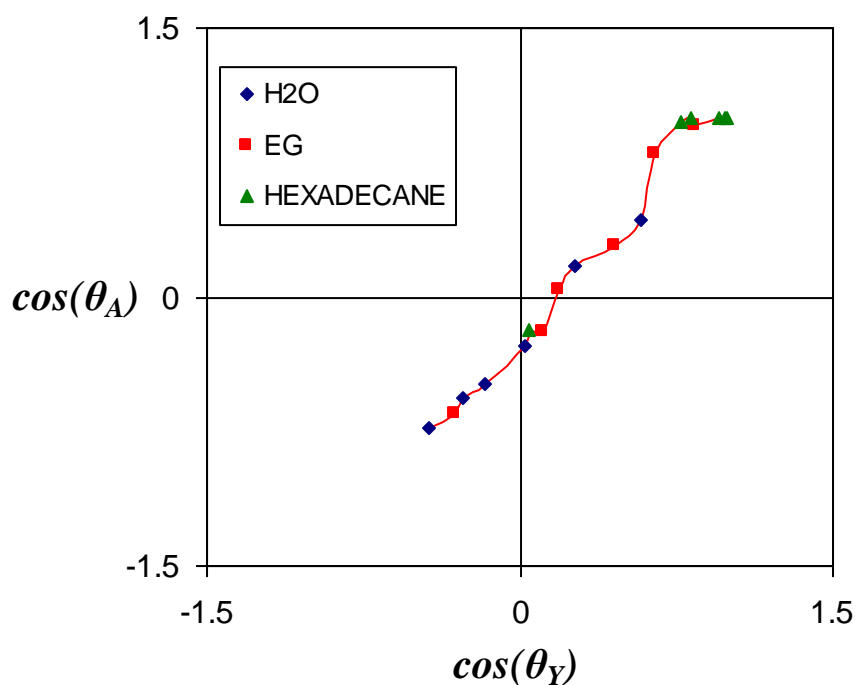


Figure 2.14 Cosine of apparent contact angle θ_A on a pyramidal Si (100) surface as a function of the Young's angle θ_Y .

2.4 Conclusions

Superhydrophobicity and superoleophobicity on Si (111) surfaces were achieved by metal-assisted etching to form re-entrant geometrical structures followed by silane treatment. Etching conditions influence significantly the re-entrant structures formed and thus the oleophobicity established. The geometry of micro/nano structures generated

plays a critical role in achieving oleophobicity and superoleophobicity. By controlling the surface structure shape to form re-entrant structures, oleophobicity/superoleophobicity can be achieved. A wetting diagram of $\cos \theta_A$ vs. $\cos \theta_Y$ can be used to evaluate the oleophobicity/superoleophobicity of a structured surface by comparing the shift and shape of the curve (position where it crosses x-axis and the curve slope). A shift to higher $\cos(\theta_Y)$ signifies a surface with more robust superoleophobicity. Such information offers insight into the design of surfaces with specific oleophobic behavior.

CHAPTER 3

A COMBINED ETCHING PROCESS TOWARD ROBUST SUPERHYDROPHOBIC SiC SURFACES

Large-scale porous silicon carbide (SiC) was fabricated by a combination of Pt-assisted etching and reactive ion etching. It is found that the surface roughness of combined etchings increased dramatically comparing with metal assisted etching or reactive ion etching only. To reduce the surface energy, the porous SiC surface was functionalized with perfluorooctyl trichlorosilane, resulting in a superhydrophobic SiC surface with a contact angle of 169.2° and a hysteresis of 2.4° . The superhydrophobicity of the SiC surface showed a good long-term stability in an $85^\circ\text{C}/85\%$ humidity chamber. Such superhydrophobicity was also stable in acidic or basic solutions, and the pH values show little or no effect on the SiC surface status. In addition, enhancement of porosity-induced photoluminescence intensity was found in the superhydrophobic SiC samples. The robust superhydrophobic SiC surfaces may have a great potential for microfluid device, thermal ground plane and biosensor applications.

3.1 Introduction

SiC has unique physical properties such as wide bandgap, high breakdown electric fields, high electron saturation velocity, and high thermal conductivity.[91] It has promising applications for high power semiconductor microelectronics, bright blue LED photodiode, and sensors etc.[92-93] The reliability of SiC-based device is an important issue in practical applications, yet has rarely been addressed in literature. One of the general and most important issues for semiconductor device reliabilities is water/moisture uptake/absorption.[94] It has been proposed that introducing hydrophobicity or

superhydrophobicity to semiconductor surfaces will improve the device reliability and performance under hostile environments, such as high humidity, chemical contamination and thermal stress.[95]

Superhydrophobic surfaces, which display water contact angles larger than 150° with self-cleaning properties,[73, 87] have been widely used in anti-stiction and anti-contamination films in opto-electronics, biochemical sensors, and microelectromechanical systems (MEMS). To prepare a superhydrophobic SiC surface, surface chemistry and roughness are the two key factors to manipulate.[96-97] Surface chemistry of SiC can be tailored relatively easily by chemical modifications.¹³ In comparison, surface roughness control of SiC has been fairly difficult mainly due to the high chemical stability of Si-C bonds (Figure 3.1). Although superhydrophobicity has been reported for films/nets composed of surface-modified SiC nanowires on Si wafer,[98-99] where the surface roughness was realized by synthesized nanowires, no success has ever been reported on creating a superhydrophobic surface on a bulk SiC.

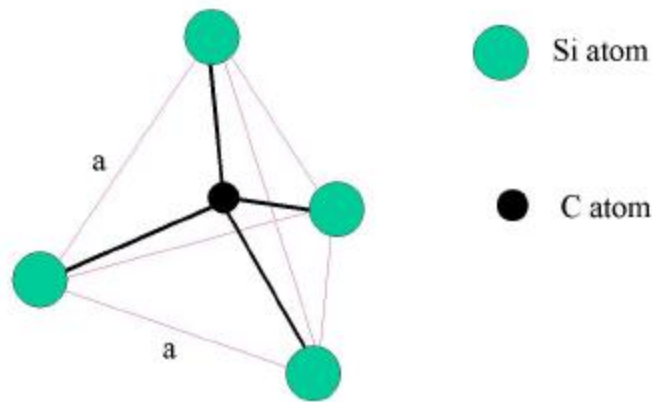


Figure 3.1 The tetrahedral crystal structure of SiC.

To generate desired surface roughness on a bulk SiC, wet chemical etching and dry etching are feasible.¹[100-101] Wet chemical etching of SiC can be realized in alkaline solutions at elevated temperatures, or with photoelectrochemical etching at room temperature.[91, 102-103] The need for high temperature (typically higher than 600°C)

and electrical contacts in the anodization process limits the large-scale production of etched SiC.[104] Alternatively, electroless chemical etching with metal catalysts, called metal-assisted etching (MAE), has been developed.[101, 105] Platinum (Pt) is a typical catalyst for MAE of SiC.[106-107] Rittenhouse *et al.*²⁰ used a solution containing HF and K₂S₂O₈ as the etchant to generate porous SiC structure. In the Pt-assisted etching process, UV illumination injects holes in the valence band of SiC, and then the holes are involved in the oxidation process.

Being different from the wet chemical etching, dry etching such as reactive ion etching (RIE)[108] has the capability of etching SiC precisely and anisotropically in both large and small dimensions.[109] RIE in fluorinated plasma has been widely applied for electronic device fabrication at room temperature. Both physical and chemical processes occur during the etching. It is reported that SiC RIE in fluorine-based plasmas produce anisotropic etching and submicron patterning with etching rate 100-1000Å/min. The etchant gases such as CHF₃, CBrF₄, CF₄, SF₆, and NF₃ are commonly used.[109]

In the present study, we develop an efficient etching method by combining MAE and RIE, which can be used for large-scale fabrication of porous SiC surface. The surface roughness and air trapping volume are enhanced significantly through the combined etching. After surface functionalization of the etched SiC with perfluorooctyltrichlorosilane (PFOS), the contact angle increases up to ~170° with a small contact angle hysteresis of 2.4°. The superhydrophobicity of SiC surface is highly stable under hostile environment, such as in an 85°C/85% humidity chamber and corrosive acid/base solutions. Moreover, the luminescent intensity of porous superhydrophobic SiC is enhanced comparing with the pristine bulk SiC.

3.2 Experimental details

The Pt-assisted etching was performed using HF and $K_2S_2O_8$ etchant at room temperature. 10 nm Pt was coated on 6H n-type SiC wafer using e-beam evaporation method. The wet etchant used was concentrated HF etchant consisting of 6.3 M HF and 0.1 M $K_2S_2O_8$. Ultraviolet irradiation, required to form the porous morphology, was applied using a 150W Hg arc-lamp. The arc-lamp emission was filtered to expose the wafer to ca. 32 mW/cm^2 at full spectrum. The distance between arc-lamp and SiC substrate is 10 cm. After etching, the remaining Pt was removed by sonication in *aqua regia* for 30 min.

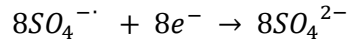
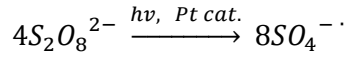
RIE was conducted on SiC in a Plasma Thermal Reactive Ion Etcher using fluorinated gas SF_6 and noble gas argon. Etching was operated at 50 mTorr pressure and 150 W power for 30 min. Etching gases were $SF_6:Ar = 1:3$ (10 sccm SF_6 and 30 sccm Ar). After etching, wafers were cleaned in ethanol.

A 3 mM solution of PFOS in hexane was used for hydrophobic treatment. Specifically, the etched silicon carbide wafers were immersed in the solution for 30 min followed by a heat treatment at $150 \text{ }^\circ\text{C}$ in air for 1 h to complete the hydrophobic surface modification. Contact angle measurements were performed with a Rame-Hart goniometer that had a CCD camera equipped for image capture. Leo 1530 scanning electron microscope (SEM) and Veeco Dimension 3100 atomic force microscope (AFM) was used to measure the surface morphology and roughness of porous SiC samples. Thermo K-Alpha X-ray photoelectron spectroscopy (XPS) was carried out for element composition and analysis. The fitting to XPS data was analyzed by XPSPEAK41 software. Photoluminescence was measured in a Shimadzu FP-5301PC spectrofluorometer.

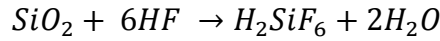
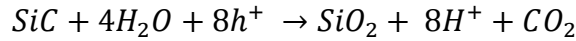
3.3 Results and Discussion

In the MAE process, Pt was deposited on SiC, which assists the chemical etching of SiC in the solution of HF and K₂S₂O₈ under UV irradiation. The proposed mechanism is described as follows:

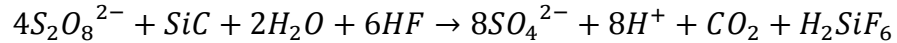
Cathode (Pt):



Anode (n-type SiC):



Overall:



The photochemistry of peroxydisulfide was reported by Bardwell et al.[110] The portion in the UV light with wavelength shorter than 310 nm generates sulfate radicals from peroxydisulfide. The sulfate radicals are catalytically reduced at the surface of the Pt nanoparticles by obtaining electrons, which generates holes in the valence band of SiC. The holes in the SiC are chemically equivalent to dangling bonds. The dangling bonds are attacked by H₂O, which is a nucleophilic species. The resulting SiO₂ can be easily dissolved/etched by HF.[111]

3.3.1 Surface morphology and roughness

The surface morphology has a great influence on the hydrophobicity. SEM and AFM were used as primary tools to investigate the surface morphology and roughness. The pore size and etching depth are studied and discussed in detail to elucidate the characteristics of MAE and RIE in producing surface roughness on SiC.

SEM and AFM analysis in Figures 3.2 and 3.3 show a porous SiC surface after MAE, and the porosity existed mainly in the near-surface region, confirmed by a small

peak to valley depth (Table 3.1). It is found that the surface roughness increased with the etching time (Table 3.2). The mean roughness (R_a) and root mean square roughness (R_q) were both ~ 10 nm after 60 min's etching. The average feature size of pores was around 150 nm.

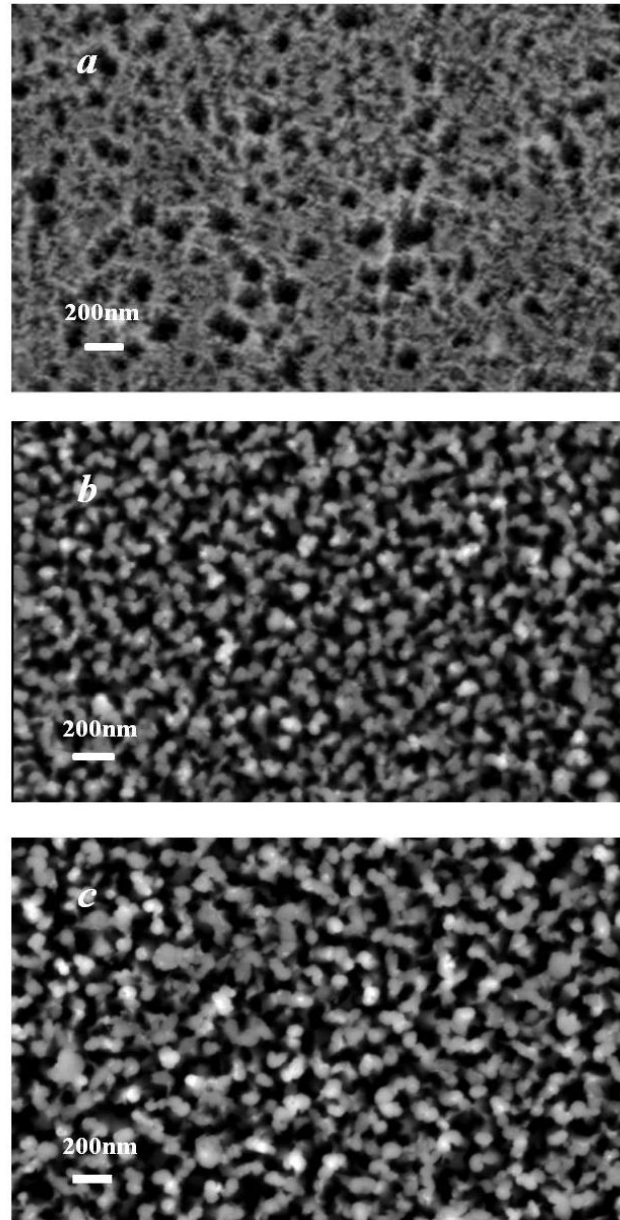


Figure 3.2 SEM images of SiC using different etching methods (a) MAE (b) RIE (c) combined MAE and RIE

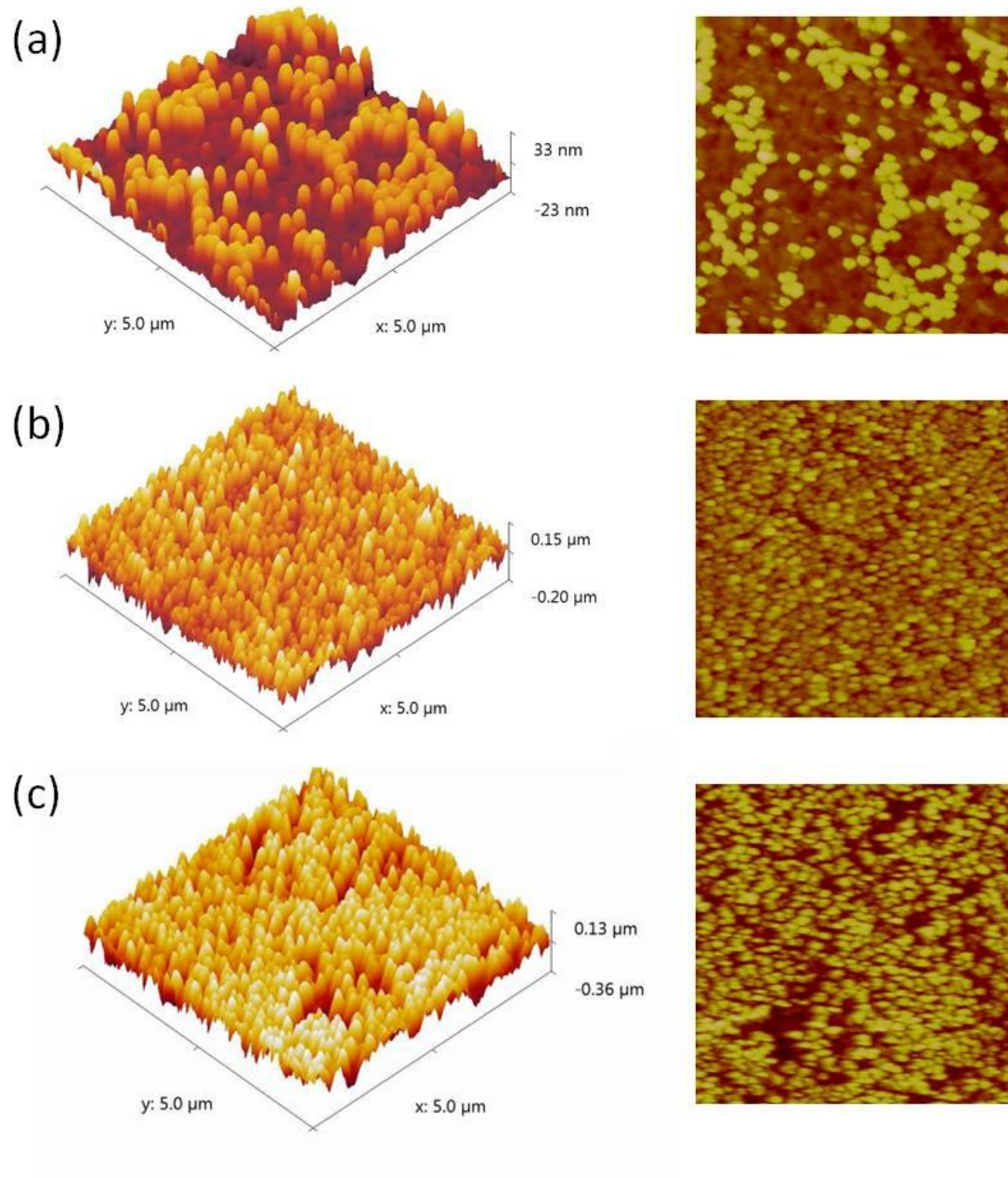


Figure 3.3 Three dimensional and one dimensional AFM images of SiC using different etching methods (a) MAE, (b) RIE and (c) combined MAE and RIE

Table 3.1 Roughness of textured SiC using different etching methods measured by AFM

<i>Etching method</i>	<i>Root mean square roughness (R_q) (nm)</i>	<i>Mean roughness (R_a) (nm)</i>	<i>Maximum peak to valley height (R_{max}) (nm)</i>
MAE only	9.11	7.68	55
RIE only	41.9	33.2	340
MAE + RIE	72.3	59	471

Table 3.2 Surface roughness of Pt-assisted etching of SiC for different time

<i>Etching time</i>	<i>MAE-SiC</i>	
	<i>RMS roughness (R_q) (nm)</i>	<i>Mean roughness (R_a) (nm)</i>
15min	1.34	0.93
30min	4.24	2.62
60min	9.11	7.68

Reactive ion etching on SiC was conducted using fluorinated gas SF₆ and Ar. Ar, a typical noble gas, is added to facilitate the ignition of plasma and to enhance the ion assisted component of the etching. Some reports indicate that the addition of noble gas enables more efficient power deposition and greater ion/radical production, which also helps increase the sheath potential for larger self-biases under the same gas pressure [112-113]. Comparing with MAE, RIE generates a higher density of porous structure and larger etching depth. The R_a was ~40 nm when etching time was 30 min, and the maximum peak to valley height (R_{max}) increased to 340 nm comparing with 55 nm of MAE. The averaged pore size was about 50 nm.

To fabricate superhydrophobic SiC surfaces, it's essential to control the surface roughness and morphology. Therefore we combined two etching methods to increase the surface roughness significantly. Since the feature surface (e.g. along the wall) by MAE etching may have more dangling bonds; so the exposed surfaces that are generated by the MAE etching but locate beneath the top surface may exhibit higher chemical reactivity. Therefore the etching depth of combined etchings was greatly enhanced comparing with RIE or MAE only. The R_q and R_{max} are 72.3 and 471 nm, respectively. Moreover, the pore size increased to ~100 nm, which allows more air trapped within the unit structures.

3.3.2 Hydrophobic treatment

The silane treatment was performed to further lower the surface energy of porous SiC (Figure 3.4). The surface treatment of PFOS is critical to achieve superhydrophobic surfaces. XPS was used to study the surface chemical composition before and after silane treatment. Figure 3.5 shows the XPS survey of porous SiC with combined etchings before and after hydrophobic treatment. The Si, C, O and F peaks have been identified in both untreated and treated SiC spectra. The O_{1s} peaks of ~ 533.3 eV indicates that the surface oxygen exists in the form of hydroxyls, which are capable of reacting with PFOS. The F_{1s} peak in untreated SiC may be due to the etchant residual (HF or H_2SiF_6). After treatment, the F_{1s} peak becomes intense as a result of the introduction of PFOS layer which contains CF_2 and CF_3 groups. The existence of PFOS layer is also confirmed by high resolution C_{1s} spectra as show in Figure 3.6. Before treatment, only peaks from SiC (283.4 eV) and CH_2 (285.6 eV) groups are observed. After treatment, new peaks of 293.9 eV and 291.6 eV appear which can be attributed to CF_3 and CF_2 groups. Moreover, the peak of SiC is suppressed after treatment, possibly due to the dense PFOS coating.

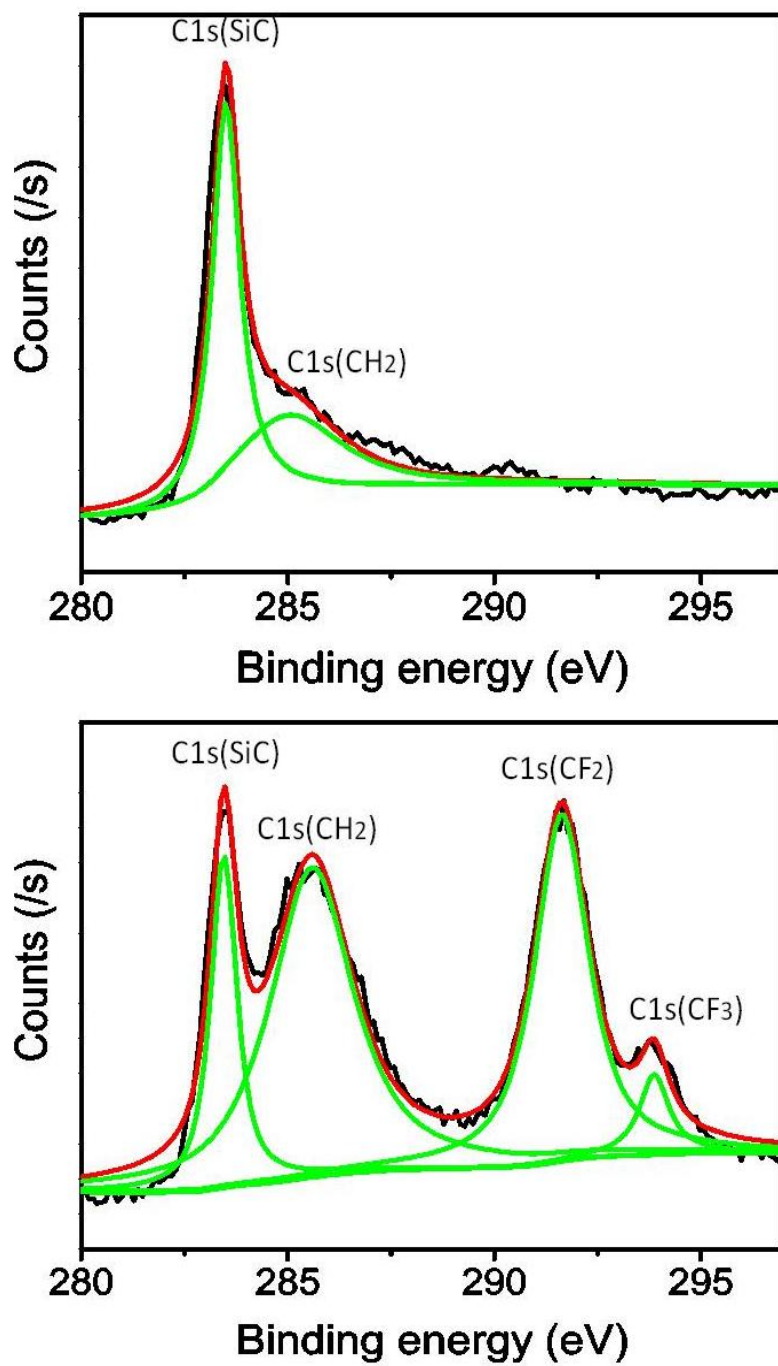


Figure 3.6 High resolution C1s spectra of (a) porous SiC before silane treatment, (b) porous SiC after silane treatment

We compared the contact angles on SiC fabricated by different etching methods. After hydrophobic treatment, the contact angle of MAE-SiC was 110.8°. For RIE-SiC, the contact angle was 168° with a large hysteresis of ~ 28.4°, as shown in Table 3.3. The high contact angle and contact angle and hysteresis indicate a combined Wenzel-Cassie state (drops that are partially in the Cassie and partially in the Wenzel state), which is probably due to the low etching depth. Thus there is not enough air trapped in the gap between etched structures to achieve low hysteresis superhydrophobicity. After combined etchings and silane treatment, the contact angle was 169.7° and hysteresis reduced to only 2.4°. This low hysteresis indicates a Cassie state, and a self-cleaning porous SiC surface. The increased surface roughness and pore size greatly enhanced the air trapping volume within each unit structure, which contributes to the high contact angle and low contact angle hysteresis.

Table 3.3 Contact angle and hysteresis of hydrophobic treated rough SiC surfaces

	<i>MAE</i>	<i>RIE</i>	<i>MAE + RIE</i>
Contact angle (degree)	117.9 ± 1.1	168.1 ± 0.8	169.7 ± 0.9
Contact angle hysteresis (degree)	---	28.4 ± 0.7	2.4 ± 0.2

The effect of combined etchings could also be explained in terms of Laplace pressure. The Laplace pressure maintains a composite interface by confining the water at the air/water interface, which can be described as⁹

$$\Delta p = p - p_0 = -\frac{\gamma \cos(\theta - \alpha)}{R_0 + h \tan \alpha}$$

where γ is the surface tension of water, θ is Young's contact angle of liquid on the surface, α is the inclination angle, h is the height as illustrated in Figure 3.7 (a), R_0 is half

of the width between base edges of two adjacent inclined walls, p is the pressure on the liquid side of the meniscus, and p_0 is atmospheric pressure.

Superhydrophobicity is achieved through the formation of a composite interface (solid/water and air/water interfaces) with air trapped within the structure. The Laplace pressure can affect the hysteresis and the transition between a Cassie state and a Wenzel state. For two inclined walls with a certain inclination angle α and young's contact angle, the increase of R_0 or h increases the laplace pressure and allows more air trapping between unit structure, therefore prevents the meniscus approaches the structure bottom. As a result, surface hydrophobicity can be enhanced with an increased apparent contact angle and reduced contact angle hysteresis (reduced contact area). The Laplace pressure of RIE and combined etching are estimated to be 1.07×10^4 Pa and 3.83×10^4 Pa respectively. Comparing with RIE only, the combined etching increases both R_0 and h , therefore Laplace pressure is increased (Figure 3.7 (b)) and contact angle hysteresis was reduced significantly. But we need to notice that the parameter R_0 can't be increased too much without increasing h , otherwise the central part of the droplet will touch the bottom of the structure, and the Cassie state will be lost.

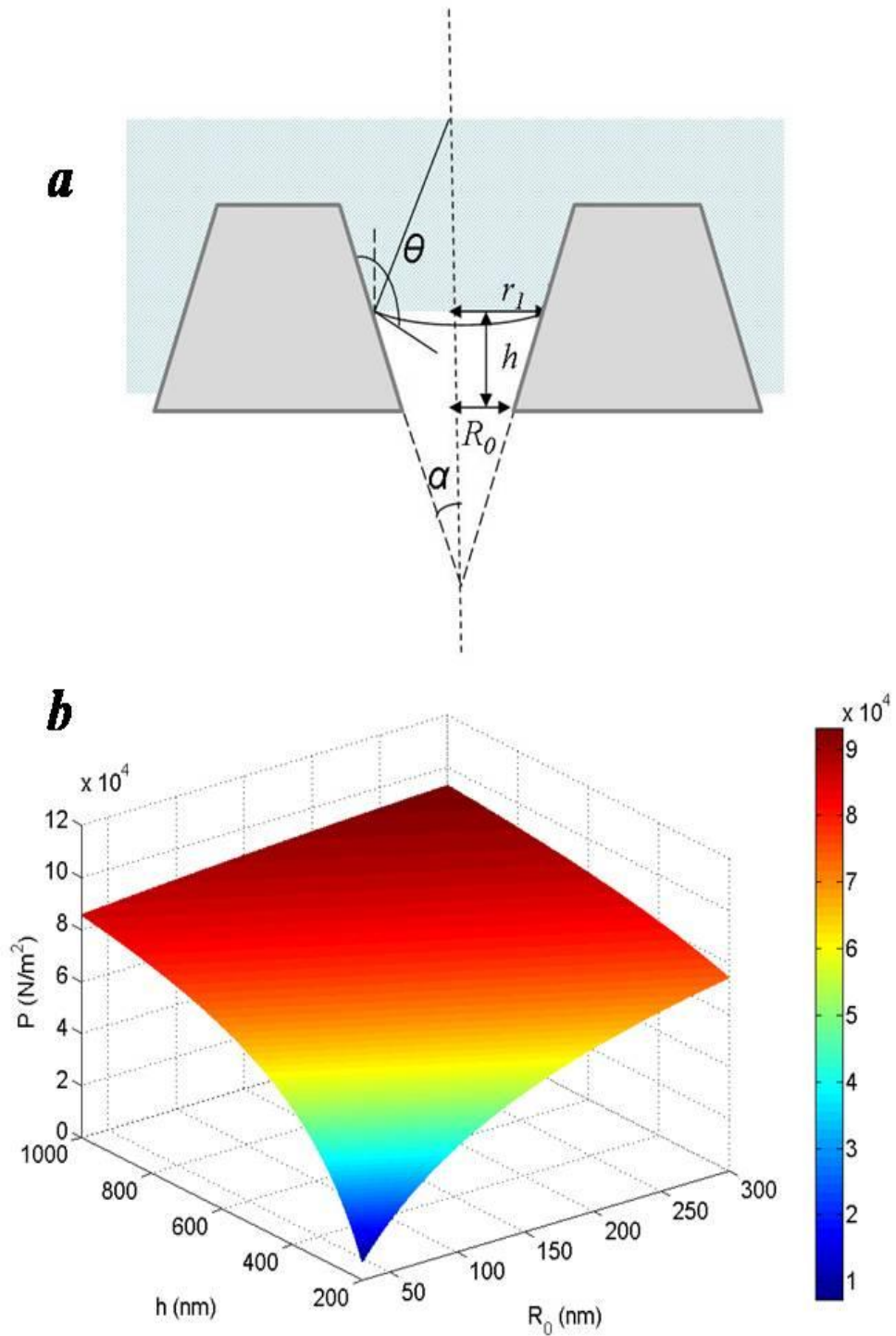


Figure 3.7 (a) Water contact at surface structures with inclined walls (b) Laplace pressure (p) changes with height (h) and half width of two adjacent inclined walls (R_0)

3.3.3 The robustness of superhydrophobic SiC

In order to test the robustness of superhydrophobic surfaces, the superhydrophobic SiC were put in an 85/85 (85 °C, 85% humidity) chamber. It is found that after four weeks the surface maintained the superhydrophobic property and showed water contact angle of 165.2°.

The SiC surface also shows superhydrophobicity to corrosive acid/base solutions with pH ranging from 1 to 14. Figure 3.8 shows the relationship between pH and CA on the superhydrophobic SiC surfaces. Contact angles keep larger than 160° when the pH of the droplet varied from 1 to 14, and no obvious fluctuation is observed. This indicates that pH values of the aqueous solution have little or no effect on CAs for superhydrophobic SiC surfaces.

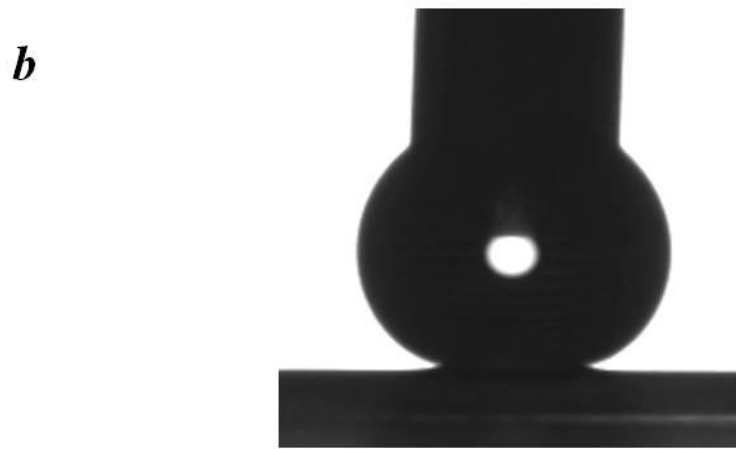
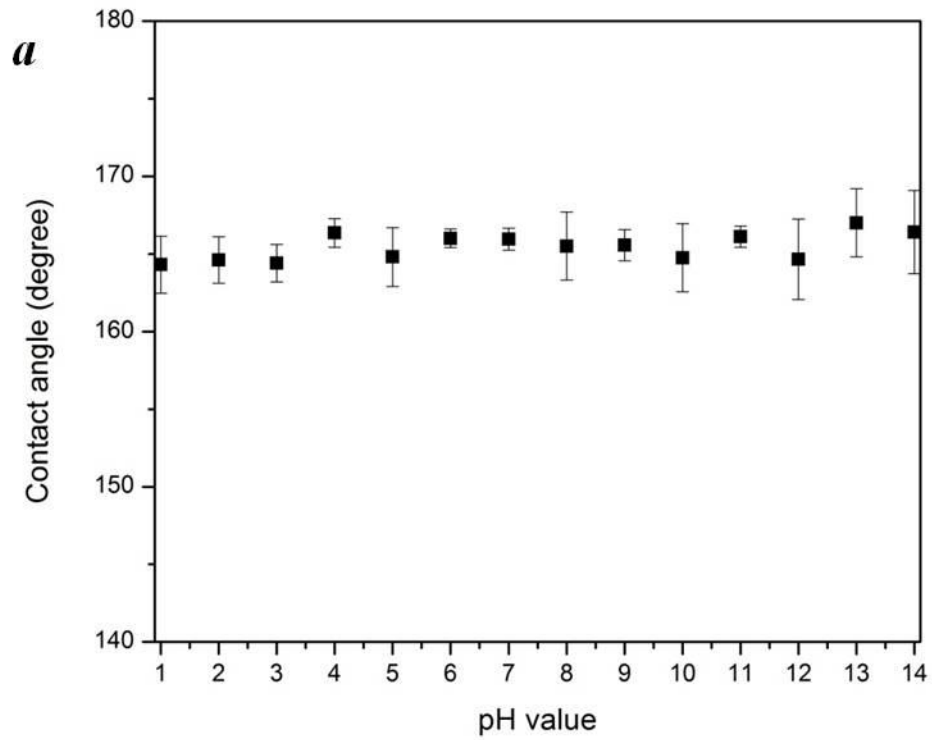


Figure 3.8 (a) The relationship between pH and the CA on a porous SiC surface by MAE and RIE combined etching (b) Typical water contact angle image on superhydrophobic SiC surfaces

3.3.4 Luminescence Property

Bulk SiC has a low emission intensity due to its indirect band gap. It is expected that nano porous SiC exhibit similar emission peak or shifted new emission peaks, because of the decreased particle size to nanometer regime.[114] The luminescent spectra of porous SiC usually span a wide spectrum range from near UV to 600nm. Many studies reported an increase in photoluminescence intensity was found in the 460–500 nm region of the spectrum upon etching.[115] In our study, the peaks for both bulk SiC and the porous SiC after combined etchings are at 471 nm, and no obvious peak blue shift is observed. This may be due to the large size of the porous structures generated by combined etchings, and therefore no quantum confinement effect was generated.[116] The luminescence intensity is increased three times comparing with the bulk one (Figure 3.9). The increasing photoluminescence intensity indicates the nanocrystalline size of the pores, and is related to the number of nanocrystals. Since SiC has good biocompatibility, the high surface area and efficient luminescence porous SiC may have potential application in the area of biolabeling and biosensing .

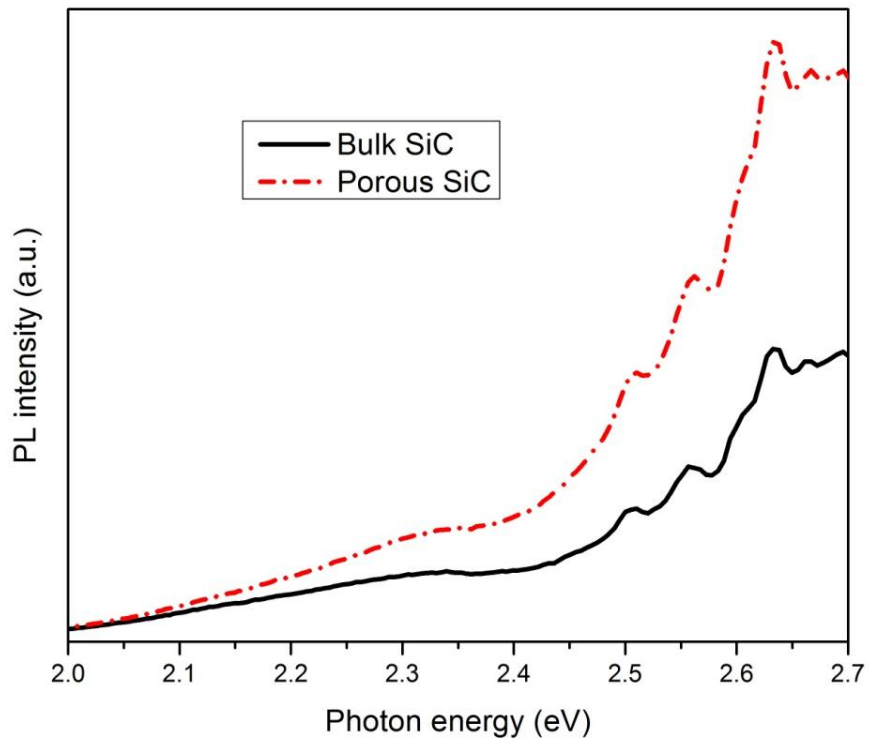


Figure 3.9 PL intensity of bulk SiC and etched porous SiC (etched by combined MAE and RIE)

3.4 Conclusions

In summary, a large scale superhydrophobic porous SiC was fabricated by combining Pt-assisted chemical etching and RIE. The surface roughness and air trapping volume of SiC increased significantly after combined etching. As a result, a self-cleaning SiC surface with high contact angle of 169.7° and low hysteresis of 2.4° was generated, which was very stable in different pH solutions. The luminescent intensity of porous SiC was enhanced comparing with bulk materials. Such stable superhydrophobic porous SiC surfaces may have potential applications for micro fluid channels, thermal ground plane, sensors etc. even under hostile environment.

CHAPTER 4

REVERSIBLE SUPERHYDROPHOBIC-SUPERHYDROPHILIC TRANSITION OF ZNO NANOROD/EPOXY COMPOSITE FILMS

Tuning the surface wettability is of great interest for both scientific research and practical applications. We demonstrated a reversible transition between superhydrophobicity and superhydrophilicity on a ZnO nanorod/epoxy composite film. The epoxy resin serves as an adhesion and stress relief layer. The ZnO nanorods were exposed after oxygen reactive ion etching of the epoxy matrix. A subsequent chemical treatment with fluoroalkyl and alkyl silanes resulted in a superhydrophobic surface with a water contact angle up to 157.8° and a hysteresis as low as 1.3° . Under UV irradiation, the water contact angle decreased gradually, and the surface eventually became superhydrophilic because of UV induced decomposition of alkyl silanes and hydroxyl absorption on ZnO surfaces. A reversible transition of surface wettability was realized by alternation of UV illumination and surface treatment. Such ZnO nanocomposite surface also showed improved mechanical robustness.

4.1 Introduction

Surface wettability, an important property for solid materials, has been known to be controlled by surface energy and morphology.[58, 96, 117-118] Modifying the surface wettability is very important for chemical and electronic applications, such as inkjet printing,[119] microfluid channels,[120] etc. For those practical applications, both superhydrophobic and superhydrophilic surfaces are very useful.[83, 121-122] Recently, materials with tunable wettability have been developed and realized on many inorganic oxide surfaces, such as TiO_2 , ZnO , WO_3 , V_2O_5 , and SnO_2 .[123-126] Under UV

irradiation, the hydrophobic/superhydrophobic oxide surfaces turns hydrophilic/superhydrophilic. In the dark, the surface turns back to hydrophobic/superhydrophobic.[123] Tunable wettability was also reported on polymers, metal oxides, and semiconductors under UV or visible light illumination.[127-130]

With a direct wide band gap of 3.37 eV and a large exciton binding energy of 60 meV at room temperature, ZnO has been demonstrated to have enormous applications in electronic and optoelectronic devices, such as ultraviolet (UV) lasers,[131-132] light-emitting diodes,[133] field emission devices,[134-135] nano generators,[136-137] and solar cells.[138-139] One-dimensional (1D) ZnO nanostructures can be synthesized by a wide range of techniques including vapor deposition, electrodeposition, hydrothermal method, molecular beam epitaxy and so on.[140] Among these methods, hydrothermal method has been widely used due to its low cost and scalability .[141] Many papers have been reported about creating superhydrophobic surfaces with 1D ZnO nanostructures (nanowires, nanorods, nanofibers).[141-142] Reversed wettability has been reported on those ZnO nanostructure films.[143-147] For example, Feng *et al.* reported superhydrophobic to superhydrophilic of aligned ZnO nanorod films switched by alternation of UV irradiation and dark storage.[148] Kwak *et al.* grew superhydrophobic ZnO nanowire surface modified by fatty acids, and switched to hydrophilic under UV irradiation.[149] A selective UV photopatterning of ZnO nanowire film with different wettability was realized.

However, most of previous researches have been focused on wettability investigation of ZnO nanostructure itself; until now no paper has been reported about preparing ZnO nanocomposites with tunable wettability. For most of superhydrophobic surfaces made of inorganic materials, the surface micro- and nano- structures are prone to mechanical damage under abrasion forces due to their brittle nature. Therefore a protective polymeric material such as epoxy resin, could be introduced as an adhesion and stress relief layer to the substrate. The inorganic nanoparticles at the surface of the

polymeric layer generates an abrasion resistant surface layer. The resulting nanocomposite is also easier to be applied by various methods such as spin coating, spraying and printing techniques. In this study, ZnO nanorods were synthesized by hydrothermal method, and mixed with epoxy resins of different filler loadings. After oxygen reactive ion etching (RIE), the top epoxy was etched and ZnO based hierarchical structure was exposed. Superhydrophobic ZnO film could be produced after surface modification for lowering down the surface energy. The ZnO nanocomposite surface showed better mechanical robustness than the previously reported superhydrophobic surface with inorganic silica nanoparticles. Tunable wettability of superhydrophobicity and superhydrophilicity was realized through UV irradiation and surface functionalization.

4.2 Experimental

4.2.1 ZnO nanorod growth and surfactant treatment

The growth solution of ZnO nanorods is composed of 5 mmol/L of zinc nitrate hexahydrate and hexamethylenetetramine (HMTA) at a mole ratio of 1:1. The reaction was carried out at 80 °C for 6 hours. After reaction, the nanorods were collected using centrifugation and rinsed repeatedly by ethanol. Then the nanorods were baked in oven at 60 °C overnight.

The solution of ethanol and water (95:5 by weight) is adjusted to pH 4.5-5.5 with acetic acid. Aminoethylaminopropyltrimethoxysilane is added with stirring for 5 minutes to yield a 2 wt% final concentration. ZnO nanorods were silylated by stirring them in solution for 5 minutes and then decanting the solution. The ZnO nanorods were rinsed twice with ethanol. The silane layer was cured at 110°C for 10 min.

4.2.2 ZnO nanorods/epoxy resin composites

The epoxy resin was composed of bisphenol A epoxy resin (EPON 828) and ERL 4221 with weight ratio of 1:2. The curing agent HMPA was added with a weight ratio of 1:0.88 to the epoxy resins. Imidazole serves as a catalyst with 1 wt% to the total weight of epoxy resin and curing agent. Then the ZnO nanorods were added into the epoxy resin and mixed by ultrasonication. ZnO nanorod/epoxy composites were prepared at different filler loadings of 17, 33 and 50 wt. %. After that, ZnO nanorod film was coated on a glass slide by doctor blade with a thickness of 70 μm . The glass slide was pre-treated by UV-ozone for 5 min. The film was cured at 150 $^{\circ}\text{C}$ in air for 2 hours.

4.2.3 Plasma etching and hydrophobic treatment

The oxygen RIE was conducted on ZnO nanorod film for 15 minutes. The power is 150 W and the pressure is 0.5 torr. Surface modification was performed by immersing coated glass slides in a hexane solution of 3 mM perfluorooctyl trichlorosilane (PFOS) or octadecyltrichlorosilane (OTS) for 30 min, followed by a heat treatment at 150 $^{\circ}\text{C}$ in air for 1 hour.

4.2.4 Abrasion resistance test

The abrasion resistance of the surfaces was evaluated using the methodology previously reported by Xiu *et al.*[121] Polyester/cellulose Technicloth II wipes served as abrasion surfaces, with the superhydrophobic surface to be tested facing this abrasion material. While a pressure (~ 3450 Pa) was applied normal to the superhydrophobic surface, the surface was moved in one direction. The contact angle and hysteresis changes of the superhydrophobic surface were then measured after abrasion (25 cm in abrasion length).

4.2.5 UV irradiation and surface characterization

UV irradiation was obtained from a 150W Hg arc-lamp. The arc-lamp emission was supplied at a distance of 10 cm and wavelength between 248 and 365 nm. Contact angle measurements were performed with a Rame-Hart goniometer that had a CCD camera equipped for image capture. The deionized water droplet volume was 4 μ L, and the measurements were taken under ambient atmospheric conditions. X-ray diffraction (XRD) analysis was carried out with a Philips X-pert alpha-1 diffractometer, using Cu K α radiation (45 kV and 40 mA). Leo 1530 Scanning Electron Microscope (SEM) was used to characterize the surface morphology of composite samples. Thermo K-Alpha X-ray photoelectron spectroscopy (XPS) was carried out for element composition and analysis.

4.3 Results and Discussion

4.3.1 Superhydrophobic ZnO nanocomposites

Figure 4.1(a) shows the schematic of fabricating superhydrophobic ZnO nanocomposites. EPON 828 is widely used in surface coatings, adhesives (microelectronics packaging), and composite materials (such as carbon fiber and fiber glass reinforced epoxy). The mixture of EPON 828 with lower viscosity resin ERL 4221 improves the processibility of ZnO-epoxy composition, especially at high filler loadings. Aminoethylaminopropyltrimethoxysilane is added as a surfactant to improve the interface between nanorods and epoxy matrix. The as synthesized ZnO nanorods have a wide size distribution, which is beneficially for generating micro/nano scale (hierarchical) roughness. After oxygen RIE, the top epoxy resin was etched and the embedded ZnO nanorods were exposed. In order to further reduce the surface energy, two different silane coatings (PFOS and OTS) were applied on the composite surface, by introducing the long hydrocarbon and fluorocarbon chains as shown in Figure 4.1(b). PFOS and OTS were chosen to verify the effect of UV light on hydrocarbon and fluorocarbon chains.

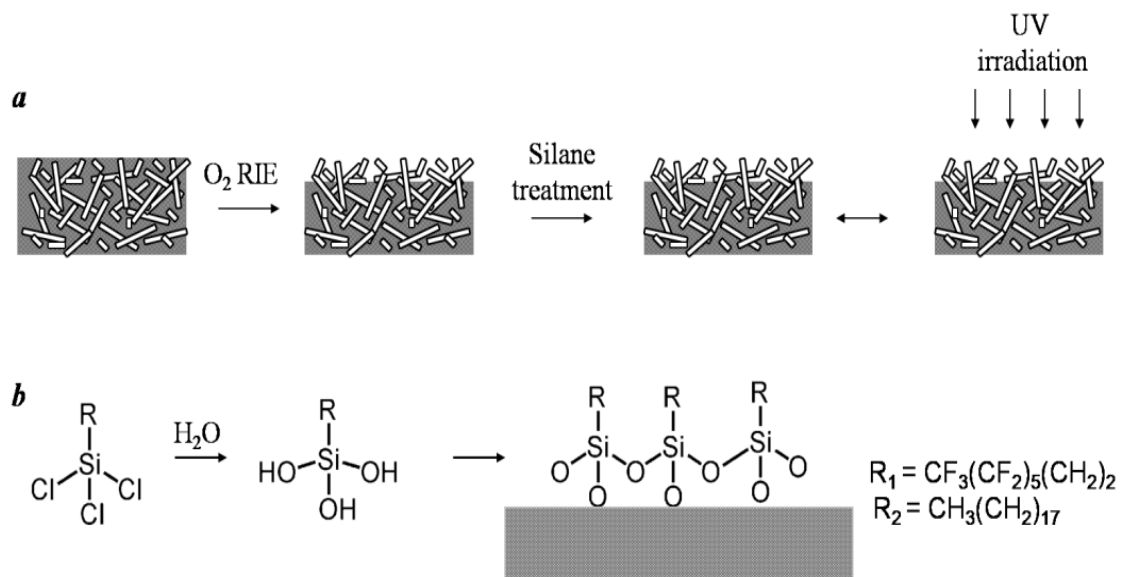
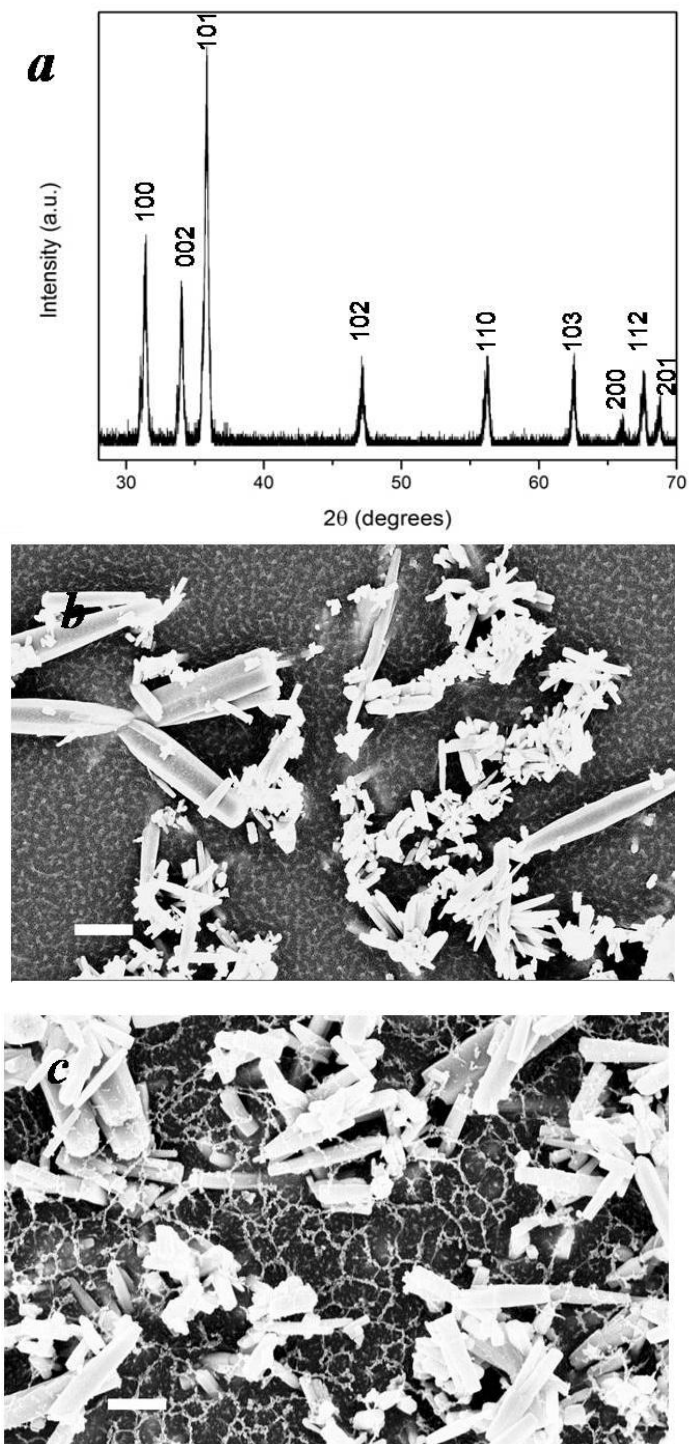


Figure 4.1 (a) Schematic of the fabrication process for superhydrophobic ZnO nanorod composite film and its transition to superhydrophilic film under UV irradiation (b) PFOS and OTS silane treatment on ZnO nanorod composites

The XRD pattern of ZnO nanorods indicates that the as synthesized nanorods are wurtzite ZnO crystals (Figure 4.2a). The surface morphologies of composites generated with different filler loadings are shown in Figures 4.2(b-d), where it is evident that the surface roughness increased continuously with the increase of filler loading. Such change yields an increase in water CA and a decrease of CA hysteresis after surface hydrophobic modification by PFOS (Figure 4.3 and Table 4.1). The contact angle of epoxy is 88.4° . After surface treatment of PFOS and OTS respectively, the contact angles became 120.0° and 105.1° . When the filler loading is low (17%), the surface roughness generated is insufficient to construct a superhydrophobic surface. The water CA is only $131.6^\circ \pm 1.5^\circ$. This low CA could be attributed to the fact that the water droplet makes a wetted contact with the composites, and fills in the grooves on the composite surface. As the filler loading increases to 33%, surface becomes rougher and CA increases to $157.8^\circ \pm 1.8^\circ$. However CA hysteresis shows a high value of $41^\circ \pm 1.0^\circ$. When increase the filler loading to 50%, the CA further increase to $158.4^\circ \pm 1.3^\circ$ and CA hysteresis reduced to

$1.3^\circ \pm 0.2^\circ$. The reduced CA hysteresis with increased filler loadings can be explained by the two hydrophobic states on rough solid surfaces, Wenzel and Cassie state.



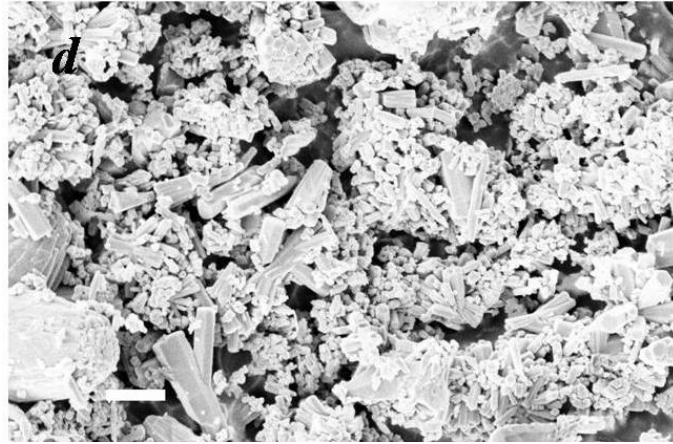
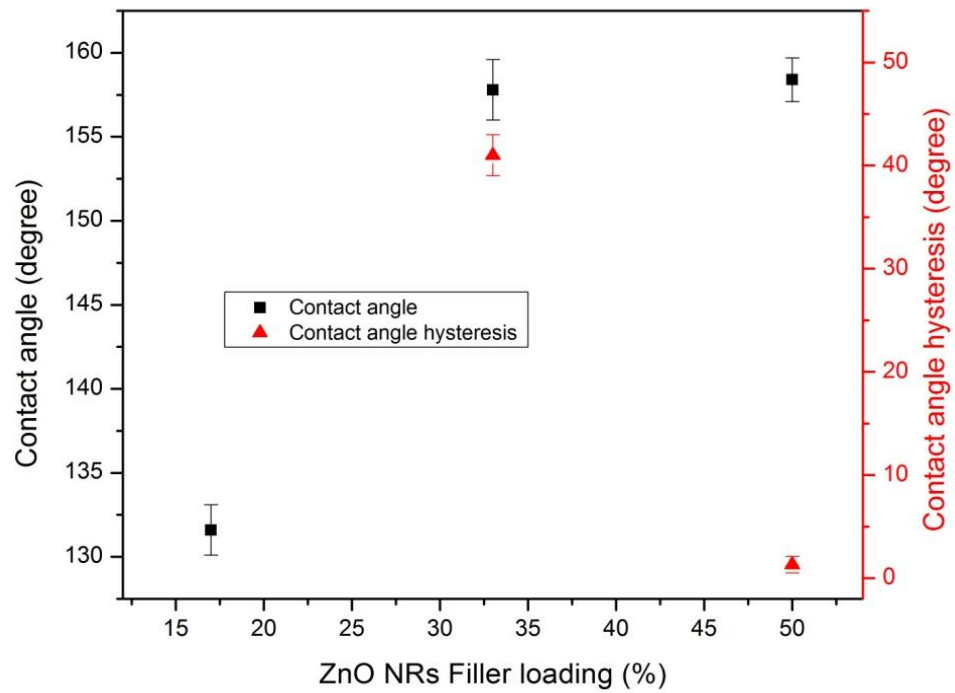


Figure 4.2 (a) X-ray diffraction of ZnO nanorods. (b-d) SEM images of ZnO nanorods composites with different filler loadings after 15 min RIE etching (b) 17% filler loading (c) 33% filler loading (d) 50% filler loading. The scale bar is 2 μm .



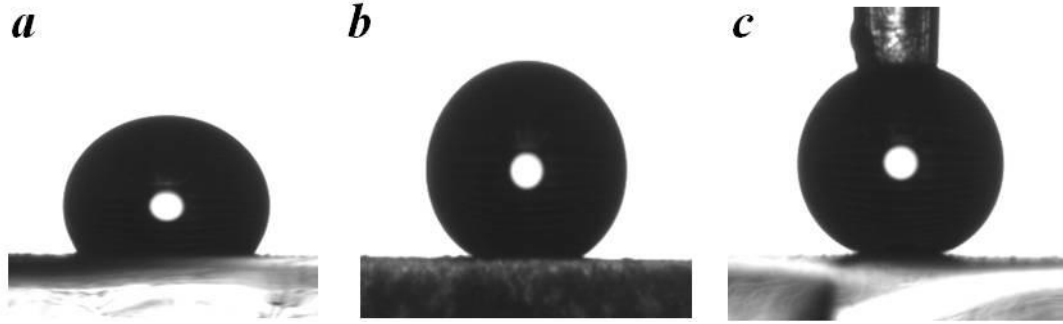


Figure 4.3 (a) Contact angle and contact angle hysteresis of ZnO nanorods composites with different filler loadings (b) Water droplet images of different filler loading ZnO nanocomposites in contact angle measurements

Table 4.1 Contact angle and contact angle hysteresis of superhydrophobic nanocomposites with different ZnO nanorods filler loadings.

ZnO NRs filler loading (%)	Contact angles	Contact angle hysteresis
17%	131.6 ± 1.5	----
33%	157.8 ± 1.8	41 ± 1.0
50%	158.4 ± 1.3	1.32 ± 0.2

The Wenzel equation,[6] Eqn (1), describes the effect of surface roughness on the water droplet CA:

$$\cos \theta_A = r \cos \theta_Y \quad (1)$$

where θ_A is the apparent CA on the rough surface, r is the ratio of the actual solid/liquid contact area to its vertical projected area, and θ_Y is the CA on a flat surface defined by Young's equation. As the roughness (r) increases, the CA also increases

reflecting an increase in relative hydrophobicity. So when the filler loading changes from 17% to 33%, surface roughness increases, and apparent CA also increases. However, such surface roughness is difficult to trap air between the interface of water droplet and the film surface, and water can easily fill the grooves on the surface, resulting in a large CA hysteresis.

The Cassie equation for a porous or composite surface,[7] Eqn. (2), indicates that the apparent CA increases when the solid surface fraction f decreases. The CA hysteresis in a Cassie state is normally less than 10° .

$$\cos \theta_A = -1 + f (\cos \theta_Y + 1) \quad (2)$$

When further increasing the filler loading to 50%, ZnO nanorods formed a densely packed layer and enhanced surface roughness significantly. Solid surface fraction decreases, and more air could be trapped at the water and composite interface. The composite surface is composed of both microstructures and nanostructures, such hierarchical structure results in a much reduced CA hysteresis of 1.3° . Air may become trapped between ZnO nanostructures underneath a water droplet, which would further enhance the surface hydrophobicity and reduce the CA hysteresis.

Similarly, we used OTS solution for hydrophobic treatment on 50% loading ZnO nanocomposites. Superhydrophobicity was achieved with a water CA of $152.3^\circ \pm 1.2^\circ$ and CA hysteresis of $2.3^\circ \pm 0.6^\circ$.

4.3.2 UV-induced wettability change

The UV induced wettability change of ZnO nanocomposites was studied by CA measurements and XPS. Under UV irradiation, the water CA of ZnO nanocomposite film by both silane treatments decreased gradually with exposure time, as shown in Figure 4.4. The CA is reduced abruptly at the beginning, because of the high speed yielding of electron-hole pairs at the initial stage under UV irradiation, as reported by Liu *et al.*[143] After 90 min, the change slowed down. After 9 hours, the water droplet spread out the film, and CA reaches a low value of $\sim 0^\circ$ for OTS treated samples and 12.4° for PFOS

treated samples, indicating the wettability change from superhydrophobicity to superhydrophilicity/highly hydrophilicity. For the PFOS treated samples, the water CA is higher (12.4°) than the OTS treated samples after UV irradiation, which may due to the remaining fluorocarbons on the film surface.

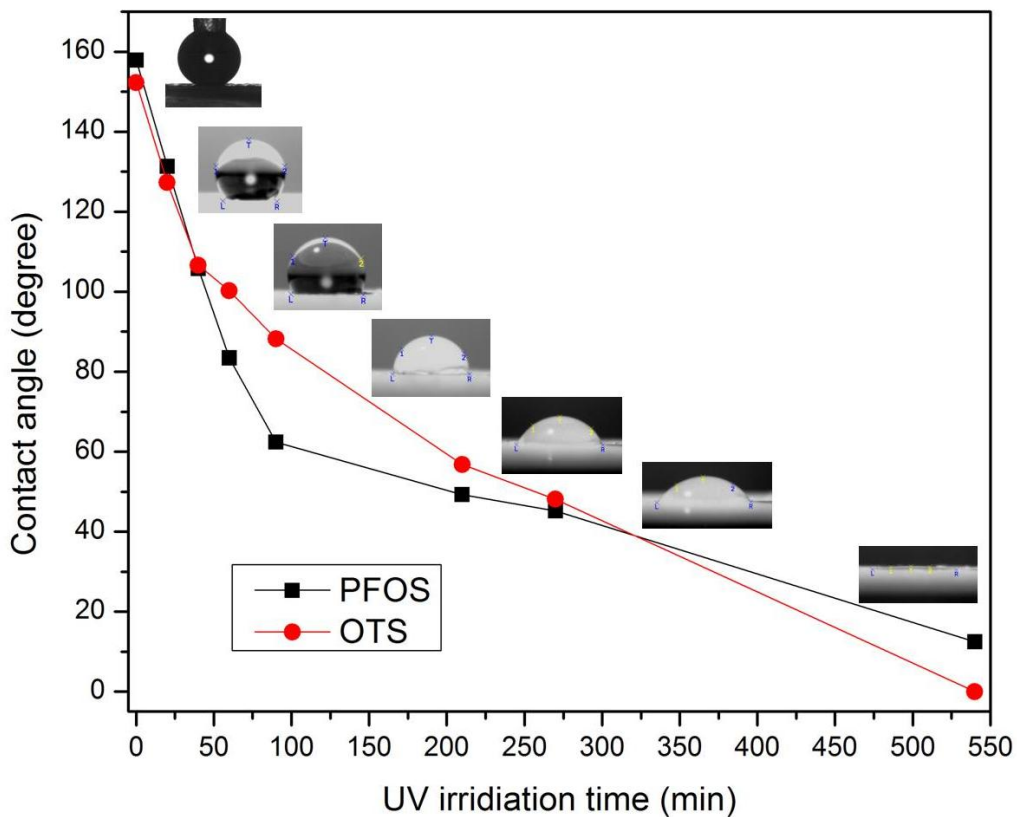


Figure 4.4 Water contact angle of ZnO nanocomposite modified by PFOS and OTS as a function of UV irradiation time.

The mechanism for superhydrophobicity to superhydrophilicity transition involves the UV effect on both ZnO and silane hydrophobic coatings. Under UV irradiation, the electrons and holes are generated on the ZnO surface. Some of the holes can react with lattice oxygen, and form oxygen vacancies. When a surface defective site is generated, water and oxygen may compete to dissociatively adsorb on it. The defective site tends to be kinetically more favorable for hydroxyl absorption than oxygen absorption. This

mechanism is supported by XPS results. The Zn 2p_{3/2} spectra of ZnO nanocomposites before and after UV irradiation are shown in Figure 4.5. The Zn 2p_{3/2} peaks for ZnO nanocomposites can be deconvoluted into two components at 1021.7 (± 0.1) eV and 1022.7 (± 0.1) eV, corresponding to ZnO and Zn(OH)₂ respectively. After the UV irradiation for Zn 2p_{3/2} spectra, the Zn(OH)₂ ratio of PFOS treated composites increases from 22.98% to 45.03%, and Zn(OH)₂ ratio of OTS treated samples increases from 7.52% to 18.22%. These indicate Zn(OH)₂, which are more hydrophilic, are formed after UV irradiation. As a result, the water CA decreases, indicating an enhanced surface hydrophilicity. Moreover, the alkylsioxane layer from the OTS based silane coating can be decomposed by active oxygen radicals.[150] First, the reactive oxidizing species (e.g. ·OH, O₂^{·-}, and ·OOH) generated on the ZnO surface through UV irradiation abstract hydrogen atoms from alkyl chains. Then alkoxy radicals and carbonyls are produced by continuously attacking of oxidizing species to alkyl radicals, and they are further decomposed by photocatalysis. As a result, shorter alkyl chains are formed with loss of carbon.

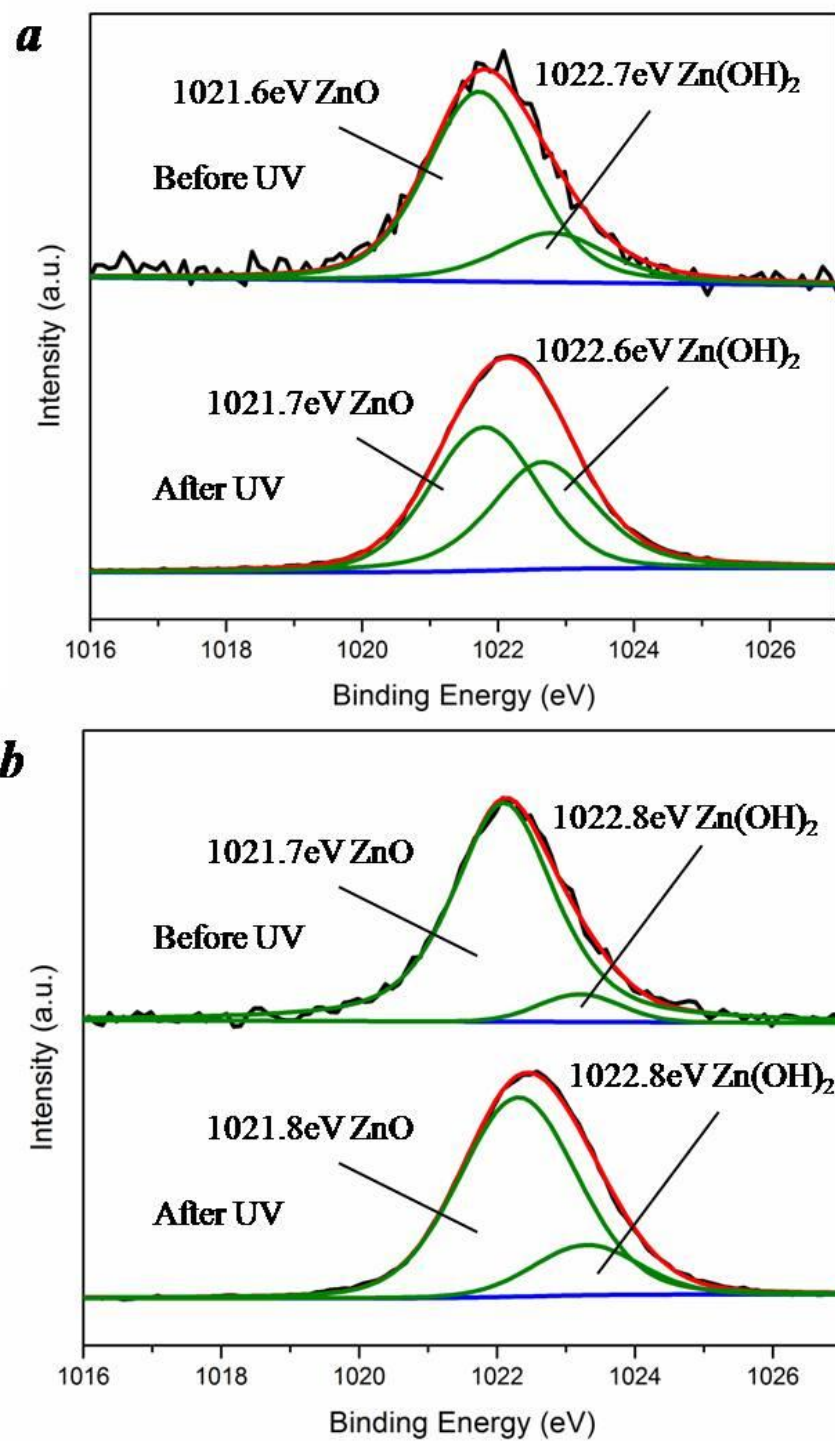


Figure 4.5 XPS spectra of Zn $2p_{3/2}$ of ZnO nanocomposites modified by (a) PFOS (b) OTS before and after UV irradiation

4.3.3 Mechanical robustness of the nanocomposites

One of the limitations in the application of superhydrophobic surface coatings is the poor abrasion resistance of surfaces. For example, in the previous work of our group (Table 4.2), the superhydrophobic silica surface was generated by sol gel method using tetramethoxysilane and isobutyltrimethoxysilane.[54] After abrasion test, the silica surface superhydrophobicity was lost as contact angles decreased to 124.3° and hysteresis increased to more than 60° , and the self-cleaning effect vanished. The robustness of ZnO nanocomposite was tested under a similar condition, which is schematically shown in Figure 4.6. It is found that the surface superhydrophobicity remained after abrasion with a contact angle of 150.9° . The possible reason is that the polymeric materials serves as stress relief layer, and therefore most of the roughness was maintained in the valleys between the sub micro and nanorods (Figure 4.7). The increased contact angle hysteresis is due to the flattened top ZnO nanostructure surface. Similar mechanism was also reported in our previous work about robust superhydrophobic silica epoxy nanocomposites.[151]

Table 4.2 Abrasion test of superhydrophobic surfaces.

Superhydrophobic surfaces	Initial contact angles	Initial contact angle hysteresis	Contact angles after abrasion	Contact angle hysteresis after abrasion
Silica ³⁵	165.4 ± 1.5	$2-3^\circ$	124.3 ± 5.0	$> 60^\circ$
ZnO/epoxy nanocomposites	$158.4^\circ \pm 1.3^\circ$	1.3°	$150.9^\circ \pm 1.0^\circ$	25°

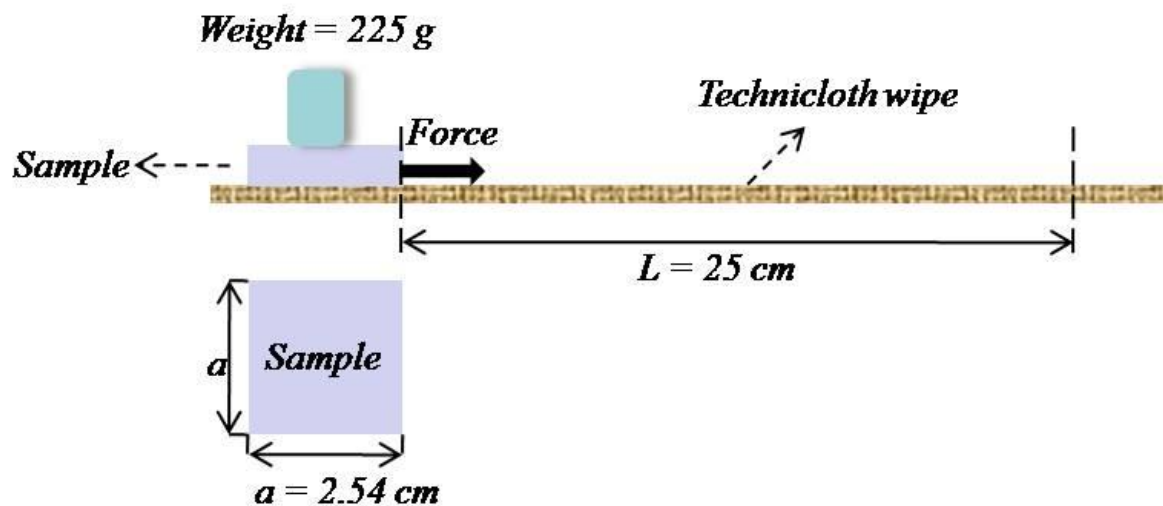


Figure 4.6 Schematic of the abrasion test employed to evaluate robustness on a superhydrophobic surface.

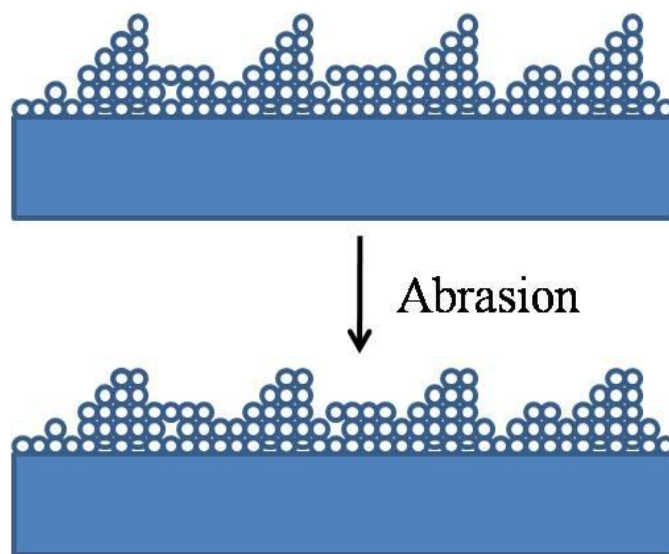


Figure 4.7 Schematic of the nanocomposite surface before and after abrasion test

The reversibility of surface wettability was also realized on the ZnO nanocomposite film surface. After surface treatment of OTS, the CA recovered to 150° with CA hysteresis of $\sim 5^\circ$ and superhydrophobic surface was generated. After UV irradiation for 9 hours, the surface returned to superhydrophilicity with a CA of $\sim 0^\circ$. As shown in Figure

4.8, a good reversability was achieved between superhydrophobicity and superhydrophilicity after repeating for five cycles. Such coating can be applied to many surfaces to realize tunable wettability for biological, chemical and electrical applications.

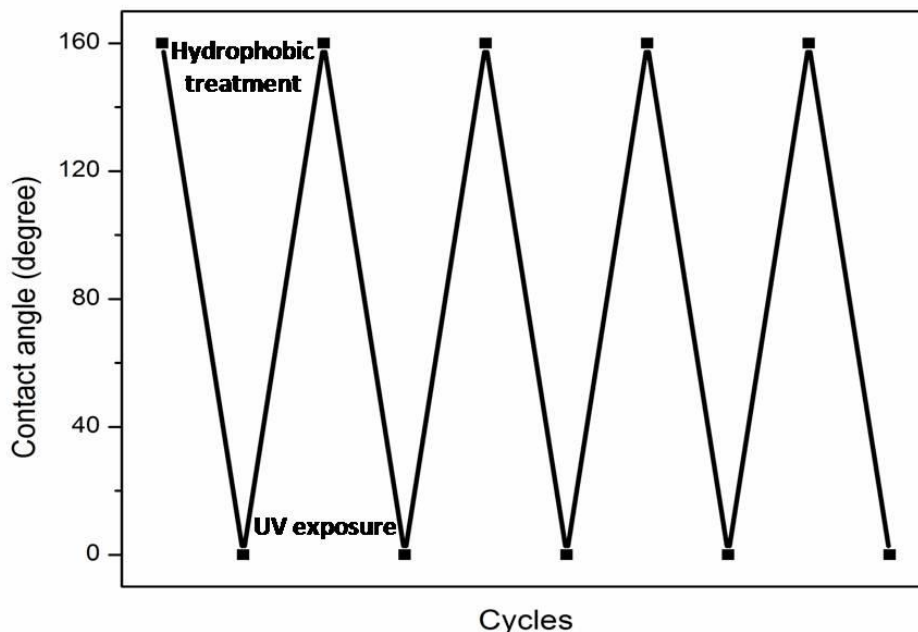


Figure 4.8 Reversible transition between superhydrophobicity induced by silane treatment and superhydrophilicity induced by UV irradiation

4.4 Conclusions

In summary, ZnO nanorod/epoxy composite films with tunable wettability from superhydrophobicity to superhydrophilicity were realized in our study. The composite surface exhibits hierarchical structure with both sub-micro and nano sized ZnO rods exposed after RIE. The surface showed superhydrophobicity by hydrophobic treatment in silane solution, and it can be transferred to superhydrophilicity by UV induced photocatalytic effect. A good reversability of wettability was achieved through cycling between UV irradiation and silane treatment. The ZnO nanocomposite surface showed improved mechanical robustness comparing with inorganic nanoparticle films. Such

coating can be applied to many surfaces for wettability modifications, which have great potential for functional materials and devices.

CHAPTER 5

SUPERHYDROPHOBIC NANOCOMPOSITES COATING FOR RELIABILITY IMPROVEMENT OF MICROELECTRONICS

We developed superhydrophobic silica/epoxy nanocomposite coating as an encapsulant to improve the device reliability. The superhydrophobic surface was generated by spin-coating of a silica/epoxy nanocomposite, followed by an oxygen reactive ion etching that exposes silica nanostructures for high surface roughness, and a subsequent hydrophobic treatment for low surface energy. As a result, a water contact angle of 161.2° and contact angle hysteresis of 1.7° were achieved under an optimized condition. Such superhydrophobic coating showed good stability under humidity at elevated temperatures and was applied on the triple track resistors (TTR) test coupons. It was found that the self-cleaning encapsulant successfully improves the test device reliability, and the coated TTR showed less degradation of resistance and leakage current in the temperature humidity bias (THB) test. In addition, the effect of different types of epoxy resin on reliability improvement was studied.

5.1 Introduction

Moisture is one of the most detrimental factors to the reliability of microelectronics. Water repelling property such as superhydrophobicity is very demanding for low cost and high reliability microelectronic packaging solution.

Self-cleaning superhydrophobic surfaces usually display a water contact angle greater than 150° and a hysteresis smaller than 10° , [96, 117-118, 139, 152-153] which was found in many natural surfaces. [5, 154] Among which, lotus leaves are one of the

most well-known examples,[75] which consist of a combination of micro and nano roughness along with a low surface energy coating.[76-77, 121, 155-156] Superhydrophobic surfaces have been widely used for stiction reduction and anti-corrosion in opto-electronics and MEMS. [58, 70, 157]

One of the most important applications for superhydrophobic surface in microelectronics packaging is to improve the reliability of devices. Moisture, mobile ions, ultraviolet light, and other hostile environment significantly affect the performance and lifetime of IC devices.[158-160] To improve the device reliability, a conformal coating of organic encapsulant is usually applied on the devices package. The commonly used encapsulants include epoxies, polyimides, polyxylylene (Parylene[®]), silicone-polyimides, and silicones (elastomers and gels).[161] The advantages and disadvantages of commonly used encapsulants are listed in Table 5.1.

It has been reported that the application of encapsulants protects the electronic components from high temperature humidity bias condition, thermal shock and temperature cycle during actual life applications. Moreover, the encapsulant coating can prevent the infusion of mobile ion contaminations and moisture, and increase the long-term reliability of non-hermetic packages.[161-163] However, till now few researches have been reported about using superhydrophobic encapsulant to protect the IC device for reliability improvement.

In this paper, superhydrophobic surface based on silica/epoxy nanocomposites is coated on TTR test coupons as an encapsulant layer to improve the device reliability. The incorporation of nanosilica particles as filler into the epoxy increases the surface roughness of the composites, which is critical for superhydrophobicity. Superhydrophobic surfaces were produced after functionalization with low surface energy PFOS. The resistance and leakage current of TTRs without coating, with epoxy coating and with superhydrophobic epoxy/silica coating were monitored under the conditions of 85°C/85% relative humidity (RH) and a constant DC bias of 13.4V. Two

types of epoxy resins were employed to compare the effect of mobile ion contents on reliability improvement.

Table 5.1 Potential IC encapsulants [22]

Encapsulants	Applications	Advantages	Disadvantages
Epoxies	Normal Dispensing or molding	Good solvent resistance; Excellent mechanical strength	Non-repairable; High stress; Marginal electrical performance
Polyimides	Normal dispensing (spin coating)	Good solvent resistance; Thermally stable	High Temp cure; Non-repairable; High stress
Silicones	Normal Dispensing	Good temp., cycling; Good electrical; Very low modulus	Weak solvent resistance; Low mechanical strength
Polyxylylene	Thermal deposition (reactor)	Good solvent resistance; Conformal coating	Thin film only; Non-repairable

5.2 Experimental Details

5.2.1 Formulation of silica/epoxy nanocomposites

Silica nanoparticles (100 nm, 10 wt. %) were dispersed in toluene by sonication and the particles are shown in Figure 5.1 (b). Epoxy resin, hardener hexahydro-4-methylphthalic anhydride (HMPA) and catalyst imidazole were added into the silica/toluene solution and stirred to form a final coating mixture. Here two kinds of epoxy resin were used, 3,4 Epoxy Cyclohexyl Methyl 3,4 epoxy Cyclohexyl Carboxylate (Union Carbide, CT) and bisphenol A diglycidyl ether (Momentive, CO) (Table 5.2).

5.2.2 Fabrication of superhydrophobic surfaces

TTR test coupons were made by deposition of Ta₂N metallization on the Al₂O₃ substrate. The test pattern consists of three parallel meandering lines with 75µm line-width and spacing between lines (Figure 5.1a). The TTR coupon was cleaned in boiling H₂O₂ for 15 min, rinsed with deionized water, and dried by N₂. The silica epoxy coating mixture was spin-coated on the TTR at 1,200 rpm for 2 min. After solvent drying, the coated TTR coupons were put into the oven to cure the polymer at 150 °C for 2 hrs. To produce superhydrophobic surfaces, oxygen RIE was conducted on the nanocomposite surface under 150 W RF power and 0.5 torr pressure. After that, surface fluorination was performed by coated with 3 mM PFOS in hexane, followed by heat treatment at 150°C for 1 hr. Three types of samples were prepared: uncoated, epoxy coated and superhydrophobic silica/epoxy coated samples. The cured test devices were subjected to 85°C and 85% RH under 13.4 Volt-DC bias for 1,000 hrs.

5.2.3 Characterizations

Scanning electron microscopy (SEM, Leo 1530) was used to observe the surface morphology. Transmission electron microscopy (TEM) images were obtained by using

JEOL TEM 100CX. Contact angle measurements were performed with a Rame-Hart goniometer with a built-in CCD camera. In the 85 °C/85% THB performance experiment, we grounded the two outer tracks and biased the center track, then measured the resistance change between the centers of the conductor lines. Resistance of TTR was measured by a Keithley 2000 multimeter. Leakage current was measured by Keithley 485 picoammeter.

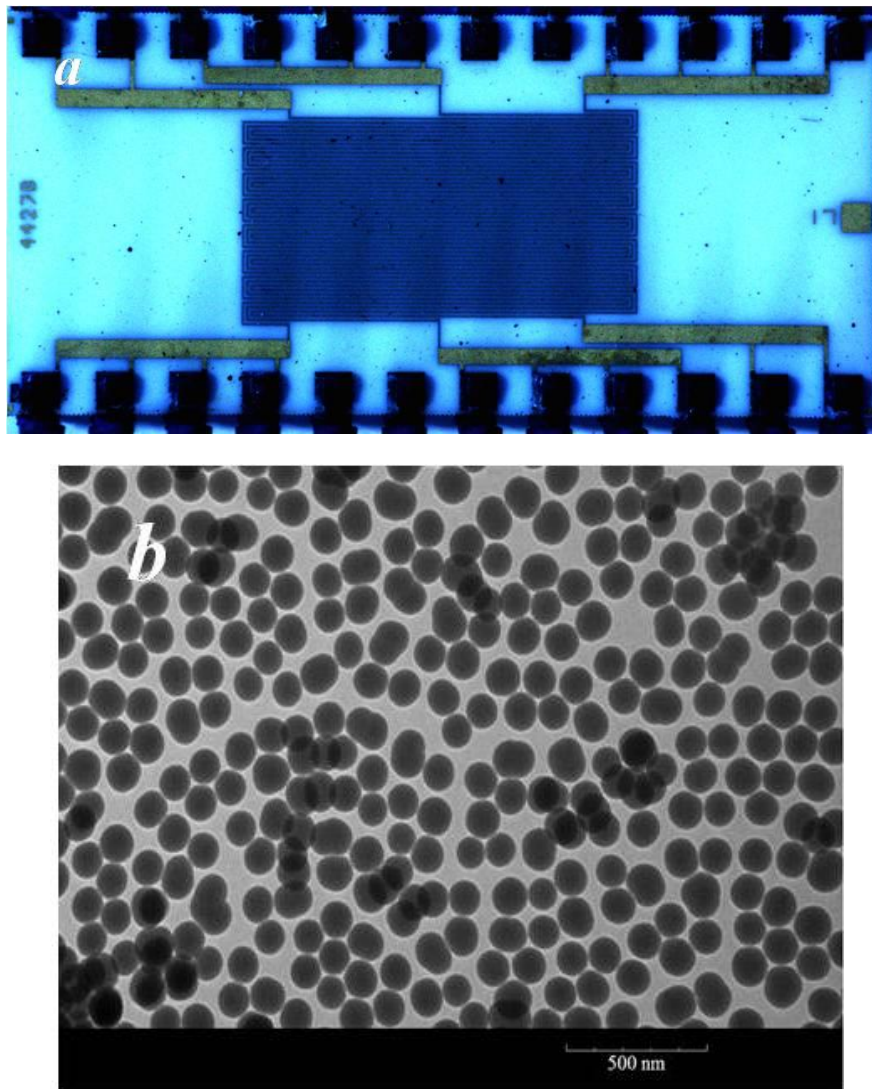
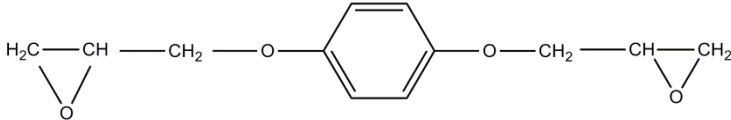
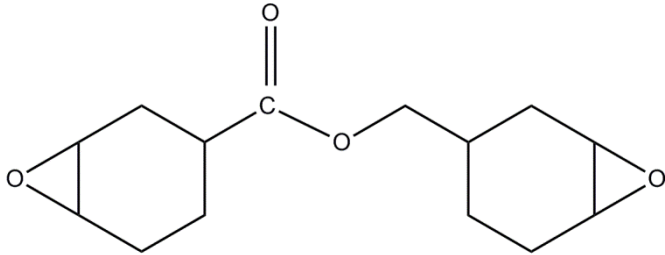
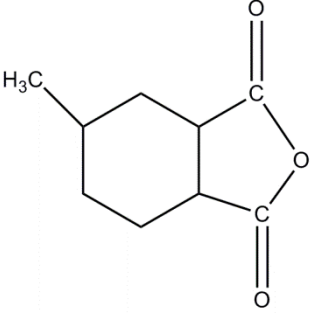
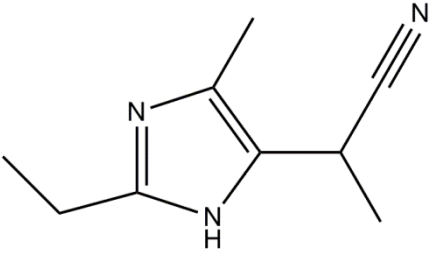


Figure 5.1 (a) Optical image of triple track resistors (b) TEM image of silica nanoparticles

Table 5.2 A list of epoxy resin, curing agent and catalyst used in this study

Molecular Structure	Synonym	Name
	EPON 828	Diglycidyl ether of bisphenol-A epoxy resin
	ERL 4221	cycloaliphatic epoxy resin
	HMPA	Methyl tetrahydro phthalic anhydride
	2E4MZCN	1-cyanoethyl-2-ethyl-4-methylimidazole

5.3 Results and Discussion

In this study, we coated the TTR coupons with epoxy filled silica nanoparticles. The fabrication of superhydrophobic coating is schematically shown in Figure 5.2a. Most of nanosilica particles incorporated into the epoxy are located inside the epoxy resin and found underneath the top epoxy after spin-coating the composites. In order to have the nanosilica exposed out of the epoxy for larger surface roughness, we used oxygen RIE to etch out epoxy molecules with different etching durations. Then, long chain fluorocarbon silane was coated on the nanosilica exposed top surface to further reduce the surface energy. As shown in Figure 5.2b, the primary anchoring site for silane molecules is on the hydroxyl group on the surface of nanosilica.

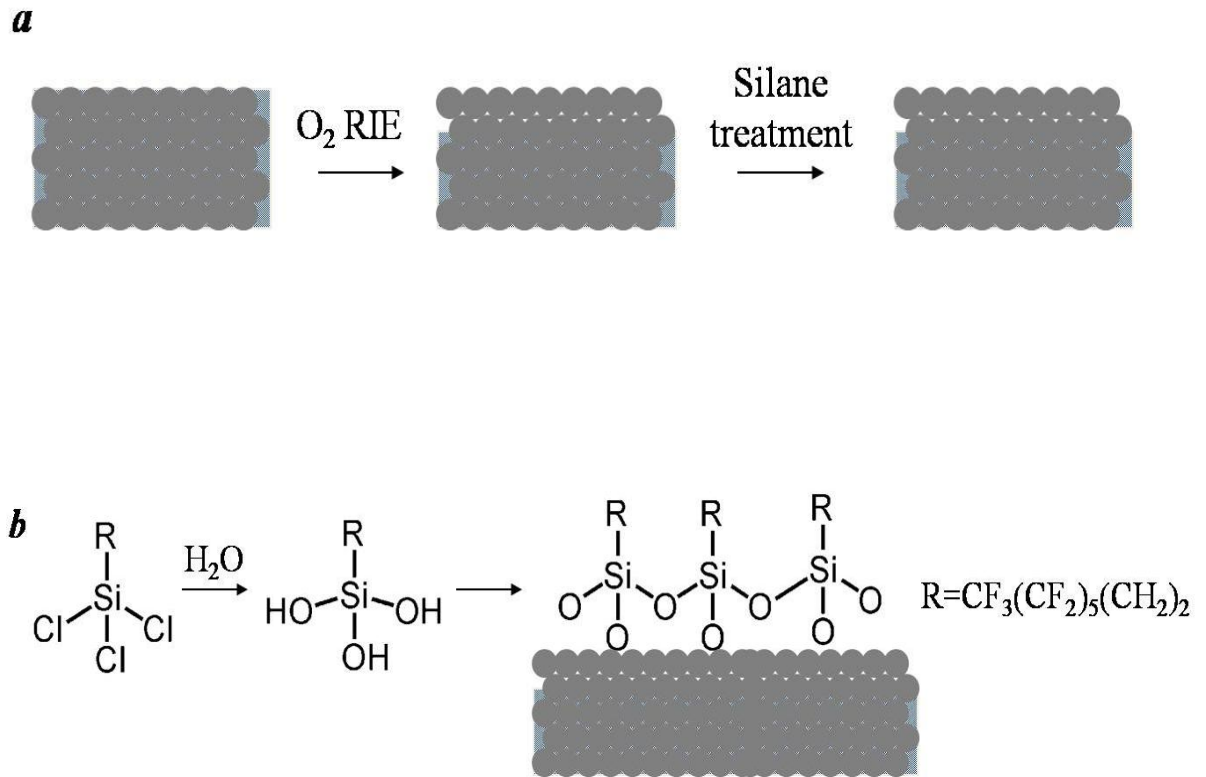


Figure 5.2 Illustration of (a) O₂ plasma etching of epoxy/SiO₂ nanoparticle composite films for surface rough structures. (b) Hydrophobic treatment with PFOS on nanocomposite surface

5.3.1 Superhydrophobic SiO₂/epoxy nanocomposites

The surface morphology plays a critical role in the formation of superhydrophobic surfaces. Here, the etching duration of oxygen RIE is a primary factor to control the surface roughness. As seen in Figure 5.3a, before oxygen RIE treatment, most of nanosilica is covered with epoxy resin and the curvature of particles has negligible contribution to surface roughness. With 5 min RIE, nanosilica was partially exposed on the surface (Figure 5.3b), while increasing the etching time to 15 min, the nanosilica surfaces are all exposed (Figure 5.3c). The increased portion of nanosilica on the surface increases the surface roughness and significantly changes the water contact angle. As shown in Figure 5.4 and Table 5.3, the water contact angle of unetched surface, 117.7°, increases to 158.6° after 5 min RIE and to 161.2° after 15 min etching. At the same time, the hysteresis dropped from 12° to 1.75° when increasing etching time from 5 min to 15 min, indicating the formation of superhydrophobic surface with self-cleaning properties.

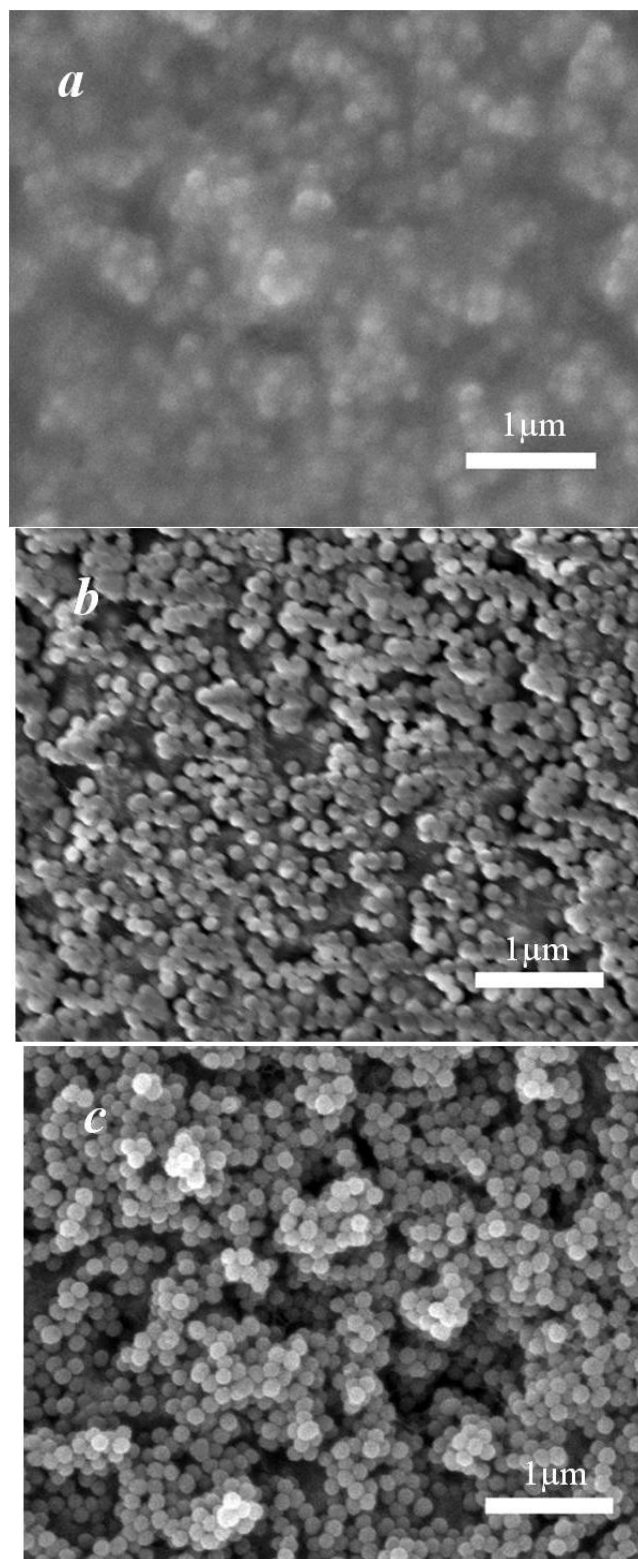


Figure 5.3 Surface morphology from SEM images: surface before etching (a), O₂ plasma etched for 5 min (b), and 15 min (c)

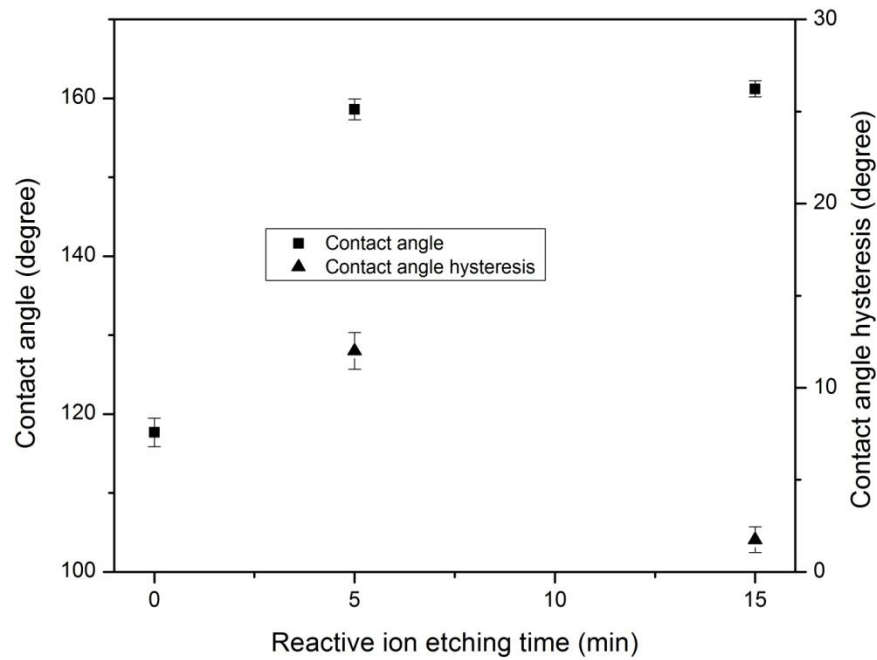


Figure 5.4 Contact angle and hysteresis for silica nanocomposite surfaces etched for different time.

Table 5.3 Contact angle and contact angle hysteresis of epoxy silica nanocomposites with different reactive ion etching time.

Reactive ion etching time (min)	Contact angles (degree)	Contact angle hysteresis (degree)
0	117.7 ± 1.8	29.4 ± 1.2
5	158.6 ± 1.3	12 ± 1.0
15	161.2 ± 1	1.75 ± 0.7

The increased contact angle and reduced contact angle hysteresis with increased etching time can be explained by two hydrophobic states on rough solid surfaces, Wenzel and Cassie states. The Wenzel equation,[6] Eqn. (1), describes the effect of surface roughness on the water droplet contact angle:

$$\cos \theta_A = r \cos \theta_Y \quad (1)$$

where θ_A is the apparent contact angle on the rough surface, r is the ratio of the actual solid/liquid contact area to its vertically projected area, and θ_Y is the contact angle on a flat surface defined by Young's equation. As the roughness (r) increases, the contact angle also increases. Surfaces etched for short time (5 min) display non uniformity in the micro-bump top surface. Epoxy was not completely etched with short RIE time, and therefore most of the silica particles remain embedded in the polymeric layer. The low roughness geometry results in high contact angle hysteresis.

The Cassie equation [7] for a porous or composite surface, Eqn. (2), indicates that the apparent contact angle increases when the solid surface fraction f is decreased.

$$\cos \theta_A = -1 + f(\cos \theta_Y + 1) \quad (2)$$

When the etching time increases to 15 min, the surface gets rougher. Consequently, the surface changes from Wenzel State to Cassie State. The silica particles are fully exposed and form a densely packed layer, which significantly enhances the surface roughness. More air is trapped at the water and composite interface. As a result, both a high contact angle and a reduced hysteresis are achieved.

5.3.2 THB test of the superhydrophobic coated TTR

In order to test the durability of superhydrophobic surfaces, the superhydrophobic silica nanocomposites were put in the 85 °C/85% RH chamber. During the 85°C/85% RH THB test, the triple track structures were biased at 13.4V from the exterior track to the middle track and at -13.4V from the interior track to the middle track to accelerate the corrosion process (Figure 5.5). It was found that after 1000 hours, the surface maintained the self-cleaning property with a water contact angle of 160° and hysteresis of ~2°.

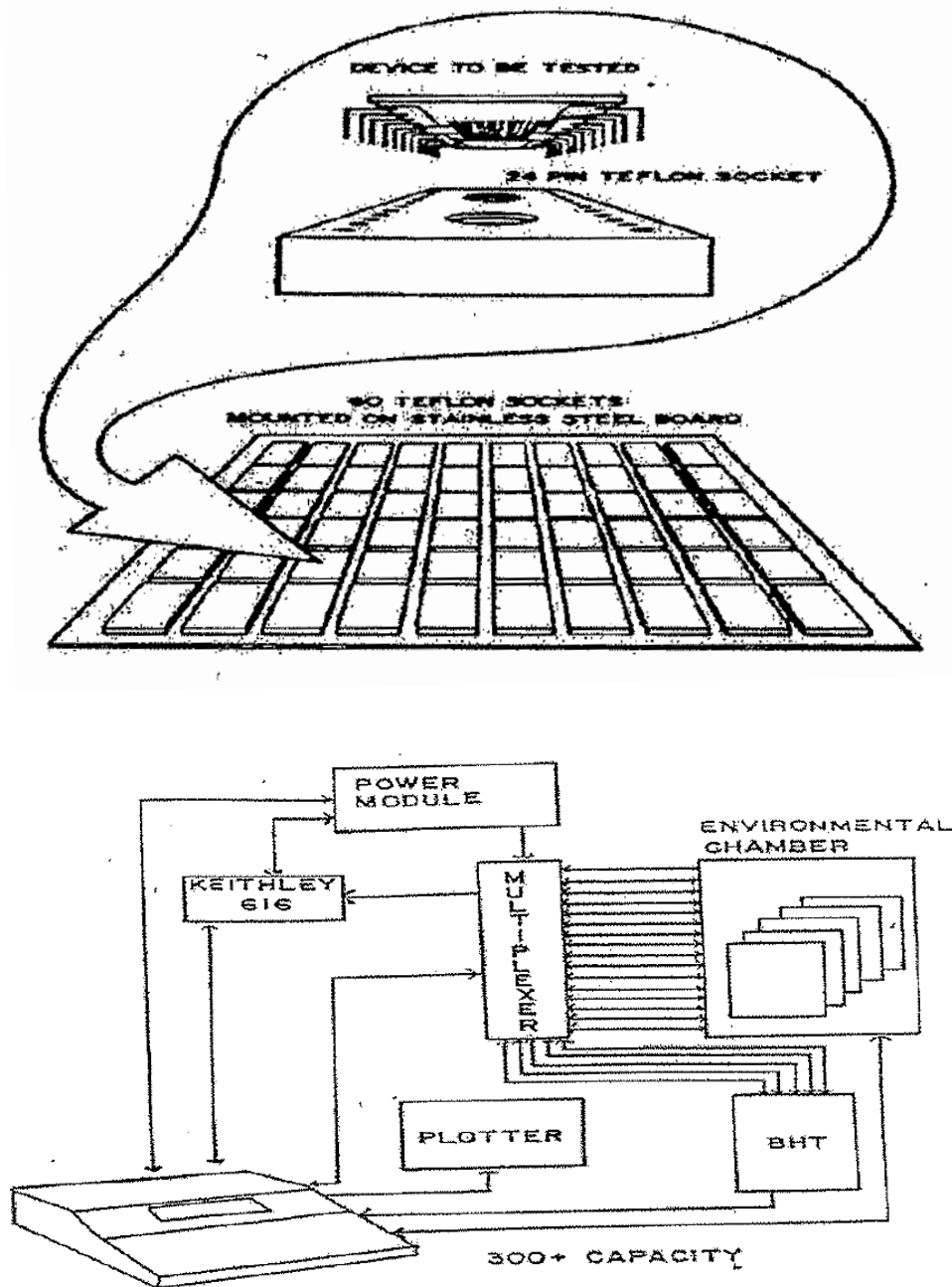


Figure 5.5 Configuration of THB testing hardware

The cycloaliphatic epoxy resin used in this study has low ionic impurity, e.g., chloride and sodium, potassium, etc. During reliability tests, the resistance and leakage current change of TTR coupons were monitored. The resistance change was a measure of

the degree of "electro-oxidation". When enough moisture diffuses through the encapsulant to form a continuous water path at the substrate interface, electro-corrosion begins with the presence of mobile ions (such as sodium and potassium) under electrical bias. The less the resistance changes with testing time, the more stable the encapsulant material is. The leakage current results from the anodization of resistors and is an indication of the amount of impurities.

It was found that the THB performance of the superhydrophobic coated samples was excellent under the accelerated aging condition, which is shown in Figure 5.6. The resistance of epoxy coated samples remained low until the first 60 hrs, showing a certain effect in improving device reliability. Remarkably, the superhydrophobic composite coated on the TTR greatly slowed down the electro-oxidation process for the first 300 hrs. The superhydrophobic nanocomposite coated on TTR showed a significantly less resistance change comparing with uncoated and epoxy coated sample in the first 300 hrs. From 300 hrs to 1,000 hrs, the resistance changes of epoxy coated and superhydrophobic nanocomposites coated samples were less significant comparing with uncoated control samples (Figure 5.6 a).

Then we measured the leakage current change with time. During the 1,000 hrs aging time, the leakage current of the control sample increased significantly from 10^{-10} amps to 10^{-5} amps. The epoxy coated samples showed stable leakage current in the first 300 hrs, and started to increase to 10^{-7} amps within 1,000 hrs cycles. The superhydrophobic nanocomposites coated samples kept stable leakage current under 10^{-9} amps in 1,000 hrs. The results of the THB testing show that the addition of the superhydrophobic layer dramatically decreases the change of resistance and leakage current during aging, and enhances the electrical reliability of test vehicles comparing with uncoated and epoxy coated samples (Figure 5.6 b). Such a superhydrophobic coating significantly reduces the influence from moisture or humidity, and is very promising for improving device reliability.

5.3.3 The effect of epoxy resin on reliability improvement

Mobile ion content in polymers also affects the device reliability. In comparison, a bisphenol-A (bis-A) type epoxy resin was also chosen, which may contain higher amount of mobile ions (chloride, potassium, etc) than the cycloaliphatic epoxy used in this study. Similarly, the bis-A epoxy and superhydrophobic silica/bis-A epoxy composites were coated on TTR. The resistance of epoxy coated and superhydrophobic nanocomposites coated samples showed less resistance change comparing with uncoated samples. The resistance of superhydrophobic nanocomposites coated sample increases gradually from 20 to 1,000 hrs, and the increase rate is smaller than the epoxy coated sample (Figure 5.7a). During 1,000 hrs, comparing with uncoated and untreated epoxy coated samples, the superhydrophobic nanocomposites coated sample showed the lowest leakage current change of the range of 10^{-10} amps to 10^{-9} amps (Figure 5.7b). The higher resistances change of bis A type epoxy than cycloaliphatic epoxy based nanocomposites may be due to higher mobile ions content in the bis A type epoxy used here.

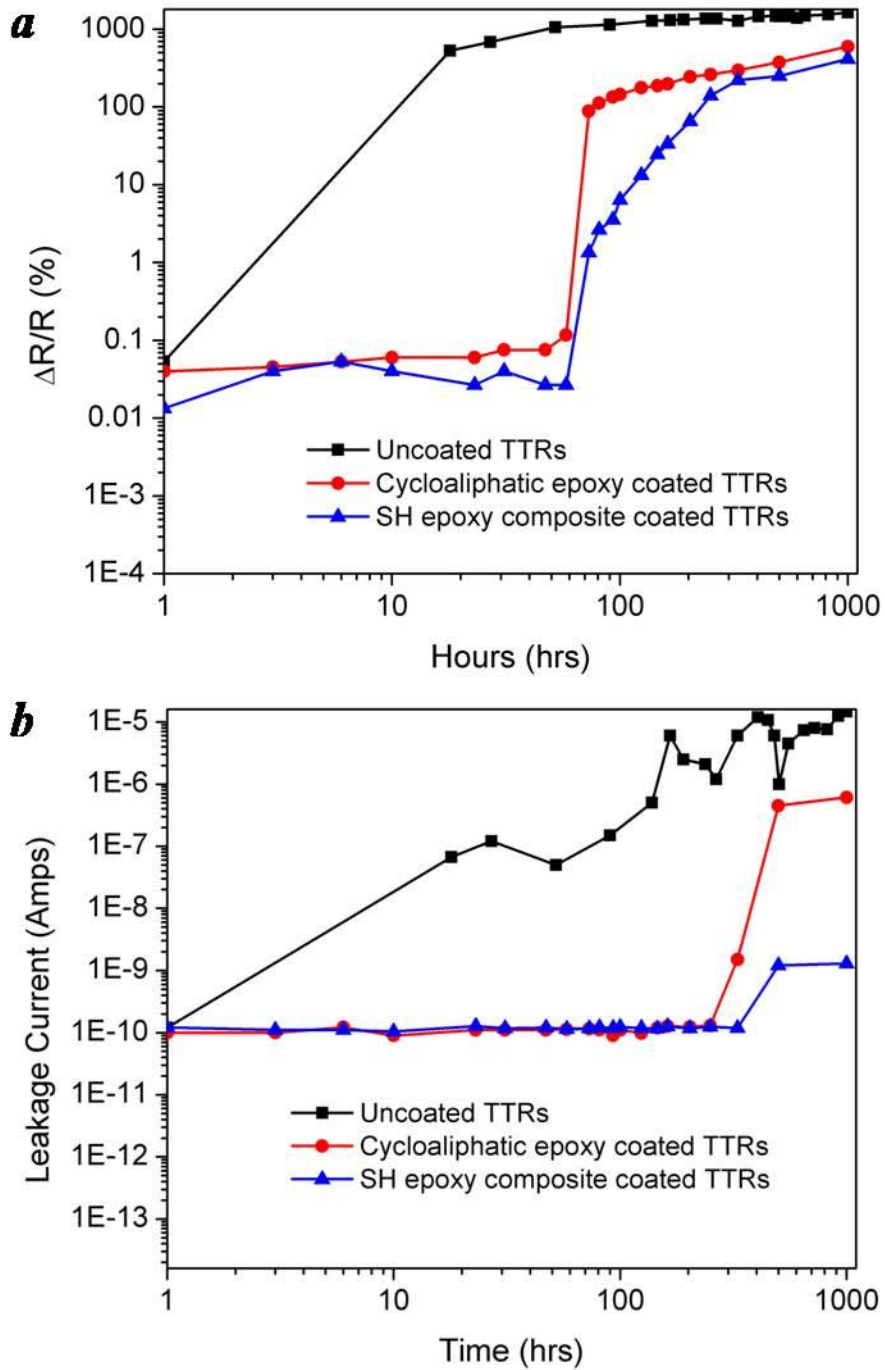


Figure 5.6 Resistance (a) and leakage current (b) change of uncoated, cycloaliphatic epoxy coated and superhydrophobic silica/cycloaliphatic epoxy composite coated samples with time in the reliability test in 85 °C/85 %RH chamber under 13.4 Volts-DC bias.

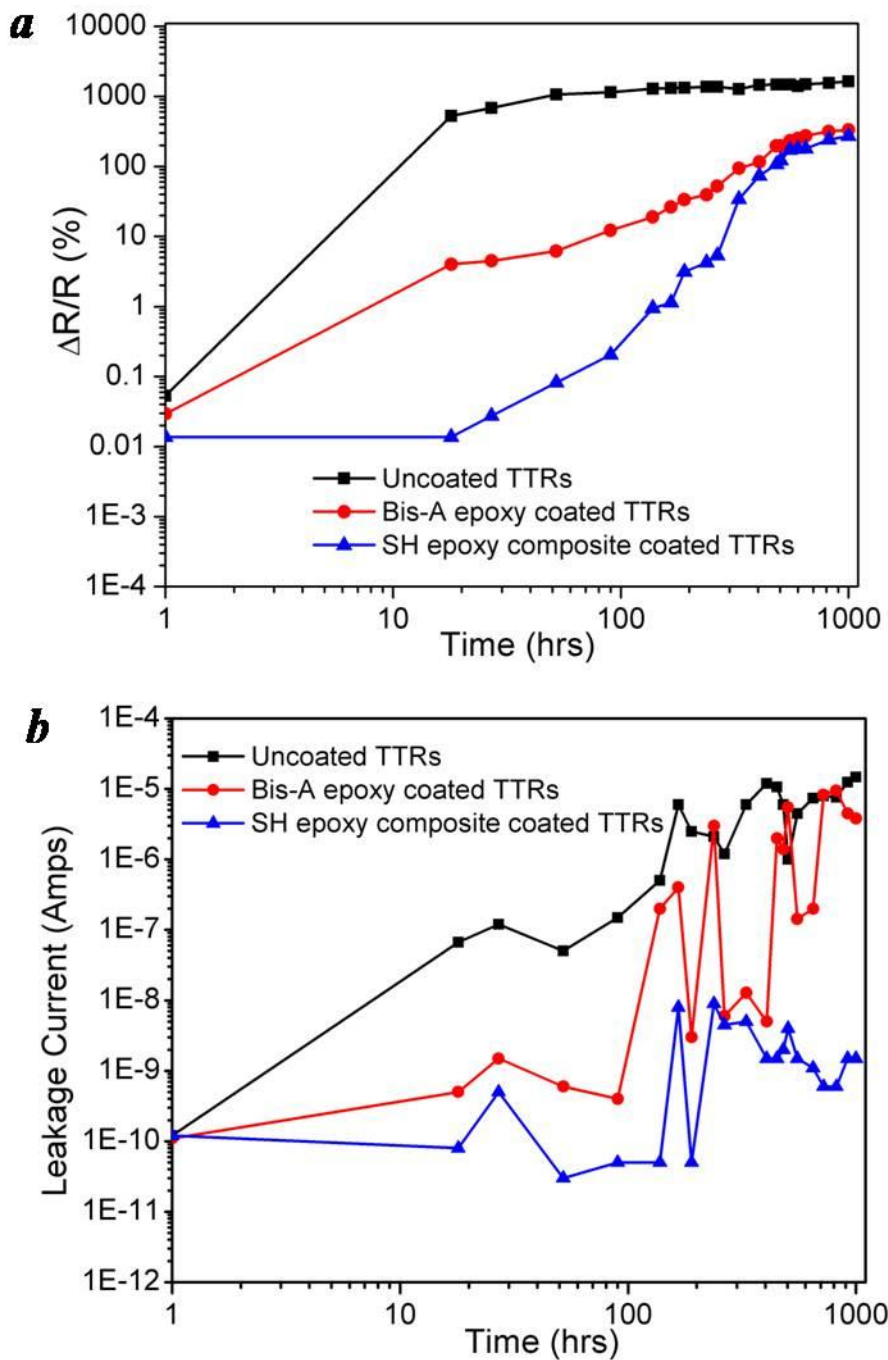


Figure 5.7 Resistance (a) and leakage currents (b) change of uncoated, bis-A epoxy coated and superhydrophobic silica bis-A epoxy composite coated samples with time in the reliability test in 85 °C/85 %RH chamber under 13.4 Volts-DC bias.

5.4 Conclusions

In this study, superhydrophobic epoxy/silica nanocomposites were fabricated. A water contact angle of 161.2° and contact angle hysteresis of 1.7° were achieved when the RIE time increased to 15 min. The superhydrophobic surface showed good stability of the TTR test coupons in $85^\circ\text{C}/85\%$ RH temperature humidity chamber and self-cleaning property remained after 1,000 hrs of testing. After the reliability test in the $85^\circ\text{C}/85\%$ RH chamber under 13.4 Volts-DC bias for 1,000 hours, superhydrophobic nanocomposite coated samples showed more stable resistance and less leakage current change than uncoated and epoxy coated samples. Cycloaliphatic epoxy coated superhydrophobic samples showed better reliability than bis-A type epoxy based samples due to its less mobile ion contents. Such coating has great potential to improve the device reliability in microelectronic packaging.

CHAPTER 6

**HYBRIDIZING ZNO NANOWIRES WITH MICROPYRAMID
SILICON WAFER AS SELF-CLEANING HIGH EFFICIENCY
SOLAR CELLS**

We report a novel hierarchical structure of integrating ZnO nanowire arrays on Si micropyramids as an effective anti-reflection layer for improving the energy conversion efficiency. This structure displays a broadband reflection suppression in the 300-1200 nm range, with an average weighted reflectance of 3.2%, much lower than the previously reported 6.6% reflectance of tapered ZnO nanostructures on planar surfaces. A cost effective screen printed solar cell was fabricated based on this hierarchical structure. A conversion efficiency of 16.0 % was obtained, which is the highest for any solar cell fabricated using ZnO nanostructures as antireflection coating layer. In addition, a surface modification enables a self cleaning property that will prevent the blocking of light by dust particles on solar panels.

6.1 Introduction

Low conversion efficiency is still the main limiting factor for current solar cell technologies. A large portion of energy loss during solar cell operation is attributed to optical loss, namely reflection loss of the incoming light.[164] To reduce the reflection loss, surface texturing and antireflection coatings are the most commonly used strategies.[165-166] Surface texturing is able to enhance the light trapping by multiplying the internal reflections. The industrial standard for the current Si-based photovoltaic (PV) industry process is alkaline fabrication of pyramid textures. An emerging focus today is

the incorporation of nanostructures as surface texturing materials.[167-171] For example, porous Si and Si nanowires (NWs) have been applied to solar cells to effectively reduce the reflection loss.[172-174] Xiu *et al.* developed a hierarchical structure through a two-tier texturing method for lower light reflection.[87] Antireflection coating (ARC) is another method to reduce the light reflectance via destructive interference of the reflected light at the air-ARC-substrate interfaces. Single-layer AR coating such as silicon nitride (SiN) is the industry standard ARC on Si PVs.[175] Further reduction of reflection can be achieved through a multi-layer ARC, or a fine control of ARC geometry, which enable a gradual transition of the refraction index from air to silicon.[176-177]

An outstanding one-dimensional nanostructure,[178-179] ZnO NWs have high transparency due to the wide bandgap, appropriate refractive index ($n \sim 2$ at 600 nm), and the capability of forming a textured coating virtually on any substrate.[180] These characteristics make it an attractive dielectric ARC material for PV applications.[181] The integration of ZnO nanowires with optical fiber and quartz waveguide has shown an enhancement of efficiency by a factor of 4-6 by utilizing three dimensional approach.[182-183] The application of ZnO nanostructures on planar Si as ARC for solar cells achieved a weighted reflectance (WR) of 6.6 % [184] and a conversion efficiency of 12.8%. [185] Based on these results, a further boost of solar cell efficiency is expected by introducing a novel ZnO nanowire-based hierarchical nanostructure.

In this study, we report a hierarchical structure with the growth of ZnO NWs on a micropylramid textured Si surface as an ARC for solar cells. In the past, the ability to use industrial contacting techniques and the physical robustness of the NWs have not been demonstrated. As screen-printing of metal electrodes is the dominant contacting method for silicon solar cells, this work examines the ability to contact solar cells through a NW ARC layer. In addition, ARC layers must be abrasion resistant to survive the screen-printing process and be useful over the 25 year lifespan of a typical cell module. We therefore also examine the effect of abrasion on the hierarchical nanostructure during

screen printing, the ARC effect and non-wetting of such structure. The ZnO NWs on Si micropyramids allow a gradual transition of the effective refractive index from the air to the substrate, while the pyramidal Si surface multiplies the light reflections within the hierarchical structure. As a result, this structure yields a low surface reflectance and significantly enhanced conversion efficiency of the photovoltaic device. Solar cells based on the hierarchal structure show high conversion efficiency as well as a superior self-cleaning property.

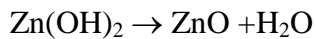
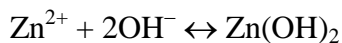
6.2 Experimental

6.2.1 Si etching:

The textured Si wafer with micropyramids was created by KOH etching at 80-85 °C for 20-30 min. The etching solution is composed of KOH (2 wt %), water, and isopropyl alcohol (5 vol %).

6.2.2 ZnO nanowire growth:

A ZnO seed layer was deposited onto the SiO₂ layer by magnetron sputtering under 5 mTorr O₂ and Ar atmosphere without additional heating. The coated Si wafer was then placed in an aqueous solution containing hexamethylenetetramine (HMTA) and zinc nitrate hexahydrate. The reactions were performed at 80 °C as follows:



6.2.3 Solar cell fabrication:

First, an Al paste was screen-printed on the backside of the Si substrate and dried at 200 °C. Ag grids were then screen-printed on top of the ZnO NWs, followed by co-firing

of both the Ag and Al contacts. During the firing step, an Al-doped Si layer, referred to as the aluminum back surface field, is also formed. To prevent erroneous measurements, the active area of the cells was defined using a dicing saw, which electrically isolates each cell from the rest of the substrate.

6.3 Results and Discussion

6.3.1 Reflectance of hierarchical structures

The structure of the solar cell with ZnO NWs on Si pyramids is shown in Figure 6.1. The Si substrate used is a single-crystal, p-type float zone substrate with a thickness of 300 μm . The textured Si surface with pyramidal structures was created by KOH etching. The wafers were then cleaned to remove surface organic and metallic contaminants, followed by POCl_3 diffusion to form the n^+ -emitter. A diffusion temperature of 860°C was used for obtaining 65 Ω/sq emitter. After the phosphorus-glass removal in a buffered HF solution, a SiO_2 passivation layer was grown at 900 °C. The treated wafer was used for ZnO NW growth on a sputtered ZnO seed layer by a low cost and scalable hydrothermal method.[186]

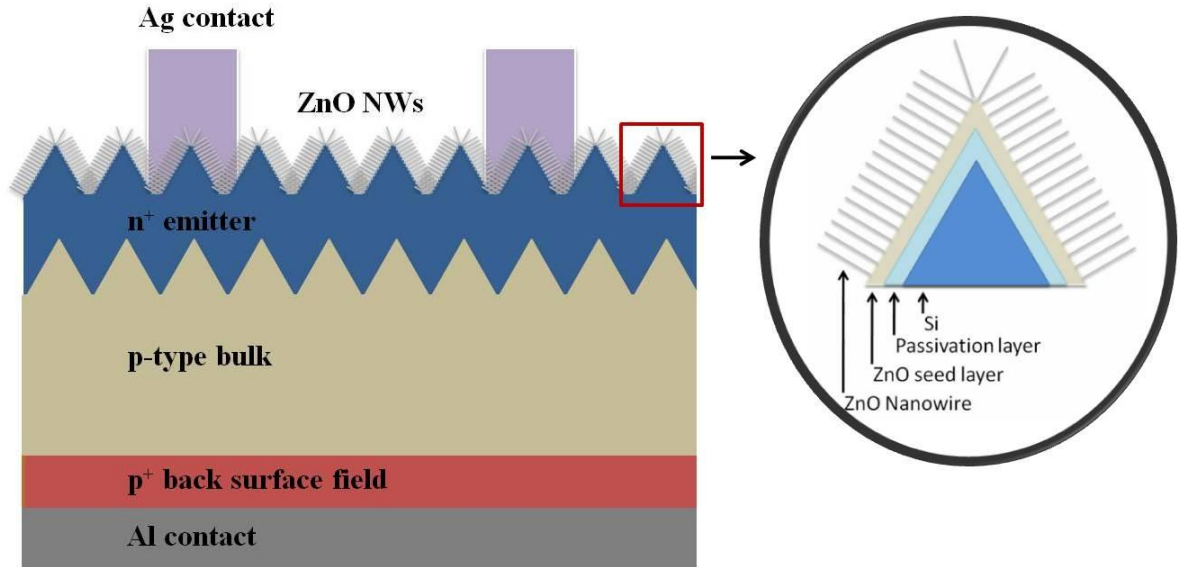
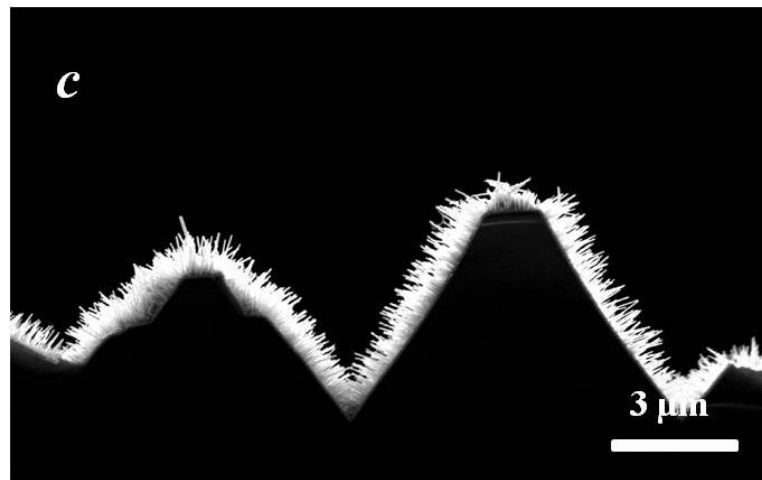
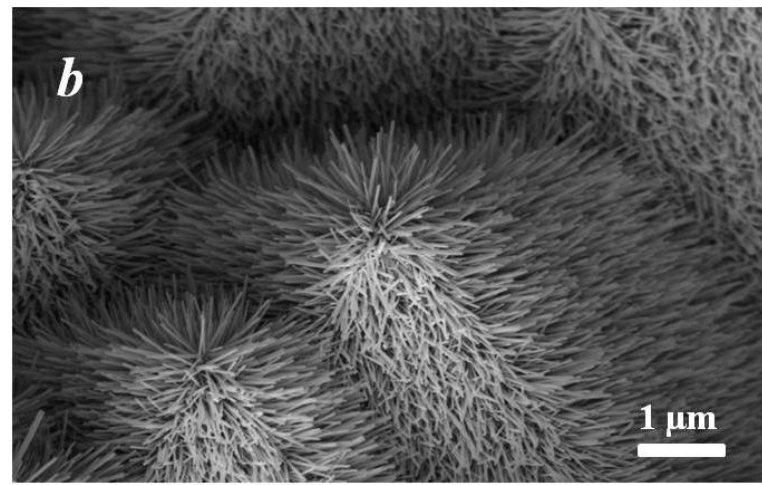
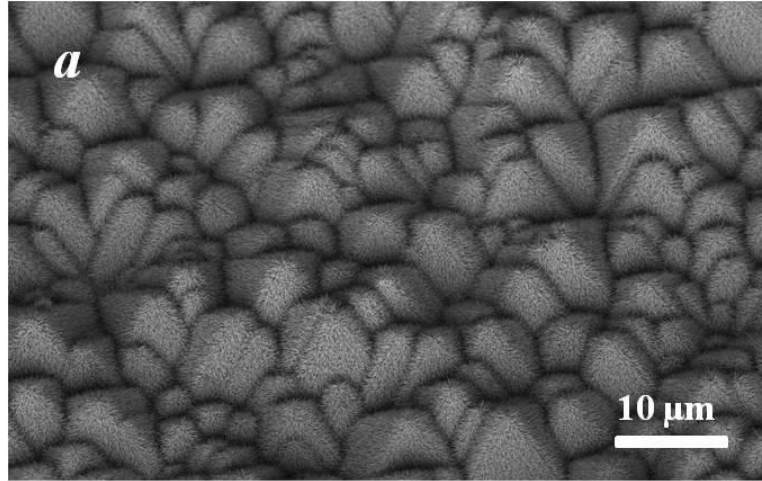


Figure 6.1 A schematic of the hierarchical ZnO NW-Si solar cell.

After the growth of ZnO NWs, screen-printed n^+ - p - p^+ solar cells (4 cm^2) were fabricated. The surface morphology of the ZnO NWs on the Si pyramid structure is shown in Figure 6.2. The Si micropylamid size is around $2\text{-}4 \mu\text{m}$ (Figure 6.2a). Highly dense ZnO NWs are hierarchically grown on top of the micropylamids. Most ZnO NWs are perpendicular to the Si pyramid, due to their anisotropic growth along c -axis. The morphology of the ZnO NWs arrays can be controlled by modifying the seed layer thickness and corresponding growth parameters.[187] The length of ZnO NWs was measured from the cross-section view. As seen from Figure 6.2d, the ZnO NWs have a length of $\sim 800 \text{ nm}$. This length was chosen according to the ray tracing simulation optimization, which will be discussed later.



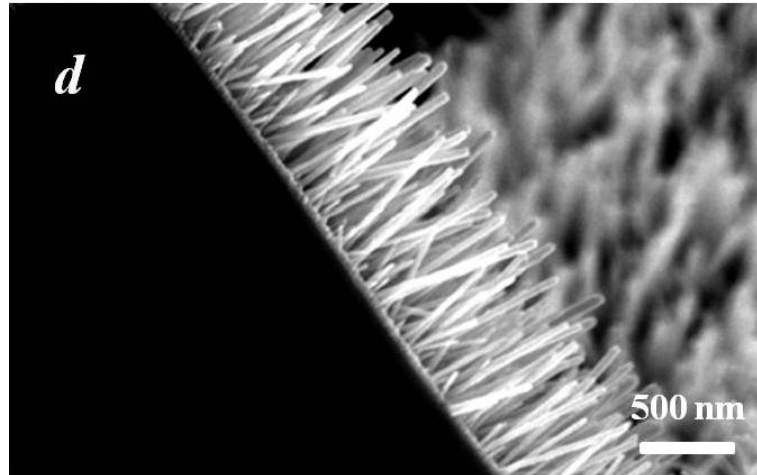


Figure 6.2 Surface morphology of hierarchical ZnO NWs on a pyramidal Si surfaces under low (a) and high (b) magnifications, as well as cross section views under low (c) and high (d) magnifications.

The weighted reflectance (WR) was calculated from the hemispherical reflectance spectrum (300-1200 nm) measured in our study. Figure 6.3a compares the measured front reflectance of bare planar Si surface and Si pyramid surfaces without and with ZnO NWs on top. Bare planar Si reflects about 35% of incident sunlight. Textured pyramid surfaces improve the light trapping by doubling the bounces of incident light, and reduce the light reflection to 11.3%. The deposition of ZnO seed layer on Si micropyramids as ARC results in a significant reduction of light reflection in all UV, visible light, and IR regions, with a WR of 4.1%. After applying the ZnO nanowires on the seed layer, further suppression of light reflectance is observed. Therefore a WR suppression of as low as 3.2% is achieved for ZnO NW hierarchical structure, which is much lower than the previously reported 6.6% WR of tapered ZnO nanostructures grown on planar Si surfaces.[184] An effective refractive index can be calculated by averaging the refractive indices of air and ZnO weighted by volume at the interface between air and ZnO, as pointed out by Zhu *et al.*[67] The enhanced WR suppression of the hierarchal structure is attributed to the effect of micro scale texturing that allows two bounces of light at the

surface, and a more gradually changing effective refractive index from air to the Si substrate compared to a single ZnO seed layer ARC (Figure 6.4).

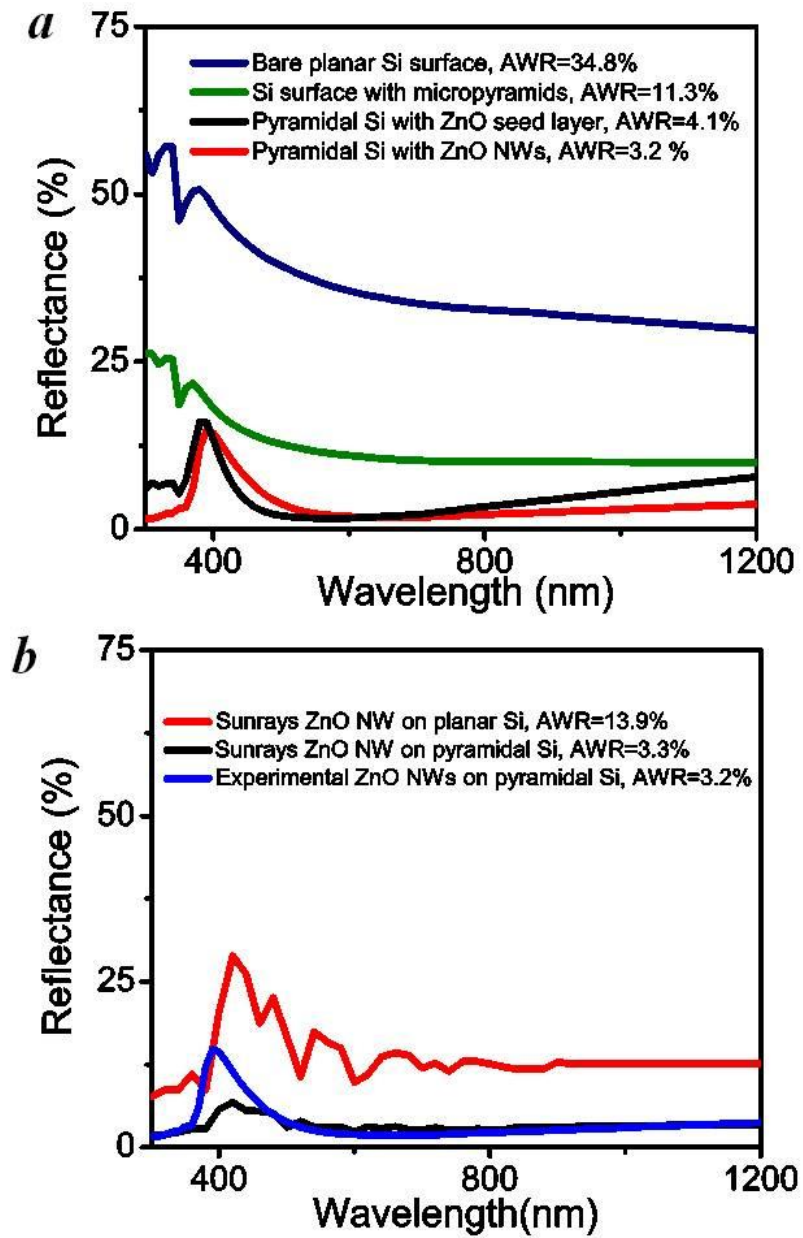


Figure 6.3 (a) Front light reflectance of ZnO NWs on pyramidal Si comparing with planar Si, pyramidal Si, and pyramidal Si with ZnO seed layer (b) Simulated light reflectance of the ZnO NW solar cell. red: Sunrays simulation data on planar surface; blue: Sunrays simulation data on textured surface; black: experimental data for ZnO NWs on pyramidal Si

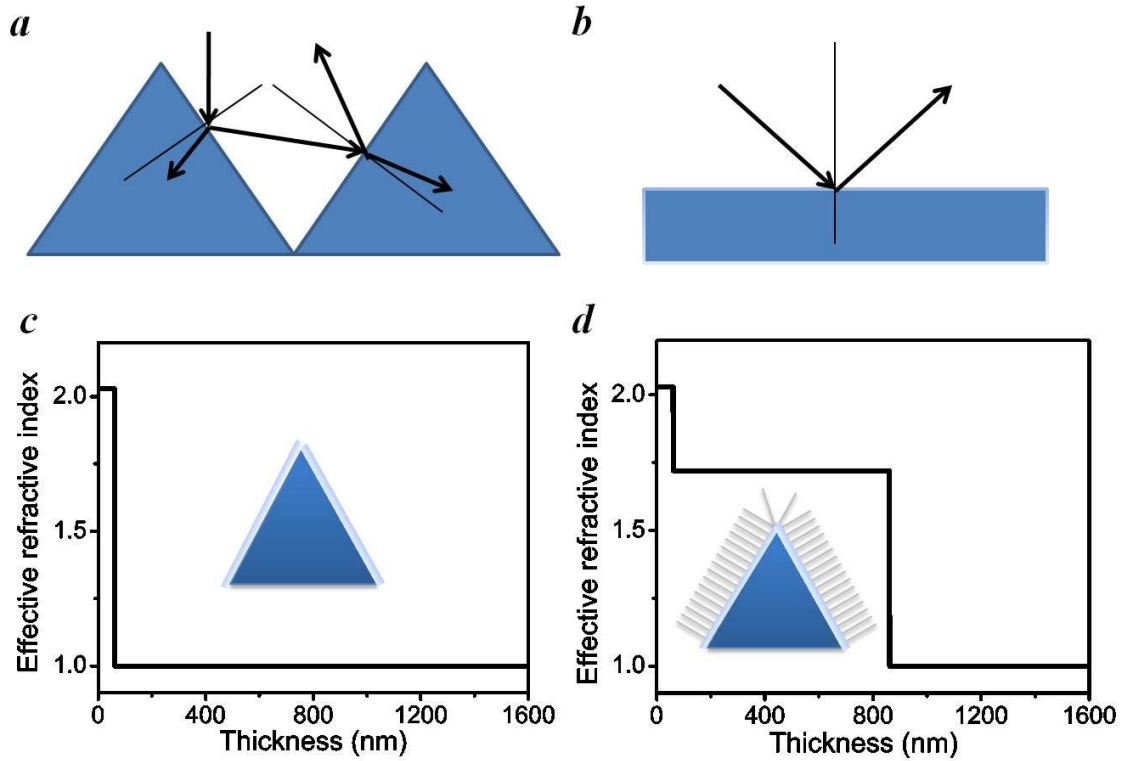


Figure 6.4 The reflection of incident light on (a) pyramidal Si (b) planar Si. The effective refractive index profile of the interface between air and (c) ZnO NWs on pyramidal Si (d) ZnO NWs on planar Si.

6.3.2 Light tracing simulation of hierarchical structures

A better understanding of the effect of hierarchical structure in reflectance suppression was obtained by Monte Carlo ray tracing simulation using Sunrays 1.3 program. The reflectance spectra of our textured solar cells were analyzed by varying the parameters of the ZnO NW ARC. The simulator takes into account the three-dimensional surface geometry of the simulated structure, as well as the optical properties (index of refraction and extinction coefficient) of every layer and interface in order to quantify the reflection and absorption in the structure.[188] We employed a 300 μm thick Si layer with an upright pyramid front texture in the simulation. The surface coating on Si pyramids was divided into three layers: a bottom passivation layer of SiO_2 (15 nm), a middle ZnO seed layer (variable thicknesses) and a top ZnO NW layer (variable

thicknesses). The dispersion relation (n and k) for the crystalline ZnO was obtained from the literature[189] and provided as an input to Sunrays, as shown in Figure 6.5. The ZnO NWs in our structure were estimated to be $\sim 70\%$ volume fraction, and the effective refractive index (n) of ZnO NW layer is calculated as the sum of $70\% n_{\text{ZnO NW}}$ and $30\% n_{\text{air}}$.

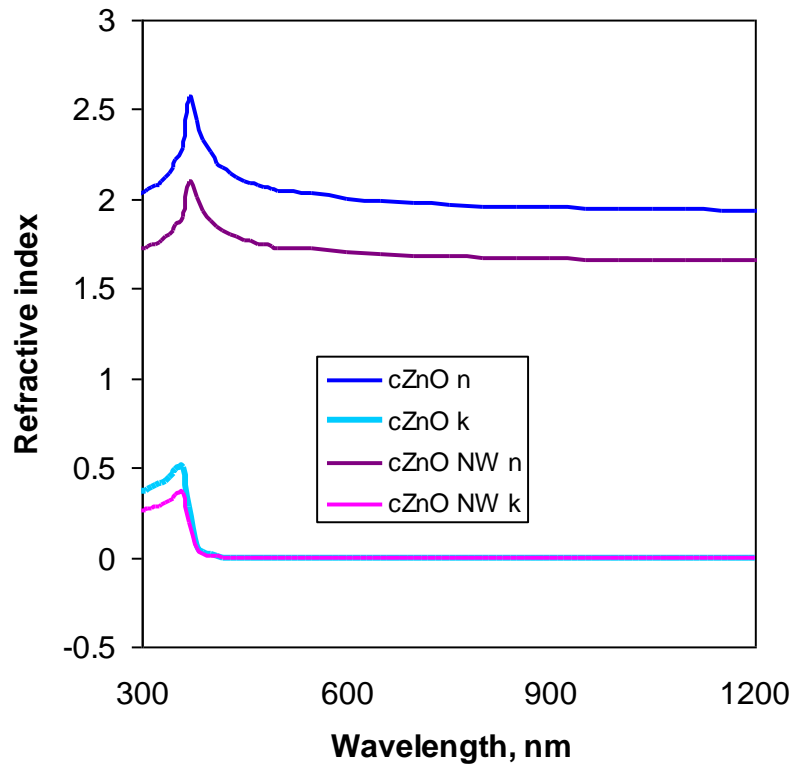


Figure 6.5 Refractive index (n) and extinction coefficient (k) curve of crystal ZnO and ZnO nanowires

Table 6.1 Sunrays simulation parameters for determining optical loss in air

	Ambient	Air
Texturing	Structure	Upright pyramid
	Width	5 μ m
	Depth	3.535 μ m
Material	Front	Air (n=1)
	Encapsulant	Air (n=1)
	Texture	Silicon
	Substrate	Silicon
	Back	Aluminum
Antireflection coating	Front/Encapsulant	Air
	Encapsulant/Texture	ZnO NW, SiO ₂
	Back Surface Reflector	Aluminum
Illumination		Normal
Spectrum		AM1.5G (1000 W/m ²)
	Polarization	Unpolarized

Initial simulations showed strong interference fringes in the simulated reflectance curves (Figure 6.6), which is similar to what have been reported using RCWA simulations.[184] The SEM cross-section images (Figure 6.2c) indicated that the length of most NWs varied +/- 75 nm from the average NW length (h). Therefore, for each NW length that was simulated, three reflectance spectra (h, h-75nm, and h+75nm) were

generated and averaged. The resulting reflectance spectrum shows an almost complete suppression of the interference fringe (Figure 6.6).

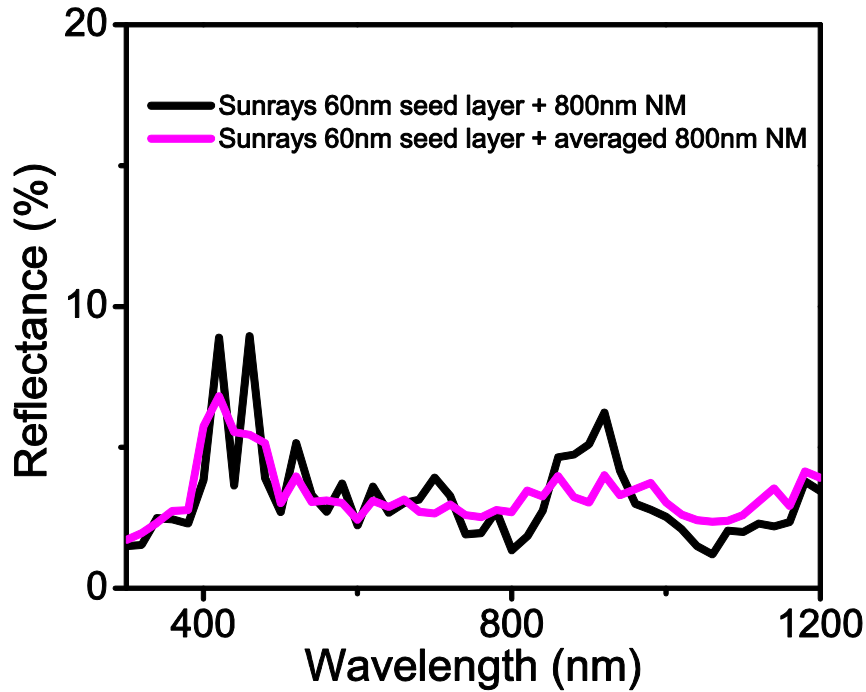


Figure 6.6 Light reflectance of ZnO NW solar cell with different ZnO NW lengths

In order to optimize the light reflection of ZnO NW solar cell, we modified the ZnO NW parameters in Sunrays1.3, including the thickness of seed layer and the length of ZnO NWs (Figure 6.7). The simulation results are listed in Table 6.2 and Table 6.3. When optimizing the seed layer in the 20-100 nm range with a constant ZnO NW length of 800 nm, the weighted reflectance has a minimum of 3.3% for a thickness of the seed layer of 60 nm,. For the NW length optimization in the 200-1500nm range with a constant seed layer thickness of 60nm, the same minimal value of 3.3% is obtained for a length of 800nm. Under air mass (AM) 1.5, it is desirable to fully utilize the visible light region while still maintaining the low reflection in UV and IR region. Therefore, the NW length of ~ 800 nm with a seed layer of 60 nm was chosen, and the resulting reflectance curve with a WR of 3.3% matches very well with the experimental reflectance spectra

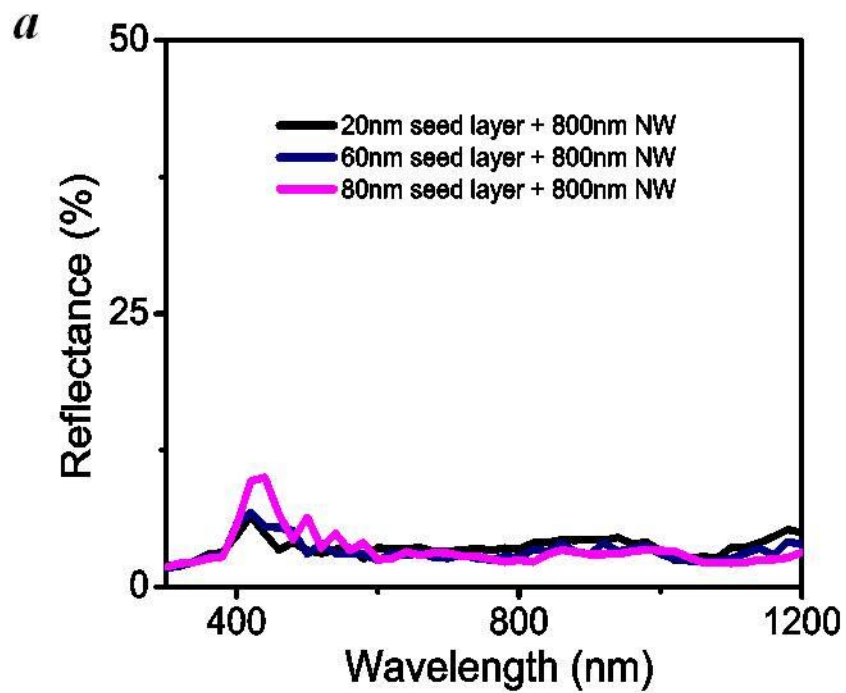
(Figure 6.3b). Sunrays 1.3 also calculates the open circuit current J_{sc} under the AM1.5 spectrum assuming a cell with 100% internal quantum efficiency. For pyramid solar cells with thin SiO_2 passivation layer only, J_{sc} was 38.18 mA/cm^2 . The additional ZnO ARC layer (60nm ZnO seed layer and 800nm ZnO NWs) results in a J_{sc} enhancement of 7.0%, which was 40.86 mA/cm^2 . In addition, Sunrays 1.3 simulation shows that ZnO NWs on textured surface enable a significantly lower light reflectance than ZnO NWs on planar surfaces with the same ZnO NW dimensions (length and thickness of seed layer, Figure 2b). This further confirms the effect of Si surface texturing in reflection suppression, as we discussed before.

Table 6.2 Effect of ZnO seed layer thickness variation on average weight reflectance (AWR) values

SiO2 thickness (nm)	ZnO Seed layer thickness (nm)	ZnO NW length (nm)	AWR (%)
15	20	800	4.39
15	40	800	3.74
15	60	800	3.36
15	80	800	3.54
15	100	800	3.75

Table 6.3 Effect of ZnO nanowire length variation on AWR values

SiO ₂ thickness (nm)	ZnO Seed layer thickness (nm)	ZnO NW length (nm)	AWR (%)
15	60	200	4.41
15	60	500	3.52
15	60	800	3.36
15	60	1100	3.62
15	60	1500	3.73



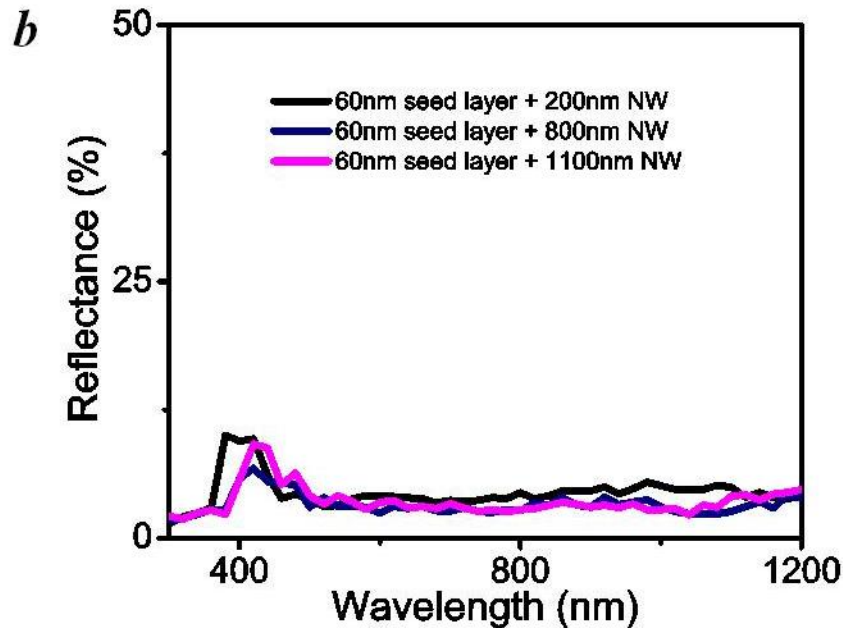


Figure 6.7 Light reflectance of ZnO NW solar cell with different ZnO seed layer thicknesses (a) and different ZnO NW lengths (b)

6.3.3 Hybridizing ZnO NWs and micropylramids for solar cells

To prove the applicability of the ZnO NWs as an antireflection coating for industrially processed Si solar cells, we fabricated screen-printed Al-back surface field (Al-BSF) solar cells with the optimized ARC parameters. The thermal stability and mechanical robustness of the ARC is an important characteristic as the screen-printed cells must survive under the pressure of the printing process from the screen and a short contact firing cycle at 700-800 °C. The difference in the WR of the ZnO NW ARC before and after screen printing is smaller than 0.1%, since only some of the ZnO NWs on pyramid peaks were destroyed and most of the side wall NWs all remained (Figure 6.8). For the screen printed n^+ -p- p^+ solar cell (Figure 6.1), ZnO NWs act as anti-reflection layer, and SiO_2 helps to improve the front surface passivation. The advantages of using the ZnO nanowire array with a conventional cell structure are: 1) Rapid application to an industrially proven solar cell structure. 2) A mature platform which will facilitate rapid

optimization and characterization of the reflection/light-trapping properties of the nanowire arrays. The cell performance was characterized by I-V curve under AM 1.5 illumination condition (Figure 6.9). The hierarchical ZnO NW/pyramidal Si solar cell exhibits a conversion efficiency of up to 16.0% with open circuit voltage of 616.3 mV, short circuit current of 35.3 mA/cm² and fill factor of 73.4%. This is a high efficiency ZnO nanostructure based solar cell, and is comparable to the commercial SiN-coated solar cells. The cells fabricated for this work used commercial Ag pastes that were formulated to provide an ohmic contact to n⁺-Si after etching through the industry standard SiN ARC – a process known as ‘fire-through’. However, the ZnO NWs were found to be much more resistant to etching than SiN resulting in either: 1) little to no contact between Ag and Si or 2) partial junction shunting if the firing temperature was increased to increase the etch rate and ensure complete etching of the NWs. The latter method provided the best contacts but is also responsible for the modest fill factors achieved on our best cells. Therefore, we believe that the efficiency of our solar cells can be further improved by increasing the fill factor through the use of an Ag paste formulated for nanostructures and optimized firing temperature.

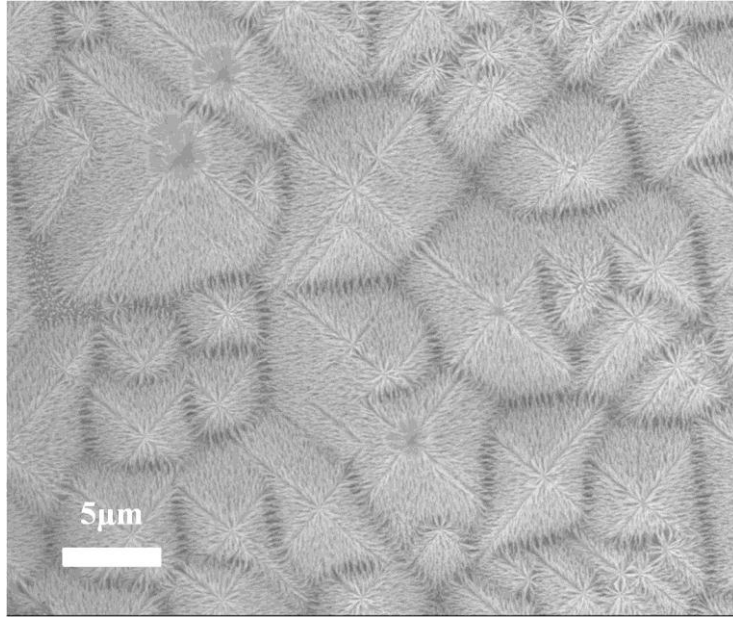


Figure 6.8 Hierarchical ZnO NWs after screen printing process showing that only the NWs on some of the pyramid tips were destroyed by the process.

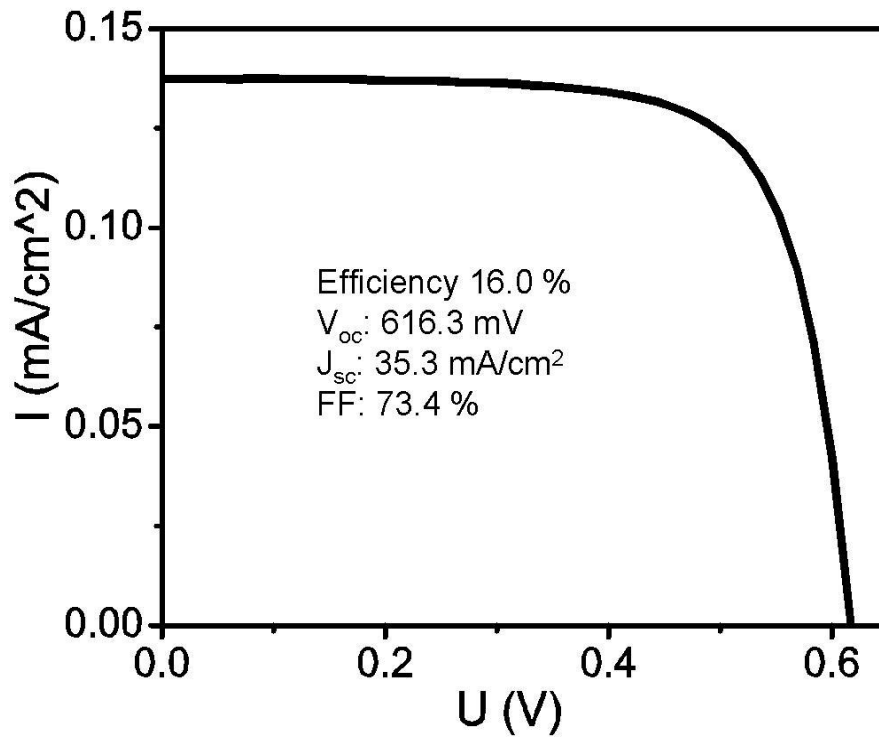


Figure 6.9 I-V curve of ZnO NW/pyramidal Si screen printed solar cell

6.3.4 Self-cleaning solar cells

For solar cells, shading is an important practical issue for light absorption, because the dust accumulation on the panel surface blocks the incident light and reduces the power output. In order to reduce dust accumulation on the solar cell surface, self-cleaning function was applied to the solar cell by surface functionalization of the hierarchical structure. Self-cleaning surface shows a water contact angle larger than 150° with a hysteresis smaller than 10° . [83, 96, 117] To fabricate the self-cleaning surface, low surface energy and surface texturing are necessary. It is well-known that the surface free energies of the various crystallographic planes differ significantly. The Wurtzite structured ZnO grows fastest along the *c* axis, and thus exposes the relatively low energy side surfaces. Therefore, the hierarchical structure presented in this study amplifies hydrophobicity due to the air trapped in between the individual NWs. The initially prepared structure showed both high surface roughness and relatively low surface energy, with a high water contact angle of $162^\circ \pm 2^\circ$ and a contact angle hysteresis of 18° . After hydrophobic coating with perfluorooctyl trichlorosilane (PFOS) and 80°C thermal treatment for 1 hr, the surface energy was further reduced and self-cleaning surface was obtained, with a contact angle of 171° and a hysteresis of 1.9° (Figure 6.10a). As shown in Figure 6.10b, the self-cleaning surfaces can effectively prevent the dust accumulation on the solar cell surface and will help maintain the high power output performance of devices. [68]

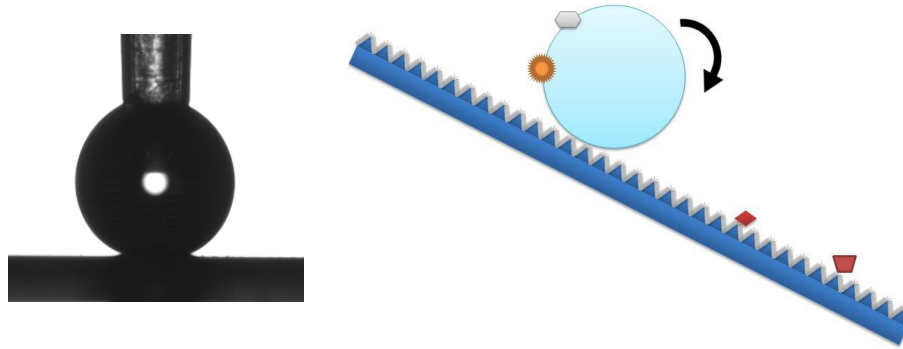


Figure 6.10 Self-cleaning superhydrophobic ZnO nanowire solar cell (a) water droplet on self-cleaning surface with a contact angle of 171° (b) schematic view of the self-cleaning property.

6.4 Conclusions

In summary, we have demonstrated a superhydrophobic high efficiency solar cell based on ZnO nanowires decorated on Si micropyramids as antireflection coating. The ZnO nanowires provide effective antireflection with a weighed reflectance of 3.2% over the 300-1200 nm spectral range. A screen printed solar cell based on this hierarchical structure shows a high conversion efficiency of 16.0 %. The structure showed good mechanical robustness after screen printing process. Moreover, the functionalized hierarchical surface enables superhydrophobic and self cleaning properties of the solar cell.

CHAPTER 7

HIERARCHICAL ROBUST TEXTURED STRUCTURES FOR LARGE SCALE SELF-CLEANING BLACK SILICON SOLAR CELLS

We explored hierarchically textured Si for large scale, low reflection, and self-cleaning solar cells. The hierarchically textured Si was fabricated from micropylramids with additional nanostructures generated by Au-assisted chemical etching. Such structure allows a gradient effective refractive index from air to Si and leads to a black appearance, which displays a broadband reflection suppression in the 300-1200 nm range. A front average weighted reflectance of 1.4% was achieved, which is one of the lowest values of reported black Si solar cells. The effect of micro and nano scale roughness on light reflection suppression is studied. A cost effective screen printed solar cell was fabricated based on this hierarchical structure. A conversion efficiency of 8.1% was obtained, and it was further improved to 16.5% (under improvement) after Al₂O₃ and SiN passivation. In addition, surface modification enables a self-cleaning property that will prevent the blocking of light by dust particles on solar panels.

7.1 Introduction

Si solar cells have been dominating the current high efficiency solar power industry.[190] Optical loss, which attributes to the reflection loss of the incoming light, is one of the primary factors that hinder the further increasing of photovoltaic conversion

efficiency.[191] Many efforts have been made to reduce the optical loss, among which antireflection coatings and surface texturing are the most commonly used strategies. Antireflection coating (ARC) can reduce the light reflectance via destructive interference of the reflected light at the air–ARC–substrate interfaces.[192] Single-layer ARC such as silicon nitride (SiN) is the industry standard ARC on Si PVs.[193] Further reduction of reflection can be achieved through a multi-layer ARC, or a fine control of ARC geometry, which enable a gradual transition of the refraction index from air to Si.[176, 194] Surface texturing is another way to enhance the light trapping by multiplying the internal reflections.[195] The industrial standard for the current Si-based PV industry process is alkaline fabrication of pyramid textures. An emerging focus today is the incorporation of nanostructures as surface texturing materials.[171, 196] For example, nano textured black silicon has attracted more and more attention. Such surface structure has the dimension of smaller than the wavelength of incident light, and showed gradually varied refractive index.[197-199] Therefore it gives prominent light trapping and reflection reduction features. For example, good optical and electrical properties have been reported on single and multi crystalline nano textured black Si solar cells.

Many approaches have been reported for surface texturing of black Si, including wet etching, laser ablation,[200-201] and plasma etching of silicon pillars.[165, 202] Metal-assisted etching of Si surfaces has been employed to define specific structures on silicon surfaces.[36, 203] After deposition of a thin layer of a metal such as Au, Pt, or Pt/Pd onto p- or n-type silicon surfaces, nanostructures can be formed by immersing this substrate into various mixtures of hydrofluoric acid/oxidant/solvent. In our study, even

lower light reflection can be achieved by a hierarchical structure through a micro-nano scale texturing method.

In the practical application of solar cells, shading is an important practical issue for light absorption, because the dust accumulation on the panel surface blocks the incident light and reduces the power output.[69, 139, 142, 204] Therefore, self-cleaning function was applied to the solar cell by surface functionalization of the hierarchical structure, in order to reduce dust accumulation on the solar cell surface.

7.2 Experimental

7.2.1 Hierarchical Si etching:

p-Type silicon (100) wafers with the largest pyramid size of 5 μ m, 20 μ m and 25 μ m were used in all experiments. KOH etching was performed in a solution of KOH (2-3 wt %), water, and isopropyl alcohol (20 vol%). At 80-85 °C for 20-30 min to create pyramidal structures (2-4 μ m in height). To form nanostructures, a thin discontinuous layer of Au nanoparticles (2, 5 and 10 nm diameter) was deposited by electron-beam evaporation to form different nano structure size. Etching was then performed for various times in a HF/H₂O₂ solution (49% HF, 30% H₂O₂, and H₂O with a volume ratio of 1:5:10). Subsequently, the Au nanoparticles were removed by immersing the samples in KI/I₂ (100 g of KI and 25 g of I₂ per 1 L of H₂O) for 60 s.

7.2.2 Superhydrophobic coating:

After fabrication of the surface structures, surface fluorination was performed by treatment with PFOS. Typically, a 3 mM solution of PFOS in hexane was used for these treatments. Specifically, the etched silicon wafer was immersed in the solution for 30 min

followed by a heat treatment at 150 °C in air for 1 h to complete the hydrophobic surface modification.

7.2.3 Solar cell fabrication:

The Si substrate used is a single-crystal, p-type float zone substrate with a thickness of 300 µm. The textured Si surface with pyramidal structures was created by KOH etching. The metal assisted chemical etching was carried out to further generate nano texturing on micro pyramids. The wafers were then cleaned to remove surface organic and metallic contaminants, followed by POCl₃ diffusion to form the n⁺-emitter. Tystar Nitride Furnace was used for obtaining 65 Ω/sq emitter. After the phosphorus-glass removal in a buffered HF solution. First, an Al paste was screen-printed on the backside of the Si substrate and dried at 200 °C. Ag grids were then screen-printed on top of the hierarchical Si, followed by co-firing of both the Ag and Al contacts. Al₂O₃ and SiN passivation layers were coated by atomic layer deposition (Cambridge NanoTech Plasma ALD) and plasma enhanced chemical vapor deposition (Unaxis PECVD) respectively. During the firing step, an Al-doped Si layer, referred to as the aluminum back surface field, is also formed. To prevent erroneous measurements, the active area of the cells was defined using a dicing saw, which electrically isolates each cell from the rest of the substrate.

7.2.4 Characterizations:

Contact angle measurements were performed with a Rame-Hart goniometer that has a CCD camera equipped for image capture. SEM was used to investigate the surface morphology. The light reflectance was tested using a commercially available Optronic Laboratories OL 750 spectrophotometer with an integrating sphere at the University

Center of Excellence for Photovoltaics Research and Education (UCEP) at the Georgia Institute of Technology. The solar-cell efficiency was measured using an I-V tester, which was calibrated using a calibration standard cell, measured at the National Renewable Energy Laboratory (NREL). The calibration was performed before each measurement.

7.3 Results and Discussion

7.3.1 Fabricated hierarchical structure by MACE

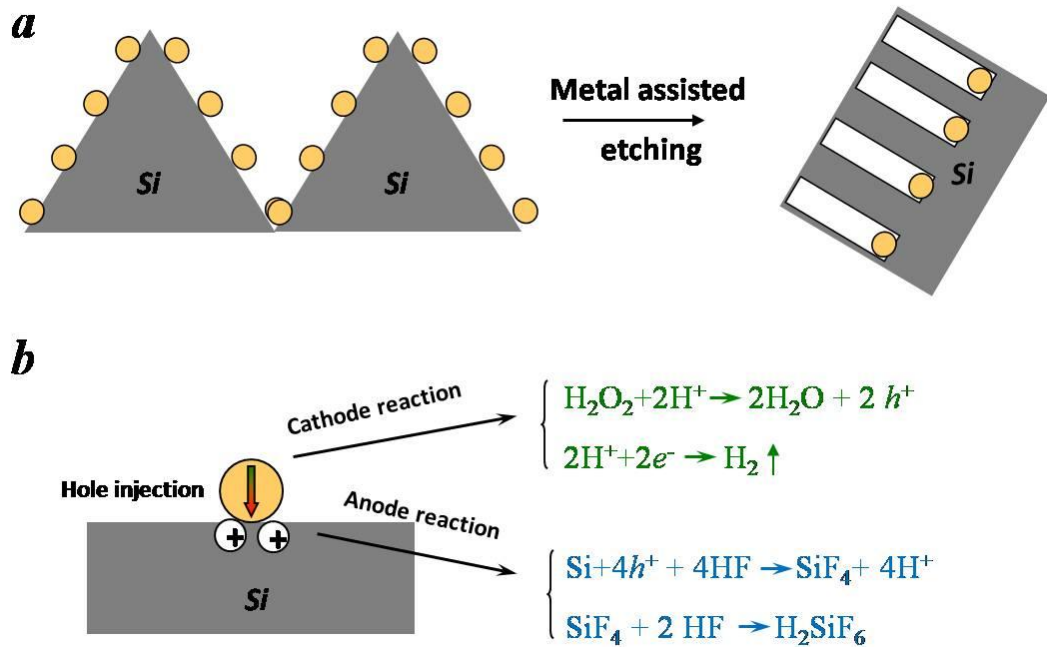


Figure 7.1 The (a) schematic and (b) mechanism of metal assisted chemical etching

In our study, we employed metal-assisted chemical etching to generate nano scale roughness on Si micro pyramids to form hierarchical structures. The mechanism of MAE is shown in Figure 7.1. Due to the presence of Au nanoparticles, electroless etching occurs at the Au/Si contact interface, which is composed of cathode reduction and anode oxidation. H_2O_2 decomposition causes injection of holes into the silicon surface, and

etching by HF proceeds in the vicinity of the Au/Si contact. As a result, pits or nanostructures are formed on the micro pyramid surface.

The weighted reflectance (WR) was calculated from the hemispherical reflectance spectrum (300-1200 nm) measured in our study. Figure 7.2a compares the measured front reflectance of bare planar Si surface, and Si pyramid surfaces without and with nano texturing on top. Bare planar Si reflects about 34.8% of incident sunlight. Textured pyramid surfaces improve the light trapping by doubling the bounces of incident light, and reduce the light reflection to 11.2%. The nano scale roughness on Si micropyramids results in a significant reduction of light reflection in all UV, visible light, and IR regions. A WR suppression of as low as 1.4 % is achieved for the hierarchical structure. The RI gradient on hierarchical structure plays an important role in suppressing the light reflection. According to effective medium approximation, an effective refractive index can be calculated by averaging the refractive indices of air and Si weighted by volume fraction at the interface between air and Si. The benefit of RI gradient has been observed in our previous results about hybridized ZnO nanowires on silicon micron pyramids. The enhanced WR suppression of the hierarchal structure is attributed to the effect of micro scale texturing that allows two bounces of light at the surface, and a more gradually changing effective refractive index of nano structures from air to the Si substrate compared to a single SiN ARC (Figure 7.2b).

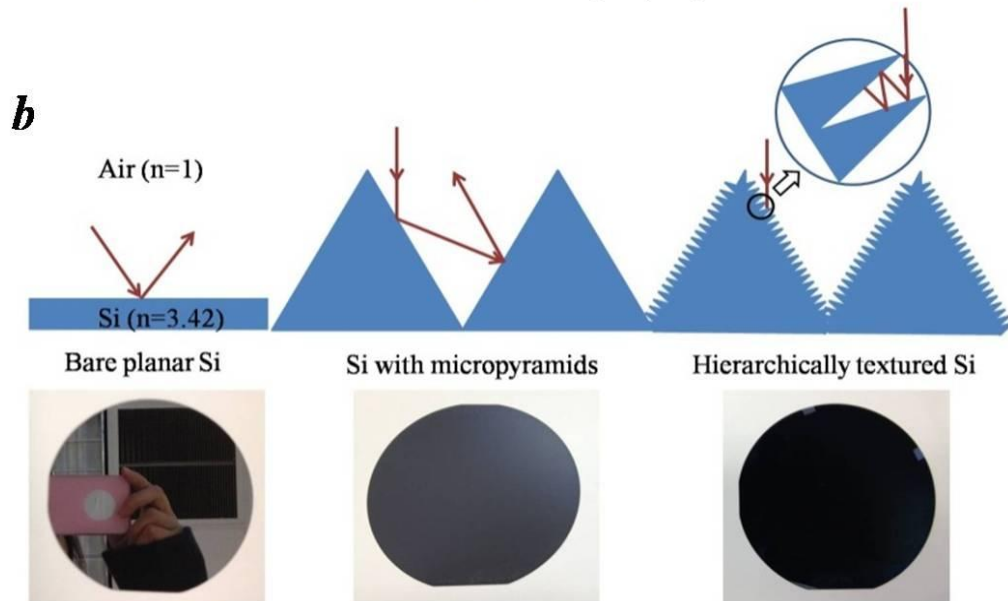
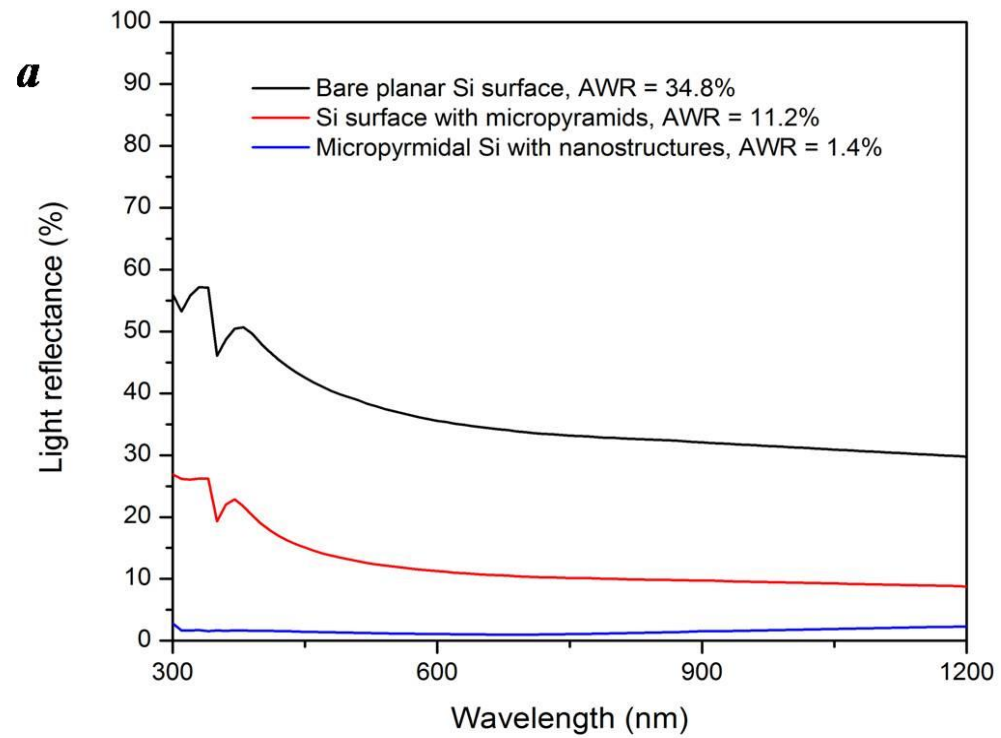


Figure 7.2 (a) Front light reflectance of micropyramidal Si with nanotexturing, compared with planar Si and pyramidal Si. (b) The reflection of incident light on a bare smooth Si, Si micro pyramids and hierarchically textured Si wafer. The images showing the difference in light reflection on three wafers.

7.3.2 Effect of micro/nano-structure on light reflectance

In order to better understand the micro/nano size effect on light reflection suppression. We fabricated different micro and nano size hierarchical Si structures. Different micro scale texturing sizes (5 μm , 20 μm and 25 μm) were prepared by modifying KOH solution concentration. The surface morphologies are shown in Figure 7.3. The light reflection results (Figure 7.4a and Table 7.1) showed that 25 μm pyramid samples have higher reflectance than the 20 μm and 5 μm pyramid samples, which is mainly due to the untextured spots or incomplete texturing between the large size pyramids. After metal-assisted etching under the same conditions, the two scale roughness silicon wafers with different micro size pyramids showed similar light reflectance, which is significantly lower than micro size pyramid silicon in the whole spectrum. The presence of surface nanostructures allows multiply bounces of incident light and reduces the reflection. Therefore, different micro size texturing didn't have a significant effect on the light reflectance of two tier roughness Si.

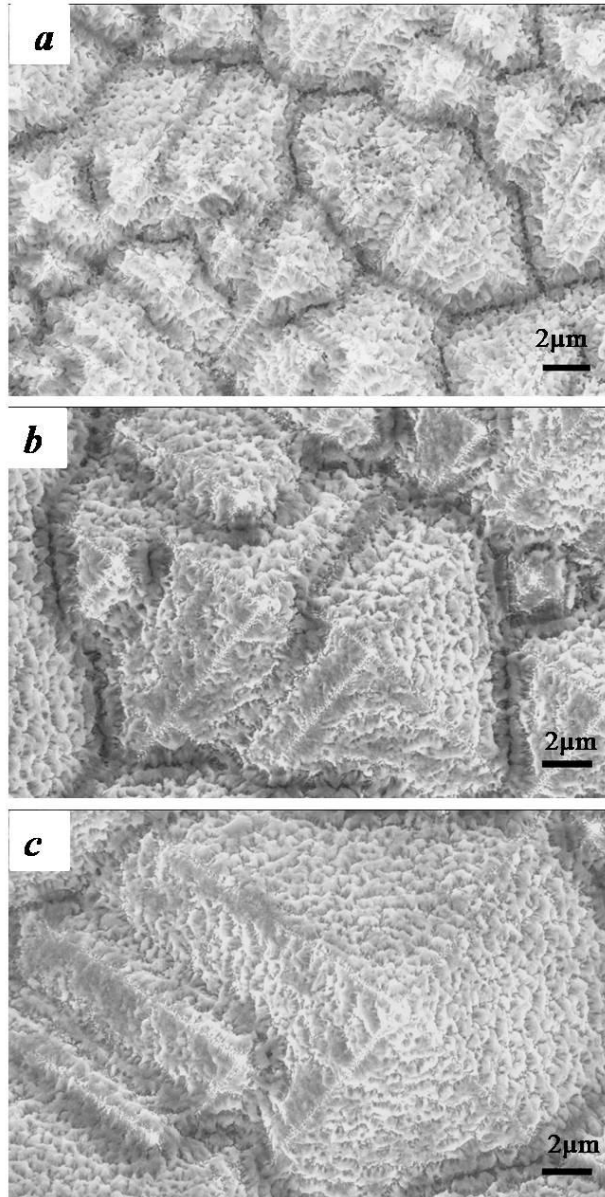


Figure 7.3 SEM images of hierarchical textured Si wafers with different micro pyramid sizes (a) pyramid size 5 μm (b) 20 μm (c) 25 μm . The nano texturing was generated by Au-assisted chemical etching for 4 min

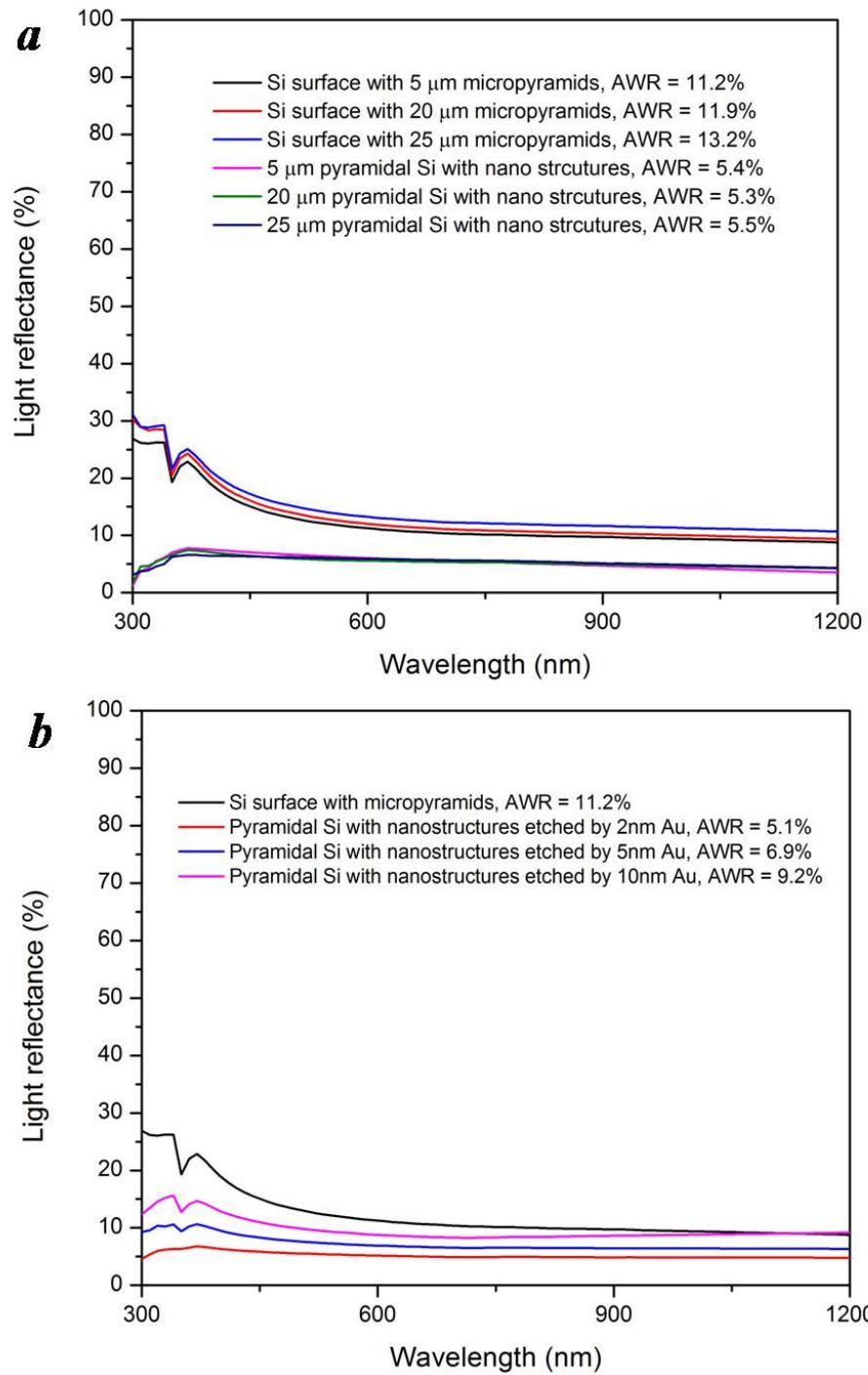


Figure 7.4 Front light reflectance comparison of micropyramidal Si and hierarchical structure Si etched by Au-assisted chemical etching (a) Effect of different micro size pyramids (b) Effect of different nano size texturing

Table 7.1 Weighted reflectance on different textured surfaces

Sample	Weighted reflectance %
5 μm pyramidal Si	15.6 %
20 μm pyramidal Si	16.0 %
25 μm pyramidal Si	17.1 %
5 μm pyramidal Si with nano texturing	10.1 %
20 μm pyramidal Si with nano texturing	9.1 %
25 μm pyramidal Si with nano texturing	9.5 %

7.3.3 Effect of nanostructure size on light reflectance

Different size nano scale roughness was fabricated by modifying the metal layer thickness in metal assisted chemical etching. We prepared Au layers of three different thicknesses on silicon surfaces: 2 nm, 5 nm and 10 nm as shown in Figure 7.5a-c. The distance between metal catalyst particles strongly influences the morphology of the etched structures. When the particle density becomes higher, smaller nanostructures were obtained. The effect of the Au layer thickness on etching morphologies is shown in Figure 7.5 d-f. As the Au layer thickness increases, the etched nanostructures decrease in roughness. Correspondingly, the light reflectance increases (Figure 7.4b and Table 7.2). This is mainly due to less bounces of light within smaller nano structures. It is found that

nano scale roughness has a significant effect on light reflection and larger nano scale roughness will lead to less light reflection.

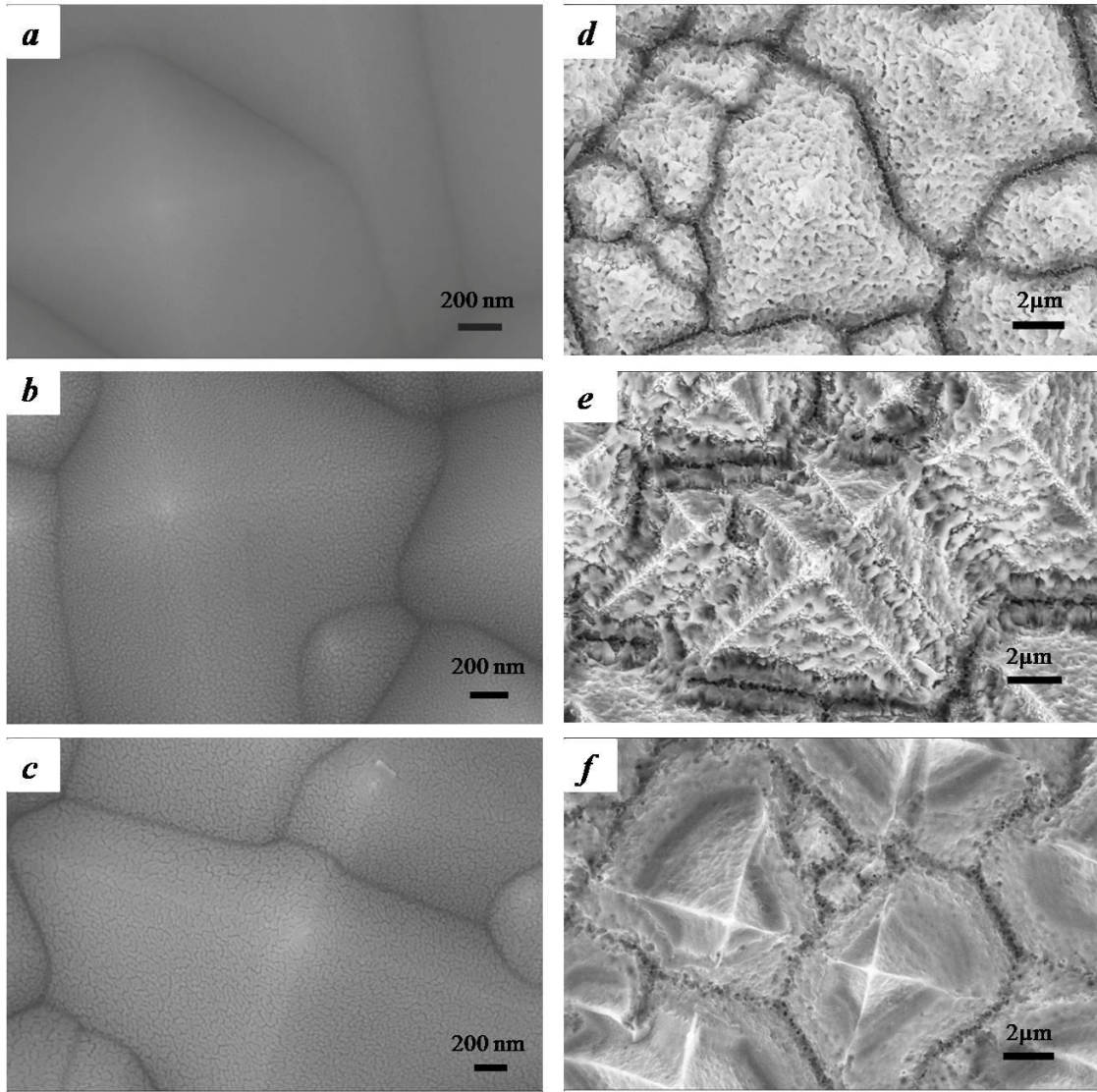


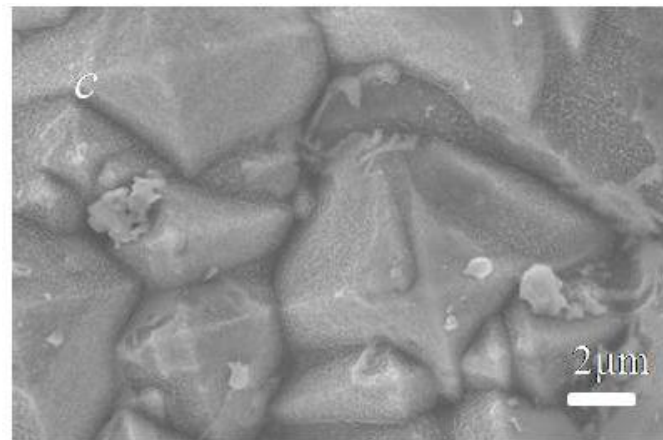
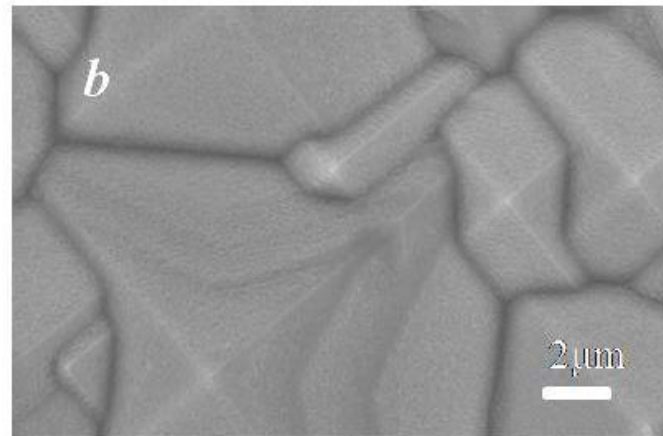
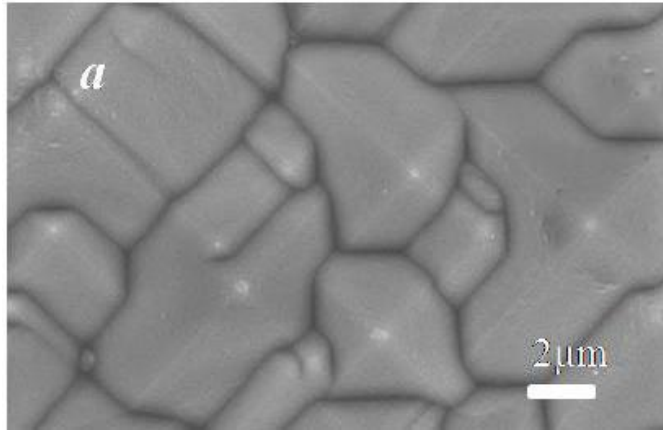
Figure 7.5 (a-c) Silicon pyramid surface with Au layers of thickness of, 2 nm, 5 nm and 10 nm respectively (d-f) SEM images of hierarchical textured Si wafers with different nano texturing sizes (d) 2nm Au (e) 5 nm Au (f) 10 nm Au. The nano texturing was generated by Au-assisted chemical etching for 4 min.

Table 7.2 Weighted reflectance on different textured surfaces

Sample	Weighted reflectance %
20 μm pyramidal Si	16 %
Two tier roughness structure etched on 2 nm Au film	8.7 %
Two tier roughness structure etched on 5 nm Au film	10.4 %
Two tier roughness structure etched on 10 nm Au film	12.8 %

7.3.4 Superhydrophobic black Si

After metal-assisted chemical etching process, hydrophobic coating was applied in order to produce superhydrophobic surface. SEM micrographs of etched silicon surfaces with different etching times are shown in Figure 7.6. Evaluation of silicon surface superhydrophobicity was made by considering both the contact angle and the contact angle hysteresis. (Figure 7.7) The nanotexturing helps reduce the hysteresis due to the generation of nanoscale roughness superimposed on the microscale roughness. All the samples showed high water contact angle ($>150^\circ$), and when the etching time was more than 4 min, a relative low contact angle hysteresis (around 1.5°) was obtained due to the increased nanoscale roughness on micro pyramids.



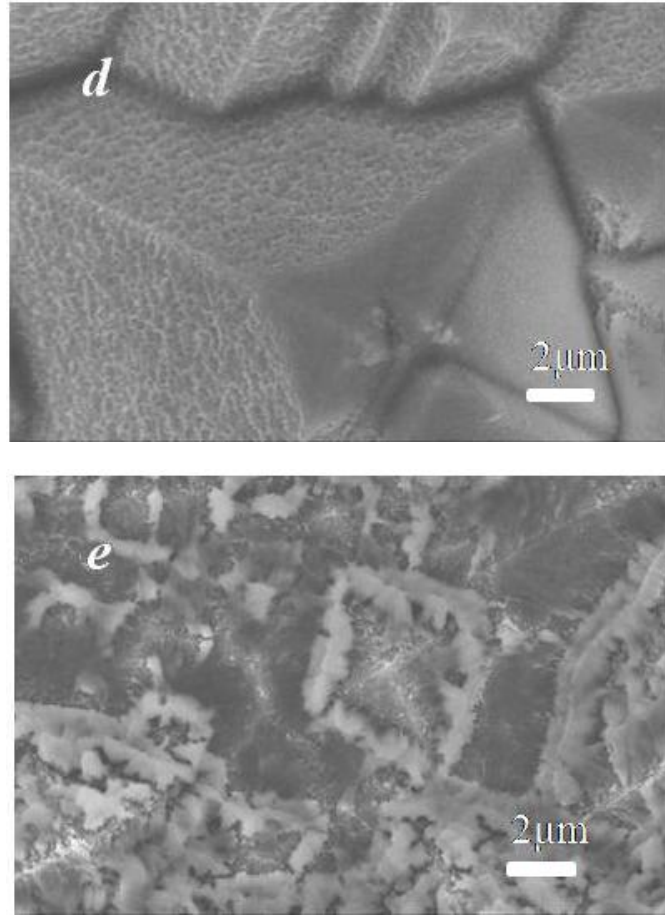


Figure 7.6 Silicon two scale rough surfaces of different magnifications resulting from pyramid size $20\ \mu\text{m}$ + nanostructure from Au-assisted HF/H₂O₂ etching for different time (a) 30s, (b) 1 min, (c) 2 min, (d) 4 min, (e) 10 min

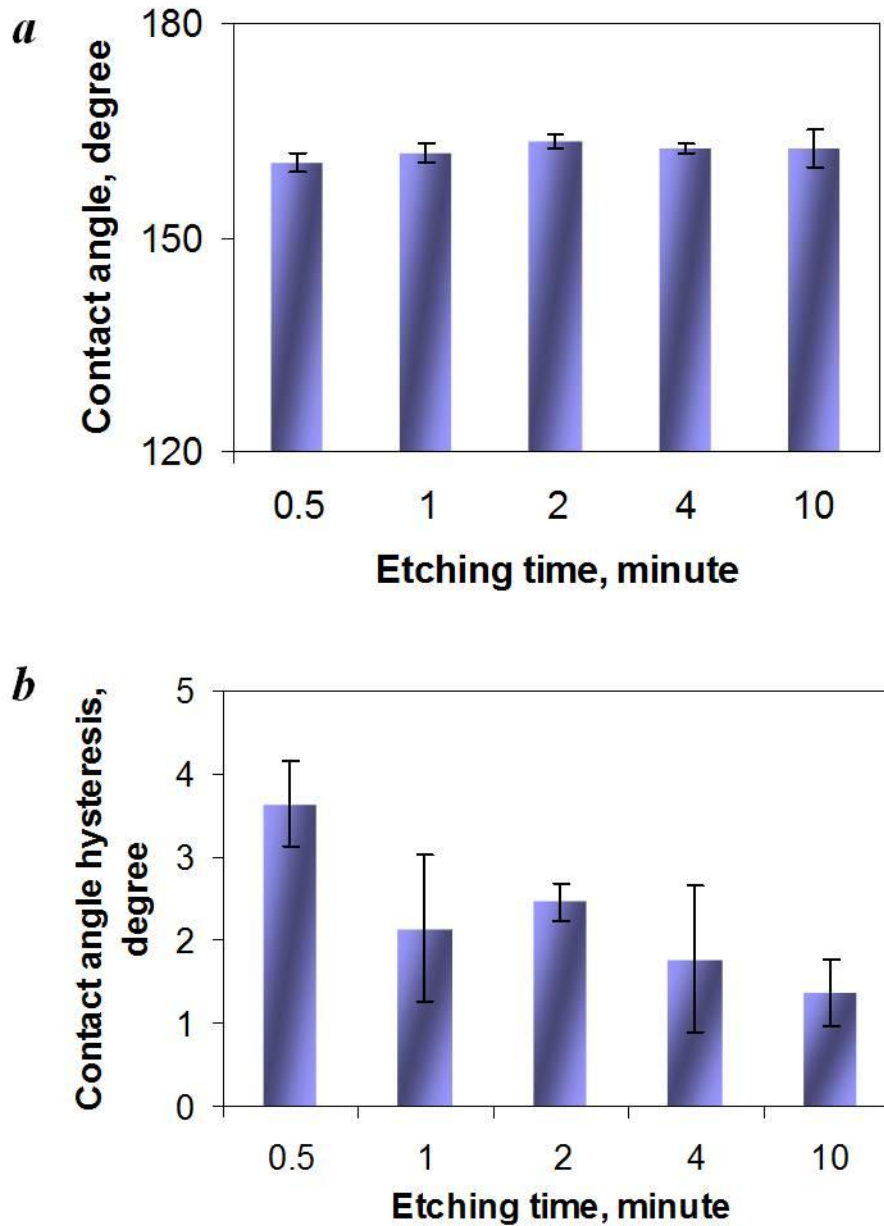


Figure 7.7 (a) Contact angle and (b) contact angle hysteresis on Si (100) surface with 20 μm pyramid size, etched by Au assisted etching in HF/H₂O₂/H₂O (v/v/v 1:5:10) for different time at room temperature

7.3.5 Fabricated self-cleaning hierarchical black Si solar cells

We fabricated screen-printed Al-back surface field (Al-BSF) solar cells with hierarchical Si structure, as shown in Figure 7.8. The Al-BSF provides the back surface

passivation. The cell performance was characterized by I-V curve under AM 1.5 illumination condition. The hierarchical Si solar cell exhibits a conversion efficiency of up to 8.1% with open circuit voltage of 561.8 mV, short circuit current of 28.6 mA/cm² and fill factor of 46.2%.

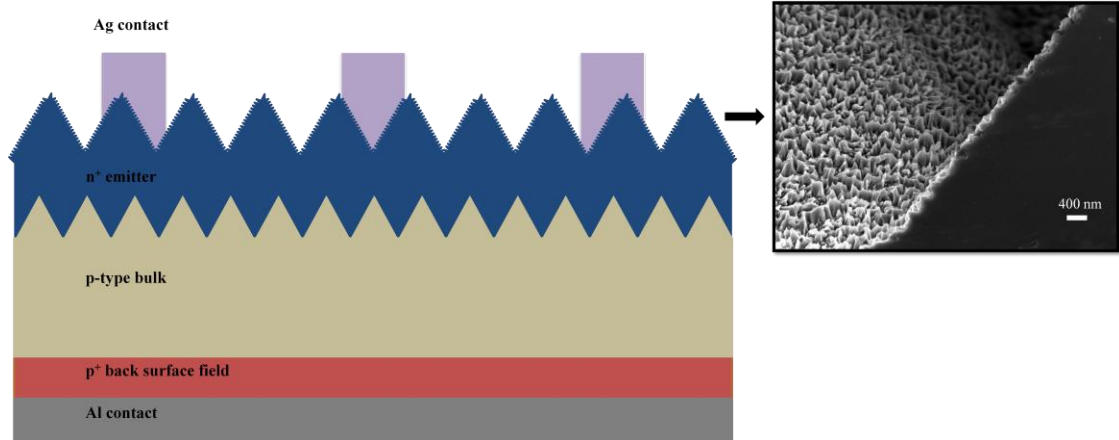


Figure 7.8 Schematic of screen printed hierarchical black Si solar cells. The inset is the cross section of hierarchical Si with surface passivation layers

For black Si solar cells, one important issue is surface passivation, because high surface area nanostructures tends to have low charge carrier lifetime and high surface recombination velocity, causing adverse effect on solar cell efficiency.[205] Commonly used passivation layers include SiN, SiO₂, and amorphous Si etc. Low temperature passivation such as Al₂O₃ has been recently developed.[206] Thin Al₂O₃ layer can form an effective chemical passivation by hydrogenation and coordination between Si and O at the interface. It has been reported that atomic layer deposition of Al₂O₃ can form a conformal layer on nano texturing. In our study, two passivation layers Al₂O₃ and SiN were deposited. Figure 7.8 inset shows the surface morphologies of the etched hierarchical Si with surface passivation layers. The nanoscale pits is on top of the microscale pyramidal Si. The cross section view show the etching depth is around 130

nm after 1 min etching. The lateral width of nano structure is around 200 nm. After surface passivation, the efficiency of black Si solar cell increased to 16.5%, with an open-circuit voltage of 621mV, a short-circuit current of 33.1mA/cm², and a filler factor of 80.2%.

In order to reduce the dust accumulation on the solar cell surface, self-cleaning function was applied to the solar cell by surface functionalization of the hierarchical structure. The pyramid Si surfaces show a contact angle of ~140° after hydrophobization with PFOS. The nanostructure on top of the pyramid surfaces is critical to achieve both a high contact angle and low hysteresis. Surface treatment with PFOS hydrophobize the surface and yields a high contact angle of 160° and low hysteresis of 1.2°. The existence of the two roughness scales resulted in a roll-off self-cleaning surface due to the reduced liquid contact area fraction.

7.4 Conclusions

Hierarchical textured silicon with micropyramids and nanostructures was fabricated by low cost wet chemical methods. A gradient effective refractive index from air to silicon leads to black appearance and low reflection of 1.4%. It was found that nanostructures on top of micropyramids play an important role in reflection suppression and achieving superhydrophobicity. Such structure is explored for large scale, low reflection, and self-cleaning solar cells. A conversion efficiency of 16.5% was achieved after Al₂O₃ and SiN passivation.

CHAPTER 8

HIGH REFRACTIVE INDEX AND TRANSPARENT NANAOCOMPOSITES AS ENCAPSULANT FOR HIGH BRIGHTNESS LED PACKAGING

For current LED packaging technology, one of the major limitations is the low light extraction efficiency, due to the refractive index (RI) difference between LED chip and air. Encapsulants such as epoxy and silicone are usually added to reduce the RI contrast and enlarge the light escape cone. But the RI of epoxy or silicone is usually limited to 1.45 to 1.55. High RI particles can be added to help increase the RI of encapsulant. The particle size should be controlled smaller than one tenth of the visible light wavelength (400-800nm), in order to reduce Rayleigh scattering and increase the transmittance of encapsulant effectively. In this study, we prepared TiO₂ silicone nanocomposites as LED encapsulant. Vinyl silane was employed to improve the dispersion of nanoparticles in polymer matrix. The RI of nanocomposites increased from 1.54 to 1.61 at 589 nm wavelength with 5 wt% filler loading while maintaining high relative transmittance of 84%. The nanocomposites showed stable high RI and transmittance after reliability test. We further investigated the effect of crystal phase, filler loading and particle size on RI and transmittance of nanocomposites.

8.1 Introduction

LED has many advantages over conventional incandescent and halogen lamps in power efficiency, lifetime and reliability.[207] For current LED packaging technology, one of the limitations is the low light extraction efficiency that is caused by the light trapping within LED chips. Since RI difference between a LED chip and air is large,

which limits the angle of light-escape cone. Moreover, the trapped light in LED may convert into heat, lower the conversion efficiency and affect the LED reliability. To improve the light extraction efficiency, a transparent encapsulant layer with a relatively high RI is desirable, which could reduce the RI contrast between chip and air, and thus improve the light extraction efficiency. It was reported that the extraction efficiency of LED will double when the RI of the encapsulant increases from 1.5 to 2.0.[208] Epoxy and silicone are usually employed as encapsulant materials. However, the RI of epoxy or silicone is limited to 1.45-1.55. Some special higher RI polymers have been developed, which contain aromatic or high π -electron structures, or organic groups like halogen, sulfur atoms.[209] However, such highly conjugated structure tends to absorb more light in the visible region. These limitations give rise to the development of higher RI nanoparticles filled polymer encapsulants.[210] The nanocomposites combine advantages of polymers (flexibility, good impact resistance, and processability) and inorganic nanoparticles (high refractive index, good chemical resistance and high thermal stability).[211]

TiO₂ nanoparticles have a high RI ($n = 2.45$ and 2.9 for anatase and rutile phase, respectively) and a very low absorption coefficient in the visible region. Therefore TiO₂ nanocomposites have been proposed as one of the promising candidates to achieve high refractive index and maintain high transparency.[212-214] One problem that appears in the nanocomposites is the aggregation of nanoparticle, which affects the physical properties of polymer matrices, such as thermal stability, modulus, toughness, etc.[215] Moreover, highly aggregated particles in transparent polymers may cause light scattering that limits their optical applications. To reduce the scattering loss of nanocomposites, many researches have been carried out using RI matching nanoparticles or introducing smaller size particle. Usually the particle size should be controlled smaller than one tenth of the visible light wavelength (400-800nm), around 20 nm, in order to reduce Rayleigh scattering and increase the transmittance of encapsulant effectively.[216] Other efforts

have also been made by using physical sonication, surface modification with organic ligands, or silane coupling agents.[217-219]

For TiO₂ based nanocomposites, “in situ” syntheses (i.e., in situ formation of nanoparticles in polymer matrix) or “ex situ” syntheses (i.e., inorganic NPs are synthesized prior to the formation of the nanocomposites) have been developed to obtain homogeneous dispersion of nanoparticles in the matrix. The in situ synthesis method results in well dispersed inorganic NPs within the polymer matrix.[220-221] However, the by-products of in-situ reaction adversely affect the properties of the composite materials. Ex situ syntheses of nanocomposites has the advantages of large scale production of NPS as well as better control of particle size and surface properties.[222] But the challenge is the compatibility and dispersion of the inorganic nanoparticles in the organic polymers.[212, 223-225] In our study, we used ex situ synthesis method for producing TiO₂ nanoparticles. Surface modification of TiO₂ nanoparticles with vinyl silane was carried out to improve the dispersion of inorganic NPs in silicone. The effect of particle size, silane treatment, and particle crystal phase on RI and transmittance of nanocomposites were investigated.

8.2 Experimental

We synthesized TiO₂ nanoparticles by hydrothermal method using hydrochloric acid (HCl) and Titanium (IV) isopropoxide (TTIP, 97%). The concentration of HCl solvents was varied, which were 0.25 M and 6 M. The 3 mL TTIP solution was added drop by drop to the HCl solvent at room temperature. The hydrothermal reaction was conducted in an autoclave at 120 °C for 6 hours. After the reaction, the precipitate was cooled to room temperature and washed by ethanol. The silicone used was OE6630 from Dow Corning. It was a high refractive index silicone with high adhesion, high purity, moisture resistance, thermal stability and optical transmittance.

The as synthesized TiO₂ nanoparticles were modified by two silanes with different vinyl chain length, which are vinyltrimethoxysilane and trimethoxy (7-octen-1-yl)silane. The solution of ethanol and water (95:5 by volume) was adjusted to pH 4.5-5.5. Silane was added with stirring to yield a 1 wt% final concentration. The mixture was heated to reflux for 24 hours. After that, the TiO₂ nanoparticles were centrifuged and rinsed twice with ethanol.

The TiO₂ nanoparticles were re-dispersed in toluene by sonication. The mixture (TiO₂ in toluene) was added into OE 6630B, and sonicated for 12 hrs. After that, the solvents were then removed in a vacuum oven at 60 °C. Then OE 6630A was added into the mixture and sonicated for 12 hrs. Finally, the nanocomposite was cured at 150 °C for 2 hrs. The reliability test of TiO₂ nanocomposites were carried out according to JEITA ED-4701 (200 203) standard. The RI and transmittance were measured after reliability test.

Powder X-ray diffraction (XRD) analysis was carried out with a Philips X-pert alpha-1 diffractometer, using Cu K_α radiation (45 kV and 40 mA). Transmission electron microscopy (TEM) images were obtained using JEOL TEM 100CX. The refractive index was measured by Woollam M2000 ellipsometer. The UV-Vis absorption and transmittance of nanocomposites were characterized by a UV-Vis spectrophotometer (DU520, Beckman, Fullerton, CA), from a wavelength of 300–900 nm.

8.3 Results and Discussion

Mont et al. reported that the calculated light-extraction efficiency increases rapidly as the refractive index of the encapsulant increases, as shown in Figure 8.1.[39] This represents the clear motivation for developing encapsulants with higher refractive indices than typical epoxy or silicones.

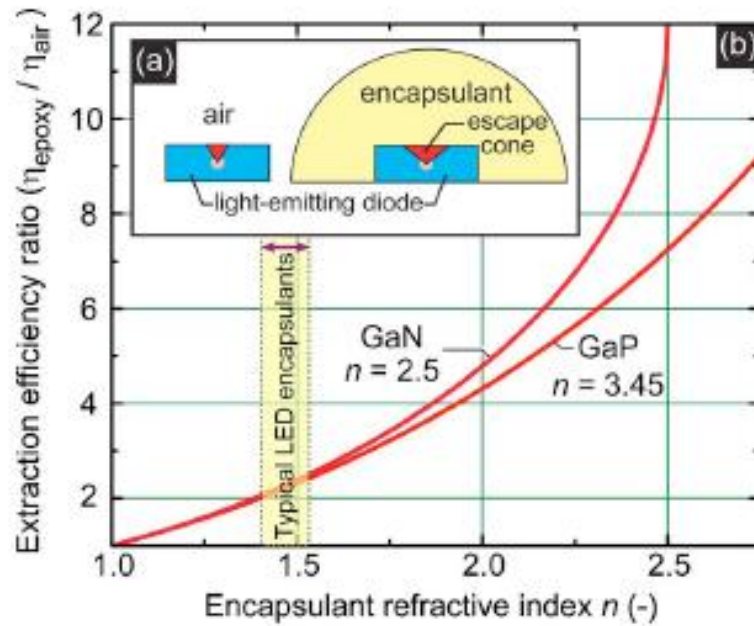


Figure 8.1 Relation of RI and light extraction efficiency[39]

The silicone OE 6630 used in our study was purchased from Dow Corning® (Table 8.1). The silicone LED (light emitting diode) encapsulants are designed to meet the challenging needs of the LED market, including high adhesion, high purity, moisture resistance, thermal stability and optical transmittance. Silicone materials can absorb stresses caused by thermal cycling inside the package, protecting the chip and the bonding wires. As the electronic industry quickly moves toward lead-free processing, silicone encapsulants, with their demonstrated, excellent stability at reflow temperatures, are a natural fit for LED applications.

Table 8.1 Properties of silicone OE 6630

Viscosity (Mixed)	2.5 Pa-sec
Heat Cure Time @ 150°C	120 minutes
Working Time at 25°C	8 hrs
Refractive Index	1.53
Impurity (Na+)	0.1 ppm
Impurity (K+)	0.2 ppm
Impurity (Cl-)	0.5 ppm

8.3.1 Crystal phase effect

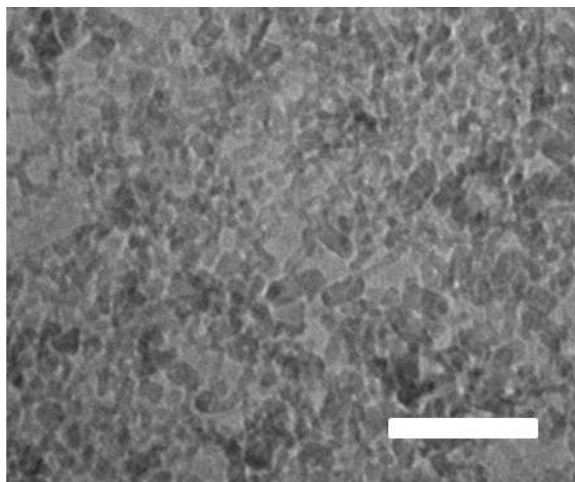


Figure 8.2 TEM images of TiO₂ nanoparticles obtained via the hydrothermal method after 6 hrs reaction (the scale bar is 25 nm)

During the formation of the TiO₂ nanoparticles, the Ti-isopropoxide serves as Ti source in the hydrothermal process. The Ti⁴⁺ ion is surrounded by OH⁻ or Cl⁻ ions in the solution, and octahedral structure is formed. When the HCl concentration is high, the number of Cl⁻ groups connect with Ti⁴⁺ increases. Therefore the deoxolation between

octahedral structures is more probable, and the corner shared bonding instead of edge shared bonding between two Ti^{4+} complex centers. As a result, rutile TiO_2 can be produced. The TEM image of TiO_2 synthesized by different HCl concentrations is shown in Figure 8.2. The TiO_2 particles have an average size of 10~15 nm. The XRD pattern of TiO_2 nanoparticles prepared by hydrothermal process was shown in Figure 8.3. The XRD patterns of rutile phase TiO_2 exhibit strong diffraction peaks at 27° , 36° and 55° , where that of anatase phase TiO_2 shows strong diffraction peaks at 25° and 48° . As shown in Figure 8.4, rutile has a primitive tetragonal unit cell. The titanium cations have a coordination number of 6. They are surrounded by an octahedron of 6 oxygen atoms. The TiO_6 octahedra are linked at the corners. Anatase has octahedrons that share four edges forming the four-fold axis. The obtained TiO_2 synthesized by 0.25M HCl showed a mixture of anatase and rutile phases. It showed rutile phase when HCl concentration is 6M. The peak positions are in good agreement with the standard pattern (JCPDS no.: 88-1175, and 84-1286). So higher concentration of hydrochloric acid is favorable for the formation of rutile TiO_2 .

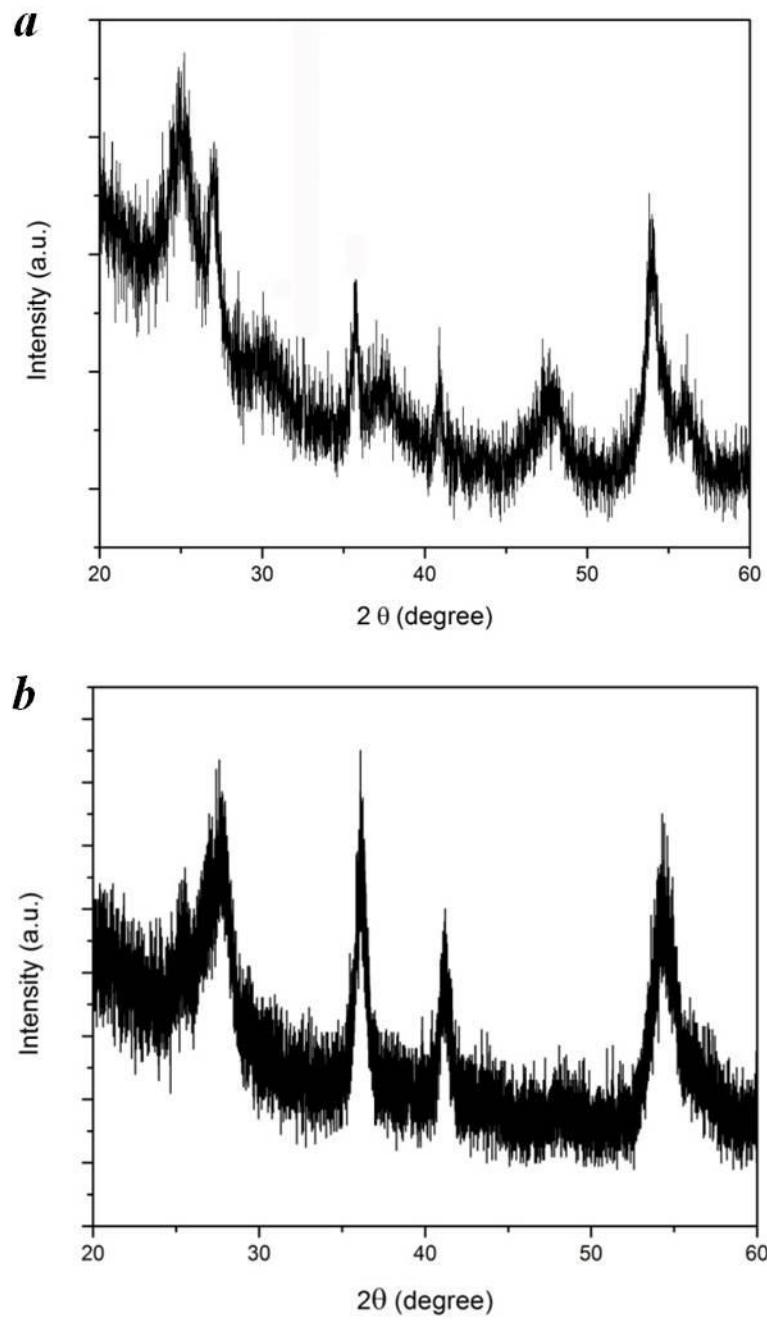


Figure 8.3 XRD patterns of TiO₂ nanoparticles prepared via hydrothermal process for 6hrs (a) 0.25 M (b) 6M HCl

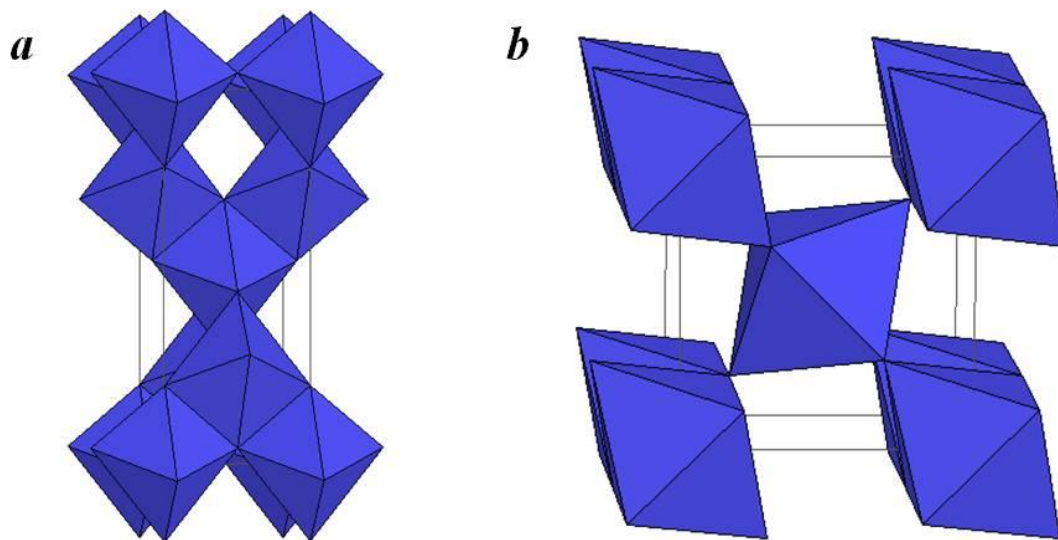


Figure 8.4 Crystal structure of TiO₂ (a) anatase (b) rutile

We measured the RI of TiO₂ nanocomposites comparing with the silicone control samples. It was found that the silicone control sample has a RI of 1.544. With the same filler loading 1 wt%, the rutile TiO₂ nanocomposite has significantly higher RI (1.559) than anatase TiO₂ composite (1.548), as shown in Figure 8.5a and Table 8.2. Since rutile TiO₂ has RI of 2.9 while anatase TiO₂ has RI of 2.5. For the transmittance, no significant difference was found for the rutile and anatase TiO₂ nanocomposites (Figure 8.5b).

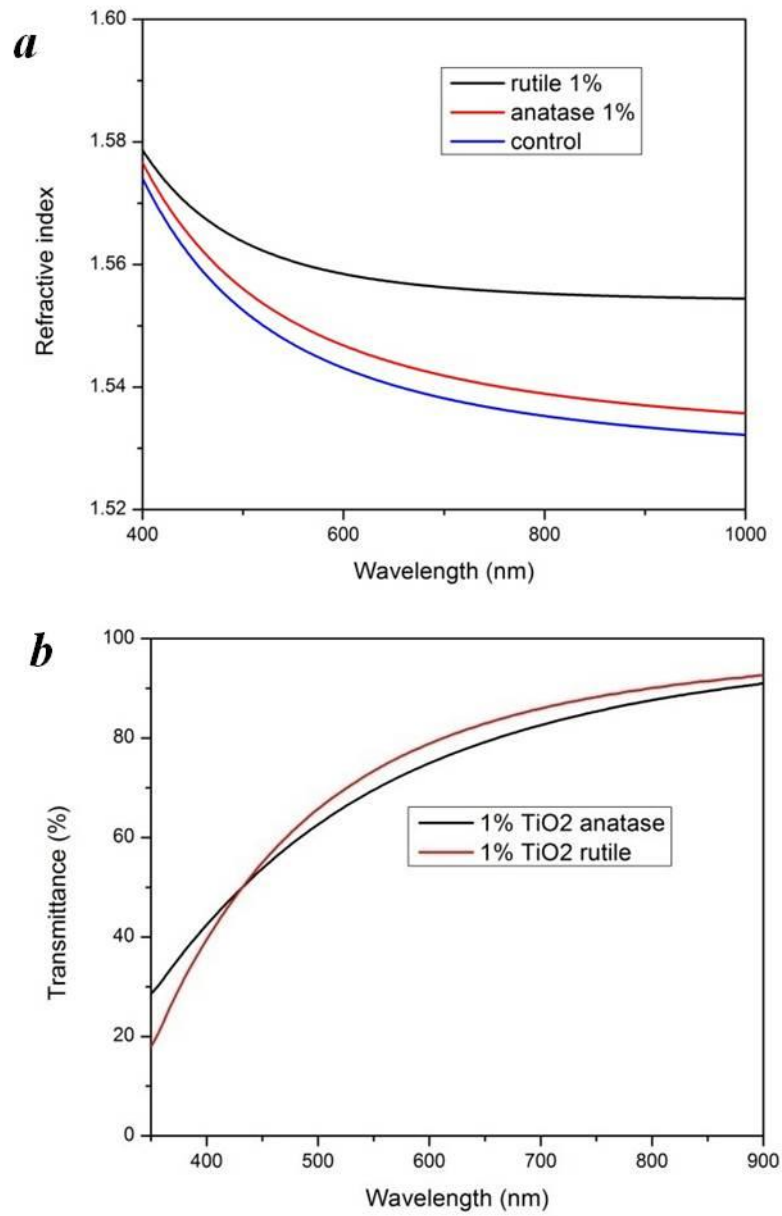


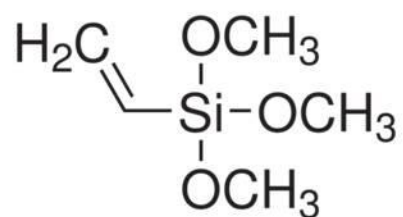
Figure 8.5 (a) Refractive index and (b) transmittance of 1% TiO₂ nanocomposites film composed of different crystal phase TiO₂ nanoparticles

Table 8.2 Refractive index of TiO₂ nanocomposites with different crystal phase nanoparticles

	control	1% anatase	1% rutile
Refractive index at 589 nm	1.544	1.548	1.559

8.3.2 Effect of silane treatment

a



b

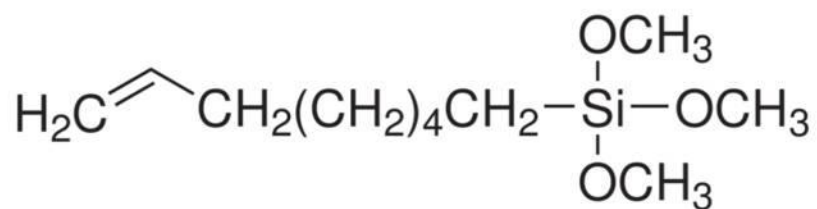


Figure 8.6 Chemical structure of (a) Vinyltrimethoxysilane
(b) trimethoxy(7-octen-1-yl)silane

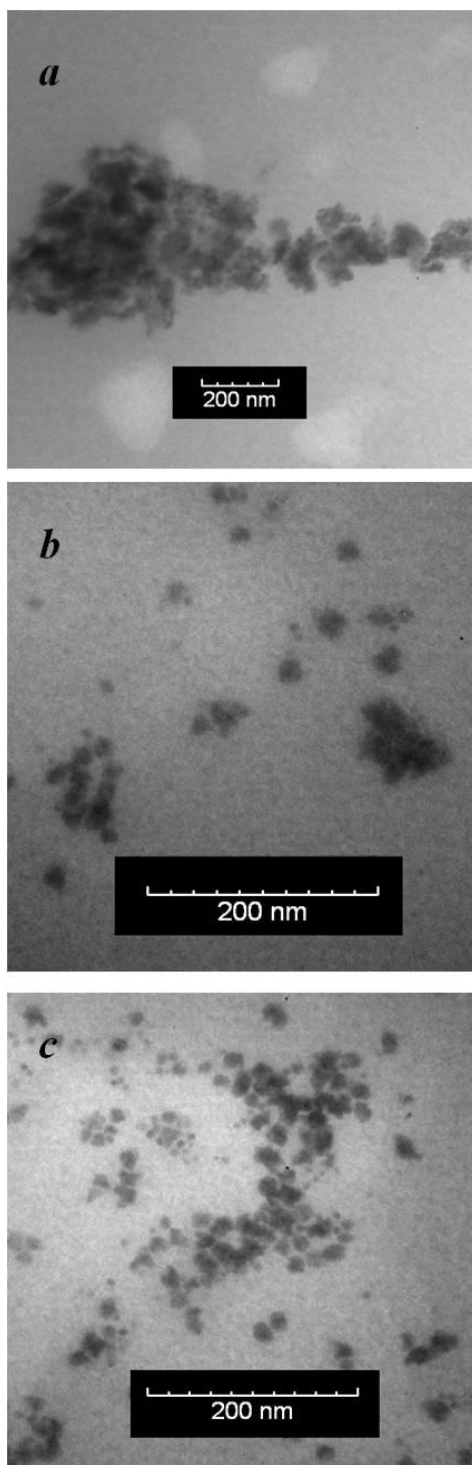


Figure 8.7 The dispersion of TiO_2 in silicone diluted by toluene (a) as synthesized TiO_2 (b) vinyltrimethoxysilane modified TiO_2 (c) trimethoxy(7-octen-1-yl)silane modified TiO_2 with different magnifications.

The as prepared TiO₂ modified by two vinyl silanes with different chain lengths (as shown in Figure 8.6) were diluted in toluene and mixed with silicone for composites. Since there are a lot of differences in surface energies of silicone and TiO₂, which are 19.8 mN/m and 60 mN/m respectively. Hydrophobic modification of TiO₂ using hydrocarbon chain silane will help match the surface energy and improve the dispersion in silicone. The dispersion of 1 wt% TiO₂ in silicone was evaluated by TEM. From Figure 8.7, we found that there are less particle agglomerations after vinyl silane modification, especially for particles modified by the long chain vinyl silane. Consistently, the transmittance of long chain vinyl silane modified TiO₂ nanocomposite thin film (20 μm) had significantly higher transmittance at 500-900 nm (Figure 8.8), which showed the highest transmittance of ~96%..

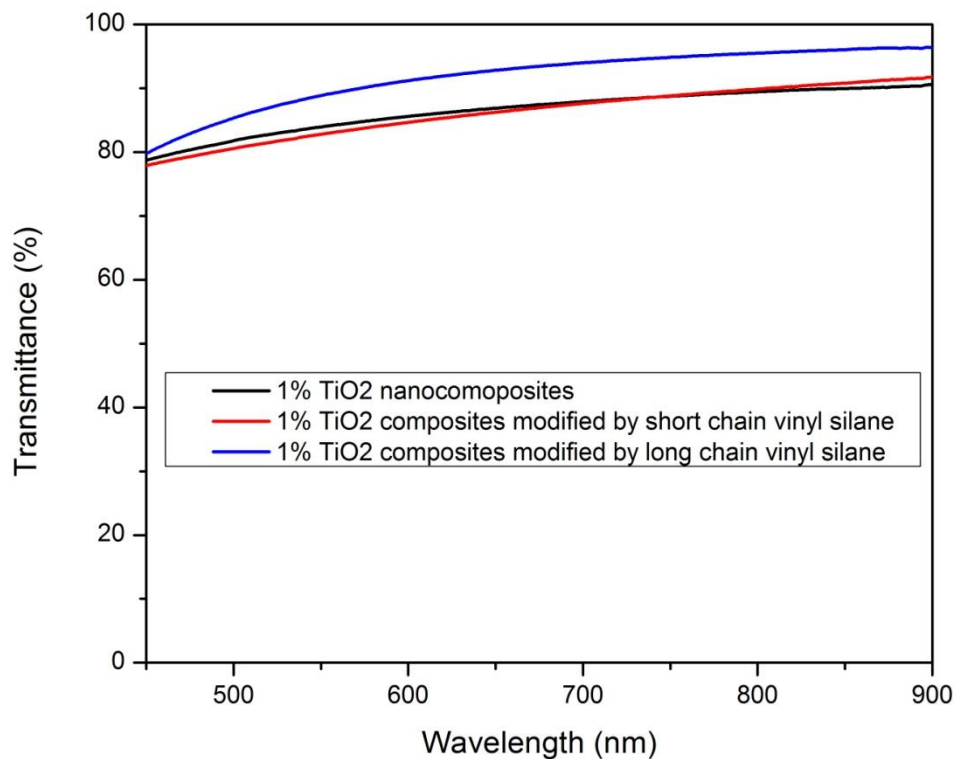


Figure 8.8 Light transmittance of 1 wt% TiO₂ nanocomposites thin film (20μm) modified by different chain length vinyl silanes.

8.3.3 Filler loading effect

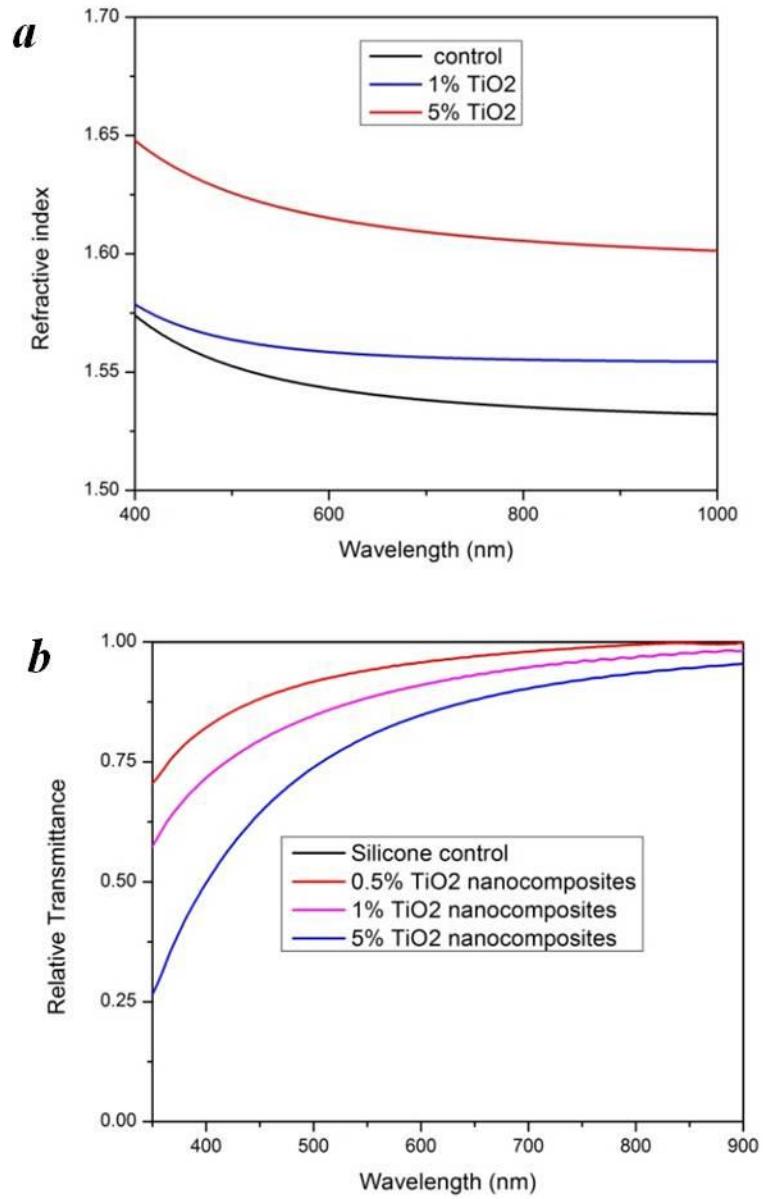


Figure 8.9 (a) Refractive index and (b) transmittance of different filler loading TiO₂ nanocomposites film after silane treatment

Table 8.3 Refractive index and relative transmittance of TiO₂ nanocomposites with different filler loadings.

	control	1% rutile	5% rutile
Refractive index at 589 nm	1.544	1.559	1.616
Relative transmittance at 589 nm	100%	91%	84%

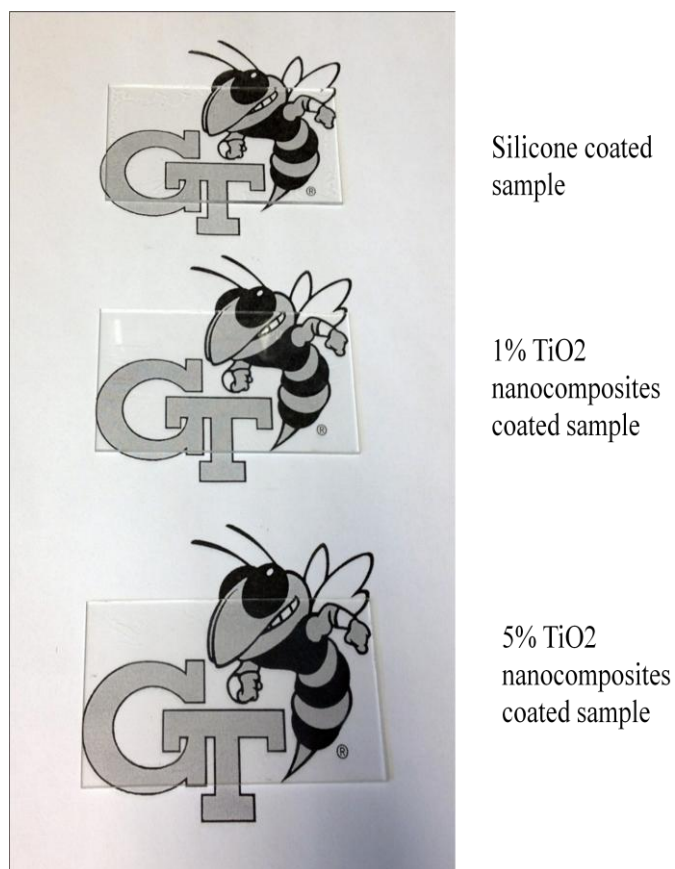


Figure 8.10 Transparency demonstration of glass slides coated with different filler loading TiO₂ nanocomposites (20 μ m thickness)

We fabricated rutile TiO₂ nanocomposites with filler loadings of 1% and 5%. The RI increased linearly from 1.559 to 1.616 comparing with 1.544 for the pure silicone (Figure 8.9a and Table 8.3). The relative transmittance was higher than 84% at 589 nm for 5% filler loading samples (20µm thickness) (Figure 8.9b and Table 8.3). The nanocomposite films with different filler loading were coated on glass slides and showed high transparency, as demonstrated in Figure 8.10.

8.3.4 Particle size effect:

We synthesized TiO₂ nanoparticles with the particle size increased from 8 nm to 12 nm by increasing the synthesis time. The intensity loss of transmitted light through nanocomposites due to light scattering can be described as:

$$\frac{I}{I_0} = \exp\left[-\frac{3V_p x r^3}{4\lambda^4} \left(\frac{n_p}{n_m} - 1\right)\right]$$

Where I and I₀ are the transmitted and incident light intensity, r is the radius of spherical particles, V_p is the volume fraction of inorganic particles, x is the optical path length, n_p and n_m are the refractive index of particles and polymer matrix. The transparency loss increases exponentially with the volume fraction and size of particle. So with the particle size increase, the transmittance decreased (Figure 8.11). However, the particle size also doesn't have a significant effect on RI of the nanocomposites (Table 8.4).

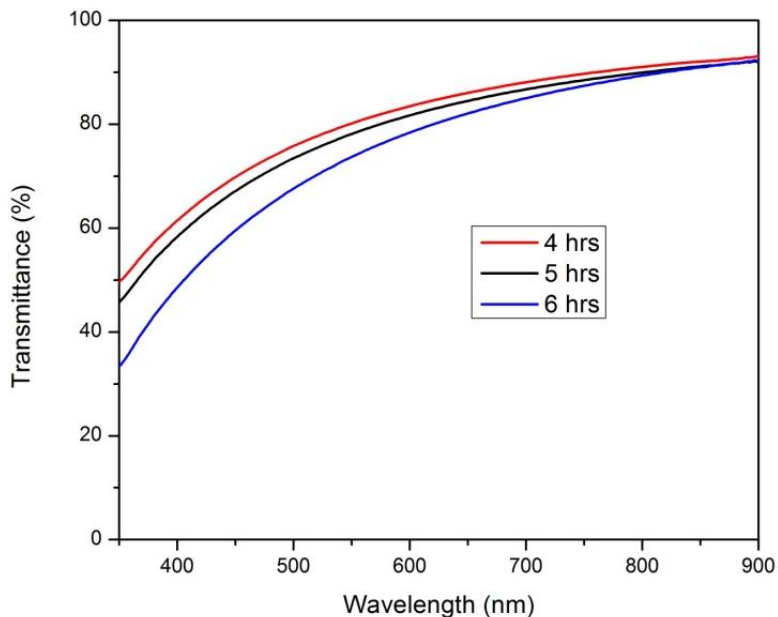


Figure 8.11 Transmittance of 1% TiO₂ nanocomposites composed of TiO₂ nanoparticles synthesized with different times.

Table 8.4 Refractive index of 1 wt% TiO₂ nanocomposites synthesized via hydrothermal method for different times.

	TiO ₂ nanocomposites made by 4 hr rutile TiO ₂	TiO ₂ nanocomposites made by 6 hr rutile TiO ₂
Refractive index at 589 nm	1.553	1.559

8.3.5 Reliability test

We put the 5 wt.% TiO₂ nanocomposites sample into the temperature humidity chamber for the reliability test. The test condition is shown in Figure 8.12. After the reliability test for 100 hours, we found that the difference of RIs before and after reliability test is less than 0.01 at 589 nm (Figure 8.13), which is within the experimental

error. The transmittance of the nanocomposites decreased 2.5% after the reliability test (Table 8.5). So no significant change of transmittance was observed after reliability test.

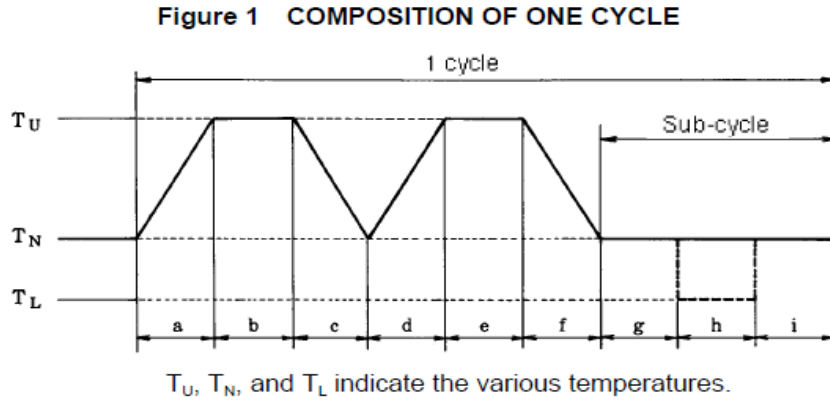


Table 1 TEMPERATURE AND HUMIDITY CYCLE CONDITIONS

Step	Conditions	Time (h)	Temperature (°C)	Relative humidity (%)
a		2.5	-	90 ~ 96
b		3.0	65±2	90 ~ 96
c		2.5	-	80 ~ 96
d		2.5	-	90 ~ 96
e		3.0	65±2	90 ~ 96
f		2.5	-	80 ~ 96
g		1 ~ 4	25±2	90 ~ 96
h		3.0	-10 _{±3}	Arbitrary
i		1 ~ 4	25±2	90 ~ 96
1 cycle		24	-	-

Figure 8.12 Reliability test conditions

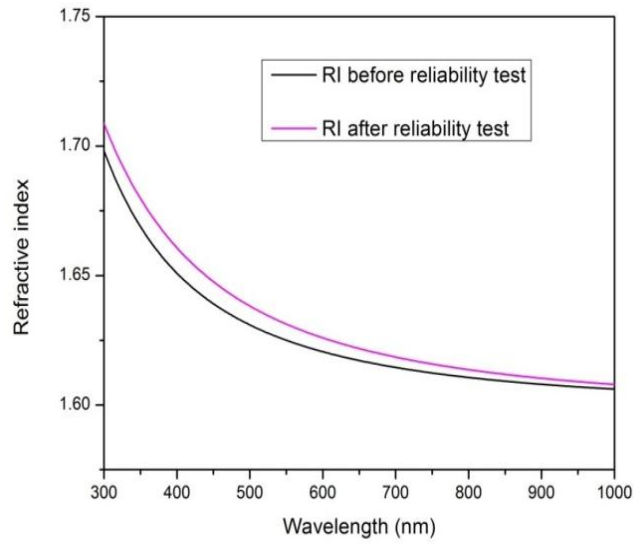


Figure 8.13 RI of 5 wt.% TiO₂ nanocomposites before and after reliability test

Table 8.5 Transmittance of nanocomposites before and after reliability test

	Before reliability test	After reliability test
Transmittance at 589 nm	73.3%	70.8%

8.4 Conclusions

We fabricated TiO₂ silicone nanocomposites as the encapsulant for LED. The RI of 5 wt.% TiO₂ nanocomposites achieved 1.62 comparing with 1.54 of the silicone sample. The crystal phase of TiO₂ significantly affects the RI and rutile TiO₂ has relatively higher RI than the anatase ones. Meanwhile, the sample still keeps high transparency, with relative transmittance of greater than 84% of pure silicone. The nanocomposites

maintained high RI and transmittance in the reliability test. They have great potential to be applied on LEDs as encapsulant for light extraction efficiency improvement.

CHAPTER 9

Future Work

9.1 Patterned superhydrophobic/superhydrophilic surfaces for electronic packaging

3D stacking of integrated circuits (ICs) has already been demonstrated by stack-bonding multiple wafers or individual dies on wafers with through silicon vias, with various bonding schemes, including copper-to-copper bonding by thermo-compression, oxide diffusion, direct covalent bonding, and copper pillar with tin-silver solder caps. Such 3D stack-bonding requires not only electrical interconnection between chips through TSVs but also environmental protection and stress-management of the stack within each of the ICs, thus needing unique underfill materials and processes for filling ultra-thin gaps ($\sim 5\text{-}15\mu\text{m}$) between chips with ultra-small pitch ($\sim 5\text{-}20\mu\text{m}$) interconnections. These dimensions are approximately an order of magnitude (10X) less than the flip-chip interconnection technology, as shown in Figure 9.1 that is currently in production.

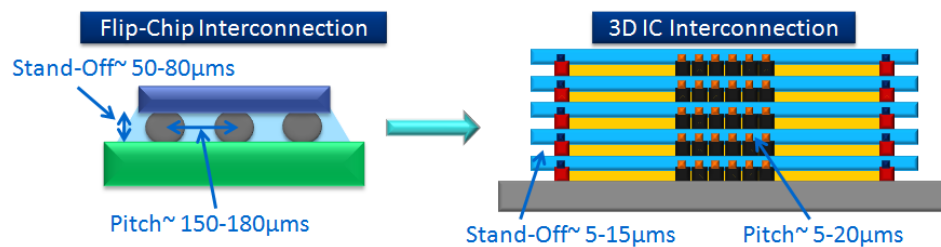


Figure 9.1 10x reduction in 3D IC interconnection pitch and stand-off height as compared to flip-chip.

There are some primary technical barriers which need to be overcome in order to meet the needs mentioned above: In this task, we propose a novel self-patterning process

and underfill materials for 3D IC stacking. Key innovations proposed in this task include unique and customized wafer-level underfills, which wet only the passivation surfaces of wafers but not the interconnection metal pads to allow for bonding while at the same time filling the gap in between (Figure 9.2a). The proposed selective underfill wetting can be achieved by multi-tier nano-structured pads surfaces with superhydrophobicity (water contact angle $>150^\circ\text{C}$). Large difference in surface energy between the two hydrophobic and hydrophilic surfaces is the driving force for selectivity. The superhydrophobic surfaces with very low surface energy (<14.5 dyne/cm) and SiN surfaces with high surface energy (40~90 dyne/cm) (Figure 9.2b), therefore, are key to achieving self-patterned underfills on the wafer (Figure 9.2c and d).

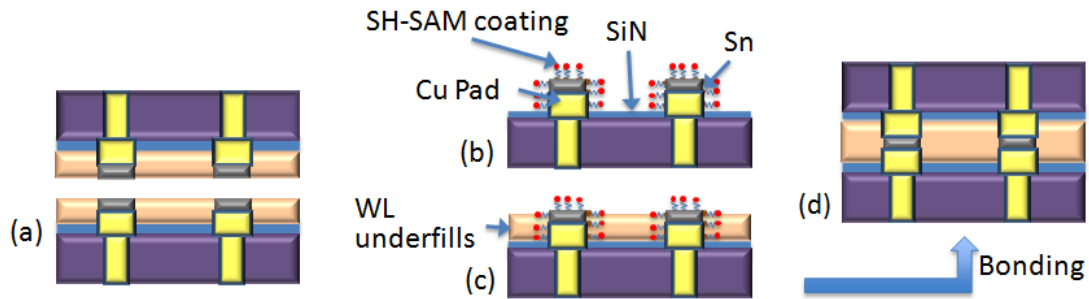


Figure 9.2 (a) Coplanar no-flow underfill, and (b)-(d) Schematic of SAM molecule coating for self-patterning underfill (selectively located on hydrophilic areas and subsequent bonding with a mating IC/TSV)

We designed and fabricated test vehicles (TVs) for selective patterns, where Cu and SiN were employed as bond pads and passivation surfaces, respectively. In order to have underfills spread only on passivation surfaces, we made superhydrophobic surfaces on Cu and hydrophilic ones on SiN. Preliminary tests of selective wettability of water droplets and epoxy resins were carried out on the TVs and the feasibility of the self-patterning has been observed. The TV preparations and the wetting tests are discussed.

9.1.1 Test vehicles design

We designed TVs with circular Cu bump on SiN (Figure 9.3a). The Cu bumps are $40\mu\text{m}$ in height, 1 cm in diameter, and the distance between bumps is around 0.5 cm. The

fabrication process of TVs is schematically shown in Figure 9.3b. The photoresist used is positive 1827 photoresist from Dupont.

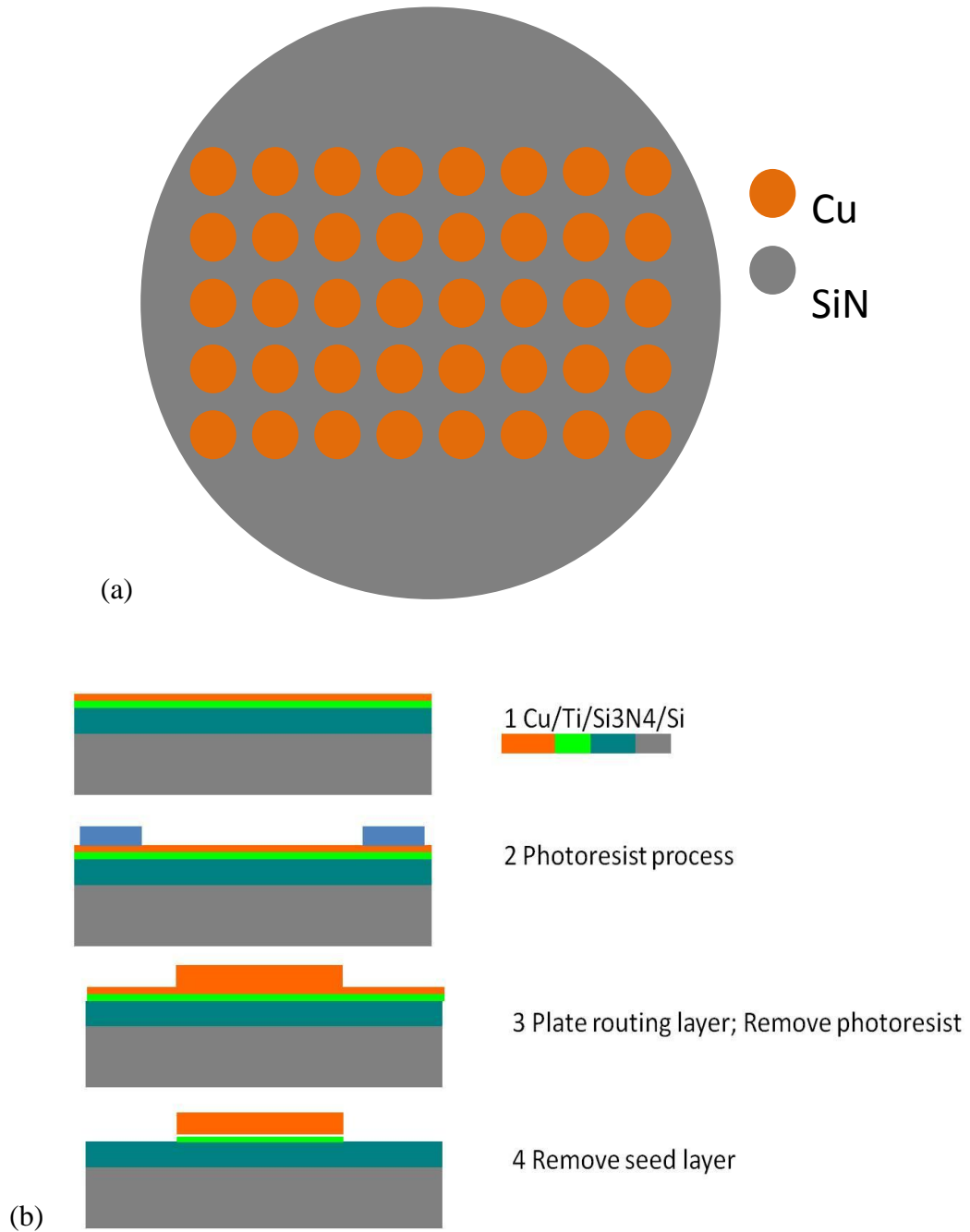


Figure 9.3 Test vehicle design (a) and fabrication process (b) with patterned Cu and SiN

9.1.2 Hydrophilic Surface Formation on SiN

Plasma treatments are widely used to modify the surface properties of materials and improve their performance for various applications. In particular, hydrophilization of a surface can be achieved by oxygen or nitrogen plasmas. When SiN is treated with oxygen plasma, polar functional groups containing oxygen are introduced to its surface, yielding the hydrophilic surface. In our study, O₂ plasma treatment was carried out under the following conditions: 150W RF power, 0.5 torr pressure and 75 sccm O₂ flow rate. After the hydrophilic treatment for 30 min, the water contact angle changes from 45.8° to 10.0°.

9.1.3 Hydrophobic Surface Formation on Cu

A 0.03M ammonia solution was prepared in a 1L glass bottle. The TVs were immersed into the solution and kept at 5°C for different time (Figure 9.4a-c). The samples were taken out of the solution and rinsed with DI water for three times, and then dried in air. The surface of Cu bump became blue after the treatment. Next, a 3 mM solution of trichloro(1H,1H,2H,2H-perfluorooctyl)silane (PFOS) in hexane was used for hydrophobic treatment (Figure 9.4d). Such coating has good thermal stability of up to 350-400°C. Specifically, the TVs were immersed in the solution for 30 min followed by a heat treatment at 150 °C in air for 1 hr.

Cu(OH)₂ nanoneedle-like networks were formed after ammonia etching, as shown in figure 3. The etching depth increases with etching time, which ranged from 12 hrs to 48 hrs. We tested the surface wettability on coated surfaces (Table 9.1). For water, the surface tension is 72 mN/m and the viscosity is 8.90×10^{-4} Pa·s at 25°C. The water contact angle increases continuously when we increase the etching time from 12 to 48 hrs. The contact angle hysteresis decreases from 4.9° to 1.5°, indicating superior superhydrophobic properties. The electrical resistance of Cu increases from 1 Ω before

etching to 200-300 Ω both after etching and hydrophobic treatment, due to the formation of $\text{Cu}(\text{OH})_2$.

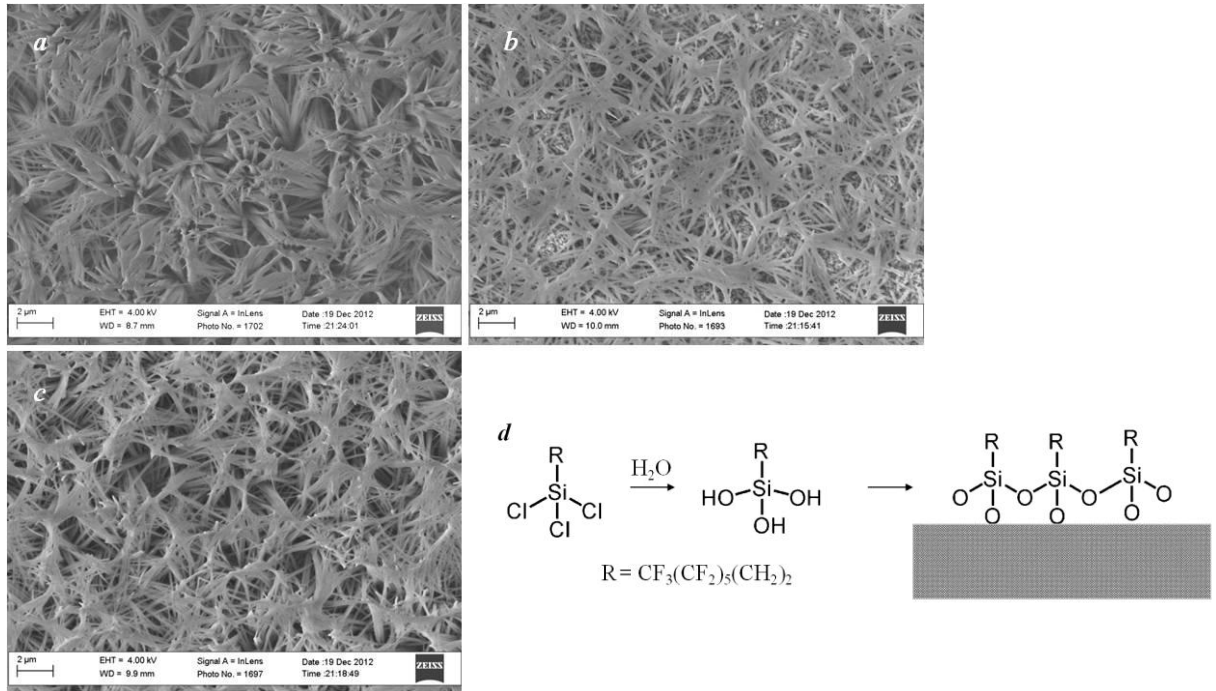


Figure 9.4 Morphology of etched copper at different etching time (a) 12 hrs (b) 24 hrs (c) 48 hrs (d) Illumination of PFOS coating on etched Cu.

Table 9.1 Contact angle and hysteresis of superhydrophobic Cu surface

	12 hrs	24 hrs	48 hrs
Water contact angle (degree)	159.6	165.4	170.0
Contact angle hysteresis (degree)	4.9	3.1	1.5

9.1.4 Selective wettability and self-patterning demonstration on TVs

In order to fabricate TVs with patterned wettability, we first did oxygen plasma treatment of the whole TVs surface, and then covered the SiN part with photoresist. Surface etching and hydrophobic treatment were made on the exposed Cu surface, and

then the photoresist was removed by acetone (Figure 9.5). The epoxy resin we tested is the mixture of EPON 828 and ERL 4221 (molar ratio 1:1). The viscosity of the resin is 1.8Pa·s at 25°C and the surface tension is around 42-46 mN/m. The contact angle of epoxy resin on Cu is ~ 150°. In the self-patterning demonstration process, we pipetted water and epoxy resin drops at the interface of Cu and SiN, and found that both water and epoxy resin droplets were repelled by the superhydrophobic Cu region, and stayed in hydrophilic SiN region (Figure 9.6). For the commercial underfill UF 8806G, after spin coating at 1000 rpm for 1 min, the underfill remained in the hydrophilic part (Figure 9.7).

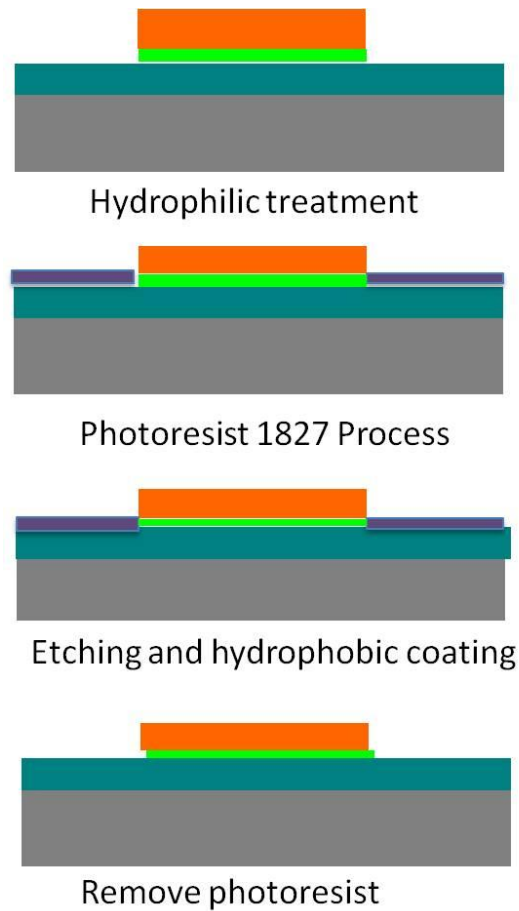


Figure 9.5 Superhydrophobic/superhydrophilic patterned wettability process.

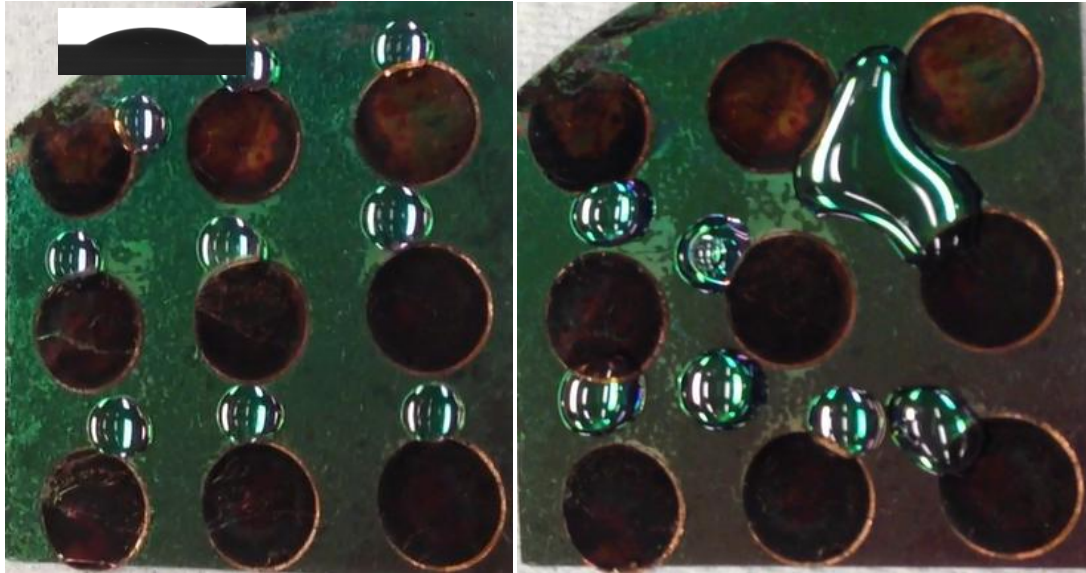


Figure 9.6 Demonstration of water droplet (a) and epoxy resin (828:4221=1:1) (b) on TVs. The inset is the side view of water droplet on TVs. The droplet stayed in hydrophilic SiN part.

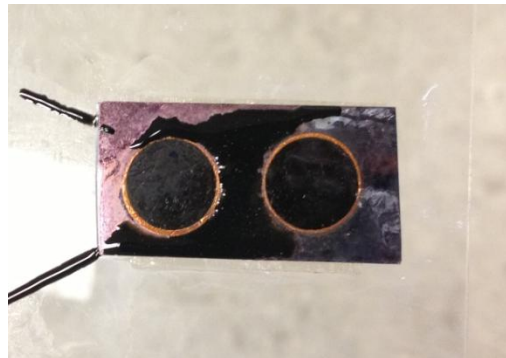


Figure 9.7 Commercial underfill UF 8806G on TVs after spin coating.

9.1.5 Conclusions and future work

We fabricated patterned TVs with superhydrophobic Cu bond pads/hydrophilic SiN passivation surfaces. Superhydrophobic Cu was fabricated by etching in ammonia solution, followed by long chain fluorocarbon silane coating. Superhydrophilic SiN was achieved by oxygen plasma treatment. The feasibility of the self-patterning process of water droplet and epoxy resin has been demonstrated. The droplets stayed in hydrophilic SiN part, and were repelled by the superhydrophobic Cu part.

In the future work, efforts will be made in the following aspects:

- (1) Fabricating TVs with smaller feature size (50 micrometers) to understand the effect of pattern geometry on self-patterning process.
- (2) Simultaneous bonding and underfilling process:
 - a. Explore and develop 3D IC bonding interconnection via thermo-diffusion or reflow.
 - b. Develop and optimize simultaneous bonding and underfilling process.
 - c. Design and fabricate test-vehicles to assess assembly defects and stack-bond reliability.

9.2 High refractive index core-shell nanophosphors for high brightness LEDs

White LED can be achieved by three methods: mixing red green and blue (RGB) LEDs, using UV LED to stimulate RGB phosphors, and combining blue LED with yellow emitting phosphors.[226] Among them, the combination of blue LED and yellow emitting phosphor is the most promising method due to the cost effectiveness and technical convenience. The first commercialized white LED from Nichia Chemical Co. in 1996, used blue InGaN LED chip and yellow emitting $Y_3Al_5O_{12}:Ce^{3+}$ (YAG:Ce) phosphors. The currently commercial LEDs uses GaN LED chip with YAG:Ce phosphor. However, the current LEDs still have drawbacks of relatively low efficiency, poor color rendering index (CRI) of smaller than 85 and high correlated color temperature (CCT) of 4000-8000 K. The low CRI indicates the missing of red component in the spectrum, and the high CCT corresponds to the neutral and cool-white color. These issues are closely related to the immature phosphor technology and the lack of proper encapsulation materials. In this work, the PI proposes to use a novel core-shell structured nanophosphor and its polymer composite as LED encapsulation, which has great potential for high brightness white LED applications.

The goal for current white LEDs researches is to achieve high luminous efficiency, brilliant color rendering properties, cost effectiveness and high chromatic stability simultaneously. Current white LEDs on the basis of yellow YGA:Ce have good luminance properties, but the high CCT and low CRI impair the quality of white light and limit their practical applications. To enrich the red emission, phosphor mixing can be employed.[227] As shown in Figure 9.8a, by using both YAG:Ce and a red emission phosphor, appropriate CRI and moderate luminescence efficiency can be achieved. The combination of green and red phosphors with UV-LEDs can also give high CRI. However, both of these two methods suffer from several issues: 1) low luminescence efficiency compared to conventional yellow YGA:Ce; 2) the additional red phosphors, typically sulfide-based or nitride-based phosphor etc. have poor chemical stability, environmental unfriendliness, and sometimes require high temperature and high pressure to process; 3) the mixture of phosphors leads to fluorescence re-absorption and non-uniformity of luminescence properties. Overall, it is still quite difficult to achieve high CRI and luminescence efficiency at the same time.

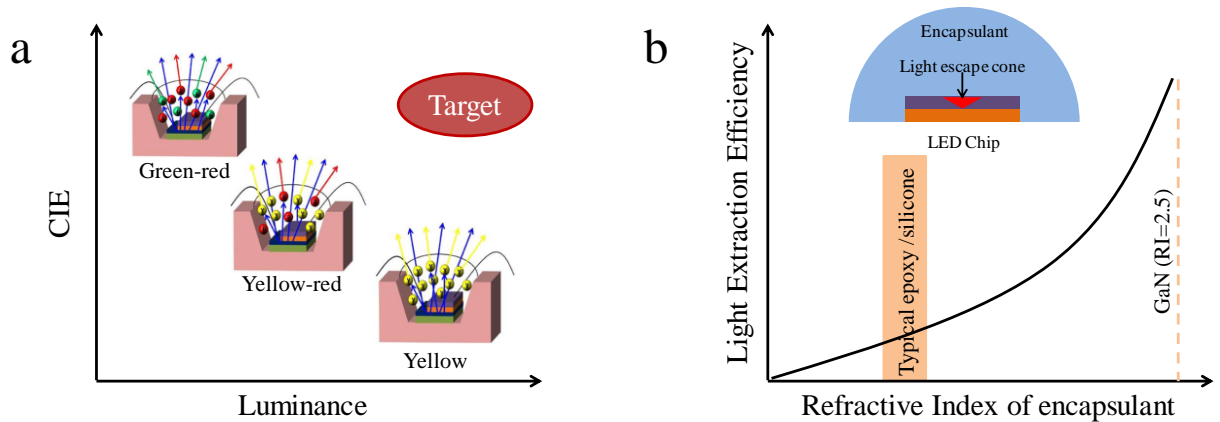


Figure 9.8 (a) Comparison of different phosphor mixing methods for white LEDs based on a blue LED chip, including yellow phosphors, yellow/red phosphors, and green/red phosphors. (b) Relationship between light extraction efficiency and RI of the encapsulant; schematic of light extraction from a GaN LED chip.

Light extraction from LED chips is another big challenge due to the large refractive index (RI) difference between III-V crystals and outer medium. As a result, a large portion of incident light will be trapped inside the LED structure.[208] From Snell's Law, there is a critical angle when light is passing from a high index to a low index material, above which light will no longer pass the interface and be internally reflected instead. Simple calculation shows that the escape-cone angle for unencapsulated AlGaInP ($n_{\text{AlGaInP}}=3.35$) is only around 17° , resulting in light-extraction efficiencies of only a few percent. Moreover, the trapped light in LED may be converted to heat, lowering the conversion efficiency and device reliability. To improve the light extraction efficiency, a transparent encapsulant layer with a relatively high RI is used to reduce the RI contrast between chip and air and improve the light extraction efficiency. Epoxy and silicone are currently employed as encapsulant materials, whose RI are ~ 1.45 - 1.55 . However, such RI is still too low to have satisfactory light extraction efficiency. It was found that the extraction efficiency of LED will double when the RI of the encapsulant increases from 1.5 to 2.0 (Figure 9.8b).[210]

To improve the RI of polymers, some special polymers have been developed, which contain aromatic or high π -electron structures, or organic groups such as halogen, sulfur atoms. However, such highly conjugated structure tends to absorb more light in the UV and visible region.[209] Another promising approach is to use high RI nanoparticles filled polymer encapsulants. When the particle size is smaller than one tenth of the wavelength of the incident light, the Raleigh scattering will be negligible. One possible issue associated with these nanocomposites is nanoparticle aggregation. It will not only causes light scattering but also may affect the physical properties of polymer matrices, such as thermal stability, modulus, toughness, etc.[215] In this regard, the development of nanophosphors and the dispersion control of nanophosphors in polymer matrix become critical for improving light extraction of LEDs.

Phosphor-converted white LEDs are considered as a new lighting source for the next generation SSL. A major drawback in current technologies is that the generated white light is cold, due to the lack of red color. White LEDs need extra red phosphors that can be excited by blue or near ultraviolet (NUV) LED chips. However, the red phosphors on the basis of sulfides or nitrides suffer from the poor chemical stability or rigorous synthesis conditions. Therefore, it is very important to develop chemically stable, high CRI and high luminous efficiency phosphors that can emit white light directly to meet with the requirements for SSL. Moreover, the low light extraction efficiency is another limitation for current LED technology, which is caused by RI contrast between the LED chip and the encapsulant and the resulting light trapping within the chips. Typical encapsulants, such as epoxy and silicone, have RI of 1.45-1.55, which is far below practical needs. It is urgent to develop high RI encapsulant (RI ~ 1.7-1.8) to improve the light extraction efficiency.

9.2.1 Proposed work

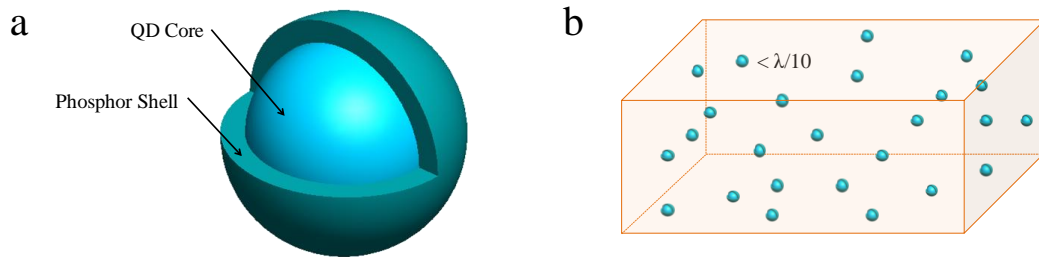


Figure 9.9 (a) Proposed structure of novel nanophosphor with a QD core and a phosphor shell. (b) Schematic of polymer composite with well dispersed nanophosphor; the diameter of nanophosphor should be smaller than one tenth of wavelength of the incident light source to avoid the light scattering.

We propose a core-shell nanophosphor to address the aforementioned issues. As shown in Figure 9.9a, the structure of the proposed nanophosphor includes the following two parts:

High RI red-emitting QDs as the core

High refractive index QDs will be incorporated into the phosphors by the core-shell structure. The addition of high RI component will effectively improve the overall RI of the composite. At the same time, size dependent emission of QDs allows tunable photoluminescence, which gives more red-emitting components to phosphors and improve the CRI. In addition, energy transfer between QDs and rare earth elements promotes the emission of rare earth doped phosphors.

Rare earth element doped white nanophosphors as the shell

We will synthesize phosphors shell that absorb excitation energy from blue or NUV LEDs and generate visible emissions. In this case, a single-phase phosphor with direct white light emission is highly advantageous to mitigate the problems of fluorescence re-absorption and non-uniformity of luminescence which are observed in mixed phosphors systems.

In addition to studying the preparation and properties of nanophosphor, we will also investigate its interfacial properties and dispersion in polymer matrix. As seen in Figure 9.9b, it is ideal to have well-dispersed nanophosphor in polymer matrix with particle size smaller than one-tenth of the wavelength of the incident light source in order to minimize the effect of light scattering.

CdSe QDs are excellent for our application because of the high refractive index of 2.7 at 589 nm with a size-dependent bandgap. When the size is ~ 7 nm, they will emit red light.

Alkaline earth orthosilicates (Sr_2SiO_4) will be used as the phosphor host materials due to high UV absorption and chemical stability. Comparing with commercial YAG:Ce phosphor, alkaline earth orthosilicates-based phosphor is not only suitable for blue LEDs but also for NUV LEDs. Recently, It was reported that GaN (400 nm chip) with a

Sr₂SiO₄-based phosphor exhibits a better luminous efficiency than that of the industrially available LEDs of InGaN (460-nm chip) with YAG:Ce.[228]

Dysprosium (Dy) is used here as a natural white light emission ion, with two dominant emission bands of blue (485 nm, $^4F_{9/2} \rightarrow ^6H_{15/2}$) and yellow (570 nm, $^4F_{9/2} \rightarrow ^6H_{13/2}$). It is necessary to note that Dy has only one luminescent center, which is a huge advantage over other single-phase phosphors with two or above luminescent centers, such as Eu²⁺/Mn²⁺, Ce³⁺/Eu²⁺, because the quenching between different centers can be avoided.

To fabricate the proposed core-shell nanophosphor, QDs will be first synthesized using standard procedures described in the literature.[229] Then, a SiO₂ shell will be added which serves as the precursor for rare-earth element doping and formation of nanophosphor shell.

Figure 9.10 shows the proposed reverse microemulsion method for the synthesis of SiO₂ coated CdSe QDs. In oil solvent, the selected surfactant can form micelles with hydrophilic inner domain and hydrophobic tails facing out. When trioctylphosphine oxide (TOPO)-capped CdSe QDs are introduced into the system and disperse in the solution, ligand exchange of TOPO with the surfactant occurs, allowing the QDs to enter the hydrophilic micelles. Ammonia solution is added to stabilize the system, and water molecules in the solution enter the micelles. When tetraethyl orthosilicate (TEOS) is added, SiO₂ particles will form within the aqueous domains in the micelles, and the CdSe QDs originally in the micelles before TEOS addition will be coated with SiO₂. Here the thickness of SiO₂ shell can be easily controlled by adjusting the amount of water and TEOS.

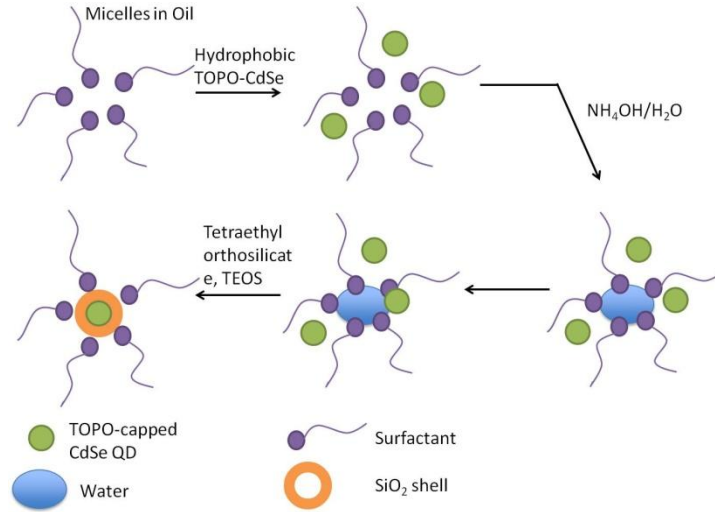


Figure 9.10 Reverse microemulsion method for silica coated CdSe QDs synthesis

After the synthesis of CdSe@SiO_2 , we will use a combustion synthesis method to incorporate the Sr^{3+} and Dy^{3+} dopants to SiO_2 shell. Sr and Dy sources, $\text{Dy}(\text{NO}_3)_3$ and $\text{Sr}(\text{NO}_3)_2$, will be added into the solution of CdSe@SiO_2 , which will be heated rapidly to elevated temperatures ($\sim 800^\circ\text{C}$) and stay for a short period of time (several minutes). At high temperature, Sr and Dy will be doped into the lattice of SiO_2 shell, generating $\text{CdSe@Sr}_2\text{SiO}_4:\text{Dy}^{3+}$ nanophosphor. This short heat treatment will effectively avoid the sintering of nanoparticles and maintain the small size with a narrow size distribution. In order to control the crystal phase of Sr_2SiO_4 , the effect of reaction temperature, time and ratio between various precursors will be studied. This method has advantages of low temperature synthesis, high quenching concentration of the activator, and a homogeneous distribution of the emission centers, which can lead to better emission efficiency. Transmission electron microscopy (TEM), X-ray diffractometer (XRD) and UV-vis spectroscopy will be used to characterize the morphology, crystallinity and performance of nanophosphor.

The RI of the core shell nanophosphors will increase with the increased filler loadings (Figure 9.11), according to effective medium approximation. The RI of nanocomposites

$n_{\text{eff}} = V_p n_p + V_h n_h$, in which V_p and V_h are volume fraction of nanoparticles and polymer matrix.

The Raleigh scattering coefficient of nanocomposites is

$$k_s = NC_{\text{scat}} = \frac{2\pi^5}{3} \left(\frac{n_p^2 - n_h^2}{n_p^2 + 2n_h^2} \right)^2 \frac{(2r_p)^6}{\left(\frac{\lambda_0}{n_h} \right)^4} \frac{L}{\left(\frac{4}{3} \right) \pi r_p^3}$$

The mean distance between scattering event, is the inverse of the scattering coefficient k_s^{-1} , which is strongly dependent on QDs radius and volume loading fraction. In our study, we will modify the core-shell nanophosphor size and filler loading to optimize scattering coefficient for higher light extraction. Light tracing simulation will also be employed to investigate the effect of optical scattering by nanoparticles in an encapsulant on light extraction efficiency.

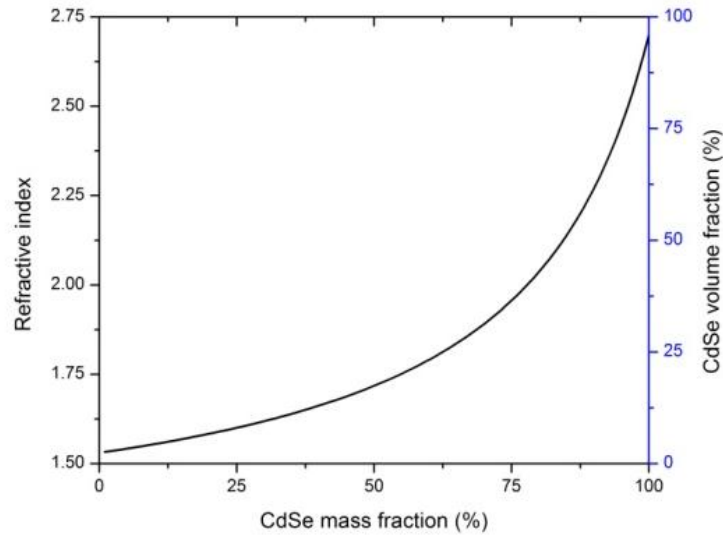


Figure 9.11 Effective RI of nanophosphor-composite vs CdSe QDs mass and volume fraction.

9.3 Mechanically Robust Superhydrophobic Surfaces

In the previous chapters, we investigated the mechanical robustness of superhydrophobic epoxy nanocomposites and hierarchical structure. It was proved that microscale texturing protects more fragile nanoscale roughness, and the superhydrophobicity was remained after the abrasion test. However, the hysteresis still increases after abrasion. The possible reason is the brittleness of the materials, which makes the damage of structure inevitable. Studies can be conducted to explore the fabrication of micro nano structures with more flexible materials silicone and polyurethane, or mechanically robust metal particles, alumina, and diamond like carbon nanostructures.

APPENDIX A

AUTHOR'S PUBLICATIONS

A.1 Book Chapters

1. **Yan Liu**, Yonghao Xiu, and C. P. Wong, "Superhydrophobic Surfaces for Photovoltaic Applications", *Biomimetic Superhydrophobicity for Self-Cleaning Applications*, Springer, submitted.
2. Yonghao Xiu, **Yan Liu**, and C. P. Wong, "Two Scale Roughness, Self-cleaning, and Low Reflectivity Silicon Surface for Solar Cell Applications", Chapter 7, *Functional Polymer Nanocomposites for Energy Storage and Conversion*, Q. Wang and L. Zhu, Ed., pp. 81-93, ACS publications (2010).

A.2 Journal Papers

3. **Yan Liu**, Arnab Das, Sheng Xu, Ziyin Lin, Chen Xu, Zhong Lin Wang, Ajeet Rohatgi, and C. P. Wong, "Hybridizing ZnO Nanowires with Micropyramid Silicon Wafers as Superhydrophobic High-Efficiency Solar Cells", *Advanced Energy Materials*, 2(1): 47-51 (2012)
4. **Yan Liu**, Ziyin Lin, Wei Lin, Kyoung Sik Moon, and C. P. Wong, "Reversible Superhydrophobic-Superhydrophilic Transition of ZnO Nanorod/Epoxy Composite Films", *ACS Applied Materials & Interfaces*, 4(8) : 3059-3964 (2012).
5. **Yan Liu**, Wei Lin, Ziyin Lin, Yonghao Xiu, and C. P. Wong, "A Combined Etching Process toward Robust Superhydrophobic SiC Surfaces", *Nanotechnology*, 23(1): pp. 255703 (2012).
6. **Yan Liu**, Yonghao Xiu, D. W. Hess, and C. P. Wong, "Silicon Surface Structure Controlled Oleophobicity", *Langmuir*, 26(11): 8908-8913 (2010)
7. Ziyin Lin*, **Yan Liu***, and Ching Ping Wong, "Facile Fabrication of Superhydrophobic Octadecylamine-Functionalized Graphite Oxide Film", *Langmuir*, 26(20): 16110-16114 (2010) (*equal contribution)

8. **Yan Liu**, Ziyin Lin, Kyoung Sik Moon, and C. P. Wong “Superhydrophobic Nanocomposites Coating for Reliability Improvement of Microelectronics”, *IEEE Transactions on Components, Packaging and Manufacturing Technology*, in press.
9. **Yan Liu**, Ziyin Lin, Xueying Zhao, Sehoon Yoo, Kyoung Sik Moon, and C. P. Wong, “High Refractive Index and Transparency Nanocomposites as Encapsulant for High Brightness LED packaging”, submitted.
10. **Yan Liu**, Arnab Das, Ziyin Lin, Ian Copper, Ajeet Rohatgi, and C. P. Wong, “Hierarchical Robust Textured Structures for Large Scale Self-cleaning Black Silicon Solar Cells”, submitted.
11. **Yan Liu**, Lixi Wang, Ziyin Lin, Xueying Zhao, Kyoung Sik Moon, and C. P. Wong, “High Refractive Index Rare Earth Doped Nanocomposites as Encapsulant for White LEDs”, in preparation.
12. Ziyin Lin, **Yan Liu**, Yagang Yao, Owen Hildreth, Zhuo Li, Kyoung Sik Moon, Josh Agar and Ching Ping Wong, “Superior Capacitance of Functionalized Graphene”, *Journal of Physical Chemistry C*, 115(14): 7120–712 (2011)
13. Yonghao Xiu, **Yan Liu**, B. Balu, Dennis W. Hess, Ching Ping Wong, “Robust Superhydrophobic Surfaces Prepared with Epoxy Resin and Silica Nanoparticles”, *IEEE Transactions on Advanced Packaging* (in press)
14. Yonghao Xiu, **Yan Liu**, Dennis W. Hess, Ching Ping Wong, “Mechanically Robust Superhydrophobicity on Hierarchically Structured Si Surfaces”, *Nanotechnology*, 21(15), pp. 155705 (2010)
15. Ziyin Lin, **Yan Liu**, Sathyanarayanan Raghavan, Kyoung-Sik Moon, Suresh Sitaraman, C. P. Wong, “Magnetic Alignment of Hexagonal Boron Nitride Platelets in Polymer Matrix: Toward High Performance Anisotropic Polymer Composites for Electronic Encapsulation”, submitted.
16. Ya Yang, Hulin Zhang, **Yan Liu**, Zong-Hong Lin, Sangmin Lee, Ziyin Lin, Ching Ping Wong, and Zhong Lin Wang, “Silicon-Based Hybrid Energy Cell for Self-Powered Electrodegradation and Personal Electronics”, *ACS Nano*, in press.
17. Ziyin Lin, Minkyu Song, **Yan Liu**, Meilin Liu, C. P. Wong, "Facile Preparation of Nitrogen-doped Graphene as a Metal-free Catalyst for Oxygen Reduction Reaction", *Physical Chemistry Chemical Physics*, 14(10): 3381-3387 (2012).
18. Ziyin Lin, Gorden Wallera, **Yan Liu**, Meilin Liu, and C. P. Wong, “Facile Synthesis of Nitrogen-doped Graphene via Pyrolysis of Graphene oxide and Urea and its

- Electrocatalytic Activity toward Oxygen Reduction Reaction”, *Advanced Energy Materials*, 2(7): pp. 884-888 (2012).
19. Ziyin Lin, Gorden Wallera, **Yan Liu**, Meilin Liu, C. P. Wong, “Simple preparation of nanoporous few-layer nitrogen-doped graphene for use as an efficient electrocatalyst for oxygen reduction and oxygen evolution reactions”. *Carbon*, 53, 130–136 (2012).
 20. Ziyin Lin, Gorden Wallera, **Yan Liu**, Meilin Liu, and C. P. Wong, “Nitrogen-doped Graphene Prepared by Pyrolysis of Graphene Oxide with Polypyrrole for Electrocatalysis of Oxygen Reduction Reaction”, *Nano Energy*, in press.
 21. Qizhen Liang, Xuxia Yao, Wei Wang, **Yan Liu** and Ching Ping Wong, “A Three-Dimensional Vertically Aligned Functionalized Multilayer Graphene Architecture - An Approach for Graphene-based Thermal Interfacial Materials”, *ACS Nano*, 5(3): pp. 2392–2401 (2011)
 22. Ziyin Lin, Yagang Yao, Zhuo Li, **Yan Liu**, Kyoung Sik Moon, and C. P. Wong, “Solvent-Assisted Thermal Reduction of Graphite Oxide”, *Journal of Physical Chemistry C*, 114(35): pp. 14819–14825 (2010)
 23. Xue Wang, Yong Ding, Dajun Yuan, Jung Il Hong, **Yan Liu**, C. P. Wong and Z. L. Wang, “Reshaping the Tips of ZnO Nanowires by Pulsed Laser Irradiation”, *Nano Research*, 5(6), pp. 412 (2012).

A.3 Conference Proceedings

24. **Yan Liu**, Ziyin Lin, Xueying Zhao, Sehoon Yoo, Kyoung Sik Moon, and C. P. Wong, “High Refractive Index and Transparency Nanocomposites as Encapsulant for High Brightness LED packaging”, Proceedings of the IEEE 63rd Electronic Components Technology Conference, Las Vegas, NV, accepted.
25. Ziyin Lin, **Yan Liu**, Kyoung Sik Moon, and C. P. Wong, “Novel Surface Modification of Nanosilica for Low Stress Underfill”, Proceedings of the IEEE 63rd Electronic Components Technology Conference, Las Vegas, NV, accepted.
26. Ziyin Lin, **Yan Liu**, Kyoung Sik Moon, and C. P. Wong, “Enhanced Thermal Transport of Hexagonal Boron Nitride Filled Polymer Composite by Magnetic Field-assisted Alignment”, Proceedings of the IEEE 63rd Electronic Components Technology Conference, Las Vegas, NV, accepted.

27. **Yan Liu**, Ziyin Lin, Kyoung Sik Moon, and C. P. Wong, "Robust and low cost superhydrophobic nanocomposites coating for reliability improvement of microelectronics", Proceedings of the IEEE 62th Electronic Components Technology Conference, pp. 2135-2139 (2012).
28. **Yan Liu**, Ziyin Lin, Xueying Zhao, Sehoon Yoo, Kyoung Sik Moon, and C. P. Wong, "ZnO Quantum Dots-filled Encapsulant for High Brightness LED Packaging", Proceedings of the IEEE 62th Electronic Components Technology Conference, pp. 2140-2144 (2012).
29. **Yan Liu**, Ziyin Lin, Kyoung Sik Moon, and C. P. Wong, "Novel ZnO Nanowires/Silicon Hierarchical Structures for Superhydrophobic, Low Reflection, and High Efficiency Solar Cells", Proceedings of the IEEE 61th Electronic Components Technology Conference, Lake Buena Vista, FL, pp. 2114-2118 (2011).
30. **Yan Liu**, Yonghao Xiu and C. P. Wong, "Micro/Nano Structure Size Effect on Superhydrophobicity and Anti Reflection of Crystalline Si Solar Cells", Proceedings of the IEEE 60th Electronic Components Technology Conference, pp. 1719-1724 (2010).
31. Ziyin Lin, **Yan Liu**, Zhuo Li and C. P. Wong, "Novel Preparation of Functionalized Graphene Oxide for Large Scale, Low cost, and Self-cleaning Coatings of Electronic Devices", Proceedings of the IEEE 61th Electronic Components Technology Conference, Lake Buena Vista, FL, pp. 358-362 (2011).
32. Ziyin Lin, **Yan Liu**, Yagang Yao, Zhuo Li, Kyoung Sik Moon, and C. P. Wong, "Surface Engineering of Graphene for High Performance Supercapacitors", Proceedings of the IEEE 61th Electronic Components Technology Conference, Lake Buena Vista, FL, pp. 236-241 (2011).
33. Yonghao Xiu, **Yan Liu**, D. W Hess and C. P. Wong, "Preparation of Superhydrophobic Silicon Surface Structures with Reduced Light Reflection", *Proceedings of Materials Research Society*, Vol. 1158, pp. F03-07 (2009)
34. Yonghao Xiu, **Yan Liu**, D. W Hess and C. P. Wong, "Superhydrophobic Silicon Surfaces with Low Light Reflectivity", *Proceedings of American Chemical Society National Meeting*, Vol. 1158, pp. 49-58 (2009)

A.4 Invention Disclosures

35. **Y. Liu**, Kyoung Sik Moon, and C. P. Wong, “Low Infrared Light Reflectance High Efficiency Self-Cleaning Solar Cell.”, GTRC Invention Disclosure No. 4854 (2009)
36. **Y. Liu**, Kyoung Sik Moon and C. P. Wong, “Incorporating ZnO Nanostructures into Etched Si Surface for Low IR Light Reflectance and High Efficiency Self-Cleaning Solar cell”, GTRC Invention Disclosure No. 572 (2010)
37. Yonghao Xiu, **Yan Liu**, and C. P. Wong, “Superhydrophobic Si Surface with Low Light Reflectance.”, GTRC Invention Disclosure No. 4864 (2009)
38. Rongwei Zhang, Kyoung Sik Moon, Wei Lin, **Yan Liu**, C. P. Wong, “Fluxless metal-metal bonding for 3D IC stacking”, GTRC Invention Disclosure No. 5382, (2010)
39. Zhuo Li, Rongwei Zhang, **Yan Liu**, and C. P. Wong, “Highly conductive, flexible, biocompatible poly-urethane based isotropic conductive adhesives for flexible electronics”, GTRC Invention Disclosure No. 6098 (2010)

REFERENCES

- [1] Quere, D., "Non-sticking drops," *Reports on Progress in Physics*, vol. 68, pp. 2495-2532, 2005.
- [2] Sun, T. L., Feng, L., Gao, X. F., and Jiang, L., "Bioinspired surfaces with special wettability," *Accounts of Chemical Research*, vol. 38, pp. 644-652, 2005.
- [3] Qurere, D., "Wetting and roughness," *Annual Review of Materials Research*, vol. 38, pp. 71-99, 2008.
- [4] "http://en.wikipedia.org/wiki/Contact_angle."
- [5] Feng, X. J. and Jiang, L., "Design and creation of superwetting/antiwetting surfaces," *Advanced Materials*, vol. 18, pp. 3063-3078, 2006.
- [6] Wenzel, R. N., "Resistance of solid surfaces to wetting by water," *Industrial and Engineering Chemistry*, vol. 28, pp. 988-994, 1936.
- [7] Cassie, A. B. D. and Baxter, S., "Wettability of porous surfaces.," *Transactions of the Faraday Society*, vol. 40, pp. 0546-0550, 1944.
- [8] "<http://en.wikipedia.org/wiki/Wetting>."
- [9] Tsujii, K., Yamamoto, T., Onda, T., and Shibuichi, S., "Super oil-repellent surfaces," *Angewandte Chemie-International Edition in English*, vol. 36, pp. 1011-1012, 1997.
- [10] Verplanck, N., Coffinier, Y., Thomy, V., and Boukherroub, R., "Wettability switching techniques on superhydrophobic surfaces," *Nanoscale Research Letters*, vol. 2, pp. 577-596, 2007.
- [11] Patankar, N. A., "Transition between superhydrophobic states on rough surfaces," *Langmuir*, vol. 20, pp. 7097-7102, 2004.
- [12] Sas, I., Gorga, R. E., Joines, J. A., and Thoney, K. A., "Literature review on superhydrophobic self-cleaning surfaces produced by electrospinning," *Journal of Polymer Science Part B-Polymer Physics*, vol. 50, pp. 824-845, 2012.

- [13] Ma, M. L. and Hill, R. M., "Superhydrophobic surfaces," *Current Opinion in Colloid & Interface Science*, vol. 11, pp. 193-202, 2006.
- [14] Wang, S. and Jiang, L., "Definition of superhydrophobic states," *Advanced Materials*, vol. 19, pp. 3423-3424, 2007.
- [15] Feng, L., Li, S. H., Li, Y. S., Li, H. J., Zhang, L. J., Zhai, J., Song, Y. L., Liu, B. Q., Jiang, L., and Zhu, D. B., "Super-hydrophobic surfaces: From natural to artificial," *Advanced Materials*, vol. 14, pp. 1857-1860, 2002.
- [16] Yan, Y. Y., Gao, N., and Barthlott, W., "Mimicking natural superhydrophobic surfaces and grasping the wetting process: A review on recent progress in preparing superhydrophobic surfaces," *Advances in Colloid and Interface Science*, vol. 169, pp. 80-105, 2011.
- [17] Li, X. M., Reinhoudt, D., and Crego-Calama, M., "What do we need for a superhydrophobic surface? A review on the recent progress in the preparation of superhydrophobic surfaces," *Chemical Society Reviews*, vol. 36, pp. 1529-1529, 2007.
- [18] "<http://www.ramehart.com/contactangle.htm>."
- [19] Barthlott, W. and Ehler, N., "Raster-Elektronenmikroskopie der Epidermis-Oberflächen von Spermatophyten.," *Tropische und subtropische Pflanzenwelt*, vol. 19, p. 110, 1977.
- [20] Barthlott, W. and Neinhuis, C., "Purity of the sacred lotus, or escape from contamination in biological surfaces," *Planta*, vol. 202, pp. 1-8, 1997.
- [21] Sarkar, D. K. and Farzaneh, M., "Superhydrophobic Coatings with Reduced Ice Adhesion," *Journal of Adhesion Science and Technology*, vol. 23, pp. 1215-1237, 2009.
- [22] Xue, C. H., Jia, S. T., Zhang, J., and Ma, J. Z., "Large-area fabrication of superhydrophobic surfaces for practical applications: an overview," *Science and Technology of Advanced Materials*, vol. 11, 2010.
- [23] Tuteja, A., Choi, W. J., McKinley, G. H., Cohen, R. E., and Rubner, M. F., "Design parameters for superhydrophobicity and superoleophobicity," *Mrs Bulletin*, vol. 33, pp. 752-758, 2008.

- [24] Shibuichi, S., Yamamoto, T., Onda, T., and Tsujii, K., "Super water- and oil-repellent surfaces resulting from fractal structure," *Journal of Colloid and Interface Science*, vol. 208, pp. 287-294, 1998.
- [25] Zheng, Y. M., Gao, X. F., and Jiang, L., "Directional adhesion of superhydrophobic butterfly wings," *Soft Matter*, vol. 3, pp. 178-182, 2007.
- [26] Liu, K. S. and Jiang, L., "Bio-inspired design of multiscale structures for function integration," *Nano Today*, vol. 6, pp. 155-175, 2011.
- [27] Liu, K. S., Yao, X., and Jiang, L., "Recent developments in bio-inspired special wettability," *Chemical Society Reviews*, vol. 39, pp. 3240-3255, 2010.
- [28] Deng, X., Mammen, L., Butt, H. J., and Vollmer, D., "Candle Soot as a Template for a Transparent Robust Superamphiphobic Coating," *Science*, vol. 335, pp. 67-70, 2012.
- [29] Kim, D. and Hwang, W., "A template-based superhydrophobic tube structure with nanofiber forests and its mass flow characteristic," *Journal of Micromechanics and Microengineering*, vol. 20, 2010.
- [30] Sheng, X. L. and Zhang, J. H., "Superhydrophobic Behaviors of Polymeric Surfaces with Aligned Nanofibers," *Langmuir*, vol. 25, pp. 6916-6922, 2009.
- [31] Sun, M. H., Luo, C. X., Xu, L. P., Ji, H., Qi, O. Y., Yu, D. P., and Chen, Y., "Artificial lotus leaf by nanocasting," *Langmuir*, vol. 21, pp. 8978-8981, 2005.
- [32] Pozzato, A., Dal Zilio, S., Fois, G., Vendramin, D., Mistura, G., Belotti, M., Chen, Y., and Natali, M., "Superhydrophobic surfaces fabricated by nanoimprint lithography," *Microelectronic Engineering*, vol. 83, pp. 884-888, 2006.
- [33] Shiu, J. Y., Kuo, C. W., Chen, P. L., and Mou, C. Y., "Fabrication of tunable superhydrophobic surfaces by nanosphere lithography," *Chemistry of Materials*, vol. 16, pp. 561-564, 2004.
- [34] Feng, J. S., Tuominen, M. T., and Rothstein, J. P., "Hierarchical Superhydrophobic Surfaces Fabricated by Dual-Scale Electron-Beam-Lithography with Well-Ordered Secondary Nanostructures," *Advanced Functional Materials*, vol. 21, pp. 3715-3722, 2011.
- [35] Hong, L. F. and Pan, T. R., "Photopatternable Superhydrophobic Nanocomposites for Microfabrication," *Journal of Microelectromechanical Systems*, vol. 19, pp. 246-253, 2010.

- [36] Huang, Z. P., Geyer, N., Werner, P., de Boor, J., and Gosele, U., "Metal-Assisted Chemical Etching of Silicon: A Review," *Advanced Materials*, vol. 23, pp. 285-308, 2011.
- [37] Kim, Y., Tsao, A., Lee, D. H., and Maboudian, R., "Solvent-induced formation of unidirectionally curved and tilted Si nanowires during metal-assisted chemical etching," *Journal of Materials Chemistry C*, vol. 1, pp. 220-224, 2013.
- [38] Asoh, H., Fujihara, K., and Ono, S., "Triangle pore arrays fabricated on Si (111) substrate by sphere lithography combined with metal-assisted chemical etching and anisotropic chemical etching," *Nanoscale Research Letters*, vol. 7, 2012.
- [39] Bang, B. M., Kim, H., Song, H. K., Cho, J., and Park, S., "Scalable approach to multi-dimensional bulk Si anodes via metal-assisted chemical etching," *Energy & Environmental Science*, vol. 4, pp. 5013-5019, 2011.
- [40] Nassiopoulou, A. G., Gianneta, V., and Katsogridakis, C., "Si nanowires by a single-step metal-assisted chemical etching process on lithographically defined areas: formation kinetics," *Nanoscale Research Letters*, vol. 6, 2011.
- [41] Zahedinejad, M., Khaje, M., Erfanian, A., and Raissi, F., "Successful definition of nanowire and porous Si regions of different porosity levels by regular positive photoresist using metal-assisted chemical etching," *Journal of Micromechanics and Microengineering*, vol. 21, 2011.
- [42] Huang, Z. P., Zhang, X. X., Reiche, M., Liu, L. F., Lee, W., Shimizu, T., Senz, S., and Gosele, U., "Extended arrays of vertically aligned sub-10 nm diameter [100] Si nanowires by metal-assisted chemical etching," *Nano Letters*, vol. 8, pp. 3046-3051, 2008.
- [43] Seo, J., Lee, S., Han, H., Chung, Y., Lee, J., Kim, S. D., Kim, Y. W., Lim, S., and Lee, T., "Reversible wettability control of silicon nanowire surfaces: From superhydrophilicity to superhydrophobicity," *Thin Solid Films*, vol. 527, pp. 179-185, 2013.
- [44] Di Mundo, R., Troia, M., Palumbo, F., Trotta, M., and d'Agostino, R., "Nanotexturing of Transparent Polymers with Plasma Etching: Tailoring Topography for a Low Reflectivity," *Plasma Processes and Polymers*, vol. 9, pp. 947-954, 2012.
- [45] Vesel, A. and Semenic, T., "Etching Rates of Different Polymers in Oxygen Plasma," *Materiali in Tehnologije*, vol. 46, pp. 227-231, 2012.

- [46] Eggert, L., Abraham, W., Stiegert, S., Hanff, R., and Kreysig, D., "Plasma-Etching of Thin-Layers of Organic Polymers .1. Pure Polymers," *Acta Polymerica*, vol. 39, pp. 376-379, 1988.
- [47] Lacroix, L. M., Lejeune, M., Ceriotti, L., Kormunda, M., Meziani, T., Colpo, P., and Rossi, F., "Tuneable rough surfaces: A new approach for elaboration of superhydrophobic films," *Surface Science*, vol. 592, pp. 182-188, 2005.
- [48] Mauer, J. L., Logan, J. S., Zielinski, L. B., and Schwartz, G. C., "Mechanism of Silicon Etching by a Cf₄ Plasma," *Journal of Vacuum Science & Technology*, vol. 15, pp. 1734-1738, 1978.
- [49] Cho, S. J., An, T., Kim, J. Y., Sung, J., and Lim, G., "Superhydrophobic nanostructured silicon surfaces with controllable broadband reflectance," *Chemical Communications*, vol. 47, pp. 6108-6110, 2011.
- [50] Roach, P., Shirtcliffe, N. J., and Newton, M. I., "Progress in superhydrophobic surface development," *Soft Matter*, vol. 4, pp. 224-240, 2008.
- [51] Li, Y., Liu, F., and Sun, J. Q., "A facile layer-by-layer deposition process for the fabrication of highly transparent superhydrophobic coatings," *Chemical Communications*, pp. 2730-2732, 2009.
- [52] Zhu, L. B., Xiu, Y. H., Xu, J. W., Tamirisa, P. A., Hess, D. W., and Wong, C. P., "Superhydrophobicity on two-tier rough surfaces fabricated by controlled growth of aligned carbon nanotube arrays coated with fluorocarbon," *Langmuir*, vol. 21, pp. 11208-11212, 2005.
- [53] Cao, L. L., Hu, H. H., and Gao, D., "Design and fabrication of micro-textures for inducing a superhydrophobic behavior on hydrophilic materials," *Langmuir*, vol. 23, pp. 4310-4314, 2007.
- [54] Xiu, Y. H., Hess, D. W., and Wong, C. R., "UV and thermally stable superhydrophobic coatings from sol-gel processing," *Journal of Colloid and Interface Science*, vol. 326, pp. 465-470, 2008.
- [55] Xue, C. H., Jia, S. T., Chen, H. Z., and Wang, M., "Superhydrophobic cotton fabrics prepared by sol-gel coating of TiO₂ and surface hydrophobization," *Science and Technology of Advanced Materials*, vol. 9, 2008.
- [56] Manca, M., Cannavale, A., De Marco, L., Arico, A. S., Cingolani, R., and Gigli, G., "Durable Superhydrophobic and Antireflective Surfaces by Trimethylsilanized

- Silica Nanoparticles-Based Sol-Gel Processing," *Langmuir*, vol. 25, pp. 6357-6362, 2009.
- [57] Yang, S. Y., Chen, S., Tian, Y., Feng, C., and Chen, L., "Facile transformation of a native polystyrene (PS) film into a stable superhydrophobic surface via sol-gel process," *Chemistry of Materials*, vol. 20, pp. 1233-1235, 2008.
- [58] Cao, L. L., Jones, A. K., Sikka, V. K., Wu, J. Z., and Gao, D., "Anti-Icing Superhydrophobic Coatings," *Langmuir*, vol. 25, pp. 12444-12448, 2009.
- [59] Lai, Y. K., Tang, Y. X., Gong, J. J., Gong, D. G., Chi, L. F., Lin, C. J., and Chen, Z., "Transparent superhydrophobic/superhydrophilic TiO₂-based coatings for self-cleaning and anti-fogging," *Journal of Materials Chemistry*, vol. 22, pp. 7420-7426, 2012.
- [60] http://www.worldenergyoutlook.org/docs/weo2008/WEO2008_es_english.pdf.
- [61] "Our solar power future," *The U.S. photovoltaics industry roadmap through 2030 and beyond*, 2004.
- [62] Green, M. A., Zhao, J., Wang, A., and Wenham, S. R., "Progress and outlook for high-efficiency crystalline silicon solar cells," *Solar Energy Materials and Solar Cells*, vol. 65, pp. 9-16, 2001.
- [63] "<http://www.solarfassade.info/en/fundamentals/components/pvmodules.php>."
- [64] Rahman, M. S., Islam, M. W., and Mozumder, M. Z. H., "Shadowing Loss Analysis for Different Top Contact Pattern of Concentration Solar Cell," *2012 International Conference on Informatics, Electronics & Vision (Iciev)*, pp. 707-710, 2012.
- [65] Meier, D. L. and Schroder, D. K., "Contact Resistance - Its Measurement and Relative Importance to Power Loss in a Solar-Cell," *Ieee Transactions on Electron Devices*, vol. 31, pp. 647-653, 1984.
- [66] Shewchun, J., Burk, D., Singh, R., Spitzer, M., and Dubow, J., "Semiconductor-Insulator-Semiconductor (Indium Tin Oxide on Silicon) Solar-Cell - Characteristics and Loss Mechanisms," *Journal of Applied Physics*, vol. 50, pp. 6524-6533, 1979.
- [67] Zhu, J., Yu, Z. F., Burkhard, G. F., Hsu, C. M., Connor, S. T., Xu, Y. Q., Wang, Q., McGehee, M., Fan, S. H., and Cui, Y., "Optical Absorption Enhancement in

- Amorphous Silicon Nanowire and Nanocone Arrays," *Nano Letters*, vol. 9, pp. 279-282, 2009.
- [68] Zhu, J., Hsu, C. M., Yu, Z. F., Fan, S. H., and Cui, Y., "Nanodome Solar Cells with Efficient Light Management and Self-Cleaning," *Nano Letters*, vol. 10, pp. 1979-1984, 2010.
- [69] Min, W. L., Jiang, B., and Jiang, P., "Bioinspired Self-Cleaning Antireflection Coatings," *Advanced Materials*, vol. 20, pp. 3914-+, 2008.
- [70] Choi, C. H., Ulmanella, U., Kim, J., Ho, C. M., and Kim, C. J., "Effective slip and friction reduction in nanograted superhydrophobic microchannels," *Physics of Fluids*, vol. 18, 2006.
- [71] Calcagnile, P., Fragouli, D., Bayer, I. S., Anyfantis, G. C., and Athanassiou, A., "Magnetoactive Superhydrophobic Foams for Oil-Water Separation," *Advances in Science and Technology*, vol. 77, pp. 159-164, 2013.
- [72] Wang, C. X., Yao, T. J., Wu, J., Ma, C., Fan, Z. X., Wang, Z. Y., Cheng, Y. R., Lin, Q., and Yang, B., "Facile Approach in Fabricating Superhydrophobic and Superoleophilic Surface for Water and Oil Mixture Separation," *Acs Applied Materials & Interfaces*, vol. 1, pp. 2613-2617, 2009.
- [73] Lafuma, A. and Quere, D., "Superhydrophobic states," *Nature Materials*, vol. 2, pp. 457-460, 2003.
- [74] Feng, X. Q., Gao, X. F., Wu, Z. N., Jiang, L., and Zheng, Q. S., "Superior water repellency of water strider legs with hierarchical structures: Experiments and analysis," *Langmuir*, vol. 23, pp. 4892-4896, 2007.
- [75] Marmur, A., "The lotus effect: Superhydrophobicity and metastability," *Langmuir*, vol. 20, pp. 3517-3519, 2004.
- [76] Gao, L. C. and McCarthy, T. J., "The "lotus effect" explained: Two reasons why two length scales of topography are important," *Langmuir*, vol. 22, pp. 2966-2967, 2006.
- [77] Cheng, Y. T., Rodak, D. E., Wong, C. A., and Hayden, C. A., "Effects of micro- and nano-structures on the self-cleaning behaviour of lotus leaves," *Nanotechnology*, vol. 17, pp. 1359-1362, 2006.

- [78] Bhushan, B. and Jung, Y. C., "Micro- and nanoscale characterization of hydrophobic and hydrophilic leaf surfaces," *Nanotechnology*, vol. 17, pp. 2758-2772, 2006.
- [79] Wang, S. T., Feng, L., and Jiang, L., "One-step solution-immersion process for the fabrication of stable bionic superhydrophobic surfaces," *Advanced Materials*, vol. 18, pp. 767-+, 2006.
- [80] Choi, C. H., Ulmanella, U., Kim, J., Ho, C. M., and Kim, C. J., "Effective slip and friction reduction in nanograted superhydrophobic microchannels," *Physics of Fluids*, vol. 18, pp. -, 2006.
- [81] Xiu, Y. H., Zhu, L. B., Hess, D. W., and Wong, C. P., "Biomimetic creation of hierarchical surface structures by combining colloidal self-assembly and Au sputter deposition," *Langmuir*, vol. 22, pp. 9676-9681, 2006.
- [82] Tuteja, A., Choi, W., Ma, M. L., Mabry, J. M., Mazzella, S. A., Rutledge, G. C., McKinley, G. H., and Cohen, R. E., "Designing superoleophobic surfaces," *Science*, vol. 318, pp. 1618-1622, 2007.
- [83] Xiu, Y., Zhu, L., Hess, D. W., and Wong, C. P., "Hierarchical silicon etched structures for controlled hydrophobicity/superhydrophobicity," *Nano Letters*, vol. 7, pp. 3388-3393, 2007.
- [84] Extrand, C. W., "Model for contact angles and hysteresis on rough and ultraphobic surfaces," *Langmuir*, vol. 18, pp. 7991-7999, 2002.
- [85] Ahuja, A., Taylor, J. A., Lifton, V., Sidorenko, A. A., Salamon, T. R., Lobaton, E. J., Kolodner, P., and Krupenkin, T. N., "Nanonails: A simple geometrical approach to electrically tunable superlyophobic surfaces," *Langmuir*, vol. 24, pp. 9-14, 2008.
- [86] Cao, L. L., Price, T. P., Weiss, M., and Gao, D., "Super water- and oil-repellent surfaces on intrinsically hydrophilic and oleophilic porous silicon films," *Langmuir*, vol. 24, pp. 1640-1643, 2008.
- [87] Xiu, Y. H., Zhang, S., Yelundur, V., Rohatgi, A., Hess, D. W., and Wong, C. P., "Superhydrophobic and low light reflectivity silicon surfaces fabricated by hierarchical etching," *Langmuir*, vol. 24, pp. 10421-10426, 2008.
- [88] Canham, L., Ed., *Properties of Porous Silicon* London, UK: Institution of Engineering and Technology 1997, p.^pp. Pages.

- [89] Tsori, Y., "Discontinuous liquid rise in capillaries with varying cross-sections," *Langmuir*, vol. 22, pp. 8860-8863, 2006.
- [90] Shibuichi, S., Onda, T., Satoh, N., and Tsujii, K., "Super water-repellent surfaces resulting from fractal structure," *Journal of Physical Chemistry*, vol. 100, pp. 19512-19517, 1996.
- [91] Zhuang, D. and Edgar, J. H., "Wet etching of GaN, AlN, and SiC: a review," *Materials Science & Engineering R-Reports*, vol. 48, pp. 1-46, 2005.
- [92] Wu, K. H., Fang, Y. K., Hsieh, W. T., Ho, J. J., Lin, W. J., and Hwang, J. D., "High-responsivity porous-SiC thin-film pn junction photodetector," *Electronics Letters*, vol. 34, pp. 2243-2244, 1998.
- [93] Connolly, E. J., Timmer, B., Pham, H. T. M., Groeneweg, J., Sarro, P. M., Olthuis, W., and French, P. J., "A porous SiC ammonia sensor," *Sensors and Actuators B-Chemical*, vol. 109, pp. 44-46, 2005.
- [94] John E. Shwop, W. H. V. A., "Semiconductor reliability volume 2," *United States. Advisory Group on Electron Tubes*, 1962.
- [95] Rosso, M., Arafat, A., Schroen, K., Giesbers, M., Roper, C. S., Maboudian, R., and Zuilhof, H., "Covalent attachment of organic monolayers to silicon carbide surfaces," *Langmuir*, vol. 24, pp. 4007-4012, 2008.
- [96] Liu, Y., Xiu, Y. H., Hess, D. W., and Wong, C. P., "Silicon Surface Structure-Controlled Oleophobicity," *Langmuir*, vol. 26, pp. 8908-8913, 2010.
- [97] Xiu, Y. H., Liu, Y., Hess, D. W., and Wong, C. P., "Mechanically robust superhydrophobicity on hierarchically structured Si surfaces," *Nanotechnology*, vol. 21, pp. -, 2010.
- [98] Niu, J. J., Wang, J. N., and Xu, Q. F., "Aligned silicon carbide nanowire crossed nets with high superhydrophobicity," *Langmuir*, vol. 24, pp. 6918-6923, 2008.
- [99] Niu, J. J. and Wang, J. N., "A Novel Self-Cleaning Coating with Silicon Carbide Nanowires," *Journal of Physical Chemistry B*, vol. 113, pp. 2909-2912, 2009.
- [100] Wang, J. J., Lambers, E. S., Pearton, S. J., Ostling, M., Zetterling, C. M., Grow, J. M., Ren, F., and Shul, R. J., "ICP etching of SiC," *Solid-State Electronics*, vol. 42, pp. 2283-2288, 1998.

- [101] Boukezzata, A., Keffous, A., Cheriet, A., Belkacem, Y., Gabouze, N., Manseri, A., Nezzal, G., Kechouane, M., Bright, A., Guerbous, L., and Menari, H., "Structural and optical properties of thin films porous amorphous silicon carbide formed by Ag-assisted photochemical etching," *Applied Surface Science*, vol. 256, pp. 5592-5595, 2010.
- [102] Kato, M., Ichimura, M., Arai, E., and Ramasamy, P., "Electrochemical etching of n-type 6H-SiC using aqueous KOH solutions," *Silicon Carbide and Related Materials - 2002*, vol. 433-4, pp. 665-668, 2002.
- [103] Bourenane, K., Keffous, A., Nezzal, G., Boukezzata, A., and Naama, S., "Chemical etching of hot-pressed p-type polycrystalline SiC surfaces by HF/K₂S₂O₈ solutions," *Surface and Interface Analysis*, vol. 39, pp. 392-396, 2007.
- [104] Chang, W. H., Schellin, B., Obermeier, E., and Huang, Y. C., "Electrochemical etching of n-type 6H-SiC without UV illumination," *Journal of Microelectromechanical Systems*, vol. 15, pp. 548-552, 2006.
- [105] Rittenhouse, T. L., Bohn, P. W., and Adesida, I., "Structural and spectroscopic characterization of porous silicon carbide formed by Pt-assisted electroless chemical etching," *Solid State Communications*, vol. 126, pp. 245-250, 2003.
- [106] Chuah, L. S., Hassan, Z., and Abu Hassan, H., "Enhanced UV photodetector responsivity in porous GaN by Pt assisted electroless etching," *Optoelectronics and Advanced Materials-Rapid Communications*, vol. 1, pp. 400-403, 2007.
- [107] Diaz, D. J., Williamson, T. L., Guo, X. Y., Sood, A., and Bohn, P. W., "Electroless deposition of gold and platinum for metallization of the intrapore space in porous gallium nitride," *Thin Solid Films*, vol. 514, pp. 120-126, 2006.
- [108] Cao, L. H., Li, B. H., and Zhao, J. H., "Etching of SiC using inductively coupled plasma," *Journal of the Electrochemical Society*, vol. 145, pp. 3609-3612, 1998.
- [109] Yih, P. H., Saxena, V., and Steckl, A. J., "A review of SiC reactive ion etching in fluorinated plasmas," *Physica Status Solidi B-Basic Research*, vol. 202, pp. 605-642, 1997.
- [110] Bardwell, J. A., Webb, J. B., Tang, H., Fraser, J., and Moisa, S., "Ultraviolet photoenhanced wet etching of GaN in K₂S₂O₈ solution," *Journal of Applied Physics*, vol. 89, pp. 4142-4149, 2001.

- [111] Cho, H., Auh, K. H., Han, J., Shul, R. J., Donovan, S. M., Abernathy, C. R., Lambers, E. S., Ren, F., and Pearton, S. J., "UV-photoassisted etching of GaN in KOH," *Journal of Electronic Materials*, vol. 28, pp. 290-294, 1999.
- [112] Scofield, J. D., Bletzinger, P., and Ganguly, B. N., "Oxygen-free dry etching of alpha-SiC using dilute SF₆ : Ar in an asymmetric parallel plate 13.56 MHz discharge," *Applied Physics Letters*, vol. 73, pp. 76-78, 1998.
- [113] Camara, N. and Zekentes, K., "Study of the reactive ion etching of 6H-SiC and 4H-SiC in SF₆/Ar plasmas by optical emission spectroscopy and laser interferometry," *Solid-State Electronics*, vol. 46, pp. 1959-1963, 2002.
- [114] Fan, J. Y., Wu, X. L., and Chu, P. K., "Low-dimensional SiC nanostructures: Fabrication, luminescence, and electrical properties," *Progress in Materials Science*, vol. 51, pp. 983-1031, 2006.
- [115] Botsoa, J., Bluet, J. M., Lysenko, V., Marty, O., Barbier, D., and Guillot, G., "Photoluminescence of 6H-SiC nanostructures fabricated by electrochemical etching," *Journal of Applied Physics*, vol. 102, pp. -, 2007.
- [116] Petrovakoch, V., Sreseli, O., Polisski, G., Kovalev, D., Muschik, T., and Koch, F., "Luminescence Enhancement by Electrochemical Etching of Sic(6h)," *Thin Solid Films*, vol. 255, pp. 107-110, 1995.
- [117] Lin, Z. Y., Liu, Y., and Wong, C. P., "Facile Fabrication of Superhydrophobic Octadecylamine-Functionalized Graphite Oxide Film," *Langmuir*, vol. 26, pp. 16110-16114, 2010.
- [118] Liu, Y., Lin, W. C., Lin, Z. Y., Xiu, Y. H., and Wong, C. P., "A combined etching process toward robust superhydrophobic SiC surfaces," *Nanotechnology*, vol. 23, p. 255703, 2012.
- [119] Kang, B. J., Kim, Y. S., Cho, Y. W., and Oh, J. H., "Effects of plasma surface treatments on inkjet-printed feature sizes and surface characteristics," *Microelectronic Engineering*, vol. 88, pp. 2355-2358, 2011.
- [120] Takei, G., Nonogi, M., Hibara, A., Kitamori, T., and Kim, H. B., "Tuning microchannel wettability and fabrication of multiple-step Laplace valves," *Lab on a Chip*, vol. 7, pp. 596-602, 2007.
- [121] Xiu, Y. H., Liu, Y., Hess, D. W., and Wong, C. P., "Mechanically robust superhydrophobicity on hierarchically structured Si surfaces," *Nanotechnology*, vol. 21, 2010.

- [122] Sinha, A. K., Basu, M., Pradhan, M., Sarkar, S., Negishi, Y., and Pal, T., "Redox-Switchable Superhydrophobic Silver Composite," *Langmuir*, vol. 27, pp. 11629-11635, 2011.
- [123] Sun, R. D., Nakajima, A., Fujishima, A., Watanabe, T., and Hashimoto, K., "Photoinduced surface wettability conversion of ZnO and TiO₂ thin films," *Journal of Physical Chemistry B*, vol. 105, pp. 1984-1990, 2001.
- [124] Feng, X. J., Zhai, J., and Jiang, L., "The fabrication and switchable superhydrophobicity of TiO₂ nanorod films," *Angewandte Chemie-International Edition*, vol. 44, pp. 5115-5118, 2005.
- [125] Lim, H. S., Kwak, D., Lee, D. Y., Lee, S. G., and Cho, K., "UV-Driven reversible switching of a rose-like vanadium oxide film between superhydrophobicity and superhydrophilicity," *Journal of the American Chemical Society*, vol. 129, pp. 4128+, 2007.
- [126] Zhu, W. Q., Feng, X. J., Feng, L., and Jiang, L., "UV-manipulated wettability between superhydrophobicity and superhydrophilicity on a transparent and conductive SnO₂ nanorod film," *Chemical Communications*, pp. 2753-2755, 2006.
- [127] Leung, K. C. F., Xuan, S. H., and Lo, C. M., "Reversible Switching between Hydrophilic and Hydrophobic Superparamagnetic Iron Oxide Microspheres via One-Step Supramolecular Dynamic Dendronization: Exploration of Dynamic Wettability," *Acs Applied Materials & Interfaces*, vol. 1, pp. 2005-2012, 2009.
- [128] Kobayashi, T., Shimizu, K., Kaizuma, Y., and Konishi, S., "Novel combination of hydrophilic/hydrophobic surface for large wettability difference and its application to liquid manipulation," *Lab on a Chip*, vol. 11, pp. 639-644, 2011.
- [129] Leng, W. G., Zhou, S. X., Gu, G. X., and Wu, L. M., "Wettability switching of SDS-doped polyaniline from hydrophobic to hydrophilic induced by alkaline/reduction reactions," *Journal of Colloid and Interface Science*, vol. 369, pp. 411-418, 2012.
- [130] Uyama, A., Yamazoe, S., Shigematsu, S., Morimoto, M., Yokojima, S., Mayama, H., Kojima, Y., Nakamura, S., and Uchida, K., "Reversible Photocontrol of Surface Wettability between Hydrophilic and Superhydrophobic Surfaces on an Asymmetric Diarylethene Solid Surface," *Langmuir*, vol. 27, pp. 6395-6400, 2011.
- [131] Tang, Z. K., Wong, G. K. L., Yu, P., Kawasaki, M., Ohtomo, A., Koinuma, H., and Segawa, Y., "Room-temperature ultraviolet laser emission from self-

- assembled ZnO microcrystallite thin films," *Applied Physics Letters*, vol. 72, pp. 3270-3272, 1998.
- [132] Huang, M. H., Mao, S., Feick, H., Yan, H. Q., Wu, Y. Y., Kind, H., Weber, E., Russo, R., and Yang, P. D., "Room-temperature ultraviolet nanowire nanolasers," *Science*, vol. 292, pp. 1897-1899, 2001.
- [133] Park, W. I. and Yi, G. C., "Electroluminescence in n-ZnO nanorod arrays vertically grown on p-GaN," *Advanced Materials*, vol. 16, pp. 87-+, 2004.
- [134] Lee, C. J., Lee, T. J., Lyu, S. C., Zhang, Y., Ruh, H., and Lee, H. J., "Field emission from well-aligned zinc oxide nanowires grown at low temperature," *Applied Physics Letters*, vol. 81, pp. 3648-3650, 2002.
- [135] Zhu, Y. W., Zhang, H. Z., Sun, X. C., Feng, S. Q., Xu, J., Zhao, Q., Xiang, B., Wang, R. M., and Yu, D. P., "Efficient field emission from ZnO nanoneedle arrays," *Applied Physics Letters*, vol. 83, pp. 144-146, 2003.
- [136] Xu, S., Qin, Y., Xu, C., Wei, Y. G., Yang, R. S., and Wang, Z. L., "Self-powered nanowire devices," *Nature Nanotechnology*, vol. 5, pp. 366-373, 2010.
- [137] Wang, Z. L. and Song, J. H., "Piezoelectric nanogenerators based on zinc oxide nanowire arrays," *Science*, vol. 312, pp. 242-246, 2006.
- [138] Law, M., Greene, L. E., Johnson, J. C., Saykally, R., and Yang, P. D., "Nanowire dye-sensitized solar cells," *Nature Materials*, vol. 4, pp. 455-459, 2005.
- [139] Liu, Y., Das, A., Xu, S., Lin, Z. Y., Xu, C., Wang, Z. L., Rohatgi, A., and Wong, C. P., "Hybridizing ZnO Nanowires with Micropyramid Silicon Wafers as Superhydrophobic High-Efficiency Solar Cells," *Advanced Energy Materials*, vol. 2, pp. 47-51, 2012.
- [140] Xu, S. and Wang, Z. L., "One-dimensional ZnO nanostructures: Solution growth and functional properties," *Nano Research*, vol. 4, pp. 1013-1098, 2011.
- [141] Xu, B. and Cai, Z. S., "Fabrication of a superhydrophobic ZnO nanorod array film on cotton fabrics via a wet chemical route and hydrophobic modification," *Applied Surface Science*, vol. 254, pp. 5899-5904, 2008.
- [142] Liu, Y., Lin, Z. Y., Moon, K. S., and Wong, C. P., "Novel ZnO Nanowires/Silicon Hierarchical Structures for Superhydrophobic, Low Reflection, and High Efficiency Solar Cells," *Proceedings of the IEEE 61th Electronic Components Technology Conference*, p. 2114, 2011.

- [143] Liu, H., Feng, L., Zhai, J., Jiang, L., and Zhu, D. B., "Reversible wettability of a chemical vapor deposition prepared ZnO film between superhydrophobicity and superhydrophilicity," *Langmuir*, vol. 20, pp. 5659-5661, 2004.
- [144] Lv, J. G., Zhu, J. B., Huang, K., Meng, F. M., Song, X. P., and Sun, Z. Q., "Tunable surface wettability of ZnO nanorods prepared by two-step method," *Applied Surface Science*, vol. 257, pp. 7534-7538, 2011.
- [145] Kumar, P. S., Raj, A. D., Mangalaraj, D., Nataraj, D., Ponpandian, N., Li, L., and Chabrol, G., "Growth of hierarchical based ZnO micro/nanostructured films and their tunable wettability behavior," *Applied Surface Science*, vol. 257, pp. 6678-6686, 2011.
- [146] Das, S. N., Choi, J. H., Kar, J. P., and Myoung, J. M., "Tunable and reversible surface wettability transition of vertically aligned ZnO nanorod arrays," *Applied Surface Science*, vol. 255, pp. 7319-7322, 2009.
- [147] Li, G. P., Chen, T., Yan, B., Ma, Y., Zhang, Z., Yu, T., Shen, Z. X., Chen, H. Y., and Wu, T., "Tunable wettability in surface-modified ZnO-based hierarchical nanostructures," *Applied Physics Letters*, vol. 92, 2008.
- [148] Feng, X. J., Feng, L., Jin, M. H., Zhai, J., Jiang, L., and Zhu, D. B., "Reversible super-hydrophobicity to super-hydrophilicity transition of aligned ZnO nanorod films," *Journal of the American Chemical Society*, vol. 126, pp. 62-63, 2004.
- [149] Kwak, G., Seol, M., Tak, Y., and Yong, K., "Superhydrophobic ZnO Nanowire Surface: Chemical Modification and Effects of UV Irradiation," *Journal of Physical Chemistry C*, vol. 113, pp. 12085-12089, 2009.
- [150] Lee, J. P., Kim, H. K., Park, C. R., Park, G., Kwak, H. T., Koo, S. M., and Sung, M. M., "Photocatalytic decomposition of alkylsiloxane self-assembled monolayers on titanium oxide surfaces," *Journal of Physical Chemistry B*, vol. 107, pp. 8997-9002, 2003.
- [151] Xiu, Y. H., Liu, Y., Balu, B., Hess, D. W., and Wong, C. P., "Robust Superhydrophobic Surfaces Prepared with Epoxy Resin and Silica Nanoparticles," *Ieee Transactions on Components Packaging and Manufacturing Technology*, vol. 2, pp. 395-401, 2012.
- [152] Liu, Y., Lin, Z. Y., Lin, W., Moon, K. S., and Wong, C. P., "Reversible Superhydrophobic-Superhydrophilic Transition of ZnO Nanorod/Epoxy Composite Films," *Acs Applied Materials & Interfaces*, p. in press, 2012.

- [153] Shang, H. M., Wang, Y., Limmer, S. J., Chou, T. P., Takahashi, K., and Cao, G. Z., "Optically transparent superhydrophobic silica-based films," *Thin Solid Films*, vol. 472, pp. 37-43, 2005.
- [154] Jin, M. H., Feng, X. J., Feng, L., Sun, T. L., Zhai, J., Li, T. J., and Jiang, L., "Superhydrophobic aligned polystyrene nanotube films with high adhesive force," *Advanced Materials*, vol. 17, pp. 1977-+, 2005.
- [155] Liu, Y., Xiu, Y. H., and Wong, C. P., "Micro/Nano Structure Size Effect on Superhydrophobicity and Anti Reflection of Single Crystalline Si Solar Cells," *2010 Proceedings 60th Electronic Components and Technology Conference (Ectc)*, pp. 1719-1724, 2010.
- [156] Liu, Y., Lin, Z. Y., Moon, K. S., and Wong, C. P., "Novel ZnO Nanowires/Silicon Hierarchical Structures for Superhydrophobic, Low Reflection, and High Efficiency Solar Cells," *2011 Proceedings 60th Electronic Components and Technology Conference (Ectc)*, pp. 2114-2118, 2011.
- [157] Xiu, Y. H., Zhu, L. B., Hess, D. W., and Wong, C. P., "Superhydrophobic durable silica thin films from sol-gel processing for the application in antistiction of MEMS devices," *Abstracts of Papers of the American Chemical Society*, vol. 231, 2006.
- [158] Wong, C. P. and Wong, M. M., "Recent advances in plastic packaging of flip-chip and multichip modules (MCM) of microelectronics," *Ieee Transactions on Components and Packaging Technologies*, vol. 22, pp. 21-25, 1999.
- [159] Iannuzzi, M., "Reliability and Failure Mechanisms of Nonhermetic Aluminum Sics - Literature-Review and Bias Humidity Performance," *Ieee Transactions on Components Hybrids and Manufacturing Technology*, vol. 6, pp. 181-190, 1983.
- [160] Sbar, N. L. and Kozakiewicz, R. P., "New Acceleration Factors for Temperature, Humidity, Bias Testing," *Ieee Transactions on Electron Devices*, vol. 26, pp. 56-71, 1979.
- [161] Wong, C. P., "High-Performance Silicone Gel as Ic Device Chip Protection-Cure Study and Electrical Reliability," *Abstracts of Papers of the American Chemical Society*, vol. 196, pp. 102-PMSE, 1988.
- [162] Mancke, R. G., "A Moisture Protection Screening-Test for Hybrid Circuit Encapsulants," *Ieee Transactions on Components Hybrids and Manufacturing Technology*, vol. 4, pp. 492-498, 1981.

- [163] Wu, J. L., Pike, R. T., Wong, C. P., Kim, N. P., and Tanielian, M. H., "Evaluation and characterization of reliable non-hermetic conformal coatings for microelectromechanical system (MEMS) device encapsulation," *Ieee Transactions on Advanced Packaging*, vol. 23, pp. 721-728, 2000.
- [164] Moule, A. J. and Meerholz, K., "Minimizing optical losses in bulk heterojunction polymer solar cells," *Applied Physics B-Lasers and Optics*, vol. 86, pp. 721-727, 2007.
- [165] Xu, H. B., Lu, N., Qi, D. P., Hao, J. Y., Gao, L. G., Zhang, B., and Chi, L. F., "Biomimetic Antireflective Si Nanopillar Arrays," *Small*, vol. 4, pp. 1972-1975, 2008.
- [166] Linn, N. C., Sun, C. H., Jiang, P., and Jiang, B., "Self-assembled biomimetic antireflection coatings," *Applied Physics Letters*, vol. 91, pp. -, 2007.
- [167] Tang, Y. B., Chen, Z. H., Song, H. S., Lee, C. S., Cong, H. T., Cheng, H. M., Zhang, W. J., Bello, I., and Lee, S. T., "Vertically Aligned p-Type Single-Crystalline GaN Nanorod Arrays on n-Type Si for Heterojunction Photovoltaic Cells," *Nano Letters*, vol. 8, pp. 4191-4195, 2008.
- [168] Wang, Z. L., "ZnO nanowire and nanobelt platform for nanotechnology," *Materials Science & Engineering R-Reports*, vol. 64, pp. 33-71, 2009.
- [169] Mor, G. K., Varghese, O. K., Paulose, M., Shankar, K., and Grimes, C. A., "A review on highly ordered, vertically oriented TiO₂ nanotube arrays: Fabrication, material properties, and solar energy applications," *Solar Energy Materials and Solar Cells*, vol. 90, pp. 2011-2075, 2006.
- [170] Huynh, W. U., Dittmer, J. J., and Alivisatos, A. P., "Hybrid nanorod-polymer solar cells," *Science*, vol. 295, pp. 2425-2427, 2002.
- [171] Huang, Y. F., Chattopadhyay, S., Jen, Y. J., Peng, C. Y., Liu, T. A., Hsu, Y. K., Pan, C. L., Lo, H. C., Hsu, C. H., Chang, Y. H., Lee, C. S., Chen, K. H., and Chen, L. C., "Improved broadband and quasi-omnidirectional anti-reflection properties with biomimetic silicon nanostructures," *Nature Nanotechnology*, vol. 2, pp. 770-774, 2007.
- [172] Peng, K. Q., Wang, X., and Lee, S. T., "Silicon nanowire array photoelectrochemical solar cells," *Applied Physics Letters*, vol. 92, pp. -, 2008.

- [173] Peng, K. Q., Wang, X., Wu, X. L., and Lee, S. T., "Platinum Nanoparticle Decorated Silicon Nanowires for Efficient Solar Energy Conversion," *Nano Letters*, vol. 9, pp. 3704-3709, 2009.
- [174] Menna, P., Difrancia, G., and Laferrara, V., "Porous Silicon in Solar-Cells - a Review and a Description of Its Application as an Ar Coating," *Solar Energy Materials and Solar Cells*, vol. 37, pp. 13-24, 1995.
- [175] Kim, J., Hong, J., and Lee, S. H., "Application of PECVD SiN_x films to screen-printed multicrystalline silicon solar cell," *Journal of the Korean Physical Society*, vol. 44, pp. 479-482, 2004.
- [176] Li, X., Gao, J. P., Xue, L. J., and Han, Y. C., "Porous Polymer Films with Gradient-Refractive-Index Structure for Broadband and Omnidirectional Antireflection Coatings," *Advanced Functional Materials*, vol. 20, pp. 259-265, 2010.
- [177] Chhajed, S., Schubert, M. F., Kim, J. K., and Schubert, E. F., "Nanostructured multilayer graded-index antireflection coating for Si solar cells with broadband and omnidirectional characteristics," *Applied Physics Letters*, vol. 93, pp. -, 2008.
- [178] Pan, Z. W., Dai, Z. R., and Wang, Z. L., "Nanobelts of semiconducting oxides," *Science*, vol. 291, pp. 1947-1949, 2001.
- [179] Xu, S., Wei, Y., Kirkham, M., Liu, J., Mai, W., Davidovic, D., Snyder, R. L., and Wang, Z. L., "Patterned Growth of Vertically Aligned ZnO Nanowire Arrays on Inorganic Substrates at Low Temperature without Catalyst," *Journal of the American Chemical Society*, vol. 130, pp. 14958-+, 2008.
- [180] Hong, J. I., Bae, J., Wang, Z. L., and Snyder, R. L., "Room-temperature, texture-controlled growth of ZnO thin films and their application for growing aligned ZnO nanowire arrays," *Nanotechnology*, vol. 20, pp. -, 2009.
- [181] Takato, H., Yamanaka, M., Hayashi, Y., Shimokawa, R., Hide, I., Gohda, S., Nagamine, F., and Tsuboi, H., "Effects of Optical Confinement in Textured Antireflection Coating Using ZnO Films for Solar-Cells," *Japanese Journal of Applied Physics Part 2-Letters*, vol. 31, pp. L1665-L1667, 1992.
- [182] Weintraub, B., Wei, Y. G., and Wang, Z. L., "Optical Fiber/Nanowire Hybrid Structures for Efficient Three-Dimensional Dye-Sensitized Solar Cells," *Angewandte Chemie-International Edition*, vol. 48, pp. 8981-8985, 2009.

- [183] Wei, Y. G., Xu, C., Xu, S., Li, C., Wu, W. Z., and Wang, Z. L., "Planar Waveguide-Nanowire Integrated Three-Dimensional Dye-Sensitized Solar Cells," *Nano Letters*, vol. 10, pp. 2092-2096, 2010.
- [184] Lee, Y. J., Ruby, D. S., Peters, D. W., McKenzie, B. B., and Hsu, J. W. P., "ZnO nanostructures as efficient antireflection layers in solar cells," *Nano Letters*, vol. 8, pp. 1501-1505, 2008.
- [185] Lin, Z., Cheng, Y. R., Lu, H., Zhang, L. A., and Yang, B., "Preparation and characterization of novel ZnS/sulfur-containing polymer nanocomposite optical materials with high refractive index and high nanophase contents," *Polymer*, vol. 51, pp. 5424-5431, 2010.
- [186] Xu, S., Lao, C., Weintraub, B., and Wang, Z. L., "Density-controlled growth of aligned ZnO nanowire arrays by seedless chemical approach on smooth surfaces," *Journal of Materials Research*, vol. 23, pp. 2072-2077, 2008.
- [187] Xu, S., Adiga, N., Ba, S., Dasgupta, T., Wu, C. F. J., and Wang, Z. L., "Optimizing and Improving the Growth Quality of ZnO Nanowire Arrays Guided by Statistical Design of Experiments," *Acs Nano*, vol. 3, pp. 1803-1812, 2009.
- [188] Brendel, R., "SUNRAYS: A versatile ray tracing program for the photovoltaic community," *Proceedings of the 12th European Photovoltaic Solar Energy Conference*, pp. 1339-1342, 1994.
- [189] Hill, M., "Handbook of Optics, 2nd edition," *Handbook of Optics, 2nd edition*, vol. 2, 1994.
- [190] Zhao, J. H., Wang, A. H., Green, M. A., and Ferrazza, F., "19.8% efficient "honeycomb" textured multicrystalline and 24.4% monocrystalline silicon solar cells," *Applied Physics Letters*, vol. 73, pp. 1991-1993, 1998.
- [191] Berginski, M., Hupkes, J., Gordijn, A., Reetz, W., Watjen, T., Rech, B., and Wuttig, M., "Experimental studies and limitations of the light trapping and optical losses in microcrystalline silicon solar cells," *Solar Energy Materials and Solar Cells*, vol. 92, pp. 1037-1042, 2008.
- [192] Linn, N. C., Sun, C. H., Jiang, P., and Jiang, B., "Self-assembled biomimetic antireflection coatings," *Applied Physics Letters*, vol. 91, 2007.
- [193] Aberle, A. G., "Overview on SiN surface passivation of crystalline silicon solar cells," *Solar Energy Materials and Solar Cells*, vol. 65, pp. 239-248, 2001.

- [194] Chhajed, S., Schubert, M. F., Kim, J. K., and Schubert, E. F., "Nanostructured multilayer graded-index antireflection coating for Si solar cells with broadband and omnidirectional characteristics," *Applied Physics Letters*, vol. 93, 2008.
- [195] Toor, F., Branz, H. M., Page, M. R., Jones, K. M., and Yuan, H. C., "Multi-scale surface texture to improve blue response of nanoporous black silicon solar cells," *Applied Physics Letters*, vol. 99, 2011.
- [196] Kumar, D., Srivastava, S. K., Singh, P. K., Husain, M., and Kumar, V., "Fabrication of silicon nanowire arrays based solar cell with improved performance," *Solar Energy Materials and Solar Cells*, vol. 95, pp. 215-218, 2011.
- [197] Yuan, H. C., Yost, V. E., Page, M. R., Stradins, P., Meier, D. L., and Branz, H. M., "Efficient black silicon solar cell with a density-graded nanoporous surface: Optical properties, performance limitations, and design rules," *Applied Physics Letters*, vol. 95, 2009.
- [198] Xia, Y., Liu, B. W., Liu, J., Shen, Z. N., and Li, C. B., "A novel method to produce black silicon for solar cells," *Solar Energy*, vol. 85, pp. 1574-1578, 2011.
- [199] Koynov, S., Brandt, M. S., and Stutzmann, M., "Black nonreflecting silicon surfaces for solar cells," *Applied Physics Letters*, vol. 88, 2006.
- [200] Zuev, D. A., Novodvorsky, O. A., Khaydukov, E. V., Khramova, O. D., Lotin, A. A., Parshina, L. S., Rocheva, V. V., Panchenko, V. Y., Dvorkin, V. V., Poroykov, A. Y., Untila, G. G., Chebotareva, A. B., Kost, T. N., and Timofeyev, M. A., "Fabrication of black multicrystalline silicon surface by nanosecond laser ablation," *Applied Physics B-Lasers and Optics*, vol. 105, pp. 545-550, 2011.
- [201] Nayak, B. K., Iyengar, V. V., and Gupta, M. C., "Efficient light trapping in silicon solar cells by ultrafast-laser-induced self-assembled micro/nano structures," *Progress in Photovoltaics*, vol. 19, pp. 631-639, 2011.
- [202] Nositschka, W. A., Voigt, O., Manshanden, P., and Kurz, H., "Texturisation of multicrystalline silicon solar cells by RIE and plasma etching," *Solar Energy Materials and Solar Cells*, vol. 80, pp. 227-237, 2003.
- [203] Srivastava, S. K., Kumar, D., Vandana, Sharma, M., Kumar, R., and Singh, P. K., "Silver catalyzed nano-texturing of silicon surfaces for solar cell applications," *Solar Energy Materials and Solar Cells*, vol. 100, pp. 33-38, 2012.

- [204] Qi, D. A. P., Lu, N., Xu, H. B., Yang, B. J., Huang, C. Y., Xu, M. J., Gao, L. G., Wang, Z. X., and Chi, L. F., "Simple Approach to Wafer-Scale Self-Cleaning Antireflective Silicon Surfaces," *Langmuir*, vol. 25, pp. 7769-7772, 2009.
- [205] Otto, M., Kroll, M., Kasebier, T., Salzer, R., Tunnermann, A., and Wehrspohn, R. B., "Extremely low surface recombination velocities in black silicon passivated by atomic layer deposition," *Applied Physics Letters*, vol. 100, 2012.
- [206] Liu, Y. P., Lai, T., Li, H. L., Wang, Y., Mei, Z. X., Liang, H. L., Li, Z. L., Zhang, F. M., Wang, W. J., Kuznetsov, A. Y., and Du, X. L., "Nanostructure Formation and Passivation of Large-Area Black Silicon for Solar Cell Applications," *Small*, vol. 8, pp. 1392-1397, 2012.
- [207] Krames, M. R., Shchekin, O. B., Mueller-Mach, R., Mueller, G. O., Zhou, L., Harbers, G., and Craford, M. G., "Status and future of high-power light-emitting diodes for solid-state lighting," *Journal of Display Technology*, vol. 3, pp. 160-175, 2007.
- [208] Mont, F. W. and Schubert, E. F., "High-refractive-index TiO₂-nanoparticle-loaded encapsulants for light-emitting diodes (vol 103, 083120, 2008)," *Journal of Applied Physics*, vol. 107, 2010.
- [209] Liu, J. G. and Ueda, M., "High refractive index polymers: fundamental research and practical applications," *Journal of Materials Chemistry*, vol. 19, pp. 8907-8919, 2009.
- [210] Ma, M., Mont, F. W., Yan, X., Cho, J., Schubert, E. F., Kim, G. B., and Sone, C., "Effects of the refractive index of the encapsulant on the light-extraction efficiency of light-emitting diodes," *Optics Express*, vol. 19, pp. A1135-A1140, 2011.
- [211] Lu, C. L. and Yang, B., "High refractive index organic-inorganic nanocomposites: design, synthesis and application," *Journal of Materials Chemistry*, vol. 19, pp. 2884-2901, 2009.
- [212] Nussbaumer, R. J., Caseri, W. R., Smith, P., and Tervoort, T., "Polymer-TiO₂ nanocomposites: A route towards visually transparent broadband UV filters and high refractive index materials," *Macromolecular Materials and Engineering*, vol. 288, pp. 44-49, 2003.
- [213] Tao, P., Li, Y., Rungta, A., Viswanath, A., Gao, J. N., Benicewicz, B. C., Siegel, R. W., and Schadler, L. S., "TiO₂ nanocomposites with high refractive index and transparency," *Journal of Materials Chemistry*, vol. 21, pp. 18623-18629, 2011.

- [214] Liu, B. T., Tang, S. J., Yu, Y. Y., and Lin, S. H., "High-refractive-index polymer/inorganic hybrid films containing high TiO₂ contents," *Colloids and Surfaces a-Physicochemical and Engineering Aspects*, vol. 377, pp. 138-143, 2011.
- [215] Jeon, I. Y. and Baek, J. B., "Nanocomposites Derived from Polymers and Inorganic Nanoparticles," *Materials*, vol. 3, pp. 3654-3674, 2010.
- [216] Liu, Y., Lin, Z. Y., Zhao, X. Y., Yoo, S., Moon, K. S., Wong, C. P., and Ieee, *ZnO Quantum Dots-filled Encapsulant for LED Packaging*. New York: Ieee, 2012.
- [217] Ruiterkamp, G. J., Hempenius, M. A., Wormeester, H., and Vancso, G. J., "Surface functionalization of titanium dioxide nanoparticles with alkanephosphonic acids for transparent nanocomposites," *Journal of Nanoparticle Research*, vol. 13, pp. 2779-2790, 2011.
- [218] Lee, S., Shin, H. J., Yoon, S. M., Yi, D. K., Choi, J. Y., and Paik, U., "Refractive index engineering of transparent ZrO₂-polydimethylsiloxane nanocomposites," *Journal of Materials Chemistry*, vol. 18, pp. 1751-1755, 2008.
- [219] Zhang, H., Han, J. S., and Yang, B., "Structural Fabrication and Functional Modulation of Nanoparticle-Polymer Composites," *Advanced Functional Materials*, vol. 20, pp. 1533-1550, 2010.
- [220] Cheng, Y. R., Lu, C., Lin, Z., Liu, Y. F., Guan, C., Lu, H., and Yang, B., "Preparation and properties of transparent bulk polymer nanocomposites with high nanophase contents," *Journal of Materials Chemistry*, vol. 18, pp. 4062-4068, 2008.
- [221] Sun, Y. P., Gu, A. J., Liang, G. Z., and Yuan, L., "Preparation and Properties of Transparent Zinc Oxide/Silicone Nanocomposites for the Packaging of High-Power Light-Emitting Diodes," *Journal of Applied Polymer Science*, vol. 121, pp. 2018-2028, 2011.
- [222] Oh, J. K., Lee, J. K., Kim, S. J., and Park, K. W., "Synthesis of phase- and shape-controlled TiO₂ nanoparticles via hydrothermal process," *Journal of Industrial and Engineering Chemistry*, vol. 15, pp. 270-274, 2009.
- [223] Yang, Y., Li, W. N., Luo, Y. S., Xiao, H. M., Fu, S. Y., and Mai, Y. W., "Novel ultraviolet-opaque, visible-transparent and light-emitting ZnO-QD/silicone composites with tunable luminescence colors," *Polymer*, vol. 51, pp. 2755-2762, 2010.

- [224] Yang, Y., Li, Y. Q., Shi, H. Q., Li, W. N., Xiao, H. M., Zhu, L. P., Luo, Y. S., Fu, S. Y., and Liu, T. X., "Fabrication and characterization of transparent ZnO-SiO₂/silicone nanocomposites with tunable emission colors," *Composites Part B-Engineering*, vol. 42, pp. 2105-2110, 2011.
- [225] Yang, Y., Li, Y. Q., Fu, S. Y., and Xiao, H. M., "Transparent and light-emitting epoxy nanocomposites containing ZnO quantum dots as encapsulating materials for solid state lighting," *Journal of Physical Chemistry C*, vol. 112, pp. 10553-10558, 2008.
- [226] Ye, S., Xiao, F., Pan, Y. X., Ma, Y. Y., and Zhang, Q. Y., "Phosphors in phosphor-converted white light-emitting diodes Recent advances in materials, techniques and properties," *Materials Science & Engineering R-Reports*, vol. 71, pp. 1-34, 2010.
- [227] Lin, C. C. and Liu, R. S., "Advances in Phosphors for Light-emitting Diodes," *Journal of Physical Chemistry Letters*, vol. 2, pp. 1268-1277, 2011.
- [228] Park, J. K., Lim, M. A., Kim, C. H., Park, H. D., Park, J. T., and Choi, S. Y., "White light-emitting diodes of GaN-based Sr₂SiO₄ : Eu and the luminescent properties," *Applied Physics Letters*, vol. 82, pp. 683-685, 2003.
- [229] Murray, C. B., Norris, D. J., and Bawendi, M. G., "Synthesis and Characterization of Nearly Monodisperse Cde (E = S, Se, Te) Semiconductor Nanocrystallites," *Journal of the American Chemical Society*, vol. 115, pp. 8706-8715, 1993.